Environmental effects on galaxy evolution at high redshift

Francesco Maria Valentino

USPC
Université Sorbonne
Paris Cité

Université Paris Diderot

Thèse de doctorat

de l'Université Sorbonne Paris Cité

Préparée à l'Université Paris Diderot

École doctorale 127 d'Astronomie et Astrophysique de l'Île de France

Laboratoire de Cosmologie et Évolution de Galaxies (CEA Saclay)

Environmental effects on galaxy evolution at high redshift

Francesco Valentino

Thèse de doctorat d'Astrophysique

Dirigée par Emanuele Daddi

Présentée et soutenue publiquement à Saclay le 12 septembre 2016

Présidente du jury : Prof. Mei, Simona (Observatoire de Paris – Univ. Paris Diderot)
Rapporteur : Dr. Kodama, Tadayuki (National Astronomical Observatory of Japan)
Rapporteur : Prof. Fynbo, Johan (Dark Cosmology Centre – Univ. of Copenhagen)
Examinateur : Prof. Dole, Hervé (Institut d'Astrophysique Spatiale d'Orsay)
Examinateur : Dr. Magdis, Georgios (Dark Cosmology Centre – Univ. of Copenhagen)
Examinatrice : Dr. Ferrari, Chiara (Observatoire de la Côte d'Azur)
Directeur de thèse : Dr. Daddi, Emanuele (CEA Saclay)

Titre : Les effets de l'environnement sur l'évolution des galaxies dans l'univers distant

Résumé : Dans cette thèse j'explore les effets de l'environnement sur les galaxies membres de l'amas CLJ1449+0856 à z=1.99 détecté en rayons X. Je me concentre en particulier sur l'accumulation et l'expulsion de gaz, la formation stellaire et l'activité des trous noirs supermassifs. Je présente les résultats d'observations spectroscopiques de galaxies actives réalisées au télescope Subaru. Les différentes propriétés des raies d'émission entre les galaxies d'amas et de champ suggèrent que les galaxies d'amas sont plus pauvres en métaux et présentent un taux spécifique de formation stellaire plus élevé. J'interprète ces observations comme étant dues à l'accumulation par ces galaxies de gaz primordial présent dans l'amas ou dans leur environnement proche. Je discute ensuite la campagne d'observation que j'ai menée au télescope Keck, en utilisant un filtre étroit pour détecter la raie Lyman-alpha (Lya) à z=1.99. Je présente la découverte d'une nébuleuse géante de gaz tiède (1e4 K) dans le coeur de l'amas. J'analyse ses propriétés physiques et j'explique sa taille et luminosité par la présence de deux noyaux actifs galactiques comme sources potentielles d'énergie, avec une contribution secondaire par des ondes de choc dues aux vents galactiques. De plus, ces derniers peuvent approvisionner la nébuleuse en gaz, ce qui est nécessaire pour contrecarrer son évaporation due à l'interaction avec le milieu intergalactique chaud détecté en rayons X (1e7 K). Finalement, j'estime la quantité d'énergie mécanique associée aux vents galactiques, et trouve qu'elle est compatible avec les prédictions de récentes simulations cosmologiques qui reproduisent les propriétés thermodynamiques des amas proches.

Mots clefs : Astrophysique – Formation et évolution des galaxies – Amas de galaxies – Univers à haut redshift – Milieu intergalactique – Milieu interstellaire – Formation stellaire

Title : Environmental effects on galaxy evolution at high redshift

Abstract : We explore the effect of the environment on galaxies in the X-ray-detected galaxy cluster CLJ1449+0856 at z=1.99, focusing on the processes regulating the gas inflow and outflow, and the consequent triggering of star formation and active galactic nuclei. First, we present a near-infrared spectroscopic follow-up of massive star-forming cluster members and their counterparts in the field with Subaru/MOIRCS. The properties of the H, N, and O nebular emission are different between the two samples, consistent with a lower metal content and a higher specific star formation rate in cluster galaxies than in the field. Physically, we interpret these difference as stemming from the extra-accretion of metal-poor gas from the cluster environment or, if triggered by mergers, the galaxy surroundings. In a second time we present the results of a Keck/LRIS narrowband imaging targeting the Lyman-alpha (Lya) transition at z=1.99. We have discovered a huge reservoir of warm gas (1e4 K) in the cluster core, shining in Lya light and extended over 100 kpc. We explore the physics of this nebula and identify two AGN as the most plausible powering sources, with a possible contribution by dissipation of mechanical energy carried by galactic winds. Moreover, we indicate galactic outflows as a source of gas supply to sustain the nebula against evaporation due to the interaction with the hot (1e7 K), X-ray emitting intracluster medium. We estimate the mechanical energy carried by outflows and injected into the surrounding medium, finding it consistent with cosmological simulations that reproduce the properties of local clusters, requiring a non-gravitational contribution to the energy budget.

Keywords : Astrophysics – Galaxy formation and evolution – Galaxy clusters – High-redshift Universe – Integalactic medium – Interstellar medium – Star formation

UNIVERSITÉ PARIS DIDEROT (PARIS 7)
ÉCOLE DOCTORALE 127 : ASTRONOMIE & ASTROPHYSIQUE

THÈSE DE DOCTORAT

FRANCESCO VALENTINO
SERVICE D'ASTROPHYSIQUE – CEA SACLAY

ENVIRONMENTAL EFFECTS ON GALAXY EVOLUTION AT HIGH REDSHIFT

THÈSE DIRIGÉE PAR EMANUELE DADDI

SOUTENUE LE 12 SEPTEMBRE 2016

JURY

Simona Mei	Présidente
Tadayuki Kodama	Rapporteur
Johan Fynbo	Rapporteur
Hervé Dole	Examinateur
Georgios Magdis	Examinateur
Chiara Ferrari	Examinatrice

ABSTRACT

Environmental effects are key drivers for galaxy evolution, as manifested in the local universe through the correlation between galaxy properties and their surrounding density. However, the importance of the environment in regulating crucial processes in galaxies, such as the formation of stars and metal enrichment, the triggering of nuclear activity, morphological transformations, and quenching, is still a subject of debate. The situation is further complicated by the simultaneous evolution of galaxies *and* the universe itself with cosmic time, and by the lack of a univocal definition of environment. The dramatic change undergone by structures through time challenges any result based on the study of the local universe only, an approach that tends to hide the physical origin of the observed environmental trends. Therefore, it is worth pushing our investigations to the distant universe, when galaxies were actively forming stars at much greater pace than today and assembling the majority of their mass.

This thesis is about the role of environment in galaxy formation and evolution at the peak of the cosmic star formation history at $z \sim 2$. In particular, I will focus on the effects induced by the most distant *bona fide* X-ray detected *cluster* known to date, CL J1449+0856 at $z = 1.99$, on its members. The cluster central region is dominated by a population of red, massive, and quiescent galaxies that resemble the objects usually found in local cluster cores. This feature and the detection of extended X-ray emission from the intracluster medium differentiate this structure from sparser *protoclusters* of star-forming galaxies at similar or higher redshift, a distinction that is not purely semantical, but physical.

First, I will present the results of a campaign of spectroscopic follow-up observations of star-forming galaxies in CL J1449+0856 with Subaru/MOIRCS. Combining the new near-IR data with previous photometric coverage and slitless spectroscopy with *HST*, I had access to a set of emission lines and continuum emission crucial to characterize the conditions of the interstellar medium in galaxies and the occurring formation of new stars. Studying the average properties of massive star-forming galaxies, I found a significant difference in the line ratio [N II]/Hα and the equivalent width of Hα with respect to mass-matched field counterparts. Not identifying any substantial deviation of the [O III]/Hβ ratio, ionization parameter or nitrogen-to-oxygen ratio, I interpreted the lower [N II]/Hα ratio in cluster galaxies as a metal deficiency induced by the inflow of fresh gas from the sur-

rounding environment. The extra-accretion of pristine or metal-poor gas and the ensuing triggering of star formation would also explain the higher equivalent width of Hα in cluster galaxies, a proxy for the specific star formation rate. Eventually, I will present two alternative scenarios involving the *local* or the *global* overdensities around cluster galaxies to justify the accretion of gas.

Gas reservoirs in CL J1449+0856 is the theme of a second project I will discuss. Here I present the outcome of a narrow-band imaging follow-up of the cluster with Keck/LRIS, targeting the Lyα transition. Originally designed to investigate the distribution of individual Lyα emitters and absorbers distributed in and around the cluster, these observations revealed a surprising emission extended over more than 100 kpc in the cluster central region. The size and luminosity of the extended emission qualify it as a "giant Lyα nebula", a class of mysterious objects currently under intense investigation by the community. This discovery confirms previous indications of a possible connection between Lyα nebulae and overdense environments and push the correlation to one of the densest peaks of matter distribution at $z \sim 2$, the core of a galaxy cluster. Intriguingly, the warm ionized nebula is spatially coincident with the X-ray emitting plasma filling the space between galaxies. On one side, this situation is reminiscent of local cool-core clusters, where strong cooling from the X-ray phase drives thermal instabilities and powers the emission of ionized gas. On the other hand, I will show that the physical properties of the nebula are inconsistent with a scenario where this high-redshift system is just a scaled-up version of local nebular filaments in clusters. Indeed, alternative powering mechanisms must be in place to explain the luminosity of the nebula and two bright active galactic nuclei and shocks are the most plausible candidates. Pushing forward the analysis, I will describe the processes regulating the time evolution of the nebula and show that the likely interaction with the X-ray emitting plasma would quickly make the warm gas evaporate. Thus, barring an improbable observational coincidence, constant replenishment of cold gas must be supplied to sustain the Lyα nebula.

Moving from the replenishment argument, I will point out that galaxies inside the cluster are credible sources for the gas supply. Assembling a map of the star formation and nuclear activity, I will derive statistical arguments showing that outflows driven by supernovae and growing supermassive black holes are generous enough to match the requirements set by the properties of the nebula. Moreover, I will show that the kinetic power and total energy associated with outflows is enough to enhance the temperature and entropy of the surrounding intracluster medium, in line with the expectations from cosmological simulations and the observed thermodynamic proper-

ties of local structures.

Finally, I will shift the focus towards ongoing and forthcoming projects linked to the main themes of this thesis. In fact, during the last three years I have dedicated a significant fraction of my time to writing observational proposals for major facilities on the ground and in space, in order to improve and develop the ideas collected in the published material. In particular, I will discuss approved and submitted programs about the identification of new high-redshift clusters, the spectroscopic characterization of their star-forming members, and the search for giant Lyα nebulae in their cores.

RÉSUMÉ

L'environnement joue un rôle fondamental dans la formation et l'évolution des galaxies. Dans l'univers proche, les effets environnementaux se manifestent par l'apparition de correlations entre les proprietés des galaxies et leur densité locale. Toutefois l'importance de l'environnement dans la régulation des processus d'évolution des galaxies, comme la formation d'étoiles et son arrêt, l'enrichissement en éléments lourds du gaz et des étoiles, l'activité nucléaire et les transformations morphologiques, est toujours débattue. De plus, les difficultés liées à l'observation sont exacerbées par l'évolution temporelle corrélée des galaxies *et* de l'univers lui-même et par l'absence d'une définition univoque d'*environnement*. Le changement profond des structures cosmiques en fonction du redshift défie toute interprétation basée uniquement sur l'observation de l'univers proche, celle-ci ayant tendance à cacher l'origine physique des correlations observées. En conséquence l'étude de l'univers lointain, à une époque où le taux de formation stellaire était plusieurs fois plus élevé qu'aujourd'hui et les galaxies formaient la majorité de leur masse, devient donc un outil crucial pour comprendre quand et comment l'environnement a commencé à exercer ses effets.

Dans cette optique, l'objectif de cette thèse est d'approfondir notre compréhension de l'action de l'environnement sur l'évolution des galaxies à l'époque du pic de formation stellaire dans l'univers, à redshift $z \sim 2$. En particulier, je présenterai une analyse détaillée de l'amas de galaxies détecté en rayons X le plus distant connu actuellement, CL J1449+0856 à $z = 1.99$. Une population de galaxies rouges, massives et passives occupe le centre de cet amas. Cet aspect et la présence d'émission de rayons X par le milieu intergalactique sont typiques des amas massifs et bien développés observés dans l'univers proche. De plus, ces proprietés constituent une différence remarquable entre CL J1449+0856 et les ancêtres des amas (*proto-amas*) à plus haut redshift, typiquement plus dispersés et principalement composés de galaxies formant activement leurs étoiles.

Dans un premier temps, je montrerai les résultats d'une campagne d'observation spectroscopique des galaxies actives dans CL J1449+0856, réalisée au télescope Subaru avec l'instrument MOIRCS. En combinaison avec une base de données photometriques et spectroscopiques d'archive, en particulier provenant du télescope spatial *Hubble*, je caractériserai les conditions physiques du milieu interstellaire de ces galaxies où la formation d'étoiles chauffe le gaz et provoque l'émis-

sion de raies observées dans les spectres infrarouges. En moyenne les galaxies de l'amas montrent un rapport de raies [N II]/Hα significativement plus bas et une largeur de raie Hα équivalente plus haute que des objets de même masse n'appartenant pas à l'amas. Cependant, ni le rapport [O III]/Hβ ni le parametre d'ionisation ou le rapport N/O ne sont différents entre galaxies d'amas et de champ. En conséquence, ces observations peuvent être interprétées comme étant dues à une pauvreté en metaux dans les galaxies d'amas suite à l'accumulation de gaz primordial ou peu enrichi en éléments lourds. De plus, l'enrichissement en gaz primordial peut expliquer les valeurs de largeur de raie Hα équivalente, dans la mesure où cela peut déclencher la formation de nouvelles étoiles. Finalement, je présenterai deux scenarios alternatifs et complémentaires liés à l'environnement local ou à grande échelle pour justifier l'accumulation de gaz dans les galaxies d'amas.

Les réservoirs de gaz dans CL J1449+0856 sont le sujet d'un deuxième projet que je discuterai. Dans cette thèse je présenterai les résultats de nouvelles observations de l'amas avec le filtre étroit NB3640 installé dans l'instrument LRIS au télescope Keck. À l'origine, le projet prévoyait de détecter la raie Lyα émise par des galaxies individuelles dans l'amas. À notre étonnement, les données révèlèrent une émission Lyα étendue sur 100 kpc dans le cœur de l'amas. La taille et la luminosité de cette émission sont telles que nous pouvons lui appliquer la définition de "nébuleuse géante Lyα", une classe d'objets mystérieux que la communauté des astrophysiciens étudie à ce jour attentivement. Cette découverte confirme l'existence d'une connexion entre les nebuleuses géantes et les environnements denses à haut redshift et montre que cette relation est valide aussi dans le cœur ultradense d'un amas bien formé. Ce qui est fascinant, c'est la présence simultanée de plasma extrêmement chaud et visible par rayons X et de gaz plus froid émettant la raie Lyα. D'un côté, cette situation rassemble à ce qui est observé dans les regions centrales des amas dits "cool-core" à bas redshift, où le refroidissement du plasma intergalactique induit des instabilités thermiques et génère l'emission Lyα dans de longs filaments gazeux. D'un autre côté, je montrerai que les proprietés physiques de la nebuleuse dans CL J1449+0856 sont incompatibles avec un scenario où ce système peut être conçu comme une variante plus puissante des filaments ionisés dans les amas cool-core. De plus, des mécanismes alternatifs sont nécessaires pour expliquer la luminosité Lyα observée. Dans ce cas, soit les photons ionisants émis par deux noyaux galactiques actifs dans l'amas, soit des ondes de choc dues aux vents galactiques peuvent générer cette émission. En poursuivant l'analyse, je discuterai les processus qui règlent l'évolution temporelle de la nebuleuse géante et je conclurai que l'interaction entre le plasma chaud et tiède est responsable de l'évaporation

du gaz à temperature plus baisse. Ainsi, en excluant la possibilité d'une heureuse coïncidence, un réapprovisionnement constant de gaz froid est indispensable pour justifier l'existence de cette nebuleuse.

Ensuite j'explorerai la possibilité que les galaxies de l'amas constituent une source de gaz suffisante pour soutenir cette nebuleuse. Je déduirai la quantité de gaz expulsé par les galaxies suite à l'instauration de vents galactiques dus à l'explosion de supernovas ou à la croissance de leurs trous noirs super-massifs, et je montrerai que cela suffit à maintenir la stabilité de la nebuleuse. De plus, je déterminerai que la quantité d'énergie cinétique liée aux vents galactiques est suffisante pour chauffer le milieu intergalactique et augmenter son entropie, comme prédit par les simulations cosmologiques et requis par les proprietés physiques du plasma chaud dans les amas de l'univers proche.

Finalement, j'introduirai les nouveaux projets sur lesquels j'ai travaillé pour développer les sujets discutés ci-dessus. En particulier, j'ai dédié une fraction importante de mon travail de thèse à la rédaction de demandes d'observation auprès des principaux télescopes existants. Je discuterai des demandes acceptées et celles en attente d'une réponse, concernant l'identification de nouveaux amas de galaxies à haut redshift et de leur caractérisation spectroscopique, et la recherche de nebuleuses géantes d'émission Lyα dans leurs cœurs.

CONTENTS

1 INTRODUCTION

Despite its complexity, the universe appears highly organized on different spatial scales. From the smallest subatomic particle to the largest cluster of galaxies, every natural component is strongly interlaced with the surrounding elements by means of only four fundamental forces. Amazingly, a relatively small set of physical principles and laws of physics is sufficient to originate a striking order in nature. The great level of structuring is immediately appreciable when we observe the sky: the Earth, as well as extrasolar planets, is part of a multi-body system with other planets, asteroids, dust, and the Sun; stars generally reside in binary systems or clusters; then stars, gas, and dust are arranged in galaxies; the latter form filaments, sheets, groups, clusters, and finally superclusters, populating the cosmic web and tracing the underlying distribution of dark matter.

Structure, intended as the way in which the parts of something are connected together, arranged or organized, is a central concept in astrophysics and science in general, and what, in my view, makes the observation of the universe so exciting to human minds. One of the most intriguing implications of the interconnection inherent to structures is that truly isolated entities are hard, arguably impossible, to identify in nature. As a consequence, the physical understanding of a system goes necessarily through the characterization of its *environment* and the effects it exerts on the object under investigation. This complicates the quest for a deep knowledge of our universe in many respects, but one clearly stands out: the difficulty to discern the manifestation of the *intrinsic* nature of objects from the *extrinsic* effects induced from the external. Frequently referred to as the *nature versus nurture* problem, this issue is an old companion of scientists and thinkers, crossing different fields of human knowledge including ecology, epigenetics, psychology, philosophy, metaphysics, and, of course, astrophysics. The task of astrophysicists is made even more complex by the impossibility to perform an ordinary controlled experiment as in a laboratory. We cannot isolate parameters and variables connected to processes internal and external to celestial objects so to separate nature from nurture, repeating the experiment whenever desired. The problem is further exacerbated when *time evolution* is involved: except from very few and peculiar cases, astrophysical timescales are immensely longer than human's, forbidding us to follow the time changing of the universe to test and disprove theories. However, despite all these difficulties, astrophysics remains an incred-

ibly powerful tool of investigation of nature. Thanks to the vastness of the universe and the finite speed of light, we can regard populations in different patches of the sky and at different cosmic times as independent pieces of the same experiment. We can *observe* the properties of conveniently selected systems, try to decouple intrinsic and extrinsic mechanisms through a statistical assessment of large populations of objects, and empirically reconstruct the time evolution connecting progenitors and descendants. Adequate choices of targets at different redshifts, intensive efforts to observe statistically meaningful samples, a rigorous treatment of selection effects, and careful analysis and modeling constitute an expensive exercise both in terms of time and resources for astrophysicists. Nevertheless, it is a very stimulating and mentally rewarding experience as this thesis, hopefully, testifies.

This manuscript summarizes the work I have been doing for the last three years. It explores the concept of structure and interconnection at the largest scales of the universe, where galaxies are the minimal elements considered. In more detail, the main purpose of this thesis is to contribute to the understanding of how the *environment* affects galaxies or, in other words, how the existence of groups and clusters of galaxies influences the physical properties of their components. *Time evolution* is also deeply involved, this study being focused on the early stage of the assembly of galaxies and their changing with redshift. The topic is vast and variegated and a thorough description of every facet would likely be hampered by incompleteness and gaps. For the sake of clarity, in this introduction I will thus focus on selected critical points and open questions that have been driving my work, conscious that they represent only a limited portion of the global issue. First, I will briefly summarize the main steps that brought to the modern concept of galaxy clusters and sketch the commonly accepted scenario for their formation. I will then present the classical observational evidence for environmental effects on galaxy evolution and caveats related to any study on this topic. I will express the reasons for a new investigation of the young universe and introduce key issues related to the definition of "environments" at high redshift. A digression on a class of objects recently discovered in the distant universe, the so-called "Lyα nebulae", comes after in order to familiarize the reader with concepts recurring in the second main project of this thesis. A possible connection between Lyα nebulae and overdense regions of the universe is currently under discussion, and their relation with high-redshift galaxy clusters will be established and clarified later on in the manuscript. Finally, I will present an important feature of galaxy clusters, frequently neglected from the perspective of galaxy evolution: the contribution of cluster members to the energy budget of the intracluster medium (ICM) and the effects on its ther-

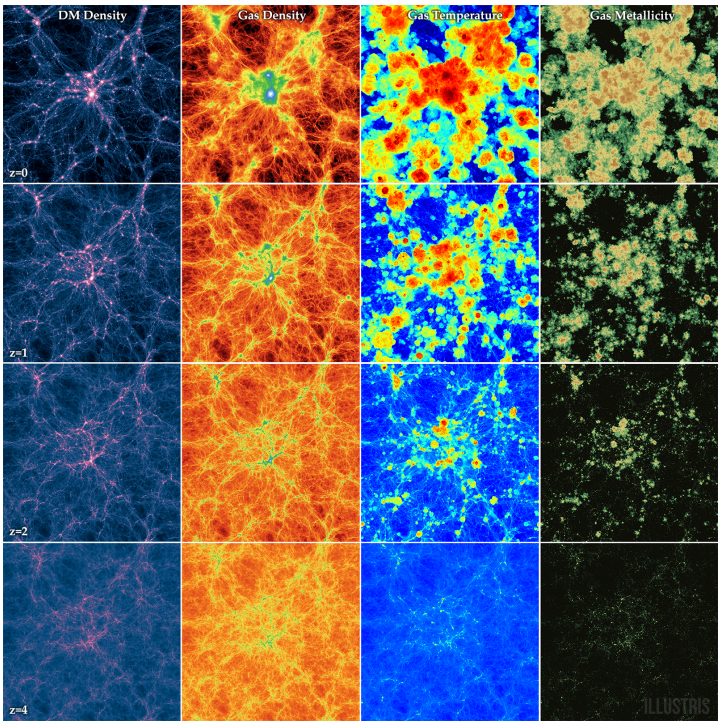

Figure 1 Redshift evolution of a full box slice (75/h comoving Mpc) of the Illustris Simulation from $z = 4$ to $z = 0$ (Vogelsberger et al. 2014). The four columns show the emergence of the large scale structure as traced by dark matter (first column), gas density (second column), gas temperature (third column), and gas metallicity (fourth column). The baryonic component follows the dark matter skeleton and flows towards the bottom of the potential wells along narrow filaments. Its temperature largely increases because of adiabatic heating and shocks at the virial radius during the infall. The metal enrichment is due to stars in galaxies, which process the pristine gas, forge the heavy metals, and redistribute them in the surrounding environment through powerful outflows. Credit: Illustris Collaboration.

modynamic properties. The main results of the thesis and specific discussions of highly related works in the literature are intentionally postponed to the next chapters in order to give them the necessary self-consistency.

1.1 A COMPENDIOUS HISTORY OF CLUSTER FORMATION

Immediately after the breakthrough discovery of the existence of galaxies other than the Milky Way (Hubble 1926), it became clear that galaxies shy away from isolation and tend to cluster in gigantic systems. The measurement of galaxy radial velocities in cluster regions

came few years later (Hubble & Humason 1931), providing the missing piece of information to reconstruct the three-dimensional structure of these systems and confirming they were not merely due to projection effects. The first estimate of the enormous cluster masses represented a further huge leap forward, disclosing astonishing new horizons for astrophysicists: based on the simple assumption of virial equilibrium of galaxy motions, Zwicky (1933) soon realized that the mass enclosed in stars was insufficient to explain the velocity dispersion of galaxies and postulated the existence of a dark matter component (DM) largely determining the depth of the cluster potential wells. Indirect confirmation of Zwicky's intuition came with the detection of X-ray emission from hot plasma smoothly filling the intergalactic space (i.e., Cavaliere et al. 1971; Gursky et al. 1971; Meekins et al. 1971), revealing a substantial fraction of the luminous baryonic matter in clusters and showing that the potential well must be dominated by the dark component. Simultaneous progress on the theoretical side paved the way for the modern understanding of cluster formation, based on the collapse of primordial density peak fluctuations and the following hierarchical assembly in cold dark matter cosmologies (i.e., Press & Schechter 1974; White & Rees 1978).

Many cluster properties, including their abundance and clustering, were lately described and well approximated by recipes including gravity and dissipationless DM, such as the 'self-similar' model (Kaiser 1986; Kravtsov & Borgani 2012). However, with the advent of the powerful X-ray telescopes XMM-Newton and Chandra in the 1990s, which allowed a detailed characterization of the hot ICM, clear inconsistencies with these simple prescriptions appeared, mainly owing to baryon physics. The inclusion of a proper treatment of gas both free in the ICM and locked in stars and galaxies allowed to derive a coherent picture of the mature clusters we observe today. Briefly, in a flat and expanding ΛCDM universe, primordial quantum fluctuations progressively grow under the effect of gravity up to the point where they detach from the global expansion and collapse. The highest density peaks collapse first, providing the seeds for cluster DM halos, whose mass grows with time through merging of smaller subunits in a hierarchical fashion (Peebles 1993). The growth of the DM structure of clusters simultaneously drives the accretion of baryons through gravity, meaning that both galaxies and gas residing in merging halos streaming along the cosmic web are eventually packed in overdense regions (Figure 1). The X-ray emission we observe is associated with the ICM and mainly due to bremsstrahlung of thermal electrons heated by adiabatic compression and shocks during the collapse, then settled in hydrostatic equilibrium in the cluster potential well. Interestingly, thermal electrons also induce distorsions in the cosmic microwave background (CMB) via inverse Compton

scattering, generating the well detectable Sunayev-Zel'dovich (SZ) effect (Sunyaev & Zeldovich 1970, 1972). Metal emission lines complete the energy budget of the observed X-ray emission (Sarazin 1988). Later gas cooling from the X-ray phase can feed supermassive black holes (SMBH) and star formation in cluster galaxies, which counteract global cooling injecting a substantial amount of energy and metals in the ICM. I will come back on this last point in Section 1.5.

1.2 OBSERVATIONAL EVIDENCE FOR NURTURE IN GALAXY EVOLUTION

Several observations have established the existence of a correlation between galaxy properties and the density of the surrounding environment in the local universe. A clear segregation of morphologies (Dressler 1980; Postman & Geller 1984; Whitmore et al. 1993), colors (Visvanathan & Sandage 1977; Bower et al. 1992a,b), ages (Kauffmann et al. 2004), stellar mass functions (Blanton & Moustakas 2009), luminosity (Blanton et al. 2005), HI gas content (Boselli & Gavazzi 2006), nuclear activity (Kauffmann et al. 2004), dust content (Kauffmann et al. 2004), and star formation (Balogh et al. 1998; Lewis et al. 2002; Gómez et al. 2003) appears when comparing cluster and field galaxies, while weaker correlations are reported for structural properties such as surface brightness, sizes, concentration or Sérsic indices, once variables connected to star formation histories and stellar masses are taken out (Kauffmann et al. 2004; Blanton et al. 2005; Blanton & Moustakas 2009). As a result, a population of smooth early-type, red, massive, and quiescent galaxies dominates the densest regions of the nearby universe, while we observe spiral and irregular, blue, star-forming galaxies (SFGs) in galaxy outskirts, 'field', and generally low-density environment.

This generic statement represents the classical view of the subject, but it should be taken with caution. Multiple causes may produce such correlations and separate each contribution is crucial to study true environmental effects. First, by definition clusters enclose a larger *absolute* number of galaxies with respect to the field. This means that *integrated* properties of populations are misleading, while *average* or *fractional* quantities are properly normalized to the absolute frequencies of the samples. Second, the large majority of the properties reported above are correlated with each other. Thus, *internally*-driven properties easily sneak in the analysis and should be canceled out to highlight genuine environmental dependences. A simple example to clarify these points is offered by the study of the star formation rate (SFR) in galaxies. Observationally, the ongoing rate of formation of new stars is tightly correlated (~ 0.3 dex dispersion, Rodighiero

et al. 2011) with the stellar mass ($M_\star$) producing the so-called "Main-Sequence" (MS) of SFGs (Brinchmann et al. 2004; Noeske et al. 2007; Elbaz et al. 2007; Daddi et al. 2007, Figure 2) in place up to $z \sim 4-6$ (i.e., Speagle et al. 2014; Schreiber et al. 2015), independently of the environment, and with few "star-bursting" outliers showing prodigious SFRs, though not dominating the total SFR density of the universe (Rodighiero et al. 2011; Sargent et al. 2014). In the $M_\star$-SFR plane, passive or quiescent galaxies with SFR ~ 0 $M_\odot$ yr^{-1} simply drop out the sequence. This distinction between SF and quiescent galaxies is partially at the origin of the bimodality observed in the color-magnitude diagram up to $z \sim 3$ (Bower et al. 1992a,b; Strateva et al. 2001; Baldry et al. 2004; Bell et al. 2004b; Cassata et al. 2008), even though in combination with stellar masses and the star formation histories (SFHs) over the lifetime of galaxies (Elbaz et al. 2007) and partial contamination due to dusty SFGs (i.e., Bell et al. 2004a). As mentioned above, clusters preferentially host quiescent galaxies in their cores, while the outskirts and the field are dominated by SFGs. Thus, the environment exerts its force on galaxies, but how does this happen? The measured *mean* SFR in cluster galaxies is lower than in the field, but this may be owing to a larger fraction of passive galaxies included in the calculation and/or an effective reduction of the SFR in SFGs. Moreover, cluster galaxies are on average more massive than field galaxies: overlooking this *intrinsic* aspect might well mimic an effect on SFRs, simply because of the positive $M_\star$-SFR correlation. To circumvent this last point, thus, it is safer to study *specific* SFR ($sSFR = SFR/M_\star$) eliding the contribution of internal mechanisms.

I have deliberately chosen an example linked to star formation primarily because it is strongly connected to what will be presented later in this thesis. However, considering the crucial role it plays in modern extragalactic astrophysics even beyond the *nature versus nurture* problem, I propose here a brief detour that will introduce useful elements I employ in this work and present the state-of-the-art knowledge of the field.

1.2.1 How do galaxies grow?

How galaxies assemble their mass is a question of primary importance to understand their evolution. Galaxy formation is naturally comprised in the theoretical framework sketched in Section 1.1, where baryons falling into collapsed DM halos decoupled from the Hubble expansion constitute the building blocks for protogalaxies, while cooling processes drive gas condensation, Jeans instabilities, fragmentation, and the lighting of the first stars. Detailed or historical descriptions of this hierarchical assembly of galaxies (Toomre 1977; White & Rees 1978) and competing scenarios such as the "monolithic collapse"

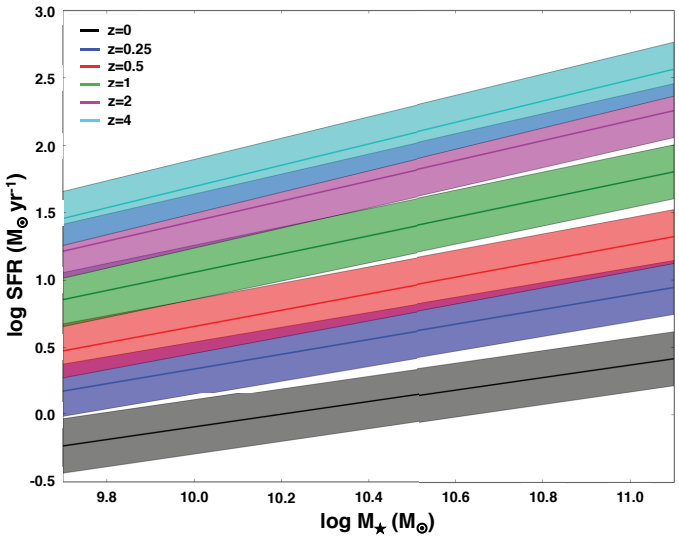

Figure 2 The evolution of the Main Sequence of SFGs with redshift. The existence of this tight correlation ($\sigma \sim 0.3$ dex) between $M_\star$ and SFR over $\sim$ 12 Gyr of cosmic time has imposed a radical change of paradigm in galaxy evolution, reducing the role of mergers in triggering star formation and favoring a smoother secular evolution. From (Speagle et al. 2014).

(Eggen et al. 1962) are beyond the scope of this thesis. Nevertheless, I believe it is worth mentioning the shift of paradigm occurred with the emergence of the Main Sequence of SFGs (Brinchmann et al. 2004; Noeske et al. 2007; Elbaz et al. 2007; Daddi et al. 2007). This relation, coupled with the correlation between the surface gas density and surface SFR (the Schmidt-Kennicutt law, Schmidt 1959; Kennicutt 1998a), reduces the importance of mergers in triggering the formation of new stars, favoring the existence of a smooth secular process (Noeske et al. 2007). As mentioned, mergers are still thought to ignite starbursts (SB) in galaxies as observed in local Ultra-Luminous InfraRed Galaxies (ULIRGs, Sanders & Mirabel 1996), but not to play a major role to shape the total SFR density ($\lesssim$ 10%, Rodighiero et al. 2011). Moreover, the normalization of the MS steadily increases with increasing redshift (Figure 2 Speagle et al. 2014; Schreiber et al. 2015), while the shape remains almost linear, excluding a possible bending at high masses due to galaxies turning passive (Whitaker et al. 2012, 2014; Lee et al. 2015; Schreiber et al. 2016). The increase of the normalization of the MS is strongly correlated with an overall increase of gas masses and fractions with redshift, fueling the star formation (Daddi et al. 2010; Tacconi et al. 2010, 2013; Genzel et al. 2015), while it is still debated if SB are connected with larger efficiencies in converting gas into stars, rather than to gigantic gas fractions (Scoville et al. 2014, 2016). Cosmological simulations show that cold gas can in-

deed smoothly reach galaxies deep into the DM potential wells along dense filaments, depending on redshift and halo mass (Kereš et al. 2005; Dekel et al. 2009a). Unfortunately, very poor and incidental evidence of cold, pristine gas flowing into galaxies from large scales is currently present in literature (i.e., Bouché et al. 2013; Martin et al. 2015). Admittedly, this is one of the major and challenging problems to solve in modern astrophysics.

Ironically, we do not know either how galaxies shift from their star forming condition to the quiescent state we observe in massive early-type systems. The observed decline of the average sSFR of galaxies since $z = 2$ (Sargent et al. 2014; Schreiber et al. 2015) and the possible bending of the MS at high masses (Schreiber et al. 2016) imply an exponential decline of SFH in the MS population, but, by definition, this is not enough to explain the drop towards the population of quiescent galaxies. Do galaxies abruptly quench the star formation or is this a long-lasting, gentle process? Do galaxies pass through a phase of intense star burst or simply drop from the MS? And, ultimately, what is the main physical driver of galaxy quenching? *Nature or nurture?*

1.2.2 How do galaxies die?

Considering that overdense regions of the universe are mainly populated by red and quiescent galaxies, the *environment* looks an attractive explanation for the problem of galaxy quenching. This solution benefits from solid physical bases: quenching may occur ensuing the stripping or cut of galactic gas reservoirs through ram pressure (Gunn & Gott 1972), viscous stripping (Nulsen 1982), thermal evaporation (Cowie & Songaila 1977), strangulation or starvation (Larson et al. 1980), harassment (Moore et al. 1996), and galaxy-galaxy or galaxy-cluster tidal interactions (Spitzer & Baade 1951; Merritt 1983). Hydrodynamic interactions between galaxies and the hot medium are likely to play a major role in local massive clusters, while gravitational processes are expected to be more efficient in lower mass, group-like systems and at high redshift, where the small velocity dispersion favors galaxy encounters and the temperature and density of the ICM are lower (Boselli & Gavazzi 2006). Timescales are also different for each of these processes and represent a way to discriminate the most relevant among them. All things considered, *environmental quenching* is probably a combination of these options, with possible variations with cosmic time, halo masses, and dynamical states of clusters. Halo masses in particular can play a significant role at low redshift, maintaining stably hot the intracluster plasma and avoiding gas replenishment in cluster members (*halo quenching*, Dekel & Birnboim 2006; Dekel et al. 2009a; Gabor & Davé 2015; Tacchella et al.

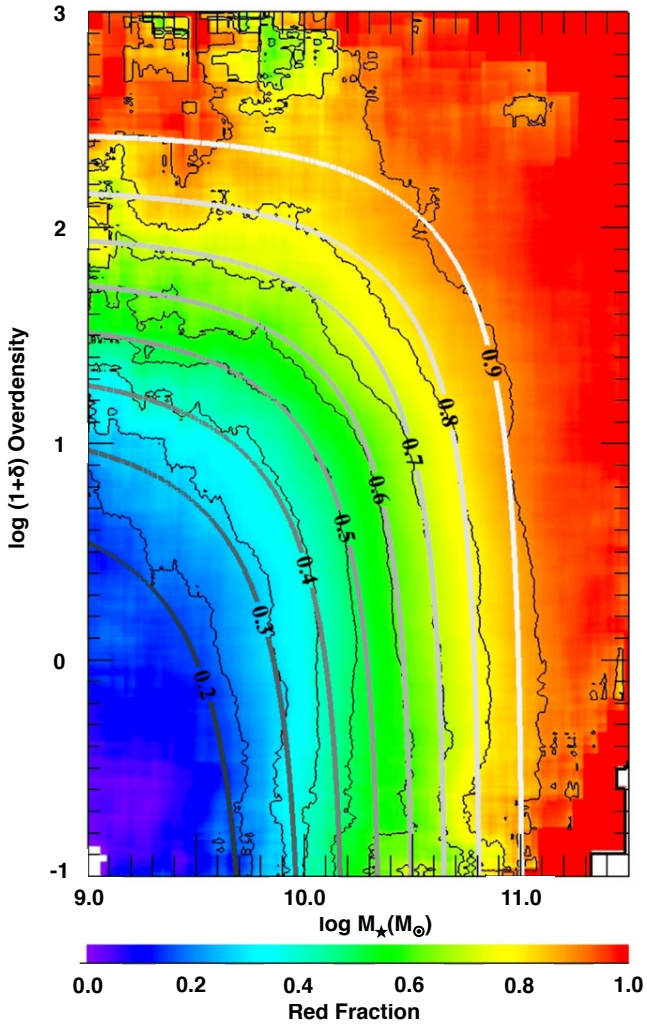

Figure 3 The fraction of red galaxies as a function of mass and overdensity in the SDSS. Red passive objects dominate the population of local galaxies at high masses and overdensities, pointing towards the existence of both internally and environmentally driven mechanisms that quench galaxies. From (Peng et al. 2010b).

2016). Nevertheless, it is still not clear if the environment simply increases the probability for a galaxy to be quenched, thus affecting the fraction of passive galaxies only (i.e., Peng et al. 2010b; Darvish et al. 2016), or whether it decreases the SFR (or sSFR) of individual SFGs (Erfanianfar et al. 2016, and references therein).

Environment does not tell the whole story about galaxy quenching. In fact, the fraction of red, passive galaxies is independent of the environment at high masses (Figure 3), so that an alternative quenching mechanism primarily due to inner galaxy properties must be invoked (*mass quenching*, Peng et al. 2010b). Even if debated (Darvish et al. 2016), environmental and mass quenching might be fully separable in terms of differential efficiencies over large mass ranges (Peng et al. 2010b, 2012), thus allowing to trace the epochs when one or the other mechanism was prevalent. It should be noted that "mass quenching" is an empirical definition that do not add any information about the physics of the process. Recently, morphological changing and feedback from supernovae (SNae) explosion or active galactic nuclei (AGN) have been put forward as plausible mechanisms. *Morphological quenching* attributes the drop in star formation in galaxies to the development of a massive bulge that stabilizes gaseous disks (Martig et al. 2009). Notably, this explanation has the virtue to connect the morphological transformation with quenching, an inescapable step to justify the existence of passive early-type galaxies in the nearby universe. On the other hand, both SNae and AGN are able to inject substantial amount of energy in the interstellar and intergalactic media (ISM and IGM, respectively), thus either blowing material away from galaxies or preventing it from cooling, cutting the reservoirs for star formation. Indeed, both an "active" and a "maintenance" mode are necessary to avoid the restart of star formation on long timescales. In particular, SN explosions and AGN activity are appealing explanations for quenching, both from a theoretical and observational point of view. First, they could reconcile halo and stellar mass functions, explaining the stellar mass - halo mass ($M_\star$-M_{halo}) relation (Conroy & Wechsler 2009; Moster et al. 2010; Behroozi et al. 2010, 2013) and the small efficiency in converting baryons into stars at low and high halo masses (Dekel & Silk 1986; Silk & Rees 1998). Then, multiphase galactic outflows are now detected ubiquitously in SFGs and AGN host (i.e., Heckman et al. 1990, 2000; Adelberger et al. 2003; Veilleux et al. 2005; Weiner et al. 2009; Feruglio et al. 2010; Cicone et al. 2014; Förster Schreiber et al. 2014) and naturally explain the metal enrichment of the IGM (Veilleux et al. 2005). AGN and radiogalaxies are also the most plausible candidates to inject energy in the ICM of groups and clusters, influencing their thermodynamic properties (Section 1.5) and preventing catastrophic cooling (McNamara & Nulsen 2007; Fabian 2012). There is evidently enough energy and mo-

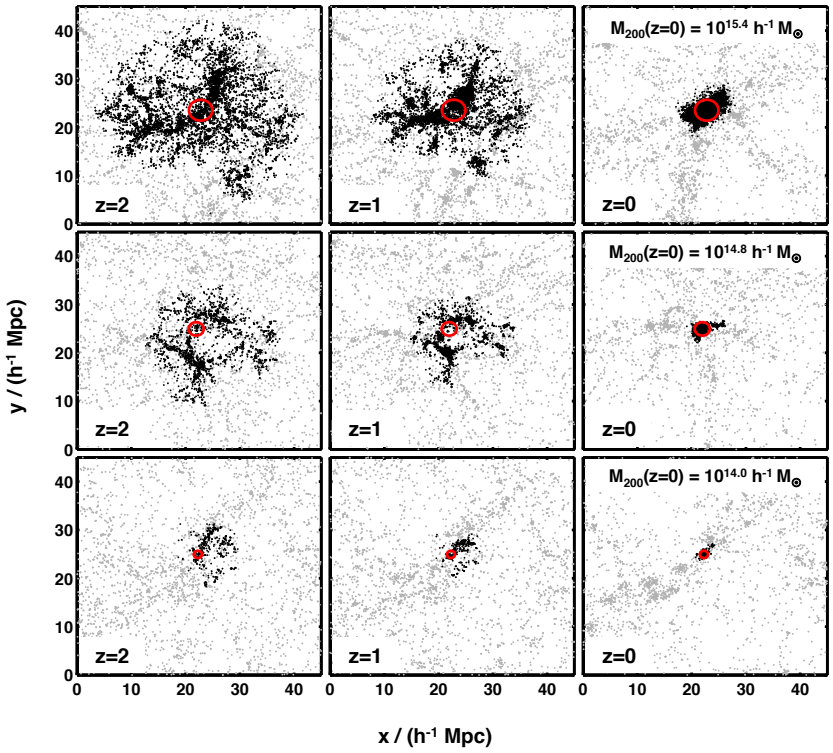

Figure 4 The spatial extent of *protoclusters* at $z = 2$ (left panel), 1 (central panel) and 0 (right panel), with final cluster masses as labeled. Each window is $45 \times 45 h^{-1}$ Mpc comoving. Black points represent galaxies of stellar mass greater than $10^8 h^{-1}$ $M_\odot$ that will end up in the cluster while grey points represent those that will not. The red circle corresponds to the $z = 0$ centre and comoving viral radius of the cluster. Up to 80% of the galaxies in the *protocluster* at $z = 2$ are not in the *main halo*, which, nevertheless, can be detected as a stand-alone, high-redshift *cluster*. From Muldrew et al. (2015).

mentum to expel the gas out of galaxies, but the jury is still out about the actual quenching power of SNae and AGN: how and how well the energy they release and the ISM/IGM are coupled is only sketched in models and simulations; we do not know when and for how long the interaction with host galaxies occurs, especially for the highly stochastic, short duty cycle AGN and SB activities; it is not clear how the SNae and AGN feedbacks combine in galaxies and how strongly they depend the on geometry of the system and the properties of the ISM; most importantly, we have in hand only incidental signatures of *negative* feedback due to galaxy outflows – *positive* feedback, i.e., AGN or SN-induced SFR and black hole accretion rate (BHARs) enhancement, is also reported in literature. For these reasons, there is ample room for improvement in the next few years both on the observational and theoretical side.

1.3 WHY STUDYING ENVIRONMENTAL EFFECTS IN THE HIGH-REDSHIFT UNIVERSE?

Most of the evidence for environmental effects presented in Section 1.2 is based on samples of galaxies in the local universe, where a wealth of detailed information is available on large patches of the sky. However, the trends we observe today are the final product of a dramatic evolution of galaxies in environments that deeply change with cosmic time, too. Half of the stellar mass observed in the universe today was formed before $z \sim 1.3$ (Madau & Dickinson 2014), due to a rapid increase of the SFR up to $z \sim 2$ and a gentle decrease at higher redshift (Lilly et al. 1996; Madau et al. 1998), as required by the SFH of galaxies on the evolving MS. AGN activity is observed to similarly increase up to $z \sim 2$ and decline at earlier times, suggesting a co-evolution of central SMBHs and their host galaxies (Mullaney et al. 2012; Rodighiero et al. 2015; Madau & Dickinson 2014) that would explain the tight black hole - bulge mass correlations (Kormendy & Ho 2013), even if a causal relation might not be straightforward to derive (Peng 2007). Furthermore, stellar abundance ratios and ages of local massive and quiescent galaxies suggest that they formed in short and intense starburst events at high redshift (Thomas et al. 2005). Dark matter halos assembled a large fraction of their mass at $z > 1$, too (Chiang et al. 2013). These well established results are thus compelling reasons to push the investigation at high redshift.

A classical example of environmental trends changing with time is the Butcher-Oemler effect (Butcher & Oemler 1978, 1984), i.e., the excess of blue spirals in distant clusters as compared with the richest nearby structures. Several studies came after, showing how galaxies in overdense and underdense regions evolve with time, up to the point that now we approach the epoch of formation of the first gravitationally bound clusters. Nonetheless, this quest is hampered by several limitations of different nature. First, observational difficulties restrict our explorations to small samples of galaxies and tiny portions of the sky, with obvious consequences on selection effects and cosmic variance uncertainties. The spectroscopic characterization of galaxies, a fundamental starting point to confirm the existence of high-redshift clusters and to reconstruct their three-dimensional structure, is particularly hard to obtain. However, the great technological advance of the last few years is allowing us to rapidly make up ground: especially the advent of near-IR spectrographs with multiplexing capabilities at 8-10 meter telescopes, such as MOIRCS (Ichikawa et al. 2006) at Subaru, MOSFIRE (McLean et al. 2010) at Keck, or KMOS (Sharples et al. 2013) at the Very Large Telescope (VLT), is opening a new window at $z \sim 2$, allowing for the spectroscopic investigation of galaxies at the peak of the cosmic star formation history. A second major problem is

connected with the evolution of clusters with time. Galaxy clusters in the present day universe are massive ($M_{halo} > 10^{14}$ $M_{\odot}$), fully virialized systems showing extended X-ray emission from the ICM, possibly detectable SZ effect, and a dominating population of red, massive, passive galaxies. However, given the hierarchical assembly of DM halos, most clusters appear completely different at high redshift. Ninety percent of the mass enclosed in clusters at $z = 0$ was outside the main parent halo at $z = 2$, dispersed over comoving distances up to 35 Mpc (Figure 4, Muldrew et al. 2015). A complete virialization of the overall structure is far from being reached at this time and the ICM is still in a phase of rapid development. Following Diener et al. (2013), we can thus distinguish between *clusters* and *protoclusters*. Galaxies are *cluster* members if they share the same DM halo at the time of observation, while *protocluster* galaxies occupy different dark matter haloes at the epoch at which they are being observed, but will later accrete into a common halo by $z = 0$ (Figure 4). Since we cannot observe halos directly in the sky, such a distinction can be operated by comparing observations and mock catalogs extracted from cosmological simulations (Diener et al. 2013, 2015). We can still resort to pure empirical definitions of high-redshift clusters, applying the same criteria we adopt at $z = 0$, i.e., the presence of extended X-ray emission from the ICM, a possible detection of the SZ effect, or a red sequence already in place. As a matter of fact, the main halo of a protocluster can often be classified as a self-standing cluster (Muldrew et al. 2015). The definition of clusters and protoclusters is not a pure lexical cavil. The two environments host galaxies immersed in different local overdensities and, presumably, exposed to distinct physical mechanisms (Section 1.2.2), potentially generating different effects on their properties. It should be noted also that significant object-to-object scatter is likely to limit current analysis based on low statistics samples. All things considered, general conclusions about environmental effects should be drawn with caution.

The search for high-redshift clusters and protoclusters is a field in remarkable expansion. On one side, new distance, mass, and richness record-breaking structures are frequently reported in literature; on the other hand, we are entering an era where systematic studies of homogeneous samples are affordable both in terms of time and resources. Nonetheless, the choice of a specific selection technique will inevitably bias the population of structures probed. Focusing on the redshift range $z \gtrsim 1 - 1.5$, detection of X-ray extended emission (Andreon et al. 2009; Papovich et al. 2010; Tanaka et al. 2010; Santos et al. 2011; Gobat et al. 2011; Stanford et al. 2012; Fassbender et al. 2011; Brodwin et al. 2016), SZ effect (Hasselfield et al. 2013; Planck Collaboration et al. 2015; Bleem et al. 2015; Brodwin et al. 2015), and a red sequence of passive galaxies (Kurk et al. 2009; Pa-

povich et al. 2010; Spitler et al. 2012; Tanaka et al. 2013; Newman et al. 2014; Strazzullo et al. 2015) trace the most massive and virialized among the halos, *clusters* according to the previous definitions. Selection with *Spitzer*/IRAC colors has proven to be very successful (Eisenhardt et al. 2008; Muzzin et al. 2009; Rettura et al. 2014), combing the $1.5 \lesssim z \lesssim 2$ redshift range. Another possibility is to look for the most massive galaxies at each cosmic time, being centrals of the likewise massive DM halos. Radio-galaxies (i.e., Pentericci et al. 2000; Best et al. 2003; Venemans et al. 2007; Hatch et al. 2011; Wylezalek et al. 2013) and sub-mm galaxies (Chapman et al. 2009; Capak et al. 2011; Walter et al. 2012; Casey et al. 2015) are among the best candidates for this technique. However, they might not be representative of the overall population of massive galaxies especially when quenching starts operating. Moreover, because of their rarity, Poisson noise scatters the overdensity of these objects at fixed DM overdensity (Miller et al. 2015). Interestingly, the possibility that strongly starbursting sub-mm galaxies could be quite clustered discloses the opportunity to detect overdensities hosting massive star-forming centrals before their main epoch of quenching. This goes towards the direction of a possible reversal of the SFR-density relation observed in local clusters (i.e., Elbaz et al. 2007) and opens new doors for detection of protoclusters and clusters in their very first early stage of assembly (Clements et al. 2014; Planck Collaboration 2015; Wang et al. 2016). Moreover, thanks to the increasing spectroscopic coverage and accuracy of photometric redshift surveys, 3D mapping is now routinely applied to find overdensities (Diener et al. 2013; Scoville et al. 2013; Chiang et al. 2014; Mei et al. 2015). Conceptually similar, the slicing of larger fields with the narrow-band imaging allows for a very efficient search for structures (Steidel et al. 2000; Møller & Fynbo 2001; Kodama et al. 2013), even if spectroscopic confirmation is always required in the end. Note that selection techniques based on the detection of SFGs are naturally tracing a population that is expected to be dominant only at the early phases of cluster assembly, at least in the densest cores, while they are generally very effective in retrieving the large scale structure ($\sim 1 - 10$ Mpc) surrounding the main halo. The advent of future all-sky surveys and projects driven by cosmological goals, such as the Hobby-Eberly Telescope Dark Energy Experiment (HETDEX, Hill et al. 2008), Euclid (Amendola et al. 2013), or with Hyper-Suprime Cam and the Prime Focus Spectrograph at Subaru (Miyazaki et al. 2002; Takada et al. 2014) , will be a gold mine for the community of extragalactic astrophysicists, largely expanding the use of the listed techniques.

1.4 GIANT LYα NEBULAE AT HIGH REDSHIFT

Since their first discovery in the late 1990s (Francis et al. 1996; Steidel et al. 2000), high-redshift, extended ($\gtrsim$ 100 kpc), and luminous (few $10^{43} - 10^{44}$ erg s^{-1}) gas reservoirs shining by the emission of Lyα photons have progressively become a matter of debate. Despite two decades of investigation, several aspects of these "Lyα nebulae" remain puzzling, including the origin of the Lyα-emitting gas, its powering mechanism, the possible effects on the evolution of the embedded galaxies, and, ultimately, its fate. Understanding where Lyα nebulae fit in the current theoretical framework of structure formation has sparked particular interest, since they call into question a cornerstone of modern astrophysics: the complex interplay of supply, consumption, and expulsion of gas that shapes high-redshift systems. Given its wide extension, it is tempting to associate this gas to the IGM illuminated by central quasars (Geach et al. 2009; Prescott et al. 2009; Overzier et al. 2013; Cantalupo et al. 2014; Borisova et al. 2016), radio-galaxies (McCarthy et al. 1990; Best et al. 2000; Villar-Martín et al. 2003; Miley et al. 2006; Venemans et al. 2007), and strong SB via galactic superwinds and shocks (Taniguchi et al. 2001; Cen & Zheng 2013; Ao et al. 2015; Cabot et al. 2016). Low metallicities estimated from UV emission lines, such as He II λ1640 Å, C IV λ1549 Å, and C III] λ1909 Å, suggest low contamination from galactic activity in Lyα nebulae around radio-quiet AGN (Dey et al. 2005; Prescott et al. 2009, 2013; Arrigoni Battaia et al. 2015; Borisova et al. 2016). However, similar line ratios might be obtained assuming shock-ionized plasma (Cabot et al. 2016). On the other hand, nebulae around radio-loud AGN show signs of significant metal enrichment, which coupled with hot kinematics (FWHM(Lyα) ∼ 1000 km s^{-1}, absence of coherent motions), points towards a different physical origin of the extended emission, presumably associated with outflows (Villar-Martín et al. 2007; Borisova et al. 2016). Being a strongly resonant line, Lyα emission might arise from scattering of photons from a central source (Dijkstra & Loeb 2008), instead of being produced in-situ, i.e., through star formation (Hatch et al. 2008). Such a mechanism would leave a clear imprint on the polarization pattern indeed detected in some cases (Hayes et al. 2011; Beck et al. 2016). Peculiar polarization patterns might be used to detect Lyα cooling radiation (Dijkstra & Loeb 2008), possibly associated with gas flowing from the cosmic web towards galaxies in the nebula to feed their star formation and AGN activity. In principle, Lyα extended emission could be the most direct way to finally track down cosmological cold flows (Haiman et al. 2000; Fardal et al. 2001; Birnboim & Dekel 2003a; Nilsson et al. 2006; Dijkstra & Loeb 2009; Goerdt et al. 2010; Rosdahl & Blaizot 2012), but no convincing candidate of Lyα nebulae not associated to any of the previous powering mechanism has been found yet. The cold flow

model itself predicts the presence of at least a massive, strongly active galaxy fed by the gas streams, thus producing plenty of energetic photons through star formation and black hole accretion that can easily ionize the surrounding IGM, inevitably contaminating the trace of gravitational cooling (Prescott et al. 2015).

An intriguing feature of high-redshift Lyα nebulae is that they preferentially reside in overdense regions of the Universe or protoclusters (Steidel et al. 2000; Matsuda et al. 2004; Venemans et al. 2007). This suggests a possible connection with the formation of massive structures, even if it is not clear in which density regimes this correlation holds. Interestingly, in the local Universe the presence of kpc-size, filamentary reservoirs of ionized gas in the center of "cool-core" X-ray emitting clusters (CCs) has been known for decades (Fabian et al. 1984b; Heckman et al. 1989; Hatch et al. 2007; McDonald et al. 2010; Tremblay et al. 2015). From this angle, it is tempting to view the high-redshift Lyα nebulae as the counterparts of local filaments, with sizes and luminosities reflecting the extreme conditions of the primordial Universe (McDonald et al. 2010; Arrigoni Battaia et al. 2015). However, the detailed physics of the nebular emission is still debated even for local clusters, despite the quality of the available data. A mix of different heating mechanisms is probably at the origin of the emission by the ionized filaments, with a possible important role played by young stars formed *in-situ* (Tremblay et al. 2015 and references therein). The origin of the cold gas has not been fully clarified either: even if modern models of auto-regulated cooling from the X-ray emitting intracluster medium (ICM) successfully reproduce several properties of the nebulae in CCs (i.e., Gaspari et al. 2012; Voit & Donahue 2015; Tremblay et al. 2015), the cold gas might also originate from a starburst event or an AGN in the central brightest cluster galaxy (BCG, Hatch et al. 2007), or uplifted by propagating radio-jets and buoyant X-ray bubbles (Churazov et al. 2001; Fabian et al. 2003), or gas stripped in a recent merger (Bayer-Kim et al. 2002; Wilman et al. 2006). Therefore physical insights might not be straightforwardly gained from the simple observation of local filaments.

The great theoretical and observational effort made by the astrophysical community is producing remarkable results about high-redshift Lyα nebulae. Detailed and complex radiative transfer models and the access to statistical observational samples spanning a large range of redshifts constitute an optimal base to draw a coherent picture of these systems that is, admittedly, lacking today. Several open questions and issues are lively debated these days: we have hard times understanding whether Lyα nebulae represent a homogeneous population or a significant variety and scatter is underlying the observational evidence we have in hand; then, if the most plausible power-

Figure 5 Multiwavelength image of NGC 1275, the brightest cluster galaxy of the Perseus cluster. The Chandra soft X-ray image reveals the complicated structure of the hot ICM surrounding the galaxy (violet): bubbles and ripples are inflated by the central radio source (pinkish lobes). *HST*/ACS image shows the emission from star-forming regions and filamentary ionized gas (RGB). Perseus is among the best laboratories to study the feedback-regulated injection of momentum and energy into the ICM due to galaxies in the local universe. Credits: NASA/CXC/SAO.

ing mechanisms have been already described, we still do not know whether one or more dominate over the others, when and for how long; we still cannot draw a time evolution of these systems and a possible connection with the structure and physics of the local clusters, a natural outcome of the Lyα nebulae-protoclusters correlation at high redshift; moreover, it is not clear how powerful Lyα nebulae are to probe the elusive cosmological cold flows or cooling flows. In the second part of this manuscript I will revisit these subjects and, in particular, the relation between Lyα nebulae and the environment, in an attempt to provide new keys of interpretation.

1.5 HOW DO GALAXIES AFFECT THE SURROUNDING ENVIRONMENT?

How the environment affects the evolution of galaxies is a classical and still very active field of research, as I have tried to summarize

in these opening remarks. I would like to conclude the introduction with a complete overturning of perspective and recall an aspect that is frequently neglected when focusing on galaxies only, namely the fact that their relation with the environment is *mutual*. In other words, *galaxies have a deep impact on groups and clusters as a whole*, as much as the latter affect the evolution of their members. A clear illustration of the influence of galaxies on the surrounding structures is the level of metal enrichment of the ICM: the same amount of metals is locked in stars and distributed in the intergalactic space by outflows ensuing star formation in galaxies (i.e., Renzini & Andreon 2014). Another striking example is linked to the enormous output of energy and momentum carried by galaxy outflows. During the last twenty years, it has been shown that relaxed clusters normally present a strongly peaked X-ray emissivity in their cores, indicating efficient gas cooling. In the most extreme cases, thousands of $M_\odot\ yr^{-1}$ should cool down, shining in the X-rays through bremsstrahlung, and moving towards the bottom of the potential well, eventually feeding star formation and black hole activity in the BCG (Fabian 1994). However, spectroscopy with Chandra and XMM-Newton clearly demonstrated that only a modest quantity of this "cooling flows" effectively reaches low temperatures (Peterson & Fabian 2006), fueling intermittent episodes of weak star formation in the BCGs (McDonald et al. 2011). This requires a heating mechanism counterbalancing the radiative losses and preventing the settling of a cooling flows. At $z = 0$, the energy injected by central giant radio-galaxies is an excellent candidate to offset global cooling, as several pieces of evidence are now suggesting (Figure 5, McNamara & Nulsen 2007; Fabian 2012). However, local thermal instabilities can still take place when radio-galaxies are less active, triggering runaway cooling of gas that is free to fall on BCGs following filamentary patterns, finally re-igniting star formation and feeding the central SMBHs. Then, enhanced activity further suppresses cooling, establishing an auto-regulated feedback mechanism that keeps the system in dynamic equilibrium (Sharma et al. 2012; Gaspari et al. 2012; Voit & Donahue 2015; Tremblay et al. 2015). At high redshift, the impact of galaxies on clusters and groups can be even more dramatic, given the typical lower halo masses. Actually, galaxy activity at the early stage of emergence of the large scale structure is frequently invoked to explain the X-ray properties of nearby structures, such as their entropy profiles and temperatures. In fact, it has been known for more than two decades that these properties are inconsistent with the predictions from pure gravitational settling of the ICM and an extra energy contribution is missing (Kaiser 1991; Ponman et al. 1999; Tozzi & Norman 2001). In cosmological simulations this energy is provided by SFGs and AGN through outflows, and their efficiencies can be calibrated to reproduce the properties of the local Universe (e.g., Le Brun et al. 2014; Pike et al. 2014). Although

the most successful models are those in which heating of the ICM happens early, such as (cosmo-)OWLS (Schaye et al. 2010; McCarthy et al. 2011), this process is still poorly constrained observationally: the timing and duration of this phenomenon, its main energy source (galactic winds from either SNae or AGN), and the energy transfer mechanism are subject to debate (i.e., McCarthy et al. 2011; Davé et al. 2008; McNamara & Nulsen 2007; Fabian 2012).

All things considered, both observations and theoretical expectations require an active role of galaxies in shaping their environment. Part of this thesis will be dedicated to the exploration of this issue focusing on high-redshift, hugely star-forming galaxies, which may be fundamentally contributing to the energy budget of the ICM while being the dominant core population at the very early stage of clusters growth.

2 METAL DEFICIENCY IN CLUSTER STAR-FORMING GALAXIES AT $z = 2$

The evolution of galaxies is regulated by the complex interplay of multiple physical mechanisms. As described in Chapter 1, distinguishing the influence of external environmental effects from internal factors is crucial to reach a comprehensive understanding of these systems, and in this perspective, galaxy clusters offer the perfect occasion to disentagle this situation, comparing samples of field and extreme overdensity galaxies *at fixed mass*. In this chapter, I will approach this issue investigating the star-formation and the ISM properties of SFGs, focusing on a key diagnostic tool: the metallicity. The metal enrichment works as a recorder of the galaxy growth: it is sensitive to the formation of new stars – the forgers of heavy elements –, the dilution of pristine gas from the cosmic web, and the expulsion of processed material through galaxy outflows, three of the main actors driving the evolution of galaxies (e.g., Davé et al. 2012; Lilly et al. 2013). Penetrating the interplay of metallicity, star formation, stellar mass growth, and environment is thus of paramount importance. The existence of a "Main Sequence" (MS) of SFGs, a tight correlation between stellar masses and SFRs up to $z \sim 6$, has been already introduced in Section 1.2.1. A Mass-Metallicity Relation (MZR) has also been shown to be in place from $z = 0$ (Lequeux et al. 1979; Tremonti et al. 2004) up to redshift $\sim 3-4$ (Savaglio et al. 2005; Erb et al. 2006; Troncoso et al. 2014; Zahid et al. 2014b; Wuyts et al. 2014; Onodera et al. 2016, and others), indicating that more massive galaxies are also more metal rich at any epoch. At increasing redshift, the gas-phase metallicity in SFGs is observed to decrease, but our knowledge of possible effects of the surrounding environment on metal enrichment is still uncertain, even in the local universe. Many studies, generally based on the wealth of information of the Sloan Digital Sky Survey (SDSS, York et al. 2000) and other local surveys, do not find evidence for strong environmental effects on galaxy metallicity, if at all present (Mouhcine et al. 2007; Cooper et al. 2008; Ellison et al. 2009; Hughes et al. 2013). Only a very mild metal enrichment in galaxies residing in the densest regions is usually reported, especially when the degeneracy with stellar mass is properly taken into account. However, most of these studies generally rely on the definition of a *local environment* based on variations of the N-th nearest companion technique. As noted in Peng et al. (2012), this definition primarily traces the position inside

the halo of rich groups and clusters, while it strongly correlates with the richness and halo mass in poor groups, depending on the choice of N. As a result, cluster or group membership, halo masses, or local overdensities trace different environments and may drive to different conclusions. Indeed, the are indications that the local overdensities might be more relevant for the metal enrichment than cluster membership (Ellison et al. 2009), which appears particularly strong when operating the distinction between satellites and centrals (Pasquali et al. 2012; Peng & Maiolino 2014). The situation in the high-redshift universe is even more complex. The recent dramatic improvement in near-IR multi-object spectrographs has opened the way to study the physical properties of ionized gas in SFGs through a set of emission lines well studied in local objects, such as Hβ, [O III] λλ4959, 5007 Å (hereafter [O III]), Hα, and [N II] λλ6549, 6584 Å (hereafter [N II]). These lines give also access to the gas-phase metallicity in SFGs, if properly calibrated. Prior to the publication of the article on which this chapter is based, studies at $z \gtrsim 2$ focused only on few protoclusters at $z > 2$ (Kulas et al. 2013; Shimakawa et al. 2015), while others followed (Kacprzak et al. 2015; Tran et al. 2015; Kewley et al. 2016). A brief comment about the latter will be included in the discussion.

In this chapter I present results relative to the farthest spectroscopically confirmed X-ray detected cluster discovered to date, CL J1449+0856 at $z = 1.99$ (Gobat et al. 2011, 2013, hereafter G11, G13). I present here a recent Subaru/Multi-Object InfraRed Camera and Spectrograph (MOIRCS) follow-up of the star-forming population in CL J1449+0856, for which Hα and [N II] emission lines have been measured. Incorporating previous information about [O III] and Hβ from *HST*/Wide Field Camera 3 (WFC3) G141 slitless spectroscopy (G13), I could estimate the metallicity through the $N2 = \log([N\,II]/H\alpha)$ and $O3N2 = \log[([O\,III]/H\beta)/([N\,II]/H\alpha)]$ indicators (Alloin et al. 1979), exploring different calibrations proposed in recent literature (Pettini & Pagel 2004; Steidel et al. 2014). I will compare the MZR and other interstellar medium (ISM) properties of SFGs in CL J1449+0856 with a mass-matched field sample at comparable redshift, allowing for a direct probe of the environmental effects of relatively evolved overdensities on SFGs at $z = 2$.

The results presented here are the fruit of the collaboration with present and past members of the extragalactic astrophysics group at CEA Saclay and were published in the Astrophysical Journal in March 2015 (Valentino et al. 2015). Section 2.1 introduces the galaxy cluster CL J1449+0856 and its main properties. Then, in Section 2.2 I describe the sample selection and the near-IR spectroscopic and ancillary data used for the analysis. In Section 2.3 I present the full photometric and spectroscopic analysis of the dataset along with the derived ISM physical condition through currently used line diagnostic diagrams. I show the results about the MZR in Section 2.4 and dis-

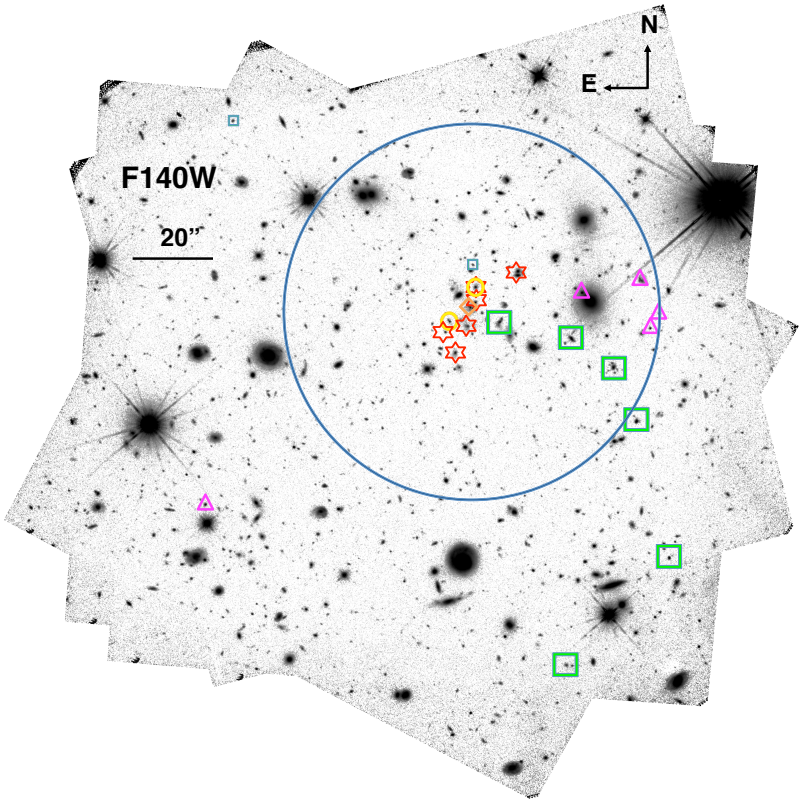

Figure 6 Deep F140W image of CL J1449+0856 and its spectroscopically confirmed members in the field observed with WFC3 (G13). Red stars mark passive galaxies. Yellow circles indicate X-ray detected AGN. Green squares indicate SFGs in the mass range $10 \leqslant \log(M_\star/M_\odot) \leqslant 11$ and blue squares indicate SFGs in the mass range $\log(M_\star/M_\odot) < 10$, both targeted and detected with MOIRCS. Purple triangles indicate other SFGs not targeted with MOIRCS. The orange diamond shows the assembling putative brightest cluster galaxy. The blue solid circle represents the virial radius $R_{200} = (0.5 \pm 0.1)$ Mpc (physical, Valentino et al. 2016).

cuss potential implications in Section 2.5. Section 2.6 summarizes the main findings of this work. Additional technical remarks are reported in the Appendix. Throughout all the paper I adopt a flat ΛCDM cosmology with $\Omega_m = 0.3$, $\Omega_\Lambda = 0.7$ and $H_0 = 70\,km\,s^{-1}\,Mpc^{-1}$, and a Salpeter initial mass function (IMF, Salpeter 1955). When necessary I converted results from literature obtained with other IMFs to a Salpeter IMF.

2.1 THE FARTHEST X-RAY EMITTING CLUSTER KNOWN TO DATE

The galaxy cluster CL J1449+0856 (R.A. = 14h 49m 14s, decl. = 8°56′21″) has been originally selected as an overdensity of galaxies with IRAC colors $[3.6] - [4.5]\,\mu m > 0$ in archival *Spitzer* observations (Daddi et al. 2000). The cluster is spectroscopically confirmed with currently 27 members identified with VLT/VIMOS, FORS2, and *HST*/WFC3 spectroscopy (G11, G13). Most spectroscopic redshifts in the field of CL J1449+0856 come from the WFC3 G141 spectroscopic follow-up (Figure 6), with 140 redshift determinations over a $\sim 4\,arcmin^2$ area, based on emission lines (typically [O II] λ3727 Å, [Ne III] λ3869 Å, Hβ, [O III] at $z \sim 2$) or on continuum breaks in the spectral range $1.1 - 1.7\,\mu m$. These include 68 [O III] emitters, 17 of which belong to the cluster, and a population of 6 red, massive, and quiescent galaxies that dominate the cluster core (G13, Strazzullo et al. 2013, hereafter S13). In the last few years, CL J1449+0856 has been also extensively imaged at wavelengths from X-ray to radio (Table 6 in Appendix). Extended X-ray emission has been detected by XMM-Newton (80 ks) and Chandra (94 ks) (Brusa et al. 2005; Campisi et al. 2009, G11). Together with the dominating quiescent population in the central regions, the X-ray detection places CL J1449+0856 in a relatively evolved phase compared with other known structures at the same epoch, making it the potential progenitor of a massive local cluster. These features physically distinguish this overdensity from lower halo mass, SFG-dominated, rapidly assembling *protoclusters* extended over several Mpc at similar or higher redshifts (e.g., Steidel et al. 2005; Kodama et al. 2013; Diener et al. 2013) and potentially these intrinsically different structures may give rise to different effects on their host galaxies (Section 1.3). A detailed recapitulation of the X-ray properties, including new Chandra observations, is postponed to Chapter 3, where it naturally fits with the description of the multi-phase ICM presented in Valentino et al. (2016). For the sake of clarity, we anticipate that the total X-ray luminosity of $L_X = (9 \pm 3) \times 10^{43}$ erg s^{-1} in the $0.1 - 2.4$ keV soft band scales to a halo virial mass of $M_{halo} = 5 - 7 \times 10^{13}\,M_\odot$, in agreement with the estimate of the velocity dispersion ($\sigma_{vel} = (830 \pm 230)$ km s^{-1}) and the observed

total stellar mass content (2×10^{12} $M_\odot$, S13). The virial radius is $R_{200} = (0.5 \pm 0.1)$ Mpc, corresponding to the clustercentric distance at which the density falls below $200\times$ the critical density of the universe at $z = 1.99$.

2.2 SAMPLE SELECTION AND DATA DESCRIPTION

Galaxy populations in CL J1449+0856 have been investigated in G11, G13, and S13. In this work, we used the same photometric catalogs as in S13, including optical/NIR photometry in 13 passbands from U to 4.5 μm. Sources were detected in the WFC3/F140W band, and photometry was measured with SExtractor (Bertin & Arnouts 1996), as well as with GALFIT (Peng et al. 2002, 2010a) modeling. Based on photometric redshifts determined on such photometry, a sample of candidate cluster members was identified in the cluster central region, virtually complete at $M_\star \gtrsim 10^{10}$ $M_\odot$, although affected by significant contamination especially below 10^{10} $M_\odot$. Galaxies were also broadly classified as "passive" or "star-forming" based on rest-frame UVJ colors (Wuyts et al. 2007; Williams et al. 2009) and spectral energy distribution fitting (SED, S13). In this work, we focus on SFGs in the mass range $10 \leqslant \log(M_\star/M_\odot) \leqslant 11$. The full sample of cluster galaxies in the F140W-based catalog includes 6 spectroscopically confirmed and 2 candidate star-forming cluster members in this mass range. For our MOIRCS near-IR follow-up, we selected a sample of 110 objects. These included 76 sources in CL 1449+0856 field, where we gave the highest priority to WFC3 spectroscopically confirmed star-forming members (10 objects: 2 with $M_\star < 10^{10}$ $M_\odot$, 6 with 10^{10} $M_\odot \leqslant M_\star \leqslant 10^{11}$ $M_\odot$, and 2 with $M_\star > 10^{11}$ $M_\odot$) and to star-forming objects from the pool of candidate members according to their probability of belonging to the cluster and irrespectively of their mass. We note here that cluster SFGs were not specifically selected to be [O III] emitters. The 2 candidates in the mass range $10 \leqslant \log(M_\star/M_\odot) \leqslant 11$ were not observed due to geometrical constraints in slit positioning. In the area covered by WFC3 we selected 13 [O III] emitters not belonging to the overdensity, which became part of the field control sample at $z \sim 2$. Outside the WFC3 field, where no spectroscopy was available, we selected field objects with $z_{phot} \geqslant 2$ with the highest chances to detect Hα, i.e., with an estimated Hα flux $\geqslant 3 \times 10^{-17}$ erg cm^{-2} s^{-1} from the SED-based SFR and reddening estimates (see Section 2.3). Finally, to further extend our field control sample, we observed 34 *BzK*-SFGs (Daddi et al. 2004) with $z_{phot} \sim 2$ with an estimated Hα flux $\geqslant 3 \times 10^{-17}$ erg cm^{-2} s^{-1} in the COSMOS field (Scoville et al. 2007). A posteriori the predicted Hα was $\sim 25\%$ lower than the measured flux for these field Hα-selected sources, probably due to Malmquist bias. We note here that,

even if the total integration time over the COSMOS field is shorter than over the cluster field, this does not substantially impact the main results of this work, based on the stacking of sources (see Section 2.3.2). The objects in the COSMOS field contributed to $\sim 30\%$ of the total number of field sources in the final stacked spectrum (10/31) and reached Hα fluxes comparable with the dimmest sources in CL 1449+0856 field (3.2×10^{-17} and 3.3×10^{-17} erg cm^{-2} s^{-1} at $> 5\sigma$ in the cluster and COSMOS field, respectively).

We carried out near-IR spectroscopy with MOIRCS at the Subaru Telescope (Ichikawa et al. 2006). Two Hawaii-2 2048×2048 detectors cover the $4' \times 7'$ FoV and up to 40 slits can be placed within the inner $6'$ diameter circular region. We used the HK500 grism with 0.7" wide slits, which provides a resolving power $R \simeq 500$ along the $13000 - 23000$ Å spectral range. A total of three masks were designed, two for the CL J1449+0856 field and one for the COSMOS field. The observations were carried out in a single run of three consecutive nights in April, 2013. A sequence of 600 s integrations was taken with a standard ABAB 1.5" dithering pattern. Calibration frames of an A0V standard star and dome flat fields were taken at the beginning or end of each night. We integrated the images for a total of 7.3, 6.7, 3.3 hr on 38, 38, and 34 galaxies for Mask 1 and 2 on CL J1449+0856 and Mask 3 in the COSMOS field, respectively, with a mean seeing of ~ 0.6" during three clear nights. The observation plan is summarized in Table 1. We reduced the data with the MCSMDP pipeline[1] (Yoshikawa et al. 2010) combined with custom IDL scripts. First, the data were flat-fielded employing dome-flat frames collected in the same configuration of science frames, and bad pixels and other detector defects were removed using masks provided in the pipeline. Then, cosmic rays were removed combining each A frame with the corresponding dithered B image. The sky subtraction was automatically performed subtracting each B frame to the corrisponding A image. Then the distortion introduced by the detectors was corrected using the coefficients used in the MOIRCS imaging reduction package. Each 2D spectrum was then cut from every global frame and wavelength calibrated on a grid of bright OH-airglow lines (Rousselot et al. 2000), with an uncertainty of half of a pixel, i.e. ~ 3.5 Å. We co-added all the 2D spectra, down-weighting the frames taken in worse atmospheric conditions to minimize the effect of variable seeing during the observing run. We finally extracted the 1D spectra and flux-calibrated them by comparing with a standard A0V stellar spectrum. We also corrected for the differential airmasses and telluric absorption by modeling the sensitivity curve in the most transparent

1 http://www.naoj.org/Observing/DataReduction/

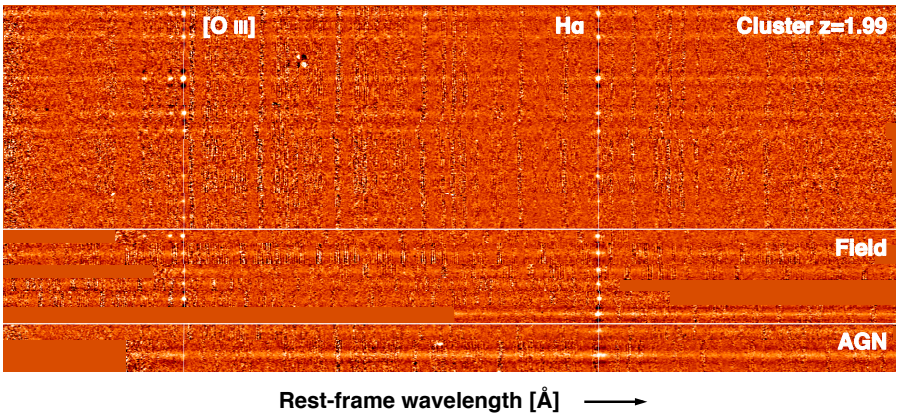

Figure 7 Subaru/MOIRCS 2D rest-frame spectra of a selection of cluster and field sources. The first 6 rows are the spectra of the stacked cluster members (Section 2.3.2). Two AGN are shown for reference (Section 2.3.3).

regions of the *H* and *Ks* bands and modifying the curve to include a factor:

$$\text{Correction} = (\text{Sensitivity curve}/\text{Fit} - 1) \times F_{AM} \qquad (1)$$

The final values of the airmass factor F_{AM} (-0.15, -0.20 and -0.375 for Mask 1, 2, and COSMOS, respectively) are obtained calibrating the spectrum of monitoring stars included in the all the masks. We estimated aperture corrections (~ 1.3 on average) comparing the integrated flux within the *H* and *Ks* band with the total photometric values. As a final step we modeled the noise at each wavelength, taking into account possible slit-to-slit and wavelength-dependent sky variations. We interpolated few 2D non flux calibrated spectra with a well extended observed spectral range ($\sim 13000 - 23000$ Å) on a grid of common wavelengths. We aligned them along the spatial direction obtaining a $n_\lambda \times n_{spatial}$ pixels mosaic, where n_λ is the number of pixels along the dispersion direction and $n_{spatial} = \sum_i n_{width_i}$ is the number of pixels along the spatial direction, given by the sum of the widths of each slit in the mosaic. Then, we computed the rms along the spatial direction and took it as the noise array. We applied a mild σ-clipping to exclude the increase of the rms at specific wavelengths due to the contribution of galaxy emissions. The use of multiple slits allows for a substantial enhancement of the number statistics of sky pixels, but possible slit-to-slit variations may further modify the noise properties. Thus, after a proper flux calibration, we removed the galaxy emission from the spectrum and computed the χ^2 statistics. Generally, gaussian profiles for the brightest lines (Hα, [O III]) and a polynomial curve for the continuum emission were sufficient. Removing the contribution of the galaxy emission from a spectrum, we should observe pure noise, and thus the reduced χ^2_{red} should return

Table 1. Observation log.

Mask ID[a]	Date[b]	Integration time[c] (hr)	Target field[d]
Mask 1	2013 Apr, 7th	4.3	CL J1449+0856
	2013 Apr, 9th	3	CL J1449+0856
Mask 2	2013 Apr, 8th	5	CL J1449+0856
	2013 Apr, 9th	1.7	CL J1449+0856
Mask 3	2013 Apr, 7th	1.7	COSMOS
	2013 Apr, 8th	1.2	COSMOS
	2013 Apr, 9th	0.5	COSMOS

[a]ID of the three MOIRCS masks.

[b]Date of observation.

[c]Total integration time per night.

[d]Pointed target field.

a value ~ 1. Finally, we simply rescaled the noise array by $\sqrt{\chi^2_{\rm red}}$, if $\chi^2_{\rm red} > 1$. We improved our noise estimation including second order, wavelength-dependent variations in each slit by computing the $\chi^2_{\rm red}$ statistics in a 1500 Å wide window running along the dispersion axis and applying a local $\sqrt{\chi^2_{\rm red}}$ correction factor if significant departures from the global $\chi^2_{\rm red}$ were present.

We successfully detected (3σ confidence level down to an observed Hα flux of 1.4×10^{-17} erg cm^{-2} s^{-1}) at least one line in 71% of the sample (78/110 galaxies). In 71, 22, 41, and 7 galaxies we detected at 3σ Hα, [N II], [O III], and Hβ, respectively. For galaxies where we detected at least one line at 3σ, we put 2σ upper limits on the other lines, if present in the observed spectral range. When available, we averaged the line fluxes from WFC3 observations with MOIRCS-detected lines, assigning higher weights to higher S/N estimates and properly taking into account the consistency of the [O III]/Hβ ratios and the total flux scaling between the two independent measurements. A total of 49 galaxies have a detection or a 2σ upper limit on all Hβ, [O III], Hα, [N II] emission lines. A selection of flux-calibrated, rest-frame, 2D MOIRCS spectra of cluster and field galaxies with significant line detections is shown in Figure 7.

Table 2. Stacked spectra properties.

Environment	No. sources	$\langle z \rangle$	$\log(M_\star)$ $(\log(M_\odot))$	SFR_{SED} $(M_\odot\ yr^{-1})$	$E(B-V)_{cont}$	$SFR_{H\alpha}$ $(M_\odot\ yr^{-1})$	$E(B-V)_{neb}$
Cluster	6	1.99	10.47	101	0.29	112	0.32
Field	31	1.92	10.57	126	0.31	68	–
Field	16	2.14	10.52	110	0.33	75	0.48

Note. — SED derived quantities are the mean values of single sources in the stacked spectra.

Table 3. Stacked spectra observed fluxes.

Environment	No. sources	[O II] (cgs)	Hβ (cgs)	[O III] (cgs)	Hα (cgs)	[N II] (cgs)	$[S\,II]_{tot}$[a] (cgs)
Cluster	6	0.800 ± 0.065[b]	0.463 ± 0.065	1.781 ± 0.043	1.915 ± 0.061	0.145 ± 0.048	0.119 ± 0.026
Field	31	–	–	–	0.754 ± 0.020	0.159 ± 0.015	0.075 ± 0.011
Field	16	–	0.128 ± 0.016	0.499 ± 0.019	0.645 ± 0.016	0.104 ± 0.012	0.070 ± 0.010

[a]Total combined flux of [S II] λλ6716, 6731 Å.

[b]Value for 5/6 cluster members with [O II] coverage.

Note. — The observed line fluxes are expressed in units of 10^{-16} erg cm^{-2} s^{-1}. [O II] fluxes come from WFC3 observations (G13).

2.3 METHODOLOGY

2.3.1 SED modeling

Stellar masses, SFRs, and dust reddening were determined using FAST (Kriek et al. 2009) on the UV to IR photometry. We used Bruzual & Charlot (2003) models with constant star formation histories (SFHs) and a Salpeter IMF (Salpeter 1955). The Calzetti et al. (2000) reddening law was used to estimate the extinction. For the COSMOS sample, for which the photometric coverage probes the rest frame UV SED with high accuracy, we allowed for a variable UV bump in the fit (Noll et al. 2009). The slope of the attenuation law was not fitted and the derived SFR estimates are consistent with those derived with the Calzetti et al. (2000) law. We note that the choice of a different SFH, possibly rising or exponentially declining, negligibly affects our mass estimates, well within systematic uncertainties (~ 0.2 dex). Indeed, for active star-forming galaxies at these redshifts the SED fit gives in most cases very short ages and comparable e-folding times, such that the actual SFH is nearly constant, no matter whether an exponentially increasing or decreasing SFR is used (Maraston et al. 2010). On the contrary, other parameters used in this work are potentially affected by the choice of the SFH, e.g. the SFR. We opted for a constant SFH as it proved to give consistent results in representing the MS of SFGs, matching the SFRs derived independently from Hα fluxes and FIR and X-ray stacking (Daddi et al. 2007; Rodighiero et al. 2014). We fitted the photometry for both the aperture-based and the GALFIT-based catalogs (see Section 2.2 and S13). Stellar masses and SFRs from the SExtractor catalog were corrected based on total-to-aperture flux ratios ($\lesssim 0.15$ dex for the sample used here). For those galaxies for which the IRAC photometry suffers from a potentially heavy contamination from neighbors ($\sim 10\%$ of our sample), we excluded the $3.6-4.5\mu$m bands from the fitting procedure. The two photometric catalogs yield broadly consistent parameter values (e.g., a ~ 0.1 dex difference in total stellar masses).

2.3.2 Spectral stacking

In order to maximize the information derivable from the observed spectra and to find an average trend for the cluster and field samples, we stacked individual spectra. We blue-shifted the spectra to the rest-frame and registered them on a common grid of ~ 2.7 Å and ~ 3.7 Å step for the cluster and field, respectively. Then for every wavelength step we averaged the flux values, weighting for the inverse variance if a sufficiently high number of spectra were co-added ($N > 10$). On the other hand, a straight mean was computed in stack-

Table 4. Properties of the 6 confirmed cluster star-forming members in the stack.

ID	RA (deg)	DEC (deg)	z_{spec}	$\log(M_\star)$ ($\log(M_\odot)$)	$E(B-V)_{neb}^{SED}$ [a]	$SFR_{H\alpha}$ ($M_\odot$ yr^{-1})
ID568	222.3024796	8.9387313	1.987 ± 0.001	10.38	0.33	118 ± 9 [b]
ID510	222.2997850	8.9369198	1.988 ± 0.001	10.52	0.53	158 ± 13
ID422	222.2983118	8.9335256	1.988 ± 0.001	10.53	0.43	361 ± 60
ID183	222.2961999	8.9248673	1.990 ± 0.001	10.05	0.10	24 ± 3
ID580	222.3070938	8.9397864	2.001 ± 0.001	10.54	0.43	189 ± 23
ID41	222.3029800	8.9186500	1.991 ± 0.001	10.63	0.50	125 ± 30

[a] $E(B-V)_{neb}^{SED}$ is the nebular reddening derived from the SED modeling as $E(B-V)_{cont}/f$ (Section 2.3.3).

[b] ID568 shows peculiar WFC3 emission line maps (Zanella et al. 2015). Using the emission line maps to compute the aperture correction and the reddening prescription from Zanella et al. (2015) would lead to $SFR_{H\alpha} = 77 \pm 9$ $M_\odot$ yr^{-1}.

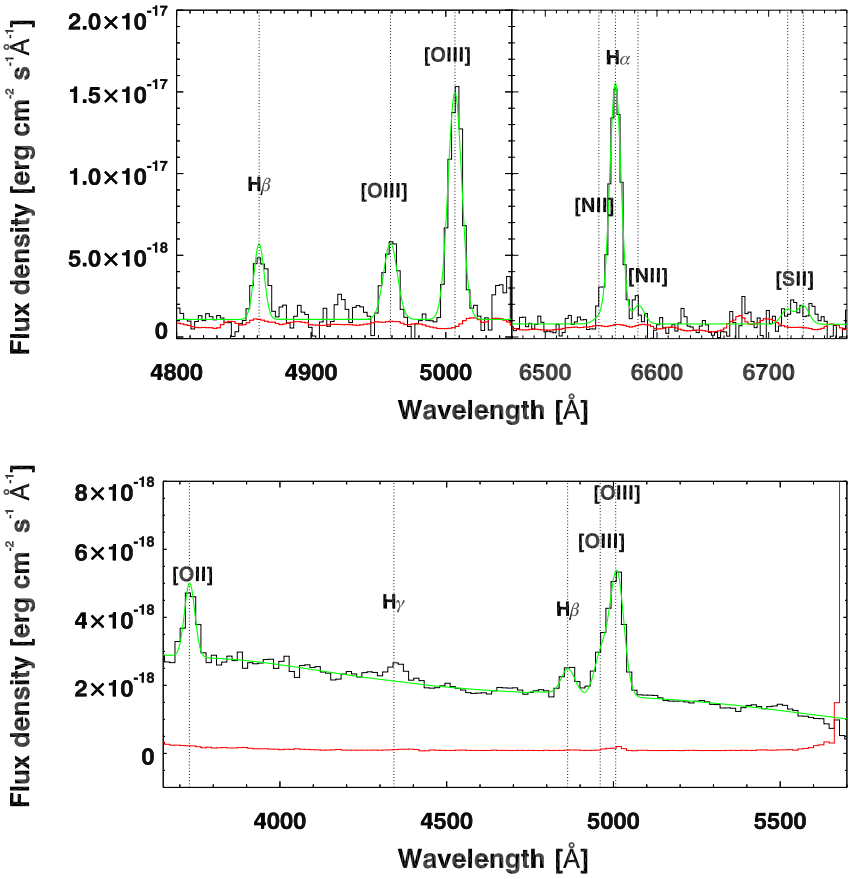

Figure 8 MOIRCS (top panel) and WFC3 (bottom panel) stacked spectra and noise of the sample of 6 cluster SFGs in the mass range $10 \leqslant \log(M_\star/M_\odot) \leqslant 11$. The black and red lines respectively represent the stacked spectra and noise. The green line shows the best fit for the emission lines. Vertical dotted lines mark the expected location of emission lines of interest, as labeled.

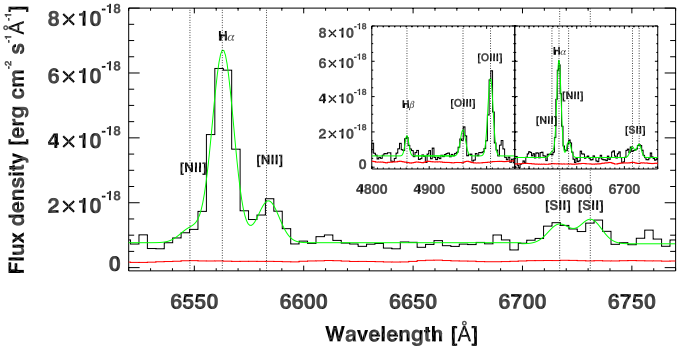

Figure 9 MOIRCS stacked spectrum and noise of the sample of 31 field SFGs in the mass range $10 \leqslant \log(M_\star/M_\odot) \leqslant 11$ with Hα and [N II] in the observed wavelength range. The black and red lines respectively represent the stacked spectrum and noise. The green line shows the best fit for the emission lines. The onset shows the MOIRCS stacked spectrum and noise for the subsample of 16 field SFGs in the same mass range with Hβ, [O III], Hα, and [N II] in the observed wavelength range. Vertical dotted lines mark the expected location of emission lines of interest, as labeled.

ing a low number of spectra ($N < 10$), not to introduce wavelength dependent biases. We note here that averaging individual spectra does not necessarily coincide with averaging spectral derived quantities. The difference between these two averaged trends depends on the relationship between line fluxes and the derived quantities. In our case we estimated the impact of this difference on the mean metallicity calculated through the line ratio [N II]/Hα for a population of MS-SFGs. For masses $M_\star \geqslant 10^{10}$ $M_\odot$, considering the low number statistics for the cluster sample, the two computed averages are similar ($< 4\%$ difference). Therefore we adopted the mean metallicities coming from the stacking procedure as representative of the population without applying any other correction. The details of this calculation are reported in the Appendix.

Considering the low number of sources with $\log(M_\star/M_\odot) < 10$ and $\log(M_\star/M_\odot) > 11$, we opted for stacking all galaxies with a spectroscopic redshift determination and Hα coverage in the mass range $10 \leqslant \log(M_\star/M_\odot) \leqslant 11$. To investigate possible environmental effects, we stacked the cluster and field sources separately, after a conservative AGN removal (see Section 2.3.3). We stacked 6 sources without implementing any weighting scheme for the cluster sample at $z = 1.99$ (Table 4). In the same mass bin we stacked 31 field sources ($\langle z \rangle = 1.92$) with Hα and [N II] in the observed range and a subsample of 16 galaxies ($\langle z \rangle = 2.14$) with Hβ and [O III] in addition. Given the number of objects, we applied the optimal weighting described above to the field sample. Unless noted otherwise, in the

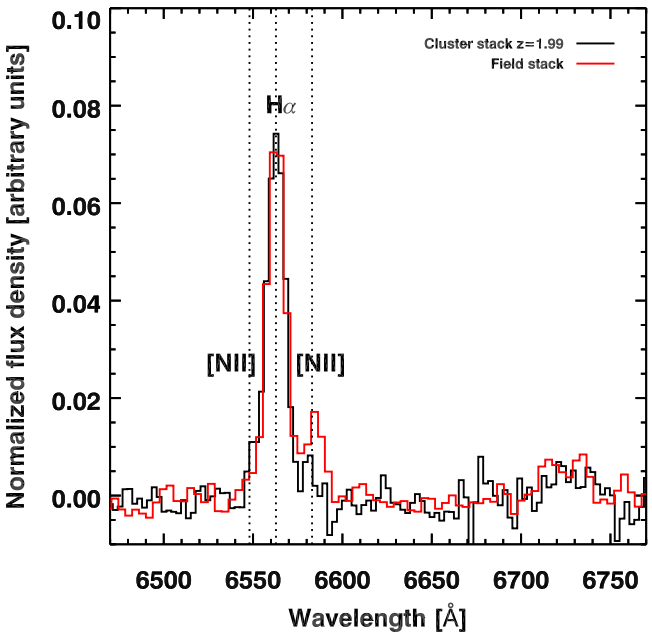

Figure 10 The black and red lines respectively represent the continuum subtracted MOIRCS stacked spectra of the sample of 6 cluster SFGs and 31 field SFGs in the mass range $10 \leqslant \log(M_\star/M_\odot) \leqslant 11$ with Hα and [N II] in the observed wavelength range, normalized to Hα fluxes. Vertical dotted lines mark the expected location of emission lines of interest, as labeled.

rest of this work we will use the 31 sources field stack as a main term of comparison for the analysis of environmental effects to exploit at maximum the sample observed with MOIRCS and we refer to it as the "field stack". However, we made use of the 16-source stacked subsample when necessary, i.e., when [O III] or Hβ fluxes were required. The [N II]/Hα ratio in the 31-source and 16-source field stacks is consistent within the uncertainties. Note that the impact of redshift uncertainties on the final stacked spectra is minimal, since we averaged only individual high signal-to-noise spectra (e.g., $\langle SNR(H\alpha)\rangle > 10$). The stacked spectra are shown in Figures 8 and 9, and their photometric and spectroscopic properties are summarized in Tables 2 and 3. In Figure 10 we plot the continuum subtracted stacked spectra normalized to their Hα total fluxes. Furthermore, we checked if the brightest Hα emitters biased the average spectra, stacking individual sources normalized by their observed and intrinsic Hα fluxes. In both cases [N II]/Hα and [O III]/Hβ are fully compatible with the non- and optimally-weighted measurements within 1σ error bars. We also stacked only the 5 cluster sources at a time to check for the impact of low number statistics. In all the cases [N II]/Hα and [O III]/Hβ

ratios are consistent within 1σ with the non-weighted measurements, except for the [O III]/Hβ ratio when stacking only the upper limits on [N II] (in this case the ratio varies within 2σ error bars, suggesting possible important physical variance within the sample). We note here that among the 6 cluster sources in the stack, only the brightest one in Hα is detected in [N II] at 2σ and corresponds to the lowest [N II]/Hα ratio, which is nevertheless consistent with the average value for the remaining 5 cluster sources. Therefore, the [N II] detection is likely the effect of the bright Hα emission. Moreover, all the 6 cluster SFGs in the $10 \leqslant \log(M_\star/M_\odot) \leqslant 11$ mass range have a WFC3 spectrum, and for 5/6 sources the $3600 - 5700$ Å rest-frame interval is covered, giving access to the [O II] $\lambda 3727$ Å emission line ([O II] in the following). Hence, we stacked the WFC3 spectra as done for MOIRCS spectra rescaling to match the absolute fluxes from broad-band photometry. The final stacked [O III] and Hβ fluxes from the WFC3 and MOIRCS spectra result fully compatible within the uncertainties. Finally, we attempted to stack the cluster sources within and outside the virial radius separately, but the low number statistics and signal-to-noise of the spectra prevented us from deriving any statistically significant conclusion about possible effects as a function of the clustercentric distance.

2.3.3 Line fluxes

We measured line fluxes fitting gaussian profiles to the emission lines on flux calibrated and aperture corrected spectra. We used the squared inverse of the noise array to weight the fitting and to estimate the errors on total fluxes, line positions, and, thus, on the redshift determination. Using the IDL script MPFIT (Markwardt 2009), we fitted at the same time three gaussian profiles lying on a flat continuum to measure [N II] $\lambda\lambda 6548, 6583$ Å and Hα fluxes. We modeled the local continuum around each emission line in wavelength ranges large enough to be dominated by continuum emission (~ 1000 Å). In the very few cases where a flat continuum did not provide a good model, we fitted a polynomial curve. We left the Hα central wavelength and FWHM free to vary in the fit, while we fixed the [N II] doublet lines to share a common line width value set by FWHM(Hα) (in terms of velocity), their expected positions relatively to Hα, and their flux ratio to 3.05 (Storey & Zeippen 2000). Similarly, we simultaneously fitted the [O III] $\lambda\lambda 4959, 5007$ Å lines, fixing their position and width according to Hα values, and their intensity ratio to 2.98. Any other line in the observed range, both single or in multiplets, was fitted following the same procedure. We estimated flux uncertainties with MPFIT and rescaled them according to the χ^2 value when $\chi^2 > 1.5$. In addition we ran Monte Carlo simulations, placing mock lines in empty spectral regions, recovering consistent uncertainties within $\sim 5\%$, confirming

the reliability of our noise estimate. We finally estimated the Hα and Hβ stellar absorption measuring the continuum at the proper wavelengths and assuming absorption equivalent widths $EW^{abs}_{H\alpha} = 3.5$ Å and $EW^{abs}_{H\beta} = 5$ Å, as estimated from SED modeling. This correction is $\lesssim 15\%$ and $\sim 30\%$ for Hα and Hβ respectively.

Line diagnostics diagrams

Following the first pioneering work by Baldwin et al. (1981), many studies have shown that the proper combination of ratios of collisionally excited and recombination lines can provide useful information not only about the element abundances in the gas in galaxies, but also about its ionization state and the primary ionizing source (e.g., Kewley & Dopita 2002; Kewley et al. 2013a). In this work we investigate the gas state using the [N II]/Hα – [O III]/Hβ diagram, commonly referred to as the BPT diagram. This can be used to distinguish line-emitting galaxies mainly powered by an AGN from those dominated by star formation: the radiation field emitted by the disk accreting around an AGN is harder, increasing the oxygen and nitrogen ionization and producing larger [O III] and [N II] fluxes with respect to the values reached by SF-powered ionization. However the situation may be considerably different at higher redshifts: an evolution of the electron density, pressure, N/O ratio, ionization parameter or the hardness of the radiation field can shift the locus of the SF sequence. Recent developments in multi-object near-IR spectroscopy have allowed for the observation of an increasing number of samples of line emitters, extending the study of the potential evolution of line ratios with cosmic time (e.g., Kewley et al. 2013a; Holden et al. 2016; Kashino et al. 2016; Shapley et al. 2015; Sanders et al. 2016) and the role of selection effects (Juneau et al. 2014) to earlier epochs, up to $z \geqslant 1.5$. Recent results by Steidel et al. (2014, S14 in the following) for a sample of $z \sim 2.3$ SFGs point towards a substantial vertical shift in the BPT diagram due to a harder field ionizing the ISM, qualitatively in agreement with some theoretical expectations (Kewley et al. 2013a,b, but see, e.g., Coil et al. 2015 for alternative results). Interestingly, S14 interpret the locus of SFGs mainly as a "ionization parameter" sequence, in contrast to the usual interpretation of a "gas-phase metallicity" sequence given in the local Universe (Kewley & Ellison 2008). However, a change in the N/O appears to be at least partially involved in the shift of the BPT locus with redshift (Masters et al. 2014; Shapley et al. 2015; Sanders et al. 2016; Masters et al. 2016), while higher ionization parameters and pressure are favored by other authors (Dopita et al. 2016; Kashino et al. 2016; Cullen et al. 2016). Figure 11 shows our sample in the BPT diagram and a reference sample at $z \sim 1.55$ from the Subaru/FMOS survey (Zahid et al. 2014b). A low-redshift ($0.04 < z < 0.2$) sample of 299,098 galaxies selected from SDSS DR7 (Abazajian et al. 2009) is

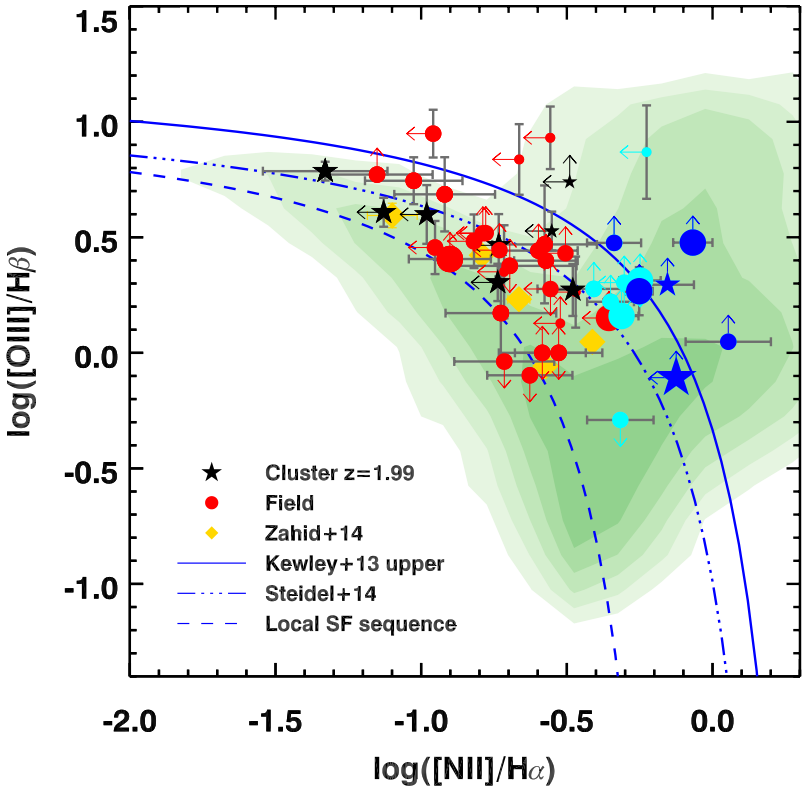

Figure 11 BPT diagram for the MOIRCS spectroscopic sample. Red circles and black stars represent the field and cluster samples, respectively. Cyan and blue symbols mark the objects excluded from the SF sample as AGN from X-ray, radio, [N II]/Hα-EW(Hα) or the solid curve shown (see text and Figure 12 for details). Symbol sizes scale as the stellar mass. Golden diamonds represent the stacked points from the FMOS survey at $z \sim 1.55$ (Zahid et al. 2014b). Arrows indicate 2σ upper limits both for the x and y axis. The blue dashed line shows the local SF sequence (Equation 3, Kewley et al. 2013a), the blue dash-dotted line indicates the empirical SF sequence at $z \sim 2.3$ from Steidel et al. (2014), and the blue solid line is the AGN-SFG dividing line at $z = 2$ (Equation 5, Kewley et al. 2013a). Green shaded contours show the SDSS $z \sim 0.1$ sample.

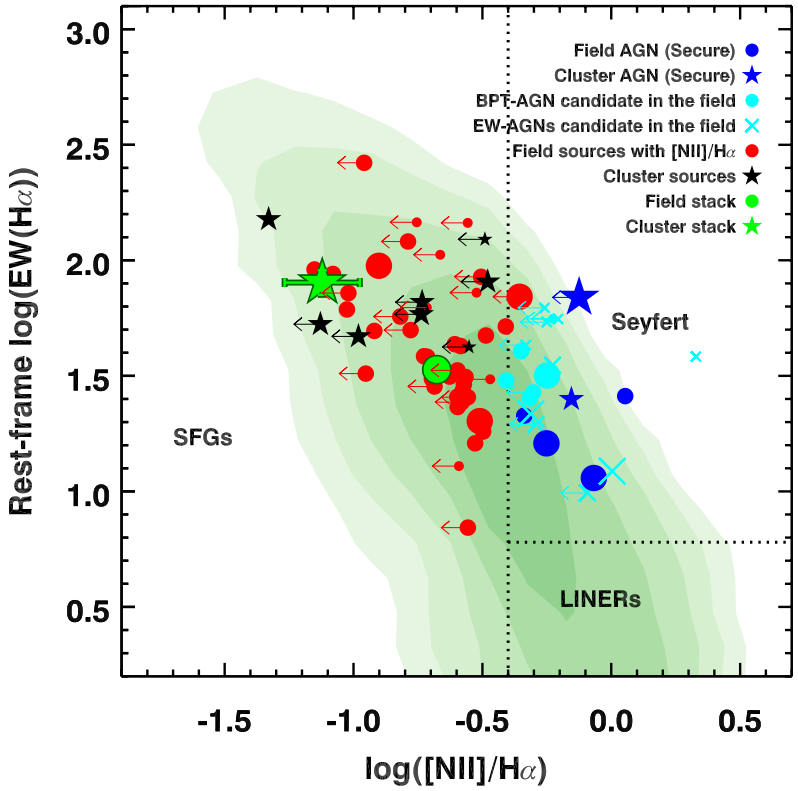

Figure 12 [N II]/Hα – rest-frame reddening uncorrected EW(Hα) diagram for the MOIRCS spectroscopic sample. Red circles and black stars represent the field and cluster samples, respectively. Blue circles and stars respectively represent field and cluster AGN known from X-ray, radio, and BPT diagram. Cyan symbols represent AGN candidates in the present diagram and in the BPT. Symbol sizes scale as the stellar mass. Arrows indicate 2σ upper limits. The green circle and star represent the field and cluster stack, respectively. Green shaded contours show the SDSS $z \sim 0.1$ sample.

shown for comparison. Following Juneau et al. (2014), galaxies were selected to have well constrained [O III]/Hβ and [N II]/Hα line ratios (S/N $> 3/\sqrt{2}$, corresponding to each line with S/N > 3 or to combinations of a weaker and a stronger line, provided that the overall line ratio is constrained to this minimum significance). Line flux measurements and uncertainties were taken from the MPA/JHU catalogs, and adjusted as detailed by Juneau et al. (2014). A systematic shift with respect to the locus of SFGs in the local Universe is present, qualitatively in agreement with a possible increase of the hardness of the radiation field, even if the data at our disposal do not allow to recognize a specific direction of the shift. To exclude AGN from our sample, we used the conservative line of exclusion as a function of redshift provided by Equation 5 in Kewley et al. (2013a). Alternative emission line diagnostics relying on [O III]/Hβ and either host color or stellar mass have been developed (e.g., Yan et al. 2011; Juneau et al. 2011). However $\sim 50\%$ of the field stacked sample (15/31 sources) does not have Hβ in the observed range. To obviate this issue, we coupled the BPT diagnostics with the [N II]/Hα – observed Hα equivalent width (EW(Hα)) diagram (Figure 12). The local SDSS sample is shown again for comparison (here we considered only galaxies with S/N(EW(Hα)) > 3, cutting the BPT local sample to 272,562 objects). In this diagram, [N II]/Hα traces the ionized gas conditions, as higher [N II]/Hα values are connected to harder powering sources, while EW(Hα) measures the power of the ionizing source in relation with the continuum emission of the underlying stellar populations (Cid Fernandes et al. 2010, 2011). In this diagram, all the potential AGN that we selected on the BPT basis occupy the same region at high [N II]/Hα ratios. In total, we conservatively excluded 22 objects as AGN-powered sources and none of these sources was included in the stacked spectra. Four points above the nominal line of exclusion in the BPT were not discarded as their upper limits on [N II]/Hα are still compatible with the star-forming region in the [N II]/Hα – observed EW(Hα) diagram. We note that 3/4 objects have $\log(M_\star/M_\odot) < 10$ and thus are not part of the stacked spectra. Excluding the fourth BPT potential outlier from the field stacked spectrum would slightly strengthen the significance (well within the uncertainties) of the main results of this work, increasing the [N II]/Hα field average value (see below). Even if we cannot exclude potential AGN contamination for these sources, we lack definitive evidence that they are mainly AGN-dominated and, keeping the most conservative approach in terms of significance of the final results, we retained these four objects in the final samples. Among these 22 sources, 2 are known to be a soft and a hard X-ray AGN in CL J1449+0856, both with $\log(M_\star/M_\odot) > 11$ (G13), while other 2 field objects are massive radio-galaxies in the COSMOS field. All these independently known AGN lie either above the line

of exclusion in the BPT diagram or above $\log([\mathrm{N\,II}]/\mathrm{H}\alpha) = -0.4$ in the $[\mathrm{N\,II}]/\mathrm{H}\alpha$ – observed $\mathrm{EW}(\mathrm{H}\alpha)$ plane, as expected. We note here that the choice of the AGN to remove does not change if we consider a dereddened $\mathrm{EW}(\mathrm{H}\alpha)$. In Figure 12 we show in addition the position of the cluster and field stacked values. Comparing these two, we note that the cluster and field samples show a $> 4\sigma$ significant difference in $[\mathrm{N\,II}]/\mathrm{H}\alpha$. Considering the subsample of 16 field galaxies with all the BPT lines, the difference is still tentatively present ($\sim 2.7\sigma$), even if the significance is reduced due to lower number statistics and signal-to-noise. Moreover, in this case the cluster and field $[\mathrm{O\,III}]/\mathrm{H}\beta$ ratios are fully compatible within the error bars (0.585 ± 0.062 and $0.591 \pm 0.058\,\mathrm{dex}$, respectively). As a consequence, the $([\mathrm{O\,III}]/\mathrm{H}\beta)/([\mathrm{N\,II}]/\mathrm{H}\alpha)$ ratio is compatible between the two samples, given the increased uncertainties. Note that a combination of low number statistics and substantial scatter in the individual spectra is unlikely to be at the origin of the difference in the $[\mathrm{N\,II}]/\mathrm{H}\alpha$ ratio. Over $4,500$ simulated stacked spectra of 6 field sources randomly selected from the pool of 31 sources of the stacked spectrum, in $< 1\%$ of the cases we recovered a value of $[\mathrm{N\,II}]/\mathrm{H}\alpha$ ratio equal or less than the cluster value. Figure 12 shows also a $0.37\,\mathrm{dex}$ difference ($\sim 4.7\sigma$ significant) in the observed $\mathrm{EW}(\mathrm{H}\alpha)$ between the cluster and the field, which reflects the $2.5\times$ higher observed $\mathrm{H}\alpha$ luminosity in the cluster stack (see Section 2.3.3 for further discussion). In this case, a Kolmogorov-Smirnov test gives a p-value of 0.0253. Finally, we observe a significant $[\mathrm{S\,II}]$ $\lambda\lambda 6716, 6731$ Å emission in the stacked spectra, but the S/N is not high enough to accurately measure the ratio of the two lines and hence directly estimate the electron density n_e (Osterbrock & Ferland 2006). Therefore, we fixed this ratio compatibly with typical n_e values in H II regions ($n_e = 100 - 1000\,\mathrm{cm}^{-3}$, Osterbrock & Ferland 2006) and measured the total combined flux $[\mathrm{S\,II}]_{\mathrm{tot}}$ $=[\mathrm{S\,II}]$ $\lambda 6716 + \lambda 6731$ reported in Table 3.

Gas-phase metallicities

Different methods have been proposed through the years to estimate the gas-phase metallicity in galaxies. The safest method involves the ratio of the $[\mathrm{O\,III}]$ $\lambda 4363$ Å auroral line and lower excitation lines as $[\mathrm{O\,III}]$ $\lambda\lambda 4959, 5007$ Å which allows to directly evaluate the oxygen abundance through the gas electron temperature (T_e). However, $[\mathrm{O\,III}]$ $\lambda 4363$ Å is weak even in low-metallicity regions and generally difficult to measure in high-redshift galaxies. Other empirical methods have been proposed to circumvent this problem, calibrating the ratios of stronger lines against T_e in H II regions. Alternatively, theoretical photoionization models may be employed to predict the line fluxes and derive the gas-phase abundances (see Kewley & Ellison 2008 for a census of gas-phase metallicity calibrations). In gen-

Table 5. Gas-phase metallicity estimates for the stacked spectra.

Environment	$\log(M_\star)$	$12+\log(O/H)$[a]			
		N2		O3N2	
	$(\log(M_\odot))$	PP04[b]	S14[c]	PP04[b]	S14[c]
Cluster	10.47	8.261 ± 0.083	8.216 ± 0.053	8.184 ± 0.051	8.182 ± 0.044
Field	10.57	8.514 ± 0.025	8.376 ± 0.016	8.287 ± 0.025[d]	8.273 ± 0.022[d]

[a]For comparison, the solar value is $12+\log(O/H) = 8.69$ (Asplund et al. 2009).

[b]Pettini & Pagel (2004) calibration.

[c]Steidel et al. (2014) calibration.

[d]Values for the subsample of 16 field SFGs with Hβ and [O III] in the observed wavelength range.

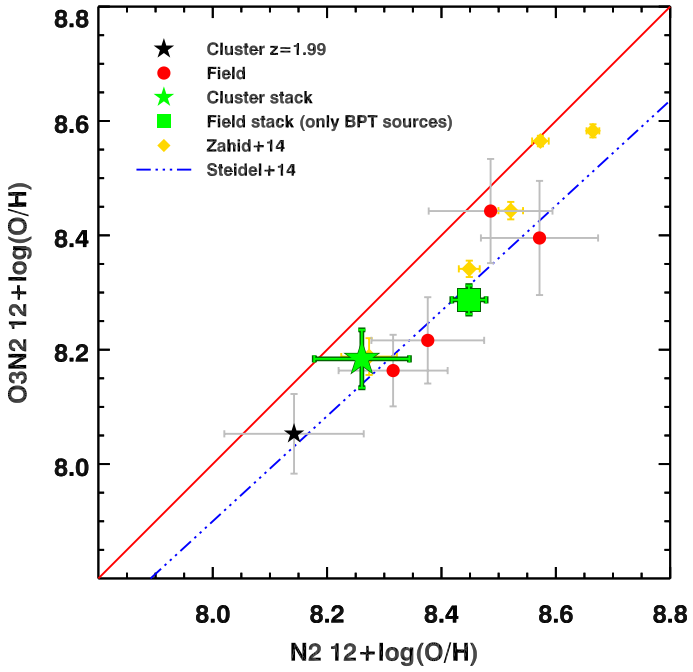

Figure 13 Gas-phase metallicities derived using the N2 and O3N2 indicators calibrated by Pettini & Pagel (2004). Red circles and black stars respectively mark individual field and cluster 3σ detections of each line in the O3N2 indicator. The green square and star respectively represent the measurement for the subsample of 16 field SFGs and cluster stacked sample in the $10 \leqslant \log(M_\star/M_\odot) \leqslant 11$ range. Golden diamonds mark the stacked values at $z \sim 1.55$ from (Zahid et al. 2014b). The blue dash-dotted line is the linear relation between N2 and O3N2 for the $z \sim 2.3$ from Steidel et al. (2014). A one-to-one red line is shown as a comparison.

eral, the use of different methods leads to a systematic difference in absolute metallicity values of up to $\sim 0.3\,\mathrm{dex}$ (Kewley & Ellison 2008). Relative comparisons among different samples from different studies are still meaningful if all the measurements are reported to the same calibration system. For this work we decided to use the $\mathrm{N2} = \log([\mathrm{N\,II}]/\mathrm{H}\alpha)$ metallicity indicator, given the presence of both [N II] and Hα in a relatively clear window of the K_s band at $z = 2$. Pettini & Pagel (2004, PP04 in the following) calibrated N2 against the T_e method in a local sample of H II regions, expressing the gas-phase metallicity as:

$$12 + \log(\mathrm{O/H})_{\mathrm{N2,PP04}} = 0.57 \times \mathrm{N2} + 8.90 \tag{2}$$

with a quoted uncertainty of $\sim 0.18\,\mathrm{dex}$. Partial drawbacks of using N2 are its sensitivity to the ionization parameter $\mathcal{U}$ and the saturation of the index at solar metallicities and above, as [N II] becomes the dominant coolant (Baldwin et al. 1981; Kewley & Dopita 2002). The impact of this saturation seems not to dramatically affect the final metallicity estimate, resulting in a $\sim 0.03\,\mathrm{dex}$ underestimate of the final abundance (Zahid et al. 2014a). Other indicators do not suffer from this saturation issue and could potentially be used to confirm the metallicity estimate. When all lines were available, we used the $\mathrm{O3N2} = \log[([\mathrm{O\,III}]/\mathrm{H}\beta)/([\mathrm{N\,II}]/\mathrm{H}\alpha)]$ as an alternative metallicity indicator. In this case the PP04 calibration gives:

$$12 + \log(\mathrm{O/H})_{\mathrm{O3N2,PP04}} = -0.32 \times \mathrm{O3N2} + 8.73 \tag{3}$$

with a quoted uncertainty of $\sim 0.14\,\mathrm{dex}$. The inclusion of [O III] in the ratio should guarantee sensitivity to increasing metallicity even above solar, as [O III] continues to decrease while [N II] saturates. In practice we could estimate this index at 3σ confidence only for very few individual sources and for the stacked spectra (Figure 13). In the local universe these two indicators provide consistent metallicity estimates (Kewley & Ellison 2008). On the contrary, for our samples of high-z galaxies the N2 indicator returns systematically higher gas-phase metallicities compared to the O3N2 indicator (Figure 13), in agreement with other recent findings (Erb et al. 2006; Yabe et al. 2012; Zahid et al. 2014b, S14). Different interpretations and prescriptions to avoid systematic errors have been proposed in several studies (i.e., S14), even if all of them remain quite speculative in absence of a direct $12 + \log(\mathrm{O/H})$ measurement, i.e., by means of the T_e method. However, all the studies agree on a probable overall change of the ISM conditions in high-z galaxies with respect to the local universe, as indicated by independent observations (Magdis et al. 2012; Kashino et al. 2013). In principle an evolution in the hardness of the radiation field, electron density, ionization parameter, or nitrogen-to-oxygen ratio can make the calibration intrinsically wrong for high-redshift galaxies. In their recent work, S14 recalibrated the N2 indicator on a

sample of local H II regions matching the physical conditions of their $z \sim 2.3$ galaxies, obtaining:

$$12 + \log(O/H)_{N2,S14} = 0.36 \times N2 + 8.62 \quad (4)$$

with a quoted total scatter of $\sim 0.13\,dex$. S14 found that N2 is less sensitive to metallicity variations than implied by the PP04 calibration, which substantially overpredicts the metallicities at high redshifts. On the contrary, after S14 recalibration, the O3N2 indicator predicts metallicities similar to those given by the PP04 calibration, especially with the inclusion of a term depending on N/O (Pérez-Montero & Contini 2009):

$$12 + \log(O/H)_{O3N2,S14} = -0.28 \times O3N2 + 8.66 \quad (5)$$

with a total uncertainty of $\sim 0.12\,dex$. Reducing the sensitivity of the N2 calibrator to the gas-phase metallicity and leaving intact the one of O3N2, the two ratios predict consistent abundances at $z \sim 2$. As mentioned, a cause of concern when estimating gas-phase oxygen abundance through indirect indicators involving other species as N2 and O3N2 is the abundance of these elements relative to oxygen. In the case of N2 and O3N2 indicators, an assumption on the N/O ratio is implied in every calibration, explicitly or implicitly, and ignoring the N/O ratio could result in a systematic effect in the O/H estimation (Pérez-Montero & Contini 2009). An estimation of N/O can be derived from the $N2O2 = \log([N\,II]/[O\,II])$ ratio, as calibrated in the local universe by Pérez-Montero & Contini (2009):

$$\log(N/O) = 0.93 \times N2O2 - 0.20 \quad (6)$$

with a standard deviation of the residuals of $0.24\,dex$. We could estimate N/O for the cluster stacked sample thanks to the WFC3 [O II] determination after proper dust reddening correction (see next Section). This was not possible for the field sample, preventing a fully consistent environmental comparison of N/O. In our case, the inclusion of a N/O correction term in the PP04 N2 calibration (Equation (13) from Pérez-Montero & Contini 2009) leaves virtually unchanged the metallicity estimate for the cluster (a $\sim 0.05\,dex$ difference, well within the calibration errors). The observed cluster N/O ratio ($\log(N/O) = -1.18 \pm 0.15$) is lower than the solar value ($\log(N/O) \simeq -0.86$, Pilyugin et al. 2012), and close to the "primary" nitrogen abundance predicted by current models ($\log(N/O) \simeq -1.5$, Charlot & Longhetti 2001; Pérez-Montero & Contini 2009; Pilyugin et al. 2012; Andrews & Martini 2013; Dopita et al. 2013) in agreement with the estimated low gas-phase metallicity value. Interestingly, recent works on samples at redshift $z \sim 2$ found a N/O ratio consistent with the solar value and only slowly or not varying with the O/H ratio, and hence with the gas-phase metallicity, at least for highly

star-forming systems typical at these redshifts (SFR $\geqslant 10\ M_\odot\ yr^{-1}$, Andrews & Martini 2013, S14). An alternative explanation is that $z \sim 2$ SFGs show higher N/O ratios at fixed metallicities than local counterparts at low masses ($M_\star \lesssim 10^{10.11}\ M_\odot$ in Shapley et al. 2015, and $M_\star \sim 10^9\ M_\odot$ in Masters et al. 2014). If we consider N/O ratios from literature as representative of a general field sample (but check Kulas et al. 2013 for the study of protocluster members in S14 sample) in a mass range and excitation conditions similar to those of our cluster sample, they result to be ~ 0.2 dex higher than the value measured on the cluster stacked spectrum.

Further indications of the lower metal content in cluster sources are the lower $[N\,II]/[S\,II]_{tot}$ and higher $(H\alpha+[N\,II])/[S\,II]_{tot}$ ratios than the field counterparts (Nagao et al. 2006), even if affected by substantial uncertainties. Moreover, for the cluster stacked sample we estimated the ionization parameter and the gas-phase metallicity using the iterative method of Kobulnicky & Kewley (2004), which involves the [O II], Hβ, and [O III] fluxes (i.e., the R_{23} and O_{32} indicators). After applying the Kewley & Ellison (2008) conversion to PP04 N2 metallicities, we obtain $12 + \log(O/H) = 8.217$ with ~ 0.15 dex accuracy, thus compatible with our estimate based on $[N\,II]/H\alpha$ (Table 5). We also obtained a ionization parameter $\mathcal{U} \simeq -2.61$, which is comparable to values measured in high redshift galaxies ($-2.9 < \mathcal{U} < -2.0$, Kewley et al. 2013a, and references therein). Hence a high ionization parameter may not be the main driver of the $[N\,II]/H\alpha$ difference that we observed between cluster and field, even if we cannot completely exclude possible effects connected to $\mathcal{U}$ in our analysis. Overall, while various metallicity estimators may differ on an absolute scale, the systematic difference found between the cluster and the field is robust. Given the lower number of sources with a safe O3N2 measurements, we privileged N2 as primary metallicity indicator. All the gas-phase metallicity estimates are reported in Table 5: in the same mass range, the cluster sample results $0.09 - 0.25$ dex (using $O3N2_{S14}$ and $N2_{PP04}$, respectively) more metal poor than the field sample, depending on the calibration used.

Nebular E(B-V) estimate

The dust reddening on stellar light ($E(B-V)_{cont}$) was estimated through SED fitting. However, the amount of dust attenuation toward the emission lines ($E(B-V)_{neb}$) is typically larger than $E(B-V)_{cont}$. Calzetti et al. (2000) find a factor $f = E(B-V)_{cont}/E(B-V)_{neb} = 0.44$ between the two color excesses in the local universe, adopting the Fitzpatrick (1999) law for the nebular reddening and their own law for the continuum reddening ($f = 0.52$ using the Calzetti et al. (2000) reddening law for both the nebular emissions and the continuum). Recent works suggest that this continuum-to-nebular emis-

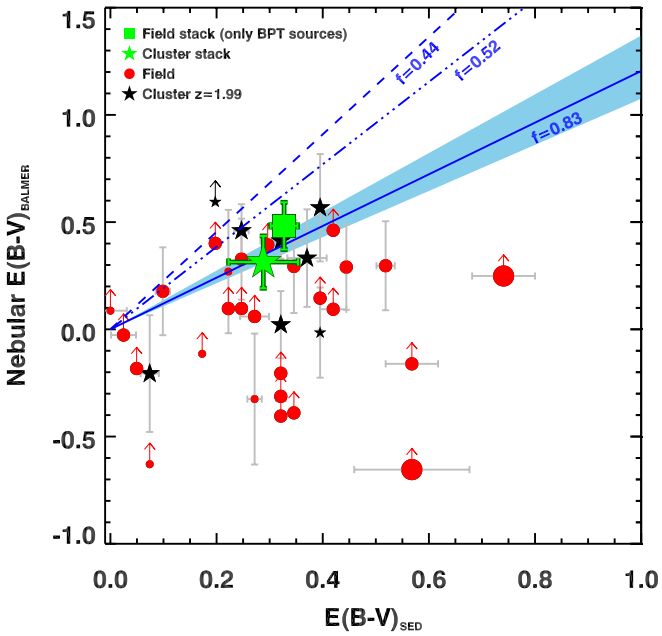

Figure 14 Reddening estimates based on SED modeling and Balmer decrement. Red circles and black stars respectively mark field and cluster SFGs with 3σ Hα and Hβ detections. Symbol sizes scale as stellar mass. Arrows mark 3σ lower limits. The green square and star indicate the subsample of 16 field sources with measured [O III] and Hβ and the cluster stacked values, respectively. The blue dashed and dotted-dashed lines represent the $f = 0.44$ ($f = 0.52$) ratio $E(B-V)_{cont}/E(B-V)_{neb}$ obtained in the local universe applying Fitzpatrick-Calzetti (Calzetti-Calzetti) laws for the nebular and continuum reddening, respectively. The blue solid line and the shaded area represent the same ratio using a Calzetti law for both the nebular and continuum reddening and the relative uncertainties quoted in Kashino et al. (2013) for the sample of $z \sim 1.55$ galaxies from the FMOS survey, where $f = 0.83$.

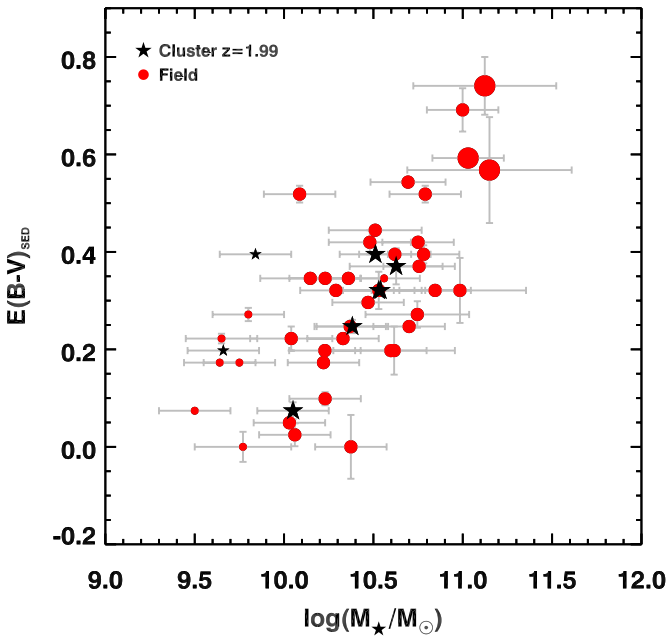

Figure 15 Mass-Reddening Relation for the MOIRCS spectroscopic sample of SFGs. Red circles and black stars mark the field and cluster samples, respectively. Symbol sizes scale as the stellar mass.

sion differential reddening factor is generally higher for high-redshift galaxies, reducing the difference between stellar and nebular continuum (Kashino et al. 2013; Pannella et al. 2015). Here we attempt to estimate this factor using the Balmer decrement $H\alpha/H\beta$ and assuming a Case B recombination with a gas temperature $T = 10^4$ K and an electron density $n_e = 100\,\mathrm{cm}^{-3}$, according to which the intrinsic ratio $H\alpha/H\beta$ is equal to 2.86 (Osterbrock & Ferland 2006). From the observed $H\alpha$ and $H\beta$ values it is possible to compute:

$$E(B-V)_{neb} = \frac{2.5}{k_{H\beta} - k_{H\alpha}} \log\left[\frac{H\alpha/H\beta}{2.86}\right] \tag{7}$$

assuming a proper extiction law. In this work we assumed the Calzetti et al. (2000) law for both the nebular and continuum reddening, for which $k_{H\beta} = 4.598$ and $k_{H\alpha} = 3.325$. A limited sample of galaxies with a safe 3σ $H\beta$ detection is available to measure the Balmer decrement on an object-by-object basis. However, we used the values from the stacked spectra to assess this issue for the mean population of SFGs in our sample. In Figure 14 we show the relation between SED based $E(B-V)_{cont}$ and $E(B-V)_{neb}$ derived from the Balmer decrement. The best fitting slope for the 3σ detected stacked values is 0.74 ± 0.22, consistent within the uncertainties with the results from the FMOS survey at $z \sim 1.55$ (Kashino et al. 2013), but still formally in agreement with the local value obtained using the same

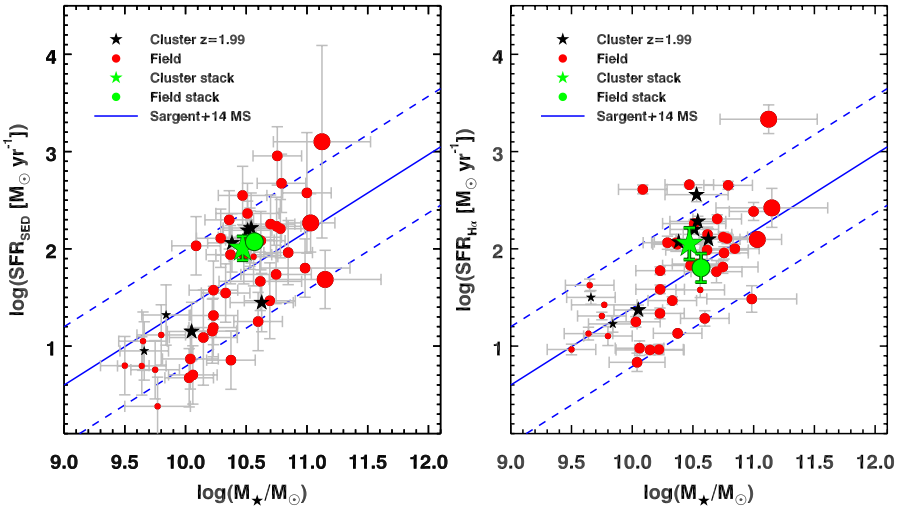

Figure 16 Stellar mass versus SFR. Red circles and black stars mark the field and cluster SFGs, respectively. Symbol sizes scale as the stellar mass. The green circle and star indicate the field and cluster stacked values, respectively. The blue solid line indicates the MS at $z = 2$ as parametrized in Sargent et al. (2014). The blue dashed lines mark the ± 0.6 dex scatter. Left panel: SED-derived SFR. Right panel: Hα-derived SFR.

reddening law. Our best fit value is in agreement with the alternative estimate that we derived from the fitting of the $E(B-V)_{cont}$ - $SFR_{H\alpha}^{uncorr}/SFR_{UV}^{uncorr}$ relation as in Figure 3 of Kashino et al. (2013), namely $f = 0.74 \pm 0.05$.

We checked for possible environmental signatures in the stellar Mass-Reddening Relation (MRR) comparing the cluster and field samples. Figure 15 shows the MRR for our sample of cluster and field SFGs. Both the stellar mass and the reddening estimates come from the SED fitting procedure. In Figure 15 both the cluster and field samples follow the same trend, not revealing any environmental signature in the MRR. Applying a simple linear regression separately for the two samples we obtain compatible slopes: 0.78 ± 0.42 and 0.59 ± 0.07 for the cluster and field sample, respectively.

A significant difference in the observed EW(Hα)

As shown in Figure 12, there is a 0.37 dex difference ($\sim 4.7\sigma$ significant) in the observed EW(Hα) between the cluster and the field. Such a difference may arise from an enhanced sSFR, a variation in the dust reddening correction $E(B-V)$, or in the continuum-to-nebular emission differential reddening factor f between cluster and field, as $EW(H\alpha) \propto sSFR \times 10^{0.4\,E(B-V)_{cont}\,k_{H\alpha}\,(1/f-1)}$. Assuming a com-

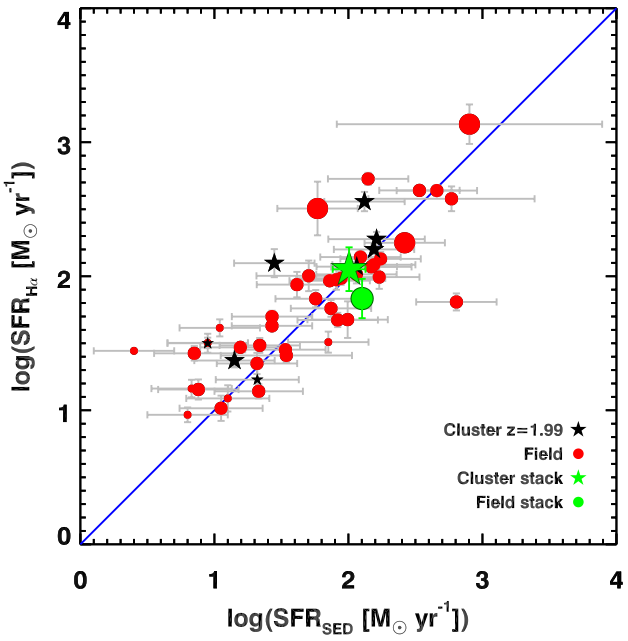

Figure 17 SFR estimates from SED fitting and intrinsic Hα luminosities for the MOIRCS spectroscopic sample of SFGs. Red circles and black stars respectively mark the field and cluster samples with 2σ detected Hα line. Symbol sizes scale as the stellar mass. The green circle indicates the field stacked value. The green star indicates the cluster stacked value. A one-to-one blue line is shown as a comparison.

mon f value in cluster and field SFGs and the average $E(B-V)_{cont}$ values in Table 2, the difference in the observed EW(Hα) is translated into a significant difference in intrinsic EW(Hα) and ascribable to enhanced sSFR in cluster sources. As f is physically linked to the average geometric dust distribution in galaxies' star-forming regions (Kashino et al. 2013), there are not immediately evident reasons why the environment should play a role in setting this factor. Hence, considering f constant within different environments would not be a strong assumption. However, we could let this parameter free as well, resulting in a more conservative approach: in this case, the f factor for the field stack is tentatively lower than for the cluster sample, reducing the difference in intrinsic EW(Hα). Moreover, individual estimates of f are hampered by large error bars on the Balmer decrement measurements (Figure 14), not allowing to fully decouple sSFR and reddening effects. Since the two stacked samples have similar stellar masses, an enhancement in sSFR would reflect the $2.5\times$ higher Hα observed luminosity in the cluster stack (Tables 2, 3). However, when converting Hα fluxes to SFR applying the Ken-

nicutt (1998b) conversion and the reddening correction, the values for cluster and field are formally compatible. In Figure 16 we show the field and cluster sources in the final stacked samples in the stellar mass-$SFR_{H\alpha}$, SFR_{SED} plane. All the SFRs have been rescaled by a factor $[(1+z)/(1+1.99)]^{2.8}$ to match the cluster redshift. We adopted as reference the MS parametrization given in Sargent et al. (2014). In the right panel, individual cluster sources seem tentatively more star-forming than the field counterparts, populating the upper envelope of the MS, and the lowest [N II]/Hα ratio corresponds to the highest $SFR_{H\alpha}$. However, the average properties of the cluster and field populations in the same mass regime are formally compatible, as shown by the stacked values, and this is likely due to the uncertainties on individual f factor estimates. The stacked values are compatible also when considering SFR_{SED}, as shown in left panel of Figure 16. However, this may be partly due to the longer timescales probed by the UV stellar emission as a SFR indicator with respect to Hα ($t_{UV} \sim 100\,Myr$, $t_{H\alpha} \sim 10\,Myr$), which makes SFR_{SED} insensitive to potentially recent episodes of star formation in cluster sources with respect to the field. For reference, we show in Figure 17 the comparison between SED- and Hα–based SFRs, where SFR_{SED} for the stacked samples is the mean of single sources values.
In the most conservative approach, considering the uncertainties on the f factor, we cannot fully disentangle the reddening and sSFR (or SFR) effects in producing the observed EW(Hα) difference. However, reasonably assuming the f factor as independent of the environment and the average $E(B-V)_{cont}$ values from SED modeling, we can decouple the two effects, ascribing the enhanced observed EW(Hα) in cluster sources to an enhancement in sSFR. In any case, we emphasize how Figure 12 shows another significant difference between cluster and field SFGs resulting from this work, in addition to the lower gas-phase metallicity.

2.4 THE MASS–METALLICITY RELATION

As mentioned above, the presence of a correlation between stellar mass and metallicity in SFGs has been known for a long time (Lequeux et al. 1979), both locally (Tremonti et al. 2004) and at increasing redshift (Erb et al. 2006; Kewley & Ellison 2008; Zahid et al. 2012; Cullen et al. 2014; Zahid et al. 2014a; Steidel et al. 2014; Wuyts et al. 2014, and many others). At high redshift the overall observed metallicity is lower than in local galaxies, virtually shifting the observed MZR vertically with redshift. In Figure 18 we show the observed [N II]/Hα ratio, a proxy for gas-phase metallicity, as a function of stellar mass. A $> 4\sigma$ significant lower ratio is observed in the cluster stack with respect to the field mass-matched sample. This result is unchanged

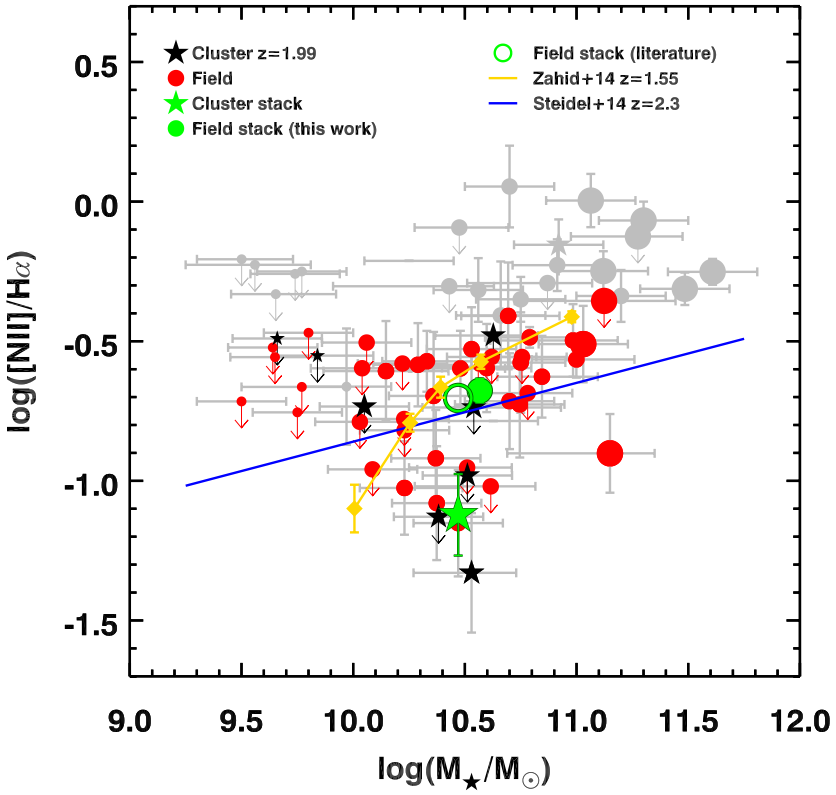

Figure 18 Mass-[N II]/Hα relation for the MOIRCS spectroscopic sample. Red circles and black stars represent the field and cluster samples, respectively. Grey symbols mark the objects excluded from the SF sample as AGN (see Section 2.3.3). Arrows indicate 2σ upper limits. Symbol sizes scale as the stellar mass. The green solid circle and star represent the field and cluster stacked samples, respectively. The green empty circle marks the expected field position at $z = 2$ from the interpolation of literature data (see text for details). Golden diamonds represent the stacked points from the FMOS survey at $z \sim 1.55$ (Zahid et al. 2014b). The blue solid line is the relation for the $z \sim 2.3$ sample from Steidel et al. (2014) (their Equation 17).

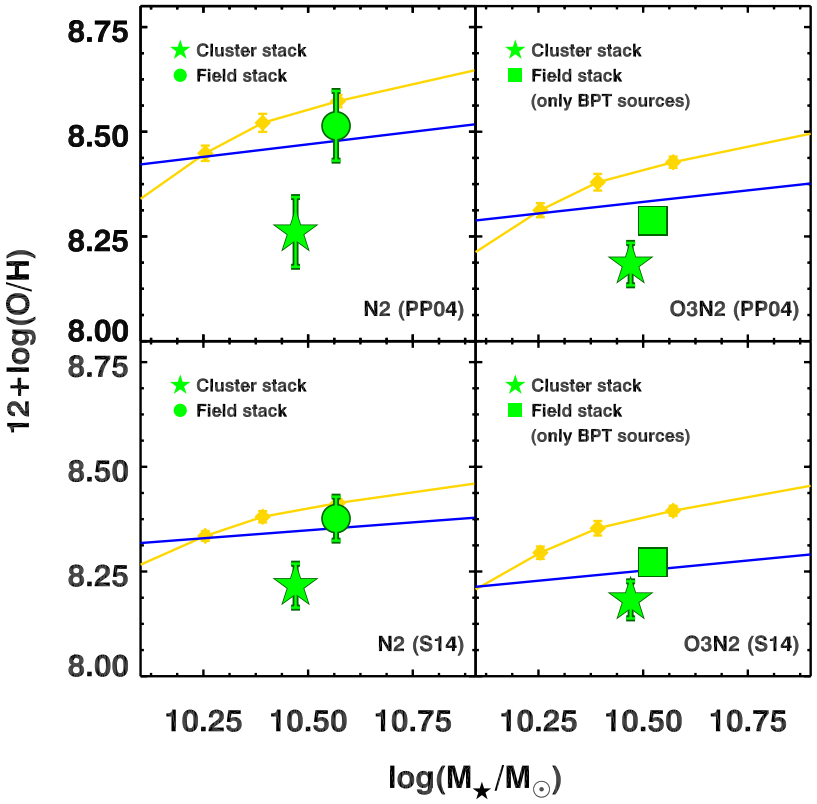

Figure 19 MZR for the MOIRCS spectroscopic stacked samples in the mass range $10 \leqslant \log(M_\star/M_\odot) \leqslant 11$. The green circle and square indicate the 31-source and 16-source field stacked values, respectively. The green star indicates the cluster stacked value. Golden diamonds represent the stacked points from the FMOS survey at $z \sim 1.55$ (Zahid et al. 2014b) and the blue solid line is the relation for the $z \sim 2.3$ sample from Steidel et al. (2014) (their Equation 17), both rescaled to match the metallicity calibration in each panel (see the legend).

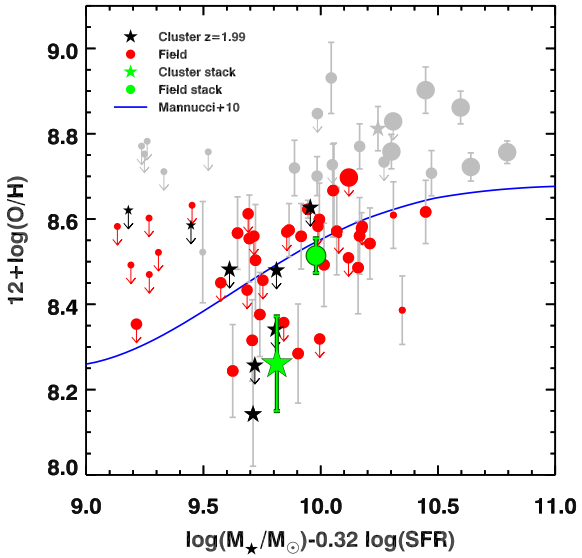

Figure 20 FMR for the MOIRCS spectroscopic sample. Red circles and black stars represent the field and cluster samples, respectively. Grey symbols mark the objects excluded from the SF sample as AGN (see Section 2.3.3). Arrows indicate 2σ upper limits. Symbol sizes scale as the stellar mass. The green solid circle and star represent the field and cluster stacked samples, respectively. SFRs are estimated from Hα fluxes (see Section 2.3.3 for details). The gas-phase metallicity is estimated from the N2 indicator as calibrated by Pettini & Pagel (2004). The blue solid line represents the polynomial parametrization of the FMR by Mannucci et al. (2010, their Equation 4).

if we consider as a field [N II]/Hα representative value the linear interpolation at $z = 1.99$ of the $z \sim 1.55$ and $z \sim 2.3$ values from Zahid et al. (2014b) and S14, at fixed mass. Quantitatively, the metallicity difference between the cluster and field samples depends on the adopted calibration for [N II]/Hα as shown in the left panels of Figure 19. In the same figure we show the metallicity derived from the O3N2 indicator (right panels) for the subsample of 16 intermediate mass field SFGs with Hβ and [O III] measurements. Also in this case, given the comparable [O III]/Hβ values of the cluster and the field samples, the difference in the final metallicity values reflects the different [N II]/Hα ratio through the slope of the adopted linear O3N2 calibration – i.e., through the sensitivity to metallicity variations assigned to [N II]/Hα. Metallicity differences vary between 0.09 dex and 0.25 dex from $O3N2_{S14}$ and $N2_{PP04}$ calibrations, respectively. Given the low number statistics, we do not attempt here any fit to the observed points in Figure 18, neither stacked nor single. Recently, the possible introduction of a third term in the MZR has been advocated to reduce the intrinsic scatter of the relation. Mannucci et al. (2010)

proposed to add the SFR to build the so called "Fundamental Mass-Metallicity Relation" (FMR) and provided a suitable description of it through the $\mu_\alpha = \log(M_\star/M_\odot) - \alpha\log(SFR/M_\odot yr^{-1})$ parameter. They found that the minimum scatter for their local sample from the SDSS is reached for $\alpha = 0.32$, and that this value does not evolve at least up to $z \sim 2.5$. This latter finding is somewhat in contrast with recent works at $z \gtrsim 1.5$ (Zahid et al. 2014a,b; Wuyts et al. 2014, S14) and, partially, with the results of the present study (but see Maier et al. 2014 for the impact of the choice of the FMR extrapolation on the evolution with z). Figure 20 shows the FMR projection on the $\mu_{0.32}$-$12 + \log(O/H)$ plane as parametrized in Equation 4 of Mannucci et al. (2010), where we used $SFR_{H\alpha}$. Again, the choice of the indicator (and especially of its calibration) is decisive for the absolute value of the metallicity which enters the FMR. In Figure 20 we show the PP04 N2 calibration, which, in the case of the field sample, is consistent with the FMR trend, after a proper conversion from the Maiolino et al. (2008) calibration system to PP04. In the same figure, the cluster value is tentatively inconsistent ($\sim 2.7\sigma$) with an unevolving FMR up to $z \sim 2.5$. After proper metallicity rescaling, we observe a similar inconsistency with the prediction of the analytically derived $Z(M, SFR)$ by Lilly et al. (2013) (left panel of their Figure 7).

2.5 DISCUSSION

2.5.1 Potential selection effects

We checked for possible biases in our field sample comparing it to trends from other surveys at similar redshifts and extrapolating them to $z = 1.99$ (Section 2.4). As shown in Figure 18, our selection of field sources gives results that are consistent with much broader samples in literature (Zahid et al. 2014b, S14). This shows that our selection is not biased towards specific high-redshift galaxy populations, but extracts a representative sample of MS-SFGs at $z \sim 2$. This result is confirmed stacking only *sBZK*-, Hα-selected galaxies from the COSMOS mask and comparing them to the general field sample, as we recover fully consistent line ratios (within 1σ uncertainties). Moreover, for the higher priority assigned to the WFC3-confirmed cluster members over candidates, another possible selection bias could have occurred in the cluster sample. In particular, even if not specifically [O III]-selected, 5/6 SF cluster members in the final stack have an [O III] detection from WFC3, which could have introduced a bias towards the metal poorer cluster members. To check this possibility we investigated the properties of the whole "parent" pool of spectroscopically confirmed and candidate star-forming members in the mass range $10 \leqslant \log(M_\star/M_\odot) \leqslant 11$ from which we chose the

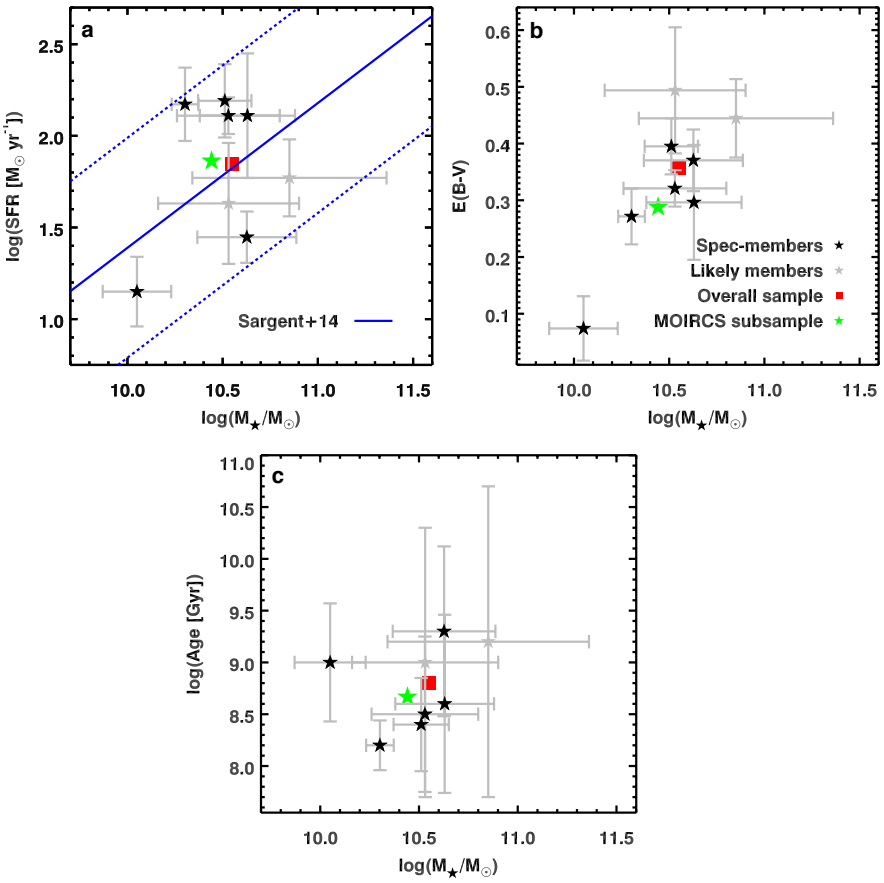

Figure 21 Photometric properties of the cluster "parent" sample from which the high priority sample for MOIRCS follow-up has been extracted. In each panel black stars mark the 6 WFC3 spectroscopically confirmed SF cluster members in the $10 \leqslant \log(M_\star/M_\odot) \leqslant 11$ mass range which have been followed-up with MOIRCS and stacked. Grey stars mark the candidate members in the same mass range not observed with MOIRCS. The green star and red circle indicate the mean value for the sample of followed-up sources and for the overall population, respectively. Panel (a): Stellar mass versus SED-based SFR. The MS at $z = 2$ is represented with a ± 0.6 dex scatter as parametrized by Sargent et al. (2014). Panel (b): Mass-Reddening Relation. Panel (c): Mass-luminosity weighted age relation for constant SFH.

high priority sample to observe. The mass cut, the constraints on the quality of photometric data, and the SF classification reduced the original pool to 8 members in the investigated mass bin. 6/8 are the WFC3 spectroscopically confirmed members that we observed with MOIRCS and which were stacked. The other 2 sources are candidate members which were not inserted in the final MOIRCS mask because of geometrical constraints in slit positioning. The photometric properties of these 8 galaxies are shown in Figure 21. Furthermore we investigated the reasons of the WFC3 non-detection of the 2 candidate members, checking if the absence of [O III] detection could have been due to high metallicities, which could have potentially influenced our subsequent analysis of the cluster metal content. From the SED-based SFR and $E(B-V)$ estimates and assuming an intrinsic $H\alpha/H\beta$ ratio equal to 2.86, we derived the expected $H\beta$ observed flux. In both cases it fell well below the WFC3 3σ detection threshold ($2\times10^{-17}\,erg\,cm^{-2}\,s^{-1}$, G13), showing that these 2 sources are intrinsically faint rather than metal rich (if the latter was the case, we should have detected them in $H\beta$ but not in [O III]). Moreover, assuming the WFC3 detection threshold, the predicted $H\beta$ flux, and an empirical track describing the observed population at $z=2$ in the BPT diagram, we estimated the $[N\,II]/H\alpha$ ratio for these two sources and the metallicity with N2, confirming their homogeneity with the sample of 6 galaxies that we stacked. This result does not change using tracks describing only cluster sources, the whole sample of $z\sim2$ galaxies, or a trend from literature. Moreover, contamination from high orders severely affected these spectra in two of the three HST visits, limiting the usable integration time to 4/18 orbits and leading to a higher detection threshold (Figure 22). This did not allow us to detect these intrinsically faint objects. Finally, we could exclude significant biases introduced by low number statistics for the cluster sample (Section 2.3.2). Therefore we can be reasonably confident that evident selection effects are not invalidating the analysis presented in this work.

2.5.2 The environmental effect

Comparison with other works

The debate about the environmental signatures in the chemical enrichment of cluster galaxies is still ongoing, even in the local universe. The situation for high redshift clusters is almost unexplored up to date. Kulas et al. (2013) studied the MZR for a sample of 23 SFGs belonging to a $z=2.3$ protocluster (Steidel et al. 2005). They find a 0.15 dex metallicity enhancement for galaxies inside the overdensity with respect to field counterparts at low masses ($\log(M/M_\odot)\lesssim10.1$, Chabrier IMF), but no difference at higher masses. Similarly, Shimakawa et al. (2015) find higher gas-phase metallicities in proto-

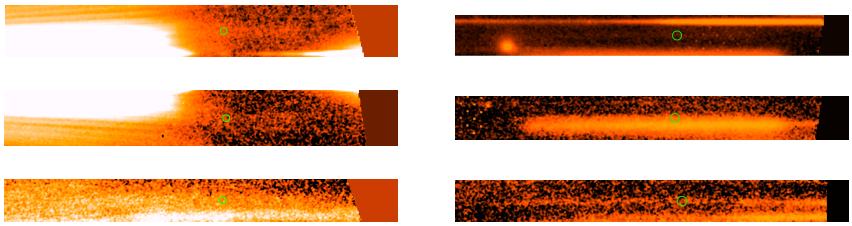

Figure 22 WFC3 G141 slitless spectra of the two cluster candidate members with masses $10 \leqslant \log(M_\star/M_\odot) \leqslant 11$ that were not observed with MOIRCS. Left column: ID 424. Right column: ID 660. The three spectra correspond to separate *HST* visits (G13). Green circles mark the expected position of [O III] if the sources were at $z = 1.99$

cluster members than in the field at $z = 2.1 - 2.5$ below 10^{11} $M_\odot$. Tran et al. (2015), Kacprzak et al. (2015), and Kewley et al. (2016) do not find any signature of environmental effects on the metal content of SFGs in large protoclusters at $z = 1.6 - 2.1$. These results are in contrast with the main finding of this work. Unfortunately, here we cannot study possible mass trends, given the low number of SFGs in CL J1449+0856 and the high mass limit for completeness. Moreover the mass range that we explored is someway in between the mass bins defined in Kulas et al. (2013), increasing the difficulty of a direct comparison. Furthermore, we note that contamination from AGN is potentially an issue in selecting SFGs at high redshift: the inclusion of type-2 AGN, which could be hosted in a non-negligible fraction of high mass galaxies at $z > 1$ (e.g., Trump et al. 2013), can bias the [N II]/Hα ratio towards higher values and hence their gas-phase metallicities derived from N2. Kulas et al. (2013) selected sources according to UV emission, which should prevent strong AGN contamination (see Steidel et al. 2014). Shimakawa et al. (2015) rejected AGN using a slight modification of the BPT diagram relying on Hα fluxes and reddening correction to estimate Hβ fluxes. In this work we coupled the BPT and [N II]/Hα–EW(Hα) diagrams, including X-ray and radio criterion, similarly to Tran et al. (2015), Kacprzak et al. (2015), and Kewley et al. (2016), and these different AGN exclusion criteria could have impacted the final results. Furthermore, despite being at comparable redshifts, these overdensities and CL J1449+0856 are structurally different. Applying the pondered definition of *protoclusters* and *clusters* by Diener et al. (2013), these structures may give rise to different effects on their host galaxies simply because they are tracing different environments: while CL J1449+0856 is identifiable as a single, stand-alone, partially virialized cluster halo (a *main halo* according to Muldrew et al. 2015) where all the galaxies analyzed

here reside, the structures analyzed in the other studies fall more easily in the protocluster class. Line-emitting galaxies far away from the putative core of the forming cluster are naturally immersed in regions only slightly overdense with respect to the field, resulting in a possible dilution of the environmental effects. Straight comparisons should, thus, be made with caution. Several competing physical scenarios may support the different findings. Shimakawa et al. (2015) detail several possible effects increasing the metallicity of their sample, including faster evolution in overdense environment and enriched gas recycling in deep cluster-like potential wells, which apply also to findings by Kulas et al. (2013). On the other side, cosmological simulations (Davé et al. 2012; Genel 2016) show only a very modest metallicity increase in cluster SFGs (~ 0.05 dex, Kacprzak et al. 2015), while we provide possible physical reasons supporting our results in the next Section. The other main finding of this work, namely higher EW(Hα) and thus sSFRs in cluster SFGs than in field counterparts, is largely debated in literature (i.e., Peng et al. 2010b; Muzzin et al. 2012; Koyama et al. 2013; Hayashi et al. 2014; Tran et al. 2015; Erfanianfar et al. 2016; Darvish et al. 2016; Wang et al. 2016). In particular, a reversal of the SFR-density relation might be expected at some point at high redshift, when SFGs largely dominate the high-mass end of the mass functions and dusty, starbursting galaxies populate the emerging structures (Casey et al. 2015; Wang et al. 2016). However, also in this case, consensus is far from reached in literature (i.e., Elbaz et al. 2007; Cooper et al. 2008; Tran et al. 2010; Ziparo et al. 2014; Darvish et al. 2016). Incidentally, we note also that a correlation between the dust content of galaxies and their environment has been recently claimed, nevertheless not coupled with a significant increase in sSFRs or metallicity (Koyama et al. 2013; Sobral et al. 2016). The discrepancies among different works are likely due to the definition of the environment (scale-dependent or scale-free, halo membership and mass, galaxy densities, friends-of-friends algorithm), the choice of the SFR or sSFR indicator ([O II] and Hα lines, near-, mid-, or far-infrared emission, UV light), different dust-reddening corrections, sample selection (based on colors, stellar masses, SFR cut in NB imaging, UV emission), AGN contamination, photometric and spectroscopic incompleteness, etc. Homogenizing all these elements will be of primary importance to gain physical insights into this subject.

The past history of CL J1449+0856: a recent transitional phase of stellar mass assembly?

The observations presented in this paper have highlighted the presence of a $> 4\sigma$ significant difference in [N II]/Hα ratio between a sample of SFGs belonging to CL J1449+0856 and a mass-matched sample in the field. This difference is directly translated in a metallicity difference with all the indicators employed in the analysis, so

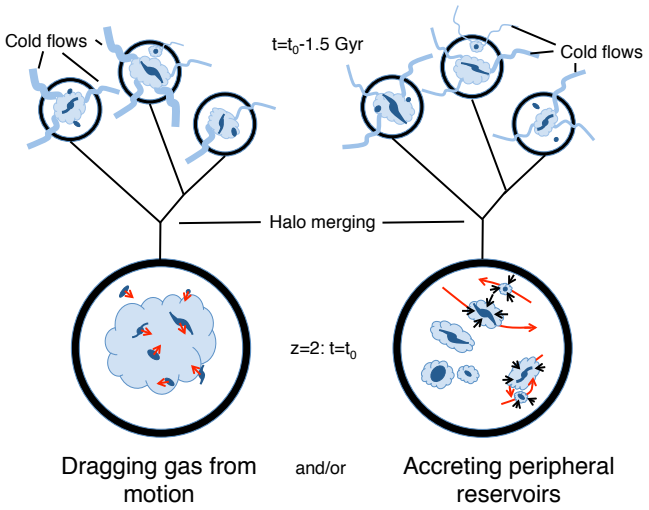

Figure 23 Sketch of the speculative model of gas accretion for SFGs residing in CL J1449+0856. Left branch refers to the possible creation of a gas rich environment in clusters close to a phase of major assembly. Right branch shows the impact of galaxy encounters on the gas halos around each galaxy. The vertical direction marks the time: at the top a phase of gas enrichment occurs $\sim 1.5\,\mathrm{Gyr}$ before a major phase of assembly of CL J1449+0856 at $z \geqslant 2$.

that cluster sources are a factor $0.09\text{-}0.25\,\mathrm{dex}$ (using $O3N2_{S14}$ and $N2_{PPo4}$, respectively) more metal-poor than the field counterparts. What follows is a speculation about the origin of this effect. As discussed above, CL J1449+0856 is partially virialized, but a relatively recent phase of assembly must have occurred. According to the model of halo mass growth by Fakhouri et al. (2010), a halo of $(5-7)\times 10^{13}\ \mathrm{M}_{\odot}$, such as the one hosting CL J1449+0856, should have increased its mass of a factor $2\times$ ($5\times$) in the previous $\sim 1\,\mathrm{Gyr}$ ($\sim 1.5\,\mathrm{Gyr}$) of its lifetime. The recent coalescence of multiple less massive halos could have impacted the hosted galaxies in a twofold way, graphically sketched in Figure 23. First, the single bricks forming the final halo could have been gas enriched through cold streams and subsequently merged, thus creating an environment rich in pristine gas. The accretion of cold gas even in quite massive halos at redshifts close to the formation epoch of CL J1449+0856 progenitors is consistent with model predictions, if high density, steady, cold streams penetrating the shock heated medium are considered (Birnboim & Dekel 2003b; Kereš et al. 2005; Brooks et al. 2009; Dekel et al. 2009a,b). In Figure 24, the mass growth track for CL J1449+0856 halo (Fakhouri et al. 2010) crosses the line separating the hot ISM and cold streams in hot ISM regimes $\sim 1\,\mathrm{Gyr}$ before $z = 2$ and thus the progenitors of the cluster halo could have been recently enriched of cold gas, before merging. If this gas is not prevented from cooling

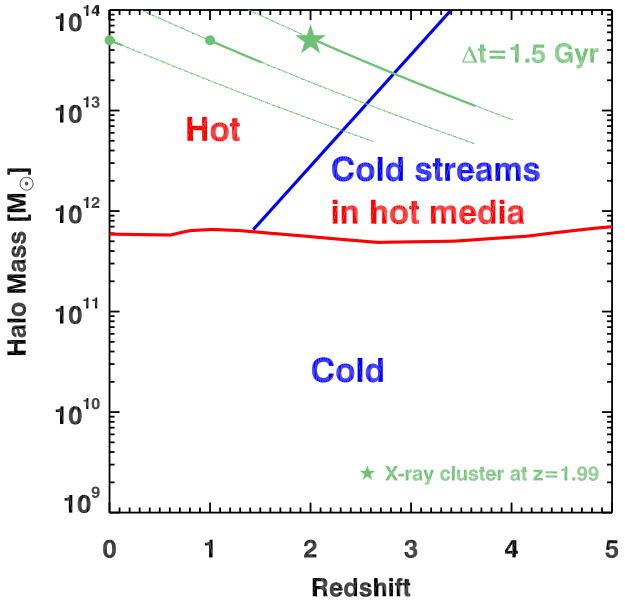

Figure 24 Analytic prediction of the "hot", "cold", and "cold streams in hot media" regimes in the mass-redshift space from Dekel et al. (2009a). The green tracks show the mass growth for halos of 5×10^{13} $M_\odot$ at $z = 0, 1, 2$ (Fakhouri et al. 2010). The solid segments represent a lookback time interval of 1.5 Gyr starting from the redshift of reference.

(Fabian 1994; Revaz et al. 2008; Salomé et al. 2011), given the high dark matter density in $z \gtrsim 2$ halos, it might be dragged and accreted on the galaxies simply moving across it, diluting the metal content. This first effect might not be effective at lower redshifts, where the gas reservoirs in halos are at lower densities, prevented from cooling after the cluster full virialization, chemically enriched by Gyrs of stellar formation, and not replenished by cosmological inflows. This latter aspect is illustrated in Figure 24, where the mass growth tracks for a halo of 5×10^{13} $M_\odot$ at $z = 0, 1$ do not enter the region of cold streams in hot media on timescales of the order of ~ 1 Gyr. Moreover, in a ΛCDM universe the baryon growth rate scales as $(1+z)^{2.25}$ at fixed mass (Neistein & Dekel 2008). Thus, at low redshifts the progenitors of a halo of such mass cannot be easily refurnished of cold gas. Secondly, a recent epoch of high merging rate of dark matter halos could have favoured encounters, fly-bys, and mergers among the galaxies hosted in the merging halos, given the low (but increasing) cluster velocity dispersion. An encounter can trigger the accretion of the reservoirs of cold, rich, and pristine gas located in the halos of single galaxies at $z \gtrsim 2$, continuously replenished by cosmological inflows (Ceverino et al. 2010; Gabor & Bournaud 2014). The accretion of such gas would lower the metallicity, as observed in our sample,

and subsequently enhance the SF. In addition galaxy minor and major mergers could lower the metal abundance themselves (Contini et al. 2012; Queyrel et al. 2012). Moreover, the final cluster potential well in which the galaxies reside and interact can facilitate the merging events through the so called "gravitational focusing" effect (Martig & Bournaud 2007; Moreno et al. 2013), accelerating the gas accretion from the galaxy outskirts. Recent observational studies have shown a SFR increase and metallicity decrease (up to $\sim$ 0.07-0.09 dex) in close pairs and post-mergers in the local universe (Ellison et al. 2013). This result is supported by simulations suggesting that mergers induce the funneling of gas reservoirs from the peripheric regions of galaxies towards the center, diluting the metallicity and triggering new SF (Torrey et al. 2012). This second effect could be effective in terms of gas accretion on galaxies entering the halo of low redshift clusters, generating a SFR enhancement in the cluster outskirts, as observed for example in Virgo (Temporin et al. 2009). However, given the chemical enrichment due to stellar formation in the last 10 Gyr, the gas accretion might not be effective in reducing the metallicity at low redshift. Deep F140W images of our sample of cluster SFGs in the final stack are shown in Figure 25. Every object shows a disturbed morphology and/or a close companion, which might be hint of high gas fractions or a close encounter, even if the lack of a redshift determination for the companions does not allow to draw a robust conclusion (see, e.g., Zanella et al. 2015 for the specific case of ID568, Figure 25, central bottom panel). We defer to a future work the detailed study of galaxy morphologies in CL J1449+0856 and a proper comparison with a morphologically characterized field sample.

The transitional epoch that we have just described could be a key phase for galaxy clusters with the assembly of a substantial fraction of stellar mass in SFGs. In a time interval of 500 Myr, typical doubling time at $z = 2$ (Daddi et al. 2007) and typical scale of gas consumption in SFGs (Daddi et al. 2010), each galaxy in our cluster sample would form stars for a total of $\sim 3 - 6 \times 10^{10}$ $M_\odot$, given the average SFR we measure ($SFR_{H\alpha} = 112\, M_\odot\ yr^{-1}$, $SFR_{SED} = 73\, M_\odot\ yr^{-1}$). This would double the stellar mass already present in cluster SFGs and increase the overall cluster stellar mass in spectroscopically confirmed members by $\sim$ 15-35% in this time interval or, if we extend this reasoning to the past history of the cluster, SFGs could have assembled an important part of the total stellar mass in a relatively short period of time during this phase. We can gain physical insight about the metal deficiency for cluster SFGs with a simple computation. To explain a 0.15 dex metallicity difference (a factor $\sim$ 40%), given that $M_\star \simeq M_{gas}$ in MS-SFGs at $z \sim 2$ (Bouché et al. 2007; Daddi et al. 2008), we would need a mass of accreted pristine gas 2×10^{10} $M_\odot$ to dilute the metal content of each galaxy. If we assume the pres-

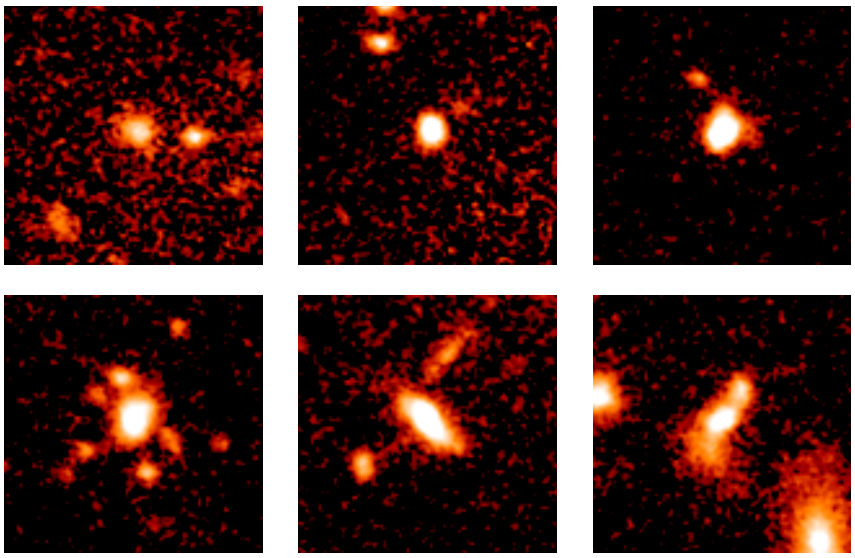

Figure 25 F140W 3" × 3" (∼ 25 × 25 kpc) cutouts of our sample of cluster SFGs in the mass range $10 \leqslant \log(M_\star/M_\odot) \leqslant 11$ (north is up, east is left).

ence in the cluster halo of a gas mass free to cool down and to be dragged and accreted by SFGs in their motion equal to the universal baryon fraction of ∼ 16% (Planck Collaboration et al. 2014) of the total halo mass ($M_{halo} \sim 5 \times 10^{13}$ $M_\odot$), the mass accretion rate would be 35 $M_\odot$ yr^{-1}, assuming a gravitational focusing term $\simeq 5$, a velocity dispersion of 500 km s^{-1}, $R_{200} = 0.5$ Mpc, and 4 kpc as a typical SFG radius ($\dot{M}_{acc} = \rho_{gas,halo} \cdot \pi R_{gal}^2 \cdot v_{disp} \cdot f_{grav}$ [$M_\odot$ yr^{-1}]). However, if we consider only the highest density regions at the core of the cluster ($R_{clu} \sim 200$ kpc), where the gas is likely to collect, the accreted gas mass could rapidly increase by a factor ∼ 8, enough to halve the metal content of the galaxy. The complementary mechanism linked to galaxy encounters could provide an extra gas accretion rate of $\geqslant 45$ $M_\odot$ yr^{-1}, considering the galaxy density within the cluster (∼ 75 Mpc^{-3} within R_{200}) and a typical distance for a fly-by of 50 kpc ($\dot{M}_{acc} = M_{res} \cdot n_{coll} \cdot f_{grav}$ [$M_\odot$ yr^{-1}], where n_{coll} is the collision rate and M_{res} the galaxy halo gas reservoir). The reservoirs available in the galaxy outskirts are expected from simulations to be a few 10^9 $M_\odot$ within a 15 kpc radius around the galaxy (Ceverino et al. 2010; Gabor & Bournaud 2014) and they can be replenished only as long as cold inflows can reach the galaxy, which may not be true once the galaxy enters deeply in the cluster halo. Moreover, we cannot rule out the possibility that the local density may be a more important driver than cluster membership (i.e., large scale environment). Unfortunately the very low number statistics of cluster SFGs does not allow for a proper comparison among objects within and outside the virial radius to check for the effective influence of the un-

derlying overdensity on the metallicity, neither considering stacked spectra. Future spectroscopic follow-up of the remaining population of spectroscopically confirmed and candidate SF members will be decisive to clarify this complex picture.

2.6 SUMMARY AND CONCLUSIONS

We have presented the results of the MOIRCS near-IR spectroscopic follow-up of the SF population residing in CL J1449+0856, an X-ray detected cluster at at $z = 1.99$. Adding the pre-existing 13-bands photometry of the field and the deep grism G141 slitless spectroscopy of WFC3, we studied the properties of our sample of cluster SFGs in the mass range $10 \leqslant \log(M_\star/M_\odot) \leqslant 11$ with respect to a mass-matched field sample at comparable redshifts through stacking. In our analysis we showed that:

- the field and cluster samples of SFGs in the studied mass range show comparable [O III]/Hβ ratios, but a $\sim 4\sigma$ significant difference in [N II]/Hα ratios. Using different calibrations of the N2 and O3N2 metallicity indicators, the lower [N II]/Hα ratio measured in cluster SFGs is translated in a $\sim 0.09 - 0.25$ dex (using $O3N2_{S14}$ and $N2_{PP04}$, respectively) metal deficiency for the objects belonging to the overdensity. The low metallicity value in cluster sources is confirmed using R_{23} and O_{32} indicators. Furthermore it is supported by the low N/O ratio that we measured ($\log(N/O) = -1.18 \pm 0.15$). The ionization parameter in the cluster stacked sample from R_{23}, O_{32} ($\mathcal{U} \simeq -2.61$) is higher than typical values for local galaxies, but consistent with other determinations at high redshift

- We observe $\sim 4.7\sigma$ significant $2.5\times$ higher Hα luminosity and EW(Hα) in the cluster stack, likely due to enhanced sSFR, even if lower dust reddening and/or an uncertain environmental dependence of the continuum-to-nebular emission differential reddening f may play a role. Thus, the metal deficiency observed in the cluster sources appears to be correlated with an increase in the SFR with respect to the field; however we report a $\sim 2.7\sigma$ inconsistency with the prediction of a FMR not evolving up to $z = 2.5$

- the nebular lines reddening at $z \sim 2$ is $\sim 1.4\times$ higher than that of stellar continuum estimated through SED fitting, lower than the previous estimates from local measurements and in agreement with recent studies at $z \geqslant 1.5$ (Kashino et al. 2013; Pannella et al. 2015)

- our sample of high redshift galaxies are offset from the local SF sequence on the BPT emission-line diagnostic diagram. This result is in agreement with previous studies at similar redshifts (Erb et al. 2006; Yabe et al. 2012; Zahid et al. 2014b; Steidel et al. 2014, and others), pointing towards a possible evolution with redshift of the physical conditions of the line emitting regions
- The metal deficiency in this $z = 1.99$ cluster could be due to the accretion of pristine gas which might have diluted the metal content. We speculate that the accretion of large galactic scale gas reservoirs facilitated by the gravitational focusing effect may be responsible for the observed low metal abundance in star-forming cluster members.

2.7 APPENDIX. AVERAGING SPECTRA

As noted in Section 2.3.2, averaging single spectra does not necessarily coincide with averaging spectral derived quantities. The difference between these two averaged trends depends on the relationship between the the fluxes of single lines and the derived quantities. In our case we have evaluated the impact of this difference on the mean metallicity calculated through the strong line ratio [N II]/Hα for a population of MS-SFGs. Assuming a functional form for the $M_\star$-SFR relation and the Hα-SFR conversion, one can easily convert the stellar mass of a galaxy into its intrinsic Hα luminosity and, given a Mass-Reddening Relation, into the observable Hα flux at a fixed redshift. For this exercise we have used Sargent et al. (2014) MS parametrization as a function of redshift and the standard Kennicutt (1998b) relation to pass from Hα intrisic luminosities to SFRs. As a MRR we have used the observed trend of our overall sample of SFGs given by the SED fitting described in Section 2.3.1 and shown in Figure 15. Then we can convert the stellar mass into the gas-phase metallicity using a parametrization of the MZR (or of the FMR if we want to include the effect of the SFR). Here we have used the Zahid et al. (2014a) parametrization, given its simple form. Finally we need a conversion from gas-phase metallicities to observed line fluxes. We adopt here the Pettini & Pagel (2004) calibration of the [N II]/Hα ratio, but in principle we could test any other strong-line ratio. All these relations are somehow scattered and we have adopted the quoted scatters to introduce a gaussian random noise to make our simple simulation more realistic. Given all these relations, we simply generate a random sample of masses in an interesting mass range and derive two estimates of the average metallicity: first we simply compute the average of the single metallicities in mass bins as obtained from the MZR (Z_{av}); then we compute the mean metallicity in the same mass bins as derivable from an hypothethic stacking of the spectra of single galaxies, namely from the average of single line fluxes (Z_{stack}). Analitically it can be shown that Z_{av} and Z_{stack} depend on [N II] and Hα fluxes in different ways, so that a priori they can be different:

$$\log\left[\frac{Z_{av}}{Z_{stack}}\right] = \log\left(\frac{1}{N}\right) + \log\left[\sum_{i=1}^{N}\left(\frac{[N\,II]}{H\alpha}\right)_i^{0.57}\right] - \log\left[\left(\frac{\sum_{i=1}^{N}[N\,II]_i}{\sum_{i=1}^{N}H\alpha_i}\right)^{0.57}\right] \quad (8)$$

where N is the total amount of observed galaxies and 0.57 is the slope of PP04 calibration. Given the parametrizations we adopted, the difference between the two mean estimates decreases with increasing stellar mass. Moreover, averaging the metallicity in smaller mass bins gives rise to smaller differences between Z_{av} and Z_{stack}.

Finally, a high number of observed points is more robust against the scatter of the relations we used, reducing the possibility to find huge $\log(Z_{av}/Z_{stack})$ ratios in a mass bin. We have stacked sources in a limited high mass regime ($10 \leqslant \log(M_\star/M_\odot) \leqslant 11$) where we have a relatively low number statistics for the cluster sample ($N \sim 10$) and a fairly more robust sample of field galaxies ($N \sim 30$). For a simulated sample of 10 galaxies at $z = 2$ in the mass bin $10 \leqslant \log(M_\star/M_\odot) \leqslant 11$ the median difference is $\log(Z_{av}/Z_{stack}) = 0.018$ ($\sim 4\%$) with a semi-interquartile range of $0.022\,\mathrm{dex}$ over 1000 runs of the simulation. At the same redshift and mass bin, but for $N = 30$ observed points, the median difference is reduced to $\log(Z_{av}/Z_{stack}) = 0.008$ ($\sim 1\%$) with a semi-interquartile range of $0.005\,\mathrm{dex}$. At these masses the impact of adopting one approach or the other is restrained, but it could be more important at lower masses – due to the steeper MZR –, at which the stacking technique is usually widely used.

Table 6. Photometric and spectroscopic coverage of CL J1449+0856.

Filter	Central wavelength (μm)	Exposure (s)	Instrument	Telescope	Observation date	References[a]
0.5-10 keV	-	80000	EPIC-MOS	XMM-Newton	2001-2003	B05, G11
0.5-8 keV	-	188000	ACIS	Chandra	2004 Jun, 7^{th}-13^{th}, 2014 May, 21^{st}	C09, G11, V16
U	0.36	14700	FORS2	VLT	2011 May, 3^{rd}	S13
NB3640	0.36	12890	LRIS	Keck	2014 Mar, 27^{th}	V16
OII/4000+45	0.37	28800	FORS2	VLT	2011 May, 3^{rd}	Gobat in prep.
V	0.55	12130	FORS2+LRIS	VLT+Keck	2011 May, 3^{rd}, 2014 Mar, 27^{th}	S13, V16
B	0.44	1500	Suprime-Cam	Subaru	2003 Mar, 5^{th}	K06
F606W	0.59	1080	WFC3	*HST*	2013 May, 20^{th}	Z15
R	0.65	3600	Suprime-Cam	WHT	1998 May, 19^{th}-21^{st}	D00
I	0.80	5400	Suprime-Cam+LRIS	Subaru+Keck	2003 Mar, 5^{th}, 2014 Mar, 27^{th}	K06
z	0.91	2610	Suprime-Cam	Subaru	2003 Mar, 4^{th}-5^{th}	K06
Y	1.02	17780	MOIRCS	Subaru	2009 Mar, 15^{th}, 2010 Feb, 7^{th}-8^{th}, 21^{st}	G11
F105W	1.06	11880	WFC3	*HST*	2013 May, 20^{th}	Z15
J	1.26	9360	MOIRCS+ISAAC	Subaru+VLT	2007 Mar, 10^{th}, Apr 5^{th}	G11
F140W	1.40	4320	WFC3	*HST*	2010 Jun, 6^{th}, 26^{th}, Jul, 1^{st} 9^{th}	G13, Z15
F160W	1.60	17920	NIC3	*HST*	2008 May, 11^{th}	G11
H	1.65	2380	MOIRCS	Subaru	2007 Apr, 8^{th}	G11
K	2.15	1890	NIRC2	Keck	2009 Apr, 4^{th}	G11
K_s	2.20	7800	MOIRCS+ISAAC	Subaru+VLT	2007 Mar, 8^{th}, Apr, 5^{th}	G11
IRAC 1	3.6	65640	IRAC	*Spitzer*	2004 Jul, 22^{nd}, 2011 Sep 8^{th}-9^{th}, 11^{th}	G11, G13, S13
IRAC 2	4.5	65640	IRAC	*Spitzer*	2004 Jul, 22^{nd}, 2011 Sep 8^{th}-9^{th}, 11^{th}	G11, G13, S13

Table 6 (cont'd)

Filter	Central wavelength (μm)	Exposure (s)	Instrument	Telescope	Observation date	References[a]
IRAC 3	5.8	65640	IRAC	*Spitzer*	2004 Jul, 22nd, 2011 Sep 8th-9th, 11th	G11, G13, S13
IRAC 4	8.0	65640	IRAC	*Spitzer*	2004 Jul, 22nd, 2011 Sep 8th-9th, 11th	G11, G13, S13
MIPS 24	24	480	MIPS	*Spitzer*	2004 Aug, 5th	G11, G13, S13
PACS Bands	100, 160	63720	PACS	Herschel	2011 Jul, 19th-20th	Strazzullo in prep.
SPIRE Bands	250, 350, 500	14400	SPIRE	Herschel	2013 Apr, 1st	Strazzullo in prep.
345 GHz	870	108000	LABOCA	APEX	2011 Aug - Sep	Dannerbauer in prep.
Band 7	870	14728	-	ALMA	2013 Jun - 2014 Dec	V16, Strazzullo in prep.
S	1.3×10^5	75600	-	JVLA	2012 Feb - Nov	Coogan in prep.
L	2×10^5	57600	-	e-MERLIN	2012 May	Béthermin in prep.
325 MHz	9.2×10^5	14400	-	GMRT	2013 Jan - May	Sargent in prep.
GRIS-300V+10	0.45-0.87	36000	FORS2	VLT	2008 Apr - Jul	G11
GRIS-300V+10	0.45-0.87	41400	FORS2	VLT	2012 Apr, 16th-17th	Gobat in prep.
LR-BLUE	0.37-0.67	9000	VIMOS	VLT	2004 Mar, 29th	G11
Optical	0.47-0.93	5400	MUSE	VLT	2015 Jun, 20th	Valentino in prep., Chapter 5
HK500	1.30-2.30	50400	MOIRCS	Subaru	2013 Apr, 7th-9th	V15
K	1.93-2.46	73800	KMOS	VLT	2015 Apr - 2016 Mar	Valentino in prep., Chapter 5
G141	1.40	44640	WFC3	*HST*	2010 Jun, 6th, 26th, Jul, 1st 9th	G13, Z15
Band 3	CO(3-2)	13794	-	ALMA	2014 May - 2015 June	Strazzullo in prep.
Band 4	CO(4-3)	13819	-	ALMA	2016 Apr - May	(Ongoing reduction)

Table 6 (cont'd)

Filter	Central wavelength (μm)	Exposure (s)	Instrument	Telescope	Observation date	References[a]
Ka	CO(1-0)	75600	-	JVLA	2012 Feb - Mar	Coogan in prep.

[a]References: D00: Daddi et al. (2000); B05: Brusa et al. (2005); K06: Kong et al. (2006); C09: Campisi et al. (2009); G11: Gobat et al. (2011); G13: Gobat et al. (2013); S13: Strazzullo et al. (2013); V15: Valentino et al. (2015); Z15: Zanella et al. (2015); V16: : Valentino et al. (2016).

3 A GIANT LYα NEBULA IN THE CORE OF AN X-RAY CLUSTER AT $z = 2$

Literature dedicated to phenomenology and physics of high-redshift "Lyα nebulae" or "blobs" – extended ($\gtrsim$ 100 kpc) and luminous (few $10^{43} - 10^{44}$ erg s^{-1}) gas reservoirs shining by the emission of Lyα photons –, has dramatically increased in the last few years. However, several aspects of Lyα nebulae are still debated, including the origin of the Lyα-emitting gas, its powering mechanism, the possible effects on the evolution of the embedded galaxies, and, ultimately, its fate. The position held by Lyα nebulae in the current description of structure formation is particularly questioned, since it requires a deep understanding of the complex gas cycle and physics in high-redshift systems.

In this chapter I focus on a specific feature of Lyα nebulae: their connection with the surrounding environment. This perspective complements the approaches already presented in the literature and allows us to shed light on several of the problematics listed in Section 1.4. First, there are observational hints that Lyα nebulae preferentially reside in overdense regions of the universe or sparse protoclusters (Steidel et al. 2000; Matsuda et al. 2004; Venemans et al. 2007). This suggests a possible connection with the formation of massive structures, even if it is not clear in which density regimes this correlation holds. Interestingly, in the local universe the presence of kpc-size, filamentary reservoirs of ionized gas in the center of "cool-core" X-ray emitting clusters (CCs) has been known for decades (Fabian et al. 1984b; Heckman et al. 1989; Hatch et al. 2007; McDonald et al. 2010; Tremblay et al. 2015). From this angle, it is tempting to view the high-redshift Lyα nebulae as the counterparts of local filaments, with sizes and luminosities reflecting the extreme conditions of the primordial universe (McDonald et al. 2010; Arrigoni Battaia et al. 2015). However, the detailed physics of the nebular emission, including the powering mechanism and the origin of the ionized gas, is still debated even for local clusters, despite the quality of the available data (Section 1.4). Therefore physical insights might not be straightforwardly gained from the simple observation of local filaments. An attempt at assessing the validity of this suggestion can be done through observation of giant Lyα nebulae in the core of high-redshift galaxy clusters. To date, we have lacked strong observational evidence primarily be-

cause of the scarcity of *bona fide* X-ray emitting structures discovered at $z \geqslant 1.5$ (i.e., Andreon et al. 2009; Papovich et al. 2010; Santos et al. 2011; Stanford et al. 2012; Gobat et al. 2011, 2013; Brodwin et al. 2015). Here I study in detail the case of the most distant among these X-ray detected structures, CL J1449+0856 at $z = 1.99$ (Section 2.1), since its advanced evolutionary stage make it a suitable candidate to start the search for nebulae in far away clusters. In Section 3.1 I present the results of a recent narrow-band imaging campaign we conducted with Keck/LRIS, with which we identified a ~ 100 kpc Lyα-emitting nebula in the cluster core, along with the results of a recent Chandra follow-up of CL J1449+0856, probing its hot ICM. Section 3.2 discusses the physical properties of the Lyα nebula, while in Section 3.3 I envisage the possible powering mechanisms, and the timescales regulating its evolution, concluding that a substantial gas replenishment is necessary to feed the system. Concluding remarks are presented in Section 3.4. Unless stated otherwise, we assume a ΛCDM cosmology with $\Omega_m = 0.3$, $\Omega_\Lambda = 0.7$, and $H_0 = 70$ km s^{-1} Mpc^{-1} and a Salpeter initial mass function (Salpeter 1955). All magnitudes are expressed in the AB system.

This chapter is based on the article published in the Astrophysical Journal in 2016 (Valentino et al. 2016) in collaboration with several co-authors at CEA and foreign institutes.

3.1 OBSERVATIONS AND DATA ANALYSIS

In this section we present the Keck/LRIS narrow-band imaging of CL 1449+0856. We also describe recent Chandra observations which we use to update the cluster X-ray properties previously constrained by XMM-Newton follow-up only. Specifically, we revise the total extended X-ray luminosity, gas temperature, and halo mass, presenting a new estimate from the velocity dispersion.

3.1.1 Lyα nebula detection: narrow-band imaging

We observed CL J1449+0856 (Figure 26) for 3.5 hr with the narrow-band filter NB3640 installed in the blue arm of the Keck/LRIS camera on March 27, 2014, reaching a magnitude limit of 27.1 (5σ) in a $r = 0.6''$ circular aperture. The average seeing during the observation was 0.79″ (full width half maximum). We processed the images in a standard way with the publicly available LRIS pipeline[1]. In particular, we modeled and subtracted a super-sky image obtained as the clipped median of all the widely dithered, processed frames. We co-added individual frames weighting them by measured seeing and

1 http://www.astro.caltech.edu/~dperley/programs/lpipe.html

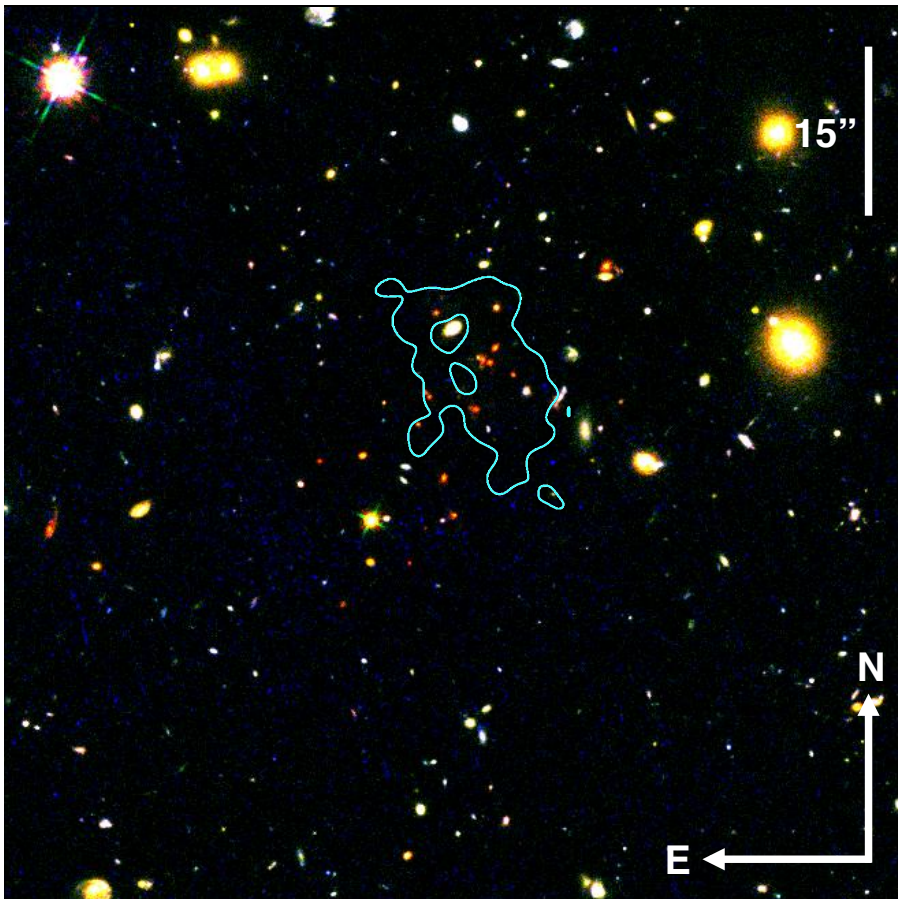

Figure 26 Cluster of galaxies CL J1449+0856 at $z = 1.99$. *HST*/F140W (red), F105W (green), and F606W (blue) RGB-composite image of CL J1449+0856. The central concentration of red galaxies represents the core of the cluster. The cyan line marks the 1σ contour of the Lyα nebula from the wavelet reconstruction.

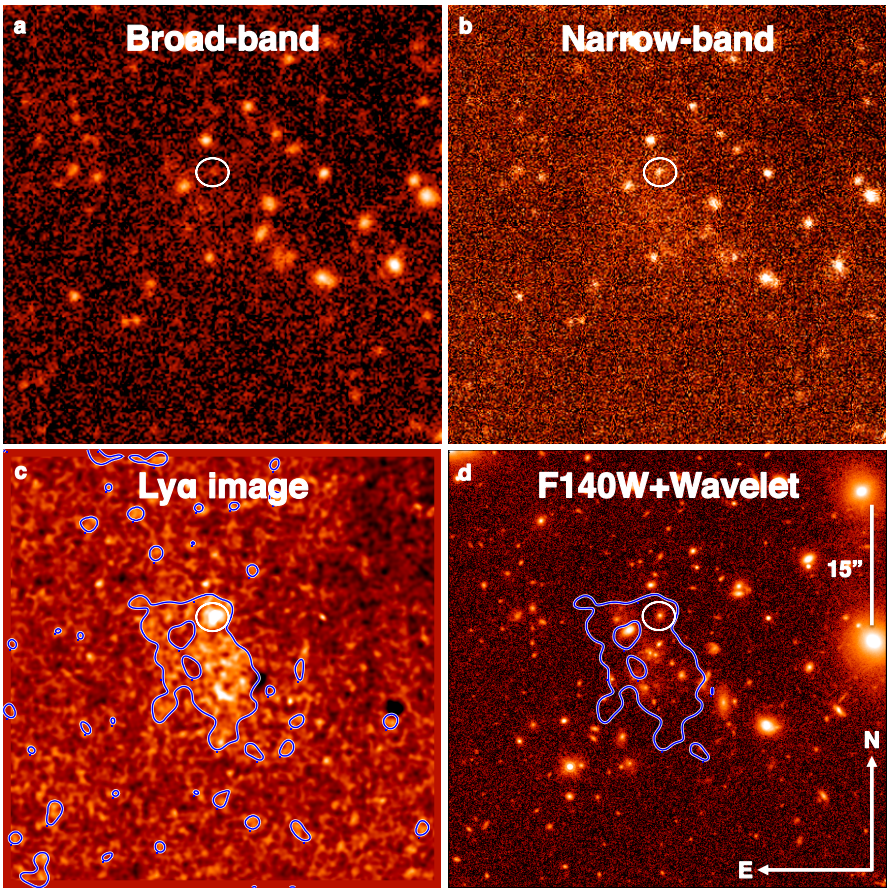

Figure 27 100-kpc extended Lyα nebula at $z = 1.99$. Images of CL J1449+0856 in the broad *U* band (panel a) and NB3640 narrow-band (panel b), and a continuum-subtracted Lyα emission line map smoothed on scales of 1" (panel c). The white circle indicates the heavily obscured AGN #661 (G13). The extended emission southwards is the Lyα nebula. Panel d shows the *HST*/WFC3 F140W image. In panels c and d the blue line marks the 1σ contour of the large scale Lyα emission from the wavelet reconstruction after the subtraction of point-like sources. For reference, 15" correspond to ~ 125 kpc at $z = 1.99$.

transparency variations during the observing night. We then combined the final narrow-band image with an aligned *U*-band frame from VLT/FORS2 (5σ limiting magnitude of 27.4, S13) using the formalism presented in Bunker et al. (1995) to obtain a Lyα emission map (Figure 27 and 33 in Appendix). Color corrections are negligible, given the optimal overlap of the central effective wavelengths of the narrow- and broad-band filters (3640, 3607 Å respectively). We checked the absolute flux calibration against Sloan Digital Sky Survey data, finding an agreement within 0.01 magnitude. We selected individual Lyα absorbers and emitters by running SExtractor in dual image mode on a χ^2 detection image and on narrow- and broad-band images. We built the χ^2 detection image averaging the *U* and NB3640 frames weighting by their signal-to-noise ratio squared. Besides an obscured AGN (#661 in G13, see Section 3.3.1 below for further details), we detected only two individual bright peaks in the Lyα emission map of the cluster core (∼ 5σ) both through a classical aperture photometry approach and a wavelet analysis (Figure 28). However, they are not associated with known cluster members within a 1″ radius in the adjacent *U* and *B* bands, nor in the deeper, but redder *HST*/F140W band or in the X-ray bands, suggesting that these peaks are not associated with SFGs in the cluster core. The uncertainty on the position of 5σ peaks of Lyα emission is 0.07". The bright knots may just be the densest regions of the extended Lyα nebula and the granularity (Figure 27, panel c) could suggest the presence of gas substructures (Cantalupo et al. 2014) or shock fronts currently beyond our detection threshold. On the other hand, several Lyα emitter and absorber candidates are spread over the $5' \times 8'$ field covered by the LRIS detectors (Appendix 3.6), but we defer their comprehensive analysis to a future work. To support the detection of Lyα photons on large scales, we performed a wavelet analysis with an iterative multi-resolution thresholding and a Gaussian noise model[2] (Starck et al. 2010). The basic concept underlying wavelet decomposition is to split an image into a set of spatial frequencies, each one including the signal from sources with power on that scale. The original image is exactly recovered by adding all the "slices". The advantage of this technique is to reduce (or remove) the impact of small-scale objects when looking for large-scale structures and its efficacy for detecting Lyα nebulae has already been shown (Prescott et al. 2012, 2013). We used this technique for the purpose of visualization (Figure 26, 27, and 33 in Appendix) and to cross-check the results from a classical aperture photometry approach. After subtraction of the contribution from the point-like, obscured AGN (< 8% of the total emission), we measure a total flux of $(8.1 \pm 1.0) \times 10^{-16}$ erg cm^{-2} s^{-1} in a ∼ 140 arcsec^2 polygonal aperture enclosing the whole nebula, fully consistent with the results provided by the wavelet analysis. The residual

2 http://www.cosmostat.org/software/isap/

Lyα flux surrounding the AGN in the wavelet image is extended on scales larger than the point spread function (PSF, with a full width half maximum of 0.79″) and contributes to the luminosity of the nebula. We also retained the flux from the other individual bright peaks since no counterparts are detected in any other band. We estimated the 1σ uncertainty as the rms of the distribution of fluxes inside circular apertures of area equal to the one in which we measured the flux of the nebula. The total flux corresponds to an observed luminosity of $L_{Ly\alpha} = (2.3 \pm 0.3) \times 10^{43}$ erg s^{-1}.

The morphology of the Lyα nebula is elongated from AGN #661 towards the center of the cluster, suggesting a physical connection (Section 3.3.1). The major axis of the 3σ contour from the wavelet analysis is ∼ 120 physical kpc long. The asymmetric shape and the mis-centered location of the AGN is observed in several other nebulae at high redshift (i.e., Borisova et al. 2016) and it might simply reflect the AGN illumination cone and the gas distribution in the cluster, which naturally concentrates towards the bottom of the potential well. In fact, the peaks of the Lyα luminosity and the extended X-ray emission traced by XMM-Newton and Chandra (Section 3.1.3) are spatially coincident in projection, and so is the peak of the stellar mass density distribution (Figure 29), implying that the nebula effectively sits in the cluster core. Note that the peaks mapped by XMM-Newton and Chandra are consistent within the positional uncertainties (16″ and 4″ respectively). In Figure 30 we show the radial profile of the Lyα surface brightness and the projected stellar mass density. For both profiles we fixed the same center at the peak of the projected stellar mass density distribution. Moreover, we merged the measurements at the two farthest positions from the cluster center to increase the signal, and we subtracted the contribution of AGN #661. As opposed to the stellar component that traces the cluster potential well, the Lyα surface brightness profile appears flat over the whole extension of the nebula. A drop is expected to occur at some radius, but Figure 30 suggests that this happens at larger scales than for the stellar component.

3.1.2 Extended continuum emission

We measured the continuum emission associated with the Lyα nebula from a pure "continuum emission map" (Bunker et al. 1995) and both Subaru/Suprime-Cam *B* (G11) and Keck/LRIS *V* band imaging. We do not expect strong emission lines from sources at $z = 2$ to fall in the observed *B* and *V* bands. These frames are respectively 2.5× and 3.3× deeper than the continuum image and provide a better constraint on the Lyα equivalent width of the nebula (EW(Lyα)). In unobscured SFGs, the flux density F_ν is roughly constant at wave-

lengths bluer than 2000 Å, and thus possible color biases in the evaluation of the EW(Lyα) using B and V bands continuum are limited. We measured the continuum emission only where we detected the extended Lyα emission at more than 5σ significance (Figure 33 in Appendix, panel d). Evident B and V band sources were masked so as not to contaminate the diffuse emission. In none of the frames we individually detected a significant integrated continuum emission. Assuming a constant F_ν and combining the three bands, we estimated an average continuum emission of $(3.38 \pm 0.95) \times 10^{-19}$ erg cm^{-2} s^{-1} Å^{-1} and a corresponding Lyα equivalent width of EW(Lyα) $= 271^{+107}_{-60}$ Å, compatible with the 2σ lower limit we derived from the sole continuum image (EW(Lyα) > 192 Å). We note here that the 3σ detection is formally reached only by including the V-band, which could contain residual contaminating emission from red passive galaxies. Thus, it would be appropriate to regard the quoted EW measurement as a lower limit.

3.1.3 Chandra X-ray observations

CL J1449+0856 has been imaged both with XMM-Newton (80 ks, G11, Brusa et al. 2005) and Chandra (94 ks, Campisi et al. 2009). Details of the XMM-Newton detection have already been reported in G11, thus we report here only the salient features. A detection was found in the soft-band ($0.5 - 2$ keV) image, extended more than the 6″ instrument PSF. After PSF fitting at the position of Chandra detected sources, the residual XMM-Newton emission in the soft band is significant at the 3.5σ level on scales of 20-30″, three to five times more extended than the PSF of the instrument. The excess flux over the background is 47 ± 13 photons, the error including systematic uncertainties due to the point source subtraction. The total flux of this extended emission in the range $0.5 - 2$ keV and over a 16″ radius is $\sim 9.3 \times 10^{-16}$ erg s^{-1}, consistent with the presence of hot ICM, typical of a "relaxed" cluster. This is thus faint emission, yet detected at a higher significance level than what reported for the $z = 1.62$ cluster at the time of publication (Tanaka et al. 2010; Papovich et al. 2010). Note that this analysis was intentionally kept simple and robust, applying classical recipes for background and point-source subtraction, and aperture photometry. However, this analysis suffered from a large uncertainty on the localization of the cluster center. Based on the statistical analysis of galaxy groups in COSMOS (George et al. 2011), the difference between the most massive members and the X-ray peak positions is typically 15″ (Figure 29, panel b). The measured distance between the core of the cluster and the XMM position is 9″.

Archival ACIS-I Chandra observations of the field consist of a mosaic of three partially overlapping pointings of ≈30 ks each, covering

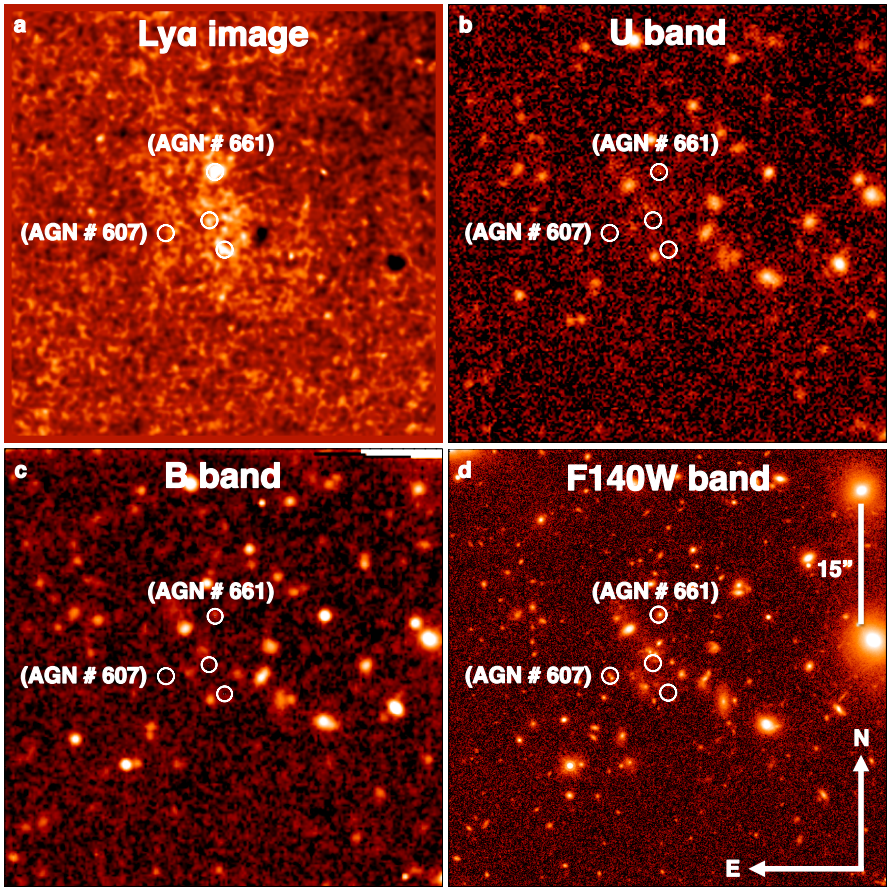

Figure 28 Bright knots in the Lyα nebula. Lyα emission line map smoothed over a 1" area (panel a) and *U*-band (panel b), *B*-band (panel c), and F140W band (panel d) images of CL J1449+0856. Individual Lyα emitters detected at $\sim 5\sigma$ are marked (white circles). The position of the AGN # 607 is reported for clarity, but this source is not identified as a Lyα emitter. For reference, 15″ correspond to ~ 125 kpc at $z = 1.99$.

a total area of ≈500 arcmin^2 at different depths. These three observations (5032, 5033, and 5034) were performed in June 2004 by the Advanced CCD Imaging Spectrometer (ACIS) with the Io CCD at the aimpoint and all ACIS-I CCDs in use. Faint mode was used for the event telemetry, and ASCA grade 0, 2, 3, 4, and 6 events were used in the analysis (full details are reported in Campisi et al. 2009). In Cycle 16 we followed-up the field with the ACIS-S camera (aimpoint at CCD=7) for a nominal exposure of 94.81 ks in very faint mode. This new Chandra observation has a higher spatial resolution because pointed at the location of the diffuse emission and, thus, improves the localization of the cluster core and the association between the extended X-ray source and the optical/near-IR counterpart. For both ACIS-I and ACIS-S data, reprocessing was carried out using CIAO version 4.6 and adopting the latest relevant calibration products. From a wavelet reconstruction of the ACIS-S image, we detected a $> 4\sigma$ extended feature co-aligned with the core (Figure 29, panel a). The X-ray source is centered on coordinates 14h 49m 13.67s, +8°56′28.25″ with a 1σ uncertainty on the position of 4″ (Figure 29, panel b) and a distance to the cluster core of 5″. We measured the extended source flux in the area where the significance of the wavelet map was higher than 2σ. We derived ACIS-S and ACIS-I counts independently, using the same extraction region. Within a 10″ aperture, the net (i.e., background-subtracted) number of counts from the extended source in ACIS-S is 11.0 ± 5.3 (94 ks exposure) in the $0.5 - 2$ keV band, corresponding to an aperture flux of $(8.5 \pm 3.0) \times 10^{-16}$ erg cm^{-2} s^{-1}. The ACIS-I counts and aperture flux are 5.2 ± 2.5 and 1.2×10^{-15} erg cm^{-2} s^{-1} respectively (49 ks exposure). The average flux of the source is therefore $(1.0 \pm 0.4) \times 10^{-15}$ erg cm^{-2} s^{-1}. This corresponds to an observed total X-ray luminosity of $L_X = (9 \pm 3) \times 10^{43}$ erg s^{-1} in the $0.1 - 2.4$ keV rest-frame band within R_{500}, defined as the radius enclosing a mean overdensity $500\times$ larger than the critical density of the universe. We do not detect bright radio sources close to the cluster core in deep Jansky Very Large Array observations at 3 GHz down to 2.7 μJy (rms), except for two galaxies with a ∼ 30 μJy continuum emission, fully consistent with pure star formation activity seen at ultra-violet and infra-red wavelengths. Thus, inverse Compton scattering off extended radio-galaxy jets is not likely to be the origin of the extended X-ray emission as in potentially similar cases (i.e., Miley et al. 2006).

3.1.4 Halo mass and gas temperature

Scaling the observed total X-ray luminosity within R_{500} (Leauthaud et al. 2010), we estimated a halo virial mass of $M_{halo} = (5 - 7) \times 10^{13}$ $M_\odot$ and a virial radius of $R_{vir} = 0.5 \pm 0.1$ Mpc, in agreement

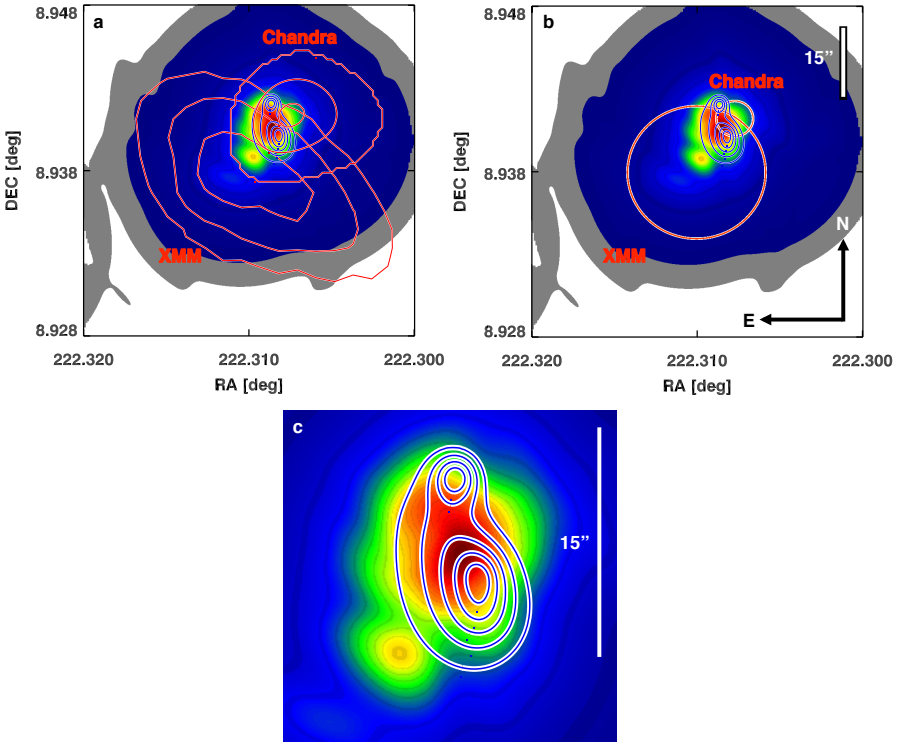

Figure 29 Spatial distributions of stellar mass density, Lyα surface brightness, and X-ray extended emission. Stellar density maps are derived from a mass complete sample of cluster members and candidates with $M_\star \geqslant 10^{10.4}\ M_\odot$ (S13, background colored image in panels a, b, and c). The prominent stellar mass density peak represents the cluster core region (red area). Lyα nebula $\geqslant 3\sigma$ contours from wavelet reconstruction are superimposed (blue lines). Note that point-like sources have been subtracted before tracing the contours. Extended X-ray contours from XMM-Newton and Chandra observations (red lines) are displayed in panel a. The positional uncertainties of the peak of the X-ray extended emission from both sets of observations are shown in panel b (red circles). A zoom on the central region is shown in panel c. For reference, 15” correspond to ~ 125 kpc at $z = 1.99$.

with previous determinations (G11, G13). This estimate is consistent with that expected from a total stellar mass enclosed in cluster members of 2×10^{12} $M_\odot$, in particular in six massive and passive galaxies in the core (S13, $M_{halo} = 4 - 7 \times 10^{13}$ $M_\odot$, including the latest calibration by van der Burg et al. 2014). We independently evaluated M_{halo} from the velocity dispersion derived from *HST*/WFC3 and Subaru/MOIRCS spectroscopy (G13, Valentino et al. 2015). After excluding obvious interlopers at redshift $z < 1.95$ and $z > 2.05$, we estimated the systemic redshift and the velocity dispersion fixing the reduced $\chi^2_{red} = (\sum_{i=1}^{N}(z_i - z_{sys})^2/(\sigma^2_{z_i} + \sigma^2_{disp}))/dof = 1$, applying a clipping at 3σ, and iterating until convergence. This procedure allows us to fully take into account the uncertainties on spectroscopic redshifts. We then estimated the uncertainties as the 15.87 - 84.13 percentile ranges of the distribution of 15,000 bootstrap simulations. We obtain $z_{sys} = 1.995^{+0.003}_{-0.004}$ and $\sigma_{vel} = (830 \pm 230)$ km s^{-1}. We find consistent results modeling a Gaussian curve on the galaxy redshift distribution (Figure 31). Assuming virialization, we find a 1σ lower limit on the virial mass of $M_{halo} \gtrsim 4 \times 10^{13}$ $M_\odot$ obtained adopting the 1σ lower limit on σ_{vel}. Then, we calculated a total intracluster mass in the hot phase of $M_{ICM} \approx 0.08 \times M_{halo} \approx 5 \times 10^{12}$ $M_\odot$ (Renzini & Andreon 2014). The gas fraction may vary with redshift, but even considering a value close to the universal baryon fraction, the main result of this work would not change. Assuming spherical geometry for the halo and a mean molecular weight of $\mu = 0.6$, the average particle density is $(8 \pm 2) \times 10^{-4}$ cm^{-3} within the virial radius. Finally, we estimated a temperature of 2.1 keV from the $L_X - T$ relation (Finoguenov et al. 2007) and an absorbing column density of N_H=2×10^{20} cm^{-2}. We stress here that the current X-ray dataset allows only for an estimate of the integrated X-ray luminosity L_X. We do not have in-hand the spatial profiles of X-ray derived quantities such as the temperature, entropy, density, or the metallicity of the hot ICM. In order to estimate these physical quantities, we rely on the extrapolation of well established relations at low and moderate redshift ($z < 1$).

3.2 PHYSICS OF THE LYα NEBULA

In this section we study the physics of the Lyα nebula. We estimate the mass and electron density from its luminosity and size, assuming it is photoionized by galaxies hosting AGN in the cluster. We further discuss the role of the volume filling factor in these estimates and a possible way to constrain it relying on the X-ray detection.

3.2.1 Mass and density

Assuming photoionization, we can estimate the mass $M_{Ly\alpha}$ and the electron density n_e of the ionized gas from the Lyα luminosity (McCarthy et al. 1990; Dey et al. 2005):

$$M_{Ly\alpha} = 1.25\, m_p\, n_e\, f\, V = (1-10) \times 10^9\, M_\odot \tag{9}$$

where m_p is the proton mass, f the volume filling factor, and V the volume of the nebula. For the sake of simplicity, we assumed a spherical geometry for the nebula with a radius $R_{neb} = 46$ kpc, the average value of the long and short axes measured in the wavelet reconstructed image. The choice of the shape does not affect the final result of this work, i.e., adopting a cylindrical symmetry the volume changes by $\approx 10\%$. We assumed $f = 10^{-3} - 10^{-5}$ as detailed in next section. The electron density is derived from the Lyα luminosity estimate through:

$$L_{Ly\alpha} = \frac{j_{Ly\alpha}}{j_{H\beta}}\, \alpha^{eff}_{H\beta}\, h\nu_{H\beta}\, n_e\, n_p\, f\, V \rightarrow n_e = 0.9 - 9\,cm^{-3} \tag{10}$$

where $j_{Ly\alpha}$ and $j_{H\beta}$ are the emission coefficients for Lyα and Hβ, $\alpha^{eff}_{H\beta}$ is the effective recombination coefficient for Hβ, $h\nu_{H\beta}$ is the energy of an Hβ photon, and n_p the proton number density ($n_e \approx 1.2\, n_p$ accounting for doubly ionized helium). The range of n_e values corresponds to $f = 10^{-3} - 10^{-5}$, assuming case B recombination (Osterbrock & Ferland 2006) and $T = 10^4$ K. We notice that the gas appears marginally optically thick to ionizing radiation, given the column density of neutral hydrogen averaged over the projected area of the nebula of $\langle N_{HI} \rangle \approx 10^{17.2}$ cm^{-2} (Hennawi & Prochaska 2013, their Equation 11). Moreover, $n_e \propto \left(\sqrt{f}\right)^{-1}$ and $M_{Ly\alpha} \propto \sqrt{f}$, reducing the 2 orders of magnitude range of uncertainty that we allowed for f. Finally, $M_{Ly\alpha}$ might be a lower limit for the total mass of cold gas reservoirs in the cluster if AGN are the powering sources (see Section 3.3.1), as beamed emission may illuminate only a portion of the gas. In addition, the true Lyα luminosity may be higher than reported due to dust and neutral hydrogen absorption.

3.2.2 Volume filling factor

The mass and density of the nebula depend on the volume filling factor f, which is not directly constrained by our observations. However, it is reasonable to assume pressure equilibrium between the ionized gas and the hot X-ray ICM, allowing us to put an upper limit on the possible values of f. To estimate the pressure exerted by the hot ICM, we assumed the universal pressure profile of galaxy clusters (Arnaud et al. 2010), properly rescaled in mass and redshift, as representative

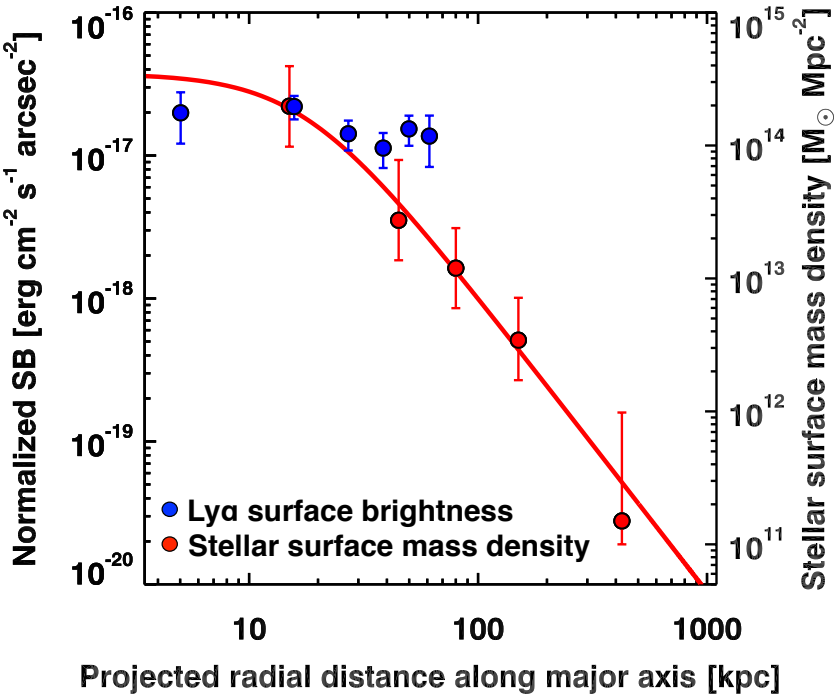

Figure 30 Lyα nebula and projected stellar mass density profiles. We show the stellar mass density (red circles) and normalized Lyα surface brightness (blue circles) radial profiles. The center of the profiles are spatially coincident and fixed at the position of the barycenter of stellar mass (S13). For the Lyα surface brightness profile we merged the measurements at the two farthest positions from the cluster center to reach the formal detection threshold. Moreover, the Lyα flux of AGN #661 has been subtracted in the corresponding bin. For the stellar mass density profile, error bars include both the Poisson error and the uncertainties in membership determination (S13). For the surface brightness profile, error bars represent the 1σ uncertainties on flux measurements. The best fit of the stellar mass profile is a classical beta-model (S13).

for CL J1449+0856. Then, dividing the pressure by $\sim 10^4$ K, the typical temperature of the Lyα gas, we obtained the radial density profile of a medium in pressure equilibrium with the X-ray emitting plasma. The range of possible values of n_e over the radial extension of the nebula is $n_e \sim 1 - 10$ cm^{-3}, corresponding to $f \sim 10^{-3} - 10^{-5}$, a pressure of $p \sim 10^4 - 10^5$ K cm^{-3}, and masses of ionized gas of $M_{Ly\alpha} \sim (1 - 10) \times 10^9$ $M_\odot$. Absent an observed X-ray profile, this is an order of magnitude calculation, given that the pressure profile in low mass systems might be different and, notably, flatter than in clusters (Le Brun et al. 2015), leaving the door open for larger values of f and lower densities. However, in addition to pressure equilibrium, higher values of f ($\sim 0.01 - 1$) are disfavored by a simple argument based on gravitational stability: if larger and more massive clouds were in place, they would be Jeans-unstable and form new stars, a scenario disfavored by the observed high value of EW(Lyα) (Section 3.3.1). On the contrary, solutions with $f \lesssim 10^{-3}$ are gravitationally stable, considering the simplified case of auto-gravitating spheres of gas at 10^4 K stably ionized. On the other hand, much smaller values of f are not easily maintained for long timescales. As recognized in classical works (Fabian et al. 1987; Crawford & Fabian 1989), lower volume filling factors and higher densities would imply clouds dissipating by thermal expansion on short timescales (10^5 yr), with consequent difficulties to explain the size of the nebula and its lifetime.

3.3 DISCUSSION

Here we discuss five different physical scenarios to explain the extended Lyα emission: hard ionizing spectra of AGN impacting gas reservoirs in the cluster core, the continuous formation of young massive stars, cooling of dense cosmological cold flows penetrating into the dark matter halo, cooling of plasma from the X-ray phase, and dissipation of the mechanical energy from galaxy outflows in the core. We conclude that the most plausible sources of ionizing photons are AGN embedded in the nebula, with a possible contribution from shocks induced by galaxy outflows. Finally, we discuss the typical timescales regulating the evolution of the nebula. We find that, barring an observational coincidence, in our favored scenario the nebula is constantly replenished with cold gas to survive evaporation due to the surrounding hot X-ray plasma.

3.3.1 Powering mechanism and origin of the gas

AGN in the cluster core

Two spectroscopically confirmed X-ray AGN in the cluster core (#607, 661 in G13) are suitable candidates for ionizing the nebula. The depth of the new Chandra observation, coupled with an optimal on-axis alignment, allowed us to perform a basic X-ray spectral analysis despite the limited photon statistics (34 and 20 net counts in the observed $0.5-7$ keV band for sources #607 and 661, respectively). Source #607 is characterized by a power-law spectrum with photon index $\Gamma = 2.0 \pm 0.6$; the observed $2-10$ keV flux is $1.7^{+1.1}_{-0.6} \times 10^{-15}$ erg cm^{-2} s^{-1}, corresponding to a rest-frame $2-10$ keV luminosity of $5.2^{+3.4}_{-1.8} \times 10^{43}$ erg s^{-1}, typical of a luminous Seyfert galaxy. The X-ray spectrum of source #661, the point-like Lyα emitter (Figure 27), is flat: fitting the data with a power-law model provides $\Gamma = -0.7^{+0.8}_{-0.9}$, highly indicative of strong obscuration. We then included an absorption component and fixed the photon index to 1.8, as expected for the intrinsic AGN emission (e.g., Piconcelli et al. 2005). This model results in a column density of $N_H = 9.3^{+5.6}_{-4.0} \times 10^{23}$ cm^{-2}, i.e., consistent with marginal Compton-thick absorption (1.5×10^{24} cm^{-2}). The tentative detection of an iron Kα emission line at 6.4 keV (with equivalent width of ≈ 2.4 keV rest frame), if confirmed, would further support the heavily obscured nature of source #661. The derived $2-10$ keV flux is $(7.4 \pm 2.2) \times 10^{-15}$ erg cm^{-2} s^{-1}, corresponding to a rest-frame luminosity of $L_{2-10\,\mathrm{keV}} = 2.9^{+0.6}_{-0.5} \times 10^{44}$ erg s^{-1}, placing source #661 in the quasar regime. We do not detect any bright counterpart in deep Jansky Very Large Array observations at 3 GHz down to 2.7 μJy (rms), and we thus classify source #661 as radio-quiet. From aperture photometry, we estimated a Lyα flux of $(6.7 \pm 0.7) \times 10^{-17}$ erg cm^{-2} s^{-1}, corresponding to a luminosity of $(1.9 \pm 0.2) \times 10^{42}$ erg s^{-1}. The spectral energy distribution (SED) of #661 is shown in Figure 32. From SED modeling, which benefits from near-, mid- and far-IR observations from Spitzer and Herschel, we estimated a bolometric luminosity for the AGN of $(2.7 \pm 1.5) \times 10^{45}$ erg s^{-1}. A similar value ($3.2 \pm 0.6 \times 10^{45}$ erg s^{-1}) is derived using the observed [O III] λ5007 Å luminosity obtained from recent Subaru/MOIRCS spectroscopy of the galaxy (Valentino et al. 2015), converted into a bolometric luminosity as $L_{bol}/L_{[OIII]} = 3500$ (Heckman et al. 2004). Assuming the luminosity-dependent bolometric correction as in Lusso et al. (2012), we predict an intrinsic $2-10$ keV luminosity for source #661 of $1.6^{+1.6}_{-0.5} \times 10^{44}$ erg s^{-1}. This value is consistent, within the uncertainties due to the adopted relations and measurements, with that derived from the X-ray spectral analysis reported above. Furthermore, we normalized the "radio-quiet AGN" template by Elvis et al. (1994) to match the estimated L_{bol}. We then integrated over wavelengths bluer than the

Lyman continuum limit to obtain the ionizing photon flux ϕ from both sources. We obtained $\phi \sim 1.3 \times 10^{55}$ and $\phi \sim 7.3 \times 10^{54}$ photons s^{-1} for source #661 and #607, respectively. Taking into account the distance between the AGN and the peak of diffuse Lyα emission, a conical illumination pattern of the neutral gas, and a covering factor of the ionized gas $f_C \sim 1$ consistent with the observations (Section 3.3.2), we estimate that $(6.5 - 15.3)\%$ and $(14.5 - 49.2)\%$ of ionizing photons from #661 and #607 reach and ionize the gas. The number of ionizing photons necessary to explain the observed Lyα luminosity is:

$$\phi = \frac{L_{Ly\alpha}}{h\,\nu_{Ly\alpha}} \frac{1}{\xi_{Ly\alpha}} \approx 1.8 \times 10^{54}\,\mathrm{photons\,s^{-1}} \tag{11}$$

where $\xi_{Ly\alpha} = 0.68$ is the fraction of ionizing photons converted in Lyα (Spitzer 1978). Thus, the AGN are likely capable of producing a sufficient amount of ionizing radiation to power the gas emission, even if f_C were a factor of several times smaller. We note that the flat Lyα surface brightness distribution in Figure 30 is not *a priori* in contradiction with powering from the AGN. The geometry of the system, the absorbing torus around the AGN, and the distribution of the cold clouds impact the observed profile: the flatness might just reflect covering factors close to unity. In fact, for volume filling factors $f = 10^{-3} - 10^{-5}$ and a covering factor $f_C \sim 1$, energetic photons from the AGN may ionize gas at large distances. Finally, we note that resonant pure scattering of Lyα photons from #661 can hardly contribute to the diffuse luminosity farther than ~ 10 kpc – less than 10% of the whole extension of the nebula –, as detailed radiative transfer modeling shows (Cantalupo et al. 2005; Dijkstra et al. 2006).

Young massive stars

Ongoing and continuous formation of young stars spread over the nebula might be a possible alternative ionizing source (Miley et al. 2006). The total SFR inferred from the Lyα luminosity is $(21 \pm 3)\,M_\odot\,yr^{-1}$ (Kennicutt 1998b), assuming an intrinsic ratio of $L_{Ly\alpha}/L_{H\alpha} = 8.7$ (Case B recombination, Osterbrock & Ferland 2006). This estimate should be regarded as a strong lower limit on the total SFR since we do not correct $L_{Ly\alpha}$ for dust obscuration and scattering from neutral hydrogen. However, both truly diffuse star formation and the emergence of undetected galaxies populating the low-mass end of the mass function and contributing to the diffuse emission (Zibetti et al. 2005) are disfavored: the high value of EW(Lyα)$= 271^{+107}_{-60}$ Å implies ages too young to be reasonably observable (Section 3.1.2 and Figure 7 in Schaerer 2003). Assuming a continuous star formation history, we should observe stars younger than $\lesssim 3$ Myr distributed over a 100-kpc scale, much larger than the typical super-star cluster

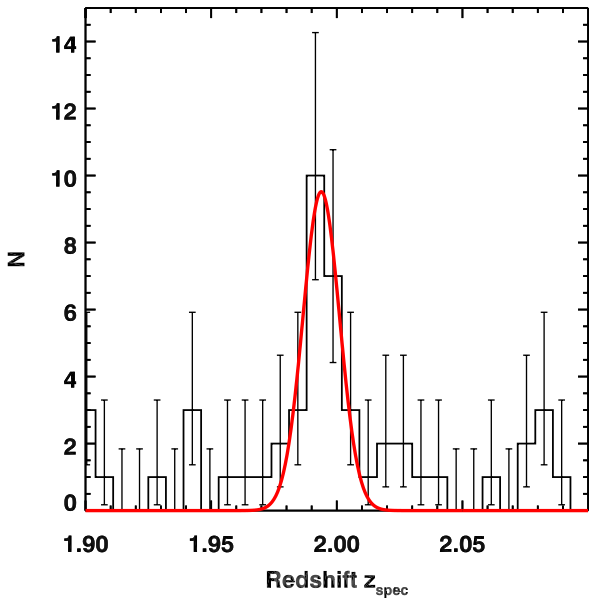

Figure 31 Cluster redshift distribution. The black histogram shows the redshift distribution of galaxies in CL J1449+0856. The red curve is the best Gaussian model fitting the curve. The uncertainties represent the formal 68.3% Poisson confidence interval.

size. For comparison, EW(Lyα) is $\sim$ 100 Å for the continuous star formation regime. A single, simultaneous star-burst event on the same scale seems even less likely. Small effects due to the choice of the initial mass function or metallicity do not change these results, unless considering extreme Population III stars (Schaerer 2003). We stress here that the weak continuum detection is formally reached only by averaging the *U* frame with redder bands, which could contain residual contaminating emission from red passive galaxies. In addition, the Lyα flux is not corrected for dust absorption and scattering from neutral hydrogen. Hence, the quoted EW measurement is reasonably a lower limit of the true value.

Cosmological cold flows

Another viable origin for the Lyα photons is the cooling of the dense streams penetrating into dark matter halos currently predicted by hydrodynamic cosmological simulations (Dekel et al. 2009a; Goerdt et al. 2010). The current status of these models disfavors this scenario showing that, given the halo mass of CL J1449+0856, these cold flows should have stopped reaching the cluster core $\sim$ 1 Gyr prior to observation, being shock-heated to the virial temperature (Figure 24, Valentino et al. 2015). Nevertheless, in the cluster core we estimate a total SFR of $\approx$ 1000 $M_\odot$ yr^{-1} (Section 4.1) that must be

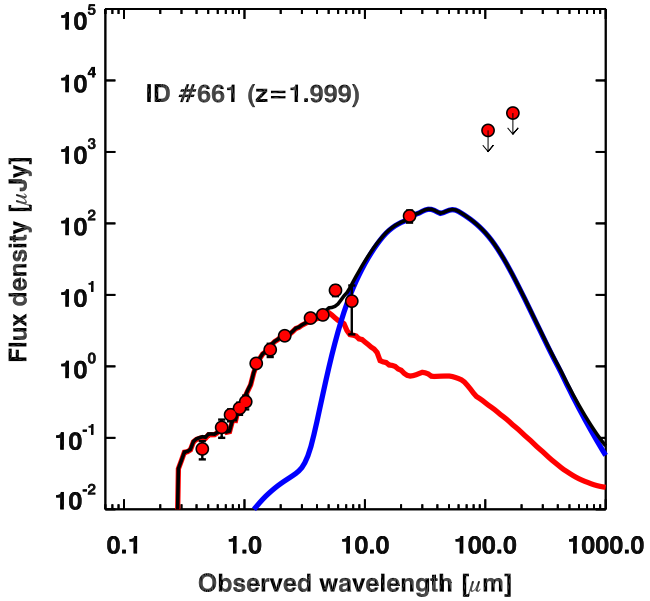

Figure 32 SED modeling of the marginally Compton-thick AGN #661. *U*-band to Herschel/SPIRE 250 μm observations are shown (red circles). The contributions of stars (red line) and the AGN (blue line) are shown independently. The full model is the sum of the two components (black line). The spectroscopic redshift is from Subaru/MOIRCS (Valentino et al. 2015).

constantly fueled by fresh cold gas given the 0.5 Gyr gas depletion timescale typical at $z = 2$ (Daddi et al. 2010; Tacconi et al. 2013). This points to an inconsistency with the prescriptions of present day models. Note, however, that the mass and redshift regimes at which cold flows should not penetrate into the hot ICM have not been observationally confirmed yet, and suffer from substantial scatter in simulations (Dekel et al. 2009a). In addition, there are hints that within this scatter a cluster progenitor at $z = 2$ may be crossed by dense gas streams supporting high SFRs and powering extended Lyα nebulae (Danovich et al. 2015). For the rest of the paper, we will adopt the predictions of current cosmological simulations, excluding a substantial contribution to the Lyα luminosity from cold flows. We defer a more detailed discussion to future work.

Classical cooling flows and cool-cores

Cooling from the X-ray emitting phase to a cold $\sim 10^4$ K temperature is known to occur at low redshift and is generally considered the origin of the nebular filaments observed in cool-core clusters (CCs, Fabian et al. 1984b; Heckman et al. 1989; Hatch et al. 2007; McDonald

et al. 2010; Tremblay et al. 2015). More extreme manifestations of the same mechanism are the classical cooling flows, though obvious cases are not currently known in the local universe (Peterson & Fabian 2006). Even though we cannot properly classify CL J1449+0856 as CC or non-CC according to the standard X-ray based definition owing to poor X-ray sensitivity at $z = 2$, we find several inconsistencies between this cluster and the typical local CCs or classical cooling flows. First, *the ratio between the Lyα luminosity of the nebula and the total X-ray luminosity of the ICM is orders of magnitude larger in CL J1449+0856 than predicted for classical cooling flows or observed in local CCs.* In CL J1449+0856 we find $L_{Ly\alpha}/L_X \sim 0.3$, while $L_{Ly\alpha}/L_X \sim 10^{-3}$ and $\sim 0.5 \times 10^{-3}$ for classical stationary cooling flows (Cowie et al. 1980; Bower et al. 2004; Geach et al. 2009) and CCs, respectively. To compute the ratio for local CCs, we collected measurements of extended Hα luminosities from the survey by McDonald et al. (2010) and the X-ray flux observed with ROSAT (Ledlow et al. 2003). Assuming $L_{Ly\alpha}/L_{H\alpha} = 8.7$ (Case B recombination, Osterbrock & Ferland 2006), we derived an average $L_{Ly\alpha}/L_X$ ratio of 5×10^{-4} (40% less when including only the extended filaments and not the flux from the BCG) for 13 structures in the Abell catalog. This is a conservative upper limit, since our Lyα measurement for CL J1449+0856 is not corrected for reddening nor scattering. The only cases when $L_{Ly\alpha}/L_X \sim 0.01$ happen in presence of strong radio-galaxies (i.e., Hydra A), while we exclude emission from such sources in CL J1449+0856 thanks to our deep JVLA 3 GHz maps down to 2.7 µJy (rms). This was already recognized in the seminal paper by Heckman et al. (1989) where the highest $L_{Ly\alpha}/L_X$ ratios strongly correlate with the presence of a bright radio-galaxy in the core (Cygnus A, 3C 295, Perseus) and consequently show high excitation lines in the spectra of the nebulae. For reference, the widely studied case of the Perseus cluster (i.e., Fabian et al. 1984a; Conselice et al. 2001; Hatch et al. 2005, 2007) shows $L_{Ly\alpha}/L_X \lesssim 5 \times 10^{-3}$. We stress once more that we do not measure a proper observed X-ray profile for the cluster. Thus, we cannot isolate the core luminosity (better correlated with the nebular luminosities, Figure 9 and 11 in Heckman et al. 1989), but we can only compare global properties (their Figure 10). Overall, the Lyα nebula we discovered is hugely overluminous with respect to local analogs: only $\ll 1\%$ of its luminosity could be explained if CL J1449+0856 were the high-redshift version of a typical low-redshift CC. Moreover, local nebular filaments are frequently connected with episodes of star formation. If not in the filaments themselves – observationally there is not clear evidence disproving this possibility (McDonald et al. 2010; O'Dea et al. 2010; Tremblay et al. 2015) – star formation should occur at least in the central galaxies, fueled by the gas cooled from the X-ray phase. The presence of large molecular gas reservoirs associated with the filaments (Salomé et al. 2011; McNamara et al. 2014) further

supports this argument. In CL J1449+0856 this is not observed: the peak of the extended Lyα emission (once removed the contribution of the offset point-like AGN) does not overlap with any cluster member, nor to any evident source in all bands from U to near-infrared *HST*/F140W. In this sense, if cooled gas is flowing towards the bottom of the potential well where the peak of the Lyα emission lies (Figure 29), it is not triggering star formation nor AGN feedback in any object.

Finally, as we will show later in Chapter 4, SFGs and AGN in the cluster core can inject a huge amount of energy into the surrounding medium. Considering only mechanical energy, this quantity is $5\times$ higher than the observed X-ray luminosity at $z = 1.99$, largely enough to offset *global* catastrophic cooling from the ICM and to strongly disfavor the hypothesis of a classical cooling flow. However, *local* rapid cooling may arise at the peak of the density distributions in the ICM, caused by onset of thermal instabilities. This argument is at the base of modern feedback regulated models of ICM cooling, which have proved to successfully reproduce several properties of the local nebular filaments (Gaspari et al. 2012; Sharma et al. 2012). Here we cannot directly test the simple prescription proposed in these models based on the ratio between the free-fall time and the timescale necessary to start the thermal instabilities. Nevertheless, we note that feedback is likely to play a role (Section 4.2), even if a circular 'on-off' auto-regulated regime might not be easily established at high redshift, given the long gas depletion timescales in galaxies ($0.5 - 1$ Gyr, Daddi et al. 2010; Tacconi et al. 2013) compared with the age of the universe.

We conclude that the observed Lyα emission is not due to cooling from the X-ray phase in the form of a classical stationary flow. On the other hand, if moderate cooling partially contributes to the total Lyα luminosity regulated by feedback, it generates very peculiar features not observed in local CCs.

Possible role of shocks

Lyα emission can be predominantly powered by shocks induced by galaxy outflows on the surrounding pressurized ICM (Cen & Zheng 2013; Cabot et al. 2016). We constrain the maximum fraction of total kinetic energy injected by winds that is lost by radiative losses simply dividing the total power radiated through emission lines ($\approx 2\times$ the observed total Lyα luminosity $L_{Ly\alpha}$) by the instantaneous energy injection $\dot{E}_{kin}$ due to galaxy outflows (Section 4.2). This fraction ($\sim$ 10%) is presumably a strong upper limit, considering the large number of ionizing photons emitted by AGN and star-forming galaxies in the core, and the low density of the ICM. If shocks were

dominating the Lyα emission, we could not estimate the mass from Equation 9, but rely on alternative working hypotheses, i.e., pressure equilibrium and geometrical assumptions. In this case, the estimate of the replenishment rate reported in Section 3.3.2 would not be valid. Future spectroscopic follow-up will help to quantify the contribution of shocks to the nebular emission, i.e., from UV lines ratios (Dey et al. 2005; Prescott et al. 2009).

3.3.2 Time evolution of the Lyα nebula

The evolution and the lifetime of the Lyα nebula are globally driven by cooling and heating processes, the dynamics of the gas, and their typical associated timescales. In the following, we envisage the time evolution of the system assuming that it is stable and exploring different physical scenarios.

Dynamics

As mentioned in Section 3.2.2, a single massive nebula at rest at the bottom of the potential well would rapidly collapse and form stars, since the pressure exerted by the particles of a 10^4 K, Lyα-emitting gas would be insufficient to balance the effect of gravity. This scenario is not consistent with our observations (Section 3.3.1). On the other hand, the Lyα nebula may be globally at rest at the bottom of the potential well if structured in smaller and denser clouds moving with a typical velocity comparable with the velocity dispersion of the cluster. However, the Lyα clouds would dissipate energy through turbulence. If not energized by external factors, they would inevitably start cooling and collapsing. All things considered, if the Lyα nebula were globally at rest in the dark matter halo, it would quickly disappear on a cooling timescale, making our discovery an unconvincingly lucky coincidence. Planned spectroscopic follow-ups will directly probe the dynamical state of the nebula and test our predictions.

Cooling and heating

Absent a strong powering mechanism, the continuous irradiation of Lyα photons would lead to the quick collapse and disappearance of the clouds. This would happen on timescales of $t_{cool} \approx 2.07 \times 10^{11}\,\mathrm{s}(T/10^4\,\mathrm{K})(n_e/1\,\mathrm{cm}^{-3})^{-1} \times (\Lambda(T)/10^{-23}\,\mathrm{erg\,cm^3\,s^{-1}})^{-1} \sim 0.1$ Myr, where $T = 10^4$ K is the gas temperature, $n_e \sim 1 - 10$ cm^{-3} the electron density corresponding to plausible values of the volume filling factor ($f = 10^{-3} - 10^{-5}$), and $\Lambda(T)$ the cooling function (Dey et al. 2005; Sutherland & Dopita 1993). Strong cooling of the Lyα clouds is disfavored by the large extension of the nebula and the ab-

sence of features of recent star-formation occurring in the ICM (Section 3.3.1). Moreover, the cold gas is immersed in a bath of energetic photons produced by the AGN that can keep a large fraction of it ionized. This would be compatible with the geometry of the system and dust absorption (Section 3.3.1). In addition, magnetic fields in the ICM can insulate and stabilize the ionized clouds, further preventing cooling and prolonging their lifetime up to ~ 10 Myr, as proposed for nebular filaments in local CCs (Conselice et al. 2001; Fabian et al. 2003, 2008).

Conversely, Lyα-emitting gas clouds in macroscopic motion with respect to the hot medium, can be thermalized through hydrodynamic instabilities and shocks. We estimate the timescale for the interaction between the cold and hot ICM phases following Klein et al. (1994):

$$t_{\rm therm} = \left(\frac{n_e^{\rm Ly\alpha}}{n_e^{\rm hot}} \right)^{1/2} \frac{R_{\rm cloud}}{c_s^{\rm hot}} \tag{12}$$

where $R_{\rm cloud}$ is the radius of individual Lyα-emitting clouds, and $c_s^{\rm hot} \approx 500$ km s^{-1} the sound speed in the hot medium. This speed is also comparable with the velocity dispersion in the cluster (Section 3.1.4). For simplicity, we adopted the classical hydrodynamic, non-radiative case where we considered the effects of hot winds moving at a typical speed of the order of $c_s^{\rm hot}$, much greater than the sound speed in the cold gas. However, a fully numerical treatment including radiative losses gives similar results (Scannapieco & Brüggen 2015). We allowed for possible clumpiness in the nebula assuming $R_{\rm cloud} < R_{\rm neb}$ when the volume filling factor is $f < 1$, where $R_{\rm neb} = 46$ kpc is the radius of the whole nebula (Section 3.2.1). To constrain $R_{\rm cloud}$, we adopted a pure geometrical approach (Hennawi & Prochaska 2013). Assuming spherical clumps spatially uniformly distributed in the spherical nebula of radius $R_{\rm neb}$ and with a single uniform clumps' gas density, we can link f to $R_{\rm cloud}$ through the covering factor f_C:

$$f = f_C \frac{R_{\rm cloud}}{R_{\rm neb}} \tag{13}$$

The relative smooth morphology of the nebula and the flat surface brightness profile are consistent with f_C of the order of unity, although we cannot determine its accurate value. Assuming $f = 10^{-3} - 10^{-5}$, we obtain a typical timescale for thermalization of $t_{\rm therm} \sim 0.1 - 3$ Myr. Relaxing the constraint on the covering factor up to a factor of 5, we find $t_{\rm therm} \sim 0.5 - 10$ Myr, consistent with the lower limit on the lifetime of filaments in local CCs.

As a direct consequence, barring an improbable observational coincidence, maintaining the nebula stable against evaporation requires a

replenishment of cold gas at a rate of $\dot{M}_{repl} = M_{Ly\alpha}/t_{therm} \gtrsim 1000$ $M_\odot$ yr^{-1}. Note that this estimate is sensitive to the presence of colder gas reservoirs not shining in Lyα and possible localized cooling partially compensating the heating, which could lower the final value. On the other hand, the quoted number could be regarded as a lower limit, since the parameters in the equations could substantially increase the replenishment rate in the plausible ranges we considered. This rate is directly proportional to f_C, but mildly depends on f through both terms of the fraction ($\dot{M}_{repl} \propto f^{-0.25}$), making the minimum replenishment stable against the range of values we allowed for the filling factor. Physically, the smaller the volume filling factor, the smaller the total mass of the nebula, but the shorter the evaporation time of the denser and clumpier gas. The density contrast term and the size of the clumps act in opposite way on t_{therm}, with R_{cloud} dominating the final value: smaller clumps are crossed by shocks or hydrodynamic perturbations more rapidly than larger clouds and, consequently, they are disrupted faster. If not continuously sustained against evaporation, the nebula would disappear on timescales of t_{therm} or, analogously, very short timescales imply unphysical replenishment rates $\dot{M}_{repl}$ to explain the presence of the nebula. We note that the evaporation timescale is shorter than the nebula crossing time ($\sim$ 90 Myr), given a radius of $R = 46$ kpc and a typical wind speed of 500 km s^{-1} (i.e., Förster Schreiber et al. 2014). This raises the problem of explaining the extension of the nebula, since the Lyα-emitting clouds should evaporate well before filling the observed volume. The issue would be naturally fixed if the clouds primarily form *in situ* by cooling from the X-ray emitting ICM. Globally, this is unlikely to be the case especially far away from the cluster center, where cooling times from bremsstrahlung are long. However, *local* thermal instabilities might be established in the densest portions of the ICM, providing part of the cold gas needed. On the other hand, if the gas replenishment is due to galaxies (as we envisage in Chapter 4), the size of the nebula is explained both by the distribution of cluster members over a large area, since in this case clouds being injected at different positions would not need to cross the whole nebula, and by recent models of radiatively cooling winds (Thompson et al. 2015). Moreover, galaxies are rapidly moving in the cluster core and, consequently, winds are naturally spread over large portions of the nebula.

3.4 SUMMARY AND CONCLUSIONS

In this work we presented the results of recent follow-ups of the galaxy cluster CL J1449+0856 with Chandra and a narrow-band filter targeting Lyα with Keck/LRIS.

- We report the discovery of a giant > 100-kpc extended nebula with a total luminosity of $L_{Ly\alpha} = (2.3 \pm 0.3) \times 10^{43}$ erg s^{-1}. Very dim continuum emission is associated to the nebula, resulting in an average equivalent width of EW(Lyα)$= 271^{+107}_{-60}$ Å. However, because of dust obscuration, scattering from neutral hydrogen, and geometrical effects, this value should be regarded as a conservative lower limit
- We confirm the previously reported detection of extended X-ray emission from the ICM and largely improve the localization of its peak and total luminosity thanks to the smaller Chandra PSF. Moreover, we unambigously identify two X-ray emitting AGN in the cluster, spatially associated with known cluster members, one of which is also a bright Lyα emitter
- We revise the halo properties of the cluster, refining its mass to $(5-7) \times 10^{13}$ M$_\odot$ from the X-ray luminosity in agreement with the first assessment of velocity dispersion of cluster members and their integrated stellar mass
- To our knowledge, this is the first case of a nebula found spatially correlated with extended X-ray emission at high-redshift. This result naturally extends the correlation between Lyα nebulae and overdensities to the extreme environment of a relatively mature cluster core, suggesting a physical connection with structure formation
- We pinpointed two X-ray AGN as the most likely candidates to power the nebula witha possible contribution from shocks, disfavoring ionization from very young stars and cooling from the X-ray phase in the form of a stationary classical cooling flow. In principle, regulated cooling as in local cool-core clusters could partially contribute to the Lyα luminosity, but several inconsistencies between CL J1449+0856 and local systems are evident. Above all, the ratio between the Lyα luminosity and the total X-ray luminosity is a factor $10 - 1000\times$ higher in CL J1449+0856 than in local CCs even in those cases where strong radio-sources are present (i.e., Perseus)
- We analysed the physics of the nebula, deriving its mass and average electron density. We studied its time evolution based on heating, cooling, and dynamics and found that the interaction between the Lyα nebula and the surrounding hot ICM requires a $\gtrsim 1000$ M$_\odot$ yr^{-1} gas replenishment rate to sustain the nebula against evaporation. Gas supply through galaxy outflows will be detailed in the next Chapter.

The advent of forthcoming facilities will allow us to drastically reduce observational uncertainties and avoid a heavy resort to assumptions. Measurements of temperature, pressure, and entropy profiles

of the hot ICM in young clusters will be possible with the foreseen Athena X-ray satellite, while the systematic follow-up of Lyα emission in clusters at $z > 2 - 3$ could start soon with new wide field integral field spectrographs on large telescopes, like MUSE and KCWI. Spectroscopy in the ultra-violet range will provide crucial information on the kinematics of the nebula, the metal enrichment, and its main powering mechanism.

3.5 APPENDIX A. WAVELET RECONSTRUCTION AND SMOOTHING

We show the unsmoothed Lyα image from the Keck/LRIS narrow-band follow-up of CL J1449+0856 in panel (a) of Figure 33. The only purpose is to demonstrate that the Lyα emission is not dominated by individual galaxies, but it is distributed fairly homogeneously over several square arcsec. The very low surface brightness regimes probed in this image make the identification of the nebula difficult by eye. It is easier to recognize it by comparing the original narrow- and broad-band images shown in Figure 27 or, alternatively, with a moderate smoothing (1″, Figure 27 and 33 panels b-d). To guide the eye and pinpoint the peak of the extended emission, in panels (b-d) of Figure 33 we show the contours of the wavelet reconstructed Lyα image. In each panel we show the contours after the subtraction of point-like sources, retaining only the signal on larger scales, namely the Lyα nebula. Panel (b) shows the maximum extension of the Lyα nebula, while the smoother denoised contours in panels (c) and (d) allow for identifying the peak of the extended emission. The appearance of two peaks in panel (c) depends on the number of scales adopted to slice the image with the wavelet technique and does not affect the main findings of this work. The region spanned by the $\geqslant 5\sigma$ detection in panel (d) is the same used to measure the extended continuum emission (Section 3.1.2). In every panel the number of contours is chosen arbitrarily to highlight the peak of the emission and does not correspond to a fixed step in surface brightness.

3.6 APPENDIX B. LYα EMITTERS AND ABSORBERS IN CL J1449+0856

Besides the individual bright peaks enclosed in the region occupied by the Lyα nebula (Section 3.1.1, Figure 28), several Lyα emitter and absorber candidates are spread over the $5' \times 8'$ ($\sim 2.5 \times 4$ Mpc^2) field covered by the LRIS detectors. In Figure 34 we show a preliminary version of the NB3640, *U*-NB3640 color-magnitude diagram that allows us to select such candidates. We identified the sources running SExtractor (Bertin & Arnouts 1996) in dual image mode on both frames and a χ^2 detection image obtained averaging the *U* and NB3640 frames weighted by their signal-to-noise ratio squared. The Lyα flux is then computed as:

$$F = (F^{\lambda}_{NB} - F^{\lambda}_{U}) \frac{A_U * A_{NB}}{(A_U - A_{NB})} \tag{14}$$

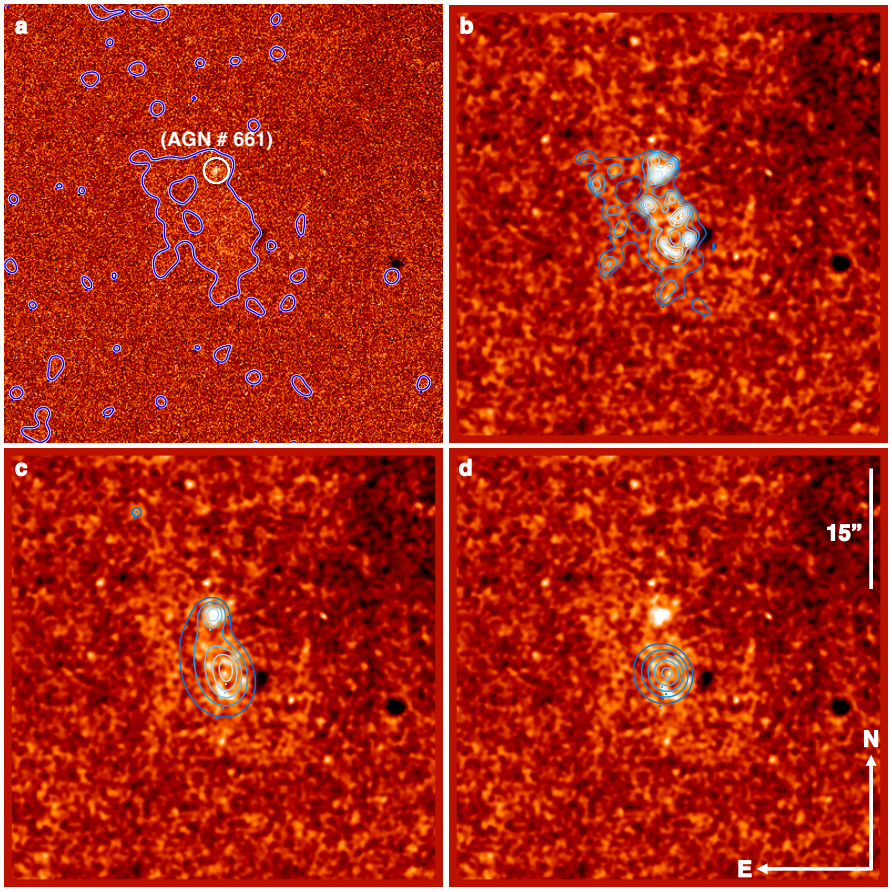

Figure 33 Wavelet reconstruction of the Lyα image. We show the original unsmoothed Lyα emission line map of the central region of CL J1449+0856 in panel a. The 1σ contour of the large scale Lyα emission from the wavelet reconstruction (blue line) and the X-ray obscured AGN (white circle) are marked for reference. Panels b, c, and d show the reconstructed wavelet contours at $\geqslant 1\sigma$, $\geqslant 3\sigma$, and $\geqslant 5\sigma$ respectively (blue lines) of the Lyα emission line map. Point-like sources have been subtracted before computing the surface brightness contours. The number of contours is arbitrary and chosen to pinpoint the peak of the extended emission. For reference, 15″ correspond to ~ 125 kpc at $z = 1.99$.

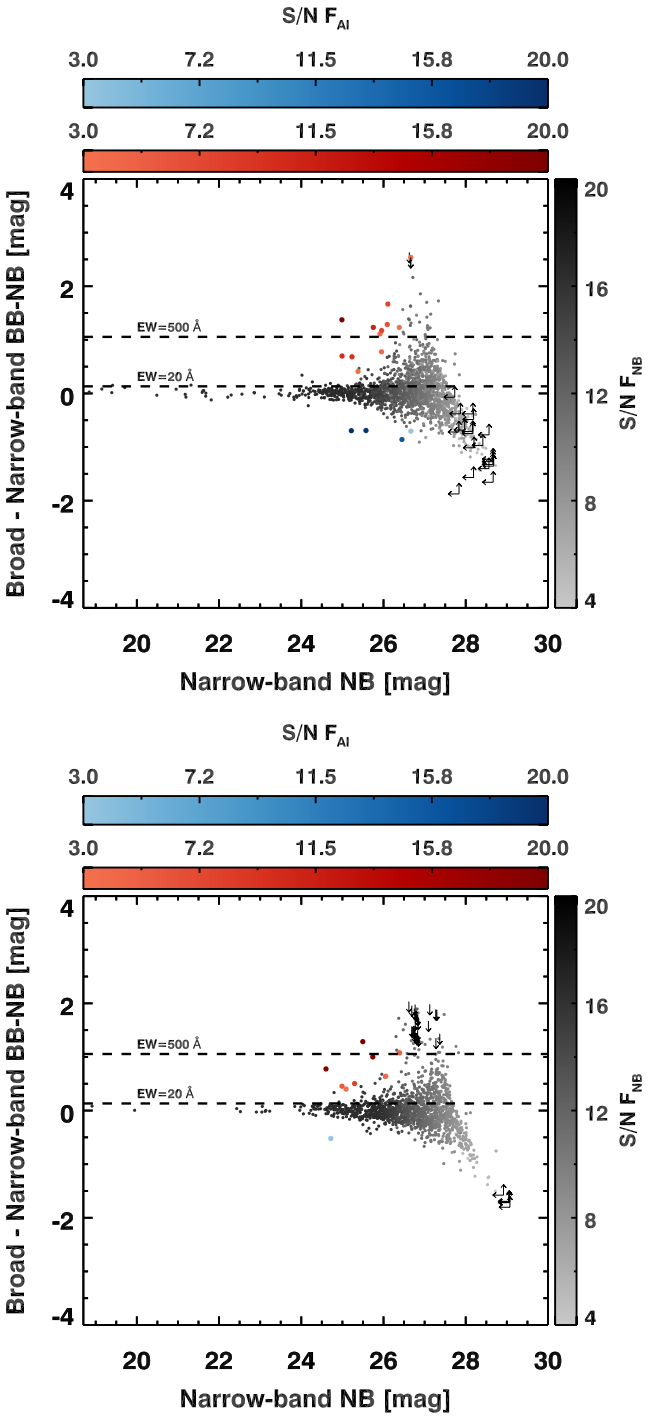

Figure 34 Color-magnitude diagrams for the left (upper panel) and right (lower panel) chips of the LRIS camera. Red and blue circles mark candidate Lyα emitters and absorbers (at 5σ significance), respectively. Arrows indicate 3σ upper limits on NB3640 and *U* magnitudes. Color intensities scale as the signal-to-noise ratio of the Lyα flux emission (red) and absorption (blue), or the NB3640 flux density (black). The black dashed lines mark the limit of EW(Lyα) = 20, 500 Å.

where F^{λ}_{NB}, F^{λ}_{U} are the NB3640 and U band flux densities and:

$$A = \int_{\lambda} T(\lambda)/T(\lambda_0) \tag{15}$$

is an "area" term linked to the filter transmission $T(\lambda)$ properties and λ_0 the observed Lyα wavelength. Note that few $M_\star > 10^{10}$ $M_\odot$ galaxies observed with Subaru/MOIRCS and part of the cluster stacked spectrum (ID #580, 510, 568, 422) are detected as Lyα absorber candidates.

4 MASS AND ENERGY INJECTION INTO THE INTRACLUSTER MEDIUM

In the current theoretical framework of structure formation, the massive, virialized clusters we observe in the local universe are the result of a hierarchical assembly of smaller subunits, whose halos detached from the Hubble expansion at different cosmic times, according to their initial density. Baryons, sensitive to the gravitational potentials of growing halos, are naturally dragged towards the concentrations of DM. When halos are massive enough, baryons are adiabatically compressed and shock heated to very large temperatures ($T \sim 10^7$ K) during their infall, finally setting to hydrodynamic equilibrium (Kravtsov & Borgani 2012). The energy baryons acquire is partially radiated away in the X-ray regimes through bremsstrahlung and line emissions, opening a crucial window for astrophysicists.

The gravitational infall is necessary to explain the high temperatures of the X-ray emitting gas, but it is not sufficient to justify the observed properties of the hot plasma. A good example is the entropy profiles of clusters. Entropy is a key quantity because it encodes information about every variation of energy occurred during the assembly of the structure and it is relatively easy to derive from X-ray observations, namely from the electron temperature and density ($S = k_B T / n_e^{2/3}$, where k_B is the Boltzmann constant). Chandra and XMM-Newton observations of cluster cores showed that entropy clearly deviates upwards from the trend expected in presence of simple gravitational infall of baryons, resulting from lower central gas densities than predicted, i.e., from the self-similar model (Vikhlinin et al. 2009; Sun et al. 2009; Pratt et al. 2010). This indicates that some non-gravitational processes are shaping the properties of the ICM. Pioneering attempts to explain the entropy excess in cluster cores introduced *pre-heating* of the ICM by SNae and AGN feedback at $z > 3$ (i.e., Kaiser 1991; Tozzi & Norman 2001), but predicting large isentropic cores and shallow pressure profiles not observed in real structures (Ponman et al. 2003; Arnaud et al. 2010). Alternatively, simple radiative cooling was brought up, since removing low entropy gas in the central regions and replacing with high entropy material flowing from the surrounding can mimic an entropy enhancement (Voit & Bryan 2001). Simulations implementing radiative cooling reproduced the entropy profiles, but catastrophically increasing the SFR

and stellar masses of the BCG (Kravtsov & Borgani 2012). Eventually, state-of-the-art cosmological simulations including radiative cooling *and* heating by SNae and AGN are approaching satisfactory representations of the group and cluster population at $z = 0$ (Le Brun et al. 2014; Pike et al. 2014). However, we still lack crucial empirical constraints on several aspects of the physical processes implemented in numerical simulations, especially concerning when and how the heating occurred, what is the role of SNae with respect to the enormous AGN feedback, the physical coupling with the ICM, and the role of cooling in auto-regulated feedback processes.

In this chapter I will apply simple statistical arguments to derive an estimate of the amount of energy that galaxies in CL J1449+0856 inject prior to or at the time of the observation at $z = 1.99$, evaluating the contribution of SFGs and AGN. The cue for this analysis is the ending point of Chapter 3, namely the need for a continuous supply of fresh gas to sustain the giant Lyα nebula in the core of the cluster against evaporation owing to the hot ICM. In Section 4.1 I will show that galaxies are plausible candidates to replenish the nebula through outflows. I will compute the instantaneous and integrated amount of energy injected in the ICM due to outflows in Section 4.2, proposing two alternative approaches and discussing possible caveats. A comparison with cosmological simulations is then enclosed in Section 4.2.1. Conclusions and reasonable expectations for forthcoming surveys are presented in Section 4.3.

This chapter is based on the article published in 2016 describing the detection of the giant Lyα nebula in CL J1449+0856 (Chapter 3, Valentino et al. 2016).

4.1 GAS REPLENISHMENT THROUGH GALAXY OUTFLOWS

In Section 3.3.2 we have shown that the giant Lyα nebula in the core of CL J1449+0856 must be constantly replenished of cold gas at a rate of $\gtrsim 1000\ M_\odot\ yr^{-1}$ in order to shine for timescales longer than ≈ 10 Myr. Replenishment of cold gas from the cosmic web is disfavored by current cosmological simulations (Figure 24 and Section 3.3.1, Dekel et al. 2009a), while strong cooling from the X-ray phase is likely to play a lesser role (Section 3.3.1). On the other hand, member galaxies are plausible candidates to supply the gas necessary to sustain the nebula through SNae- and AGN-driven outflows, a feature ubiquitously observed in high-redshift galaxies (i.e., Newman et al. 2012; Förster Schreiber et al. 2014; Genzel et al. 2014) and strongly supported by theoretical models and cosmological and zoom-in simula-

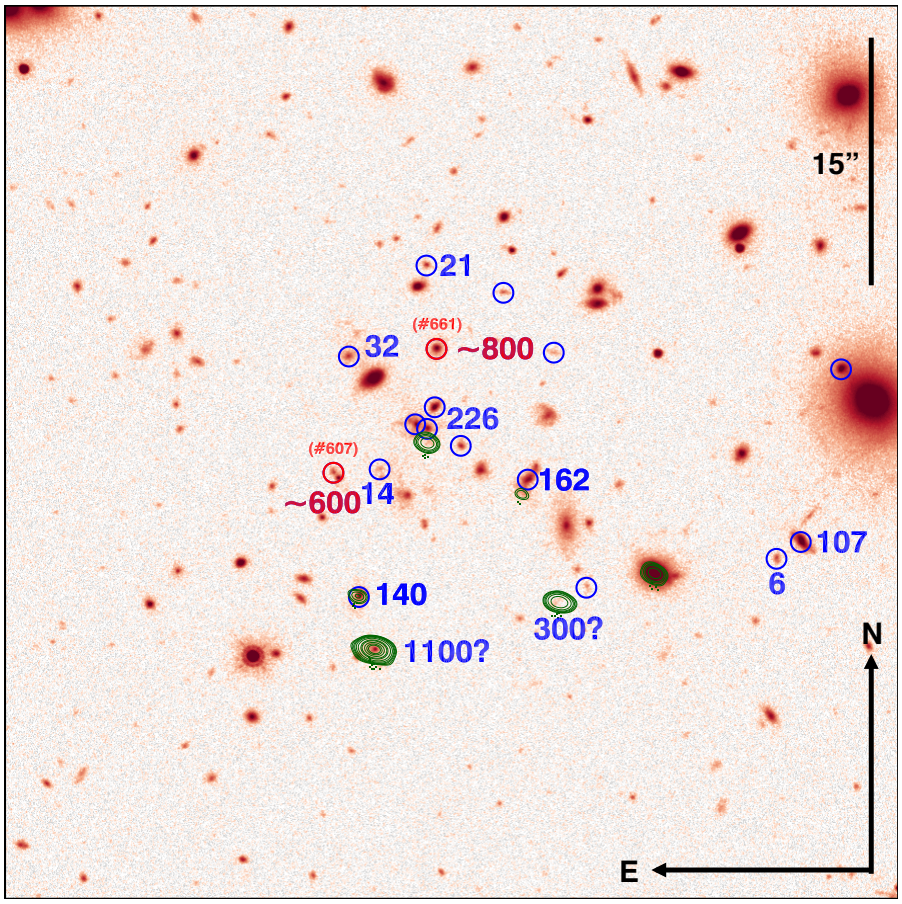

Figure 35 Map of the activity in the central cluster region. For each cluster star-forming (blue circles) or AGN (red circles) member in the *HST*/WFC3 F140W image, we indicate the indirect estimates of the outflow rate in $M_\odot$ yr^{-1} as derived in Section 4.1. When available, we provide the SFR estimated from the continuum at 870 μm from ALMA observations (green contours). Question marks denote outflow rates associated to ALMA sources without redshift confirmation and hence not included in our most conservative approach.

tions (i.e., Davé et al. 2008; Hopkins et al. 2012; Lilly et al. 2013; Gabor & Bournaud 2014). However, is the galaxy activity in CL J1449+0856's core sufficient to provide a minimal mass rate of $\gtrsim 1000\ M_\odot\ yr^{-1}$ as required by the Lyα nebula? To answer this question, we computed the total mass outflow rate, i.e., the amount of gas expelled by galaxies per unit time, considering both contributions from the observed SFR and AGN activity (Figure 35). We converted members' SFRs into mass outflow rates $\dot{M}_{out}$ by multiplying by a conservative mass loading factor $\eta = \dot{M}_{out}/SFR = 1$. This is likely to be a lower limit for the ionized and molecular gas expelled by galaxies, both observationally and theoretically (i.e., Newman et al. 2012; Hopkins et al. 2012; Gabor & Bournaud 2014; Hayward & Hopkins 2015). This order of magnitude is also necessary to explain the metal enrichment of the ICM. Indeed, the same amount of metals is locked into stars and distributed in the ICM, favoring the equality $\dot{M}_{out} \approx SFR$ (i.e., Renzini & Andreon 2014). The SFRs were derived either from SED modeling from our 13-band photometry (S13), Hα from our recent Subaru/MOIRCS follow-up (Valentino et al. 2015), or 870 μm continuum detection in ALMA maps applying a Main-Sequence galaxy template (Magdis et al. 2012). ALMA observations, reduction and analysis will be presented in a forthcoming paper (Strazzullo et al in prep.). The total SFR in the central region is $SFR \approx 1000\ M_\odot\ yr^{-1}$. An individual bright ALMA source stands out in the cluster field. Its 870 μm flux is $F_{870\mu m} = 5.5$ mJy, corresponding to a total infrared luminosity between $8-1000$ μm of $L_{IR} = 6.6 \times 10^{12}\ L_\odot$ and $SFR = 1100\ M_\odot\ yr^{-1}$ at $z = 1.99$ (Figure 35). The measurement errors are negligible with respect to the 0.15 dex uncertainty due to modeling (Strazzullo et al. in prep.). As there is no spectroscopic confirmation that the ALMA source is a member of the cluster, we have conservatively excluded it from the SFR accounting. We note that, if confirmed to be part of the cluster, this source would increase by a factor of $2\times$ the total SFR in the core.

The growth of black holes further contributes to the mass outflow rates. We estimated its order of magnitude by directly converting L_{bol} into mass outflow rates using the empirical calibration by Cicone et al. (2014):

$$\log(\dot{M}_{out}) = (-29.8 \pm 3.7) + (0.720 \pm 0.083)\log(L_{bol}) \quad (16)$$

In this case, we obtain ≈ 600 and $800\ M_\odot\ yr^{-1}$ for #607 and #661, respectively. Moreover, it appears that we have not captured the system during a phase of exceptional AGN activity. In fact, the integrated SFR/L_X ratio observed in the cluster core is close to the cosmic average value (Mullaney et al. 2012). The predicted X-ray luminosity is $\langle L_X \rangle = SFR \times 4.46 \times 10^{41}\ erg\ s^{-1} \approx 4.5 \times 10^{44}\ erg\ s^{-1}$, while the observed value from the two AGN is $3.4 \times 10^{44}\ erg\ s^{-1}$. We

remark that the calibration by Cicone et al. is based on a sample of local bright IR galaxies with previously known outflows, which, in principle, may overestimate the outflow rates if the relation captures a phase shorter than the AGN duty cycle. On the other side, contribution from phases other than molecular and the uncertain CO luminosity-to-gas mass conversion can increase the outflow rates derived with this calibration. Indeed, strong nuclear ionized winds are now observed in fractions up to 50-70% of high-redshift AGN (Harrison et al. 2015), showing how common these features are. Moreover, the calibration by Cicone et al. is in line with the expectations from simulations reproducing the relations among black hole and galaxy bulge masses or velocity dispersions. In terms of the ratio between the kinematic energy released by AGN per unit time and their bolometric luminosity, simulations usually assume a coupling efficiency $\epsilon_f \sim 0.05 - 0.15$ (i.e., Di Matteo et al. 2005; Le Brun et al. 2014, and Section 4.2.1 below). As we show in Section 4.2, the instantaneous kinetic energy associated with AGN and mass outflow rates estimated from the Cicone et al. relation is indeed $\sim 5\%$ of the observed bolometric luminosities. Therefore, all things considered, we do include an AGN contribution as detailed above in our fiducial estimate of the total mass outflow rate.

Therefore, adding up the contribution from star formation and AGN activity in the cluster core, we obtain a total mass outflow rate of $\gtrsim 1000\ M_\odot\ yr^{-1}$, compatible with the independent constraint derived from the Lyα nebula replenishment rate (Section 3.3.2). Galaxies thus inject a significant amount of gas into the ICM, largely enough to sustain the nebula. Moreover, we note that a secondary role of shocks in powering the Lyα emission is suggested by the reasonable agreement between the two replenishment estimates, which would be otherwise just incidental. We stress once more that, if shocks were dominating the Lyα emission, the estimate of the replenishment rate reported in Section 3.3.2 would not be valid, but we should resort to alternative working hypotheses to derive the mass of the Lyα nebula, i.e., pressure equilibrium and geometrical assumptions. However, the independent constraint on the energy injection by galactic winds presented in the following section would be unaffected.

4.2 ENERGY INJECTION INTO THE ICM

Together with mass, outflows extract energy from galaxies and then deposit it into the surrounding ICM through dissipation, shocks or turbulence. In the following sections we estimate the *kinetic* energy injection, neglecting alternative contributions, i.e. from radiation.

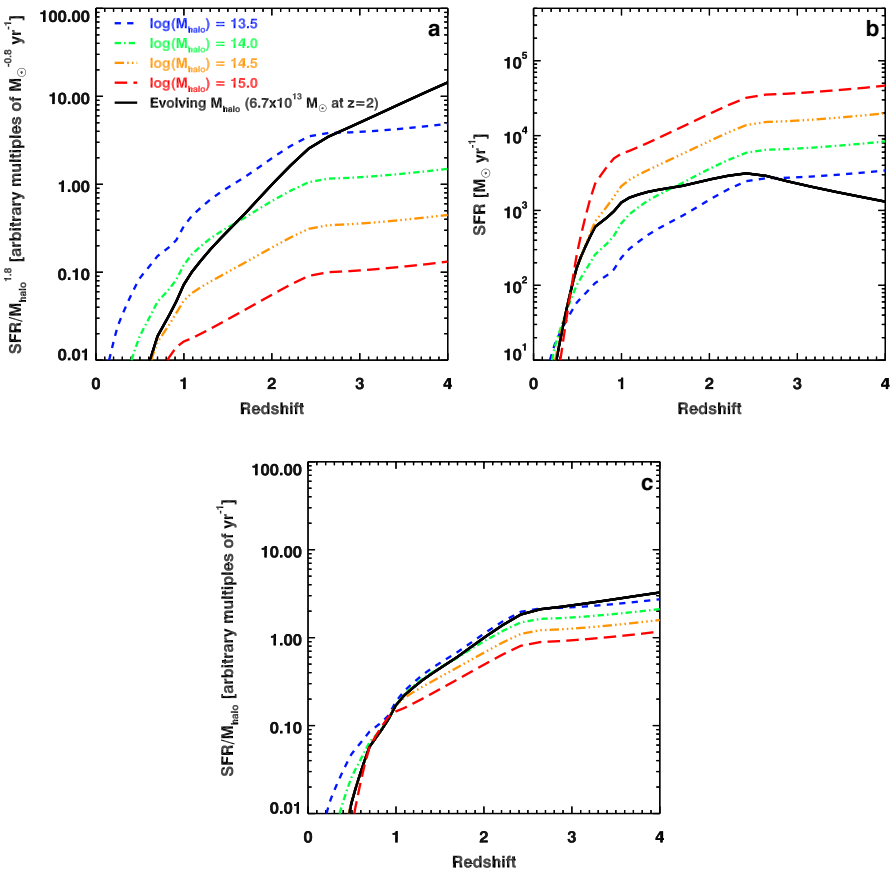

Figure 36 Expected efficacy of outflow energy injection as a function of halo mass and redshift. Based on the empirical mapping of the star formation and galaxy clustering evolution through cosmic time (Béthermin et al. 2013), we model the redshift evolution of the outflow energy injection over the thermal energy of the ICM (panel a). The mechanical energy injection scales as the integrated SFR in the halo, while the total thermal energy of the hot ICM increases as $E_{therm} \propto T_{vir} M_{gas} \propto M_{halo}^{1.8}$, assuming a gas fraction varying with the halo mass (Renzini & Andreon 2014). Hence, the y axis in panel a represents the 'efficacy' of the energy injection. In panel b we show the evolution of the SFR as a function of redshift and halo mass in Béthermin et al. (2013). The ratio SFR/M_{halo} changes slowly between $2 < z < 4$ (panel c).

Instantaneous injection

First, we can estimate the *instantaneous* injection of energy at the time of observation:

$$\dot{E}_{kin} = \frac{1}{2}\dot{M}_{out}v^2 \tag{17}$$

where $\dot{M}_{out}$ is the total amount of gas ejected per unit time at $z = 1.99$ by galaxies and v is the outflow velocity. We do not measure v in individual members in our sample, but its statistical average is quite well constrained by increasing samples of high-redshift observations. Therefore, our estimate of $\dot{E}_{kin}$ should be taken in a statistical sense. We assign a wind speed of 500 km s^{-1} to SN-driven outflows for each star-forming galaxy, while for AGN-driven outflows we assume a typical speed of 1000 km s^{-1} (Genzel et al. 2014; Förster Schreiber et al. 2014; Cicone et al. 2014). Given the baseline mass outflow rate in Section 4.1, we obtain $\dot{E}_{kin}(z = 1.99) \sim 5 \times 10^{44}$ erg s^{-1}. This energy is a factor of $20\times$ ($5\times$) larger than the observed Lyα (X-ray) extended luminosity. The $5\times$ factor with respect to the X-ray luminosity is sufficient to offset the global radiative cooling of the hot plasma. Assuming the balance between heating and the observed cooling rate as in local clusters would thus imply an energy injection $5\times$ lower than estimated above. However, net heating is necessary to justify the presence of the Lyα nebula, since the cooling from the X-ray globally occurs on long timescales and is not sufficient to explain the Lyα emission (Section 3.3.1). The injected energy is coming predominantly from AGN activity ($\sim$ 85%) with a non-negligible contribution from star formation ($\sim$ 15%), while, in terms of mass, AGN are responsible for up to 2/3 of the total gas released into the ICM. SFGs would dominate the mass and energy injection only if we largely overestimated the contribution from AGN. We note that CL J1449+0856 is not anomalous in terms of star formation activity with respect to potentially similar structures at comparable redshift (i.e., Tran et al. 2010; Yuan et al. 2014; Santos et al. 2015; Gobat et al. 2015) and it is globally consistent with the tracks reported in Figure 36 based on the model by Béthermin et al. (2013). The instantaneous energy input from AGN corresponds only to $0.05\,L_{bol}^{AGN}$, a factor of $3\times$ lower than typically assumed in simulations (Section 4.2.1), supporting the estimate of the mass outflow rates reported in Section 4.1, while from star formation it is just $0.003\,L_{bol}^{SFGs}$. In general, given the SFR/L_X cosmic average (Mullaney et al. 2012) and the adopted calibrations, we expect AGN outflows to provide $5-10\times$ more energy than winds induced by star formation.

Integrated energy injection

We can now estimate the *total* energy injection up to $z = 1.99$, integrating $\dot{E}_{kin}$ over time prior to observation:

$$E_{kin} = \int_{t(z \geqslant 1.99)} \dot{E}_{kin}\, dt \tag{18}$$

For simplicity, we assume that the *instantaneous* energy injection is proportional to the SFR:

$$\dot{E}_{kin} = \beta\, SFR \tag{19}$$

where $\beta(z = 1.99) \sim 1.6 \times 10^{49}$ erg $M_{\odot}{}^{-1}$. Then from Equation 18:

$$\begin{aligned} E_{kin} &= \int_{t(z \geqslant 1.99)} \beta\, SFR(t)\, dt \\ &= \frac{\beta}{1-R} \int_{t(z \geqslant 1.99)} SFR(t)(1-R)\, dt \\ &= \frac{\beta}{1-R} M_{\star} \end{aligned} \tag{20}$$

where $M_{\star}$ is the total stellar mass of 2×10^{12} $M_{\odot}$ observed at $z = 1.99$ (Section 3.1.4 and S13) and $R = 0.4$ is the mass return into the interstellar medium (Bruzual & Charlot 2003). Eventually, we obtain $E_{kin} \sim 5 \times 10^{61}$ erg. Considering a universal baryon fraction of $f_b = 0.15$ in the ICM (Planck Collaboration et al. 2014), the total energy per particle in the hot ICM then is ~ 2 keV. This value is $\sim 10\%$ of the binding energy of the halo at $z = 1.99$ and of the same order of magnitude in cluster progenitors. Hence, part of the ICM particles might have been expelled by the structure at some early stage. The integrated energy is also comparable with the thermal energy per particle $E_{therm} = 3/2\, k_B\, T$. Indeed, assuming virialization, $k_B T = k_B T_{vir} = G M_{halo} \mu m_H / 2 R_{vir} \sim 1.9$ keV and, thus, $E_{therm} \sim 2.8$ keV. This is an order of magnitude estimate, as the structure is unlikely to be fully virialized at this stage – simulations suggest a thermodynamic temperature $15 - 20\%$ smaller than T_{vir} (Section 4.2.1). We stress here that our estimate of the integrated energy injection is affected by uncertainties on the total mass outflow rate, outflow velocities, the halo mass, and its baryon content and it depends on the assumptions we described. All things considered, the estimate may well increase or decrease by a factor of ~ 0.5 dex.

This approach relies on the use of $M_{\star}$ in CL J1449+0856 as a proxy for the total mass ejected through outflows in the past. This presumes the adoption of a mass loading factor of $\eta = 1$ and that v depends on local galaxy properties not evolving with time. The advantage of using $M_{\star}$ is the straightforward inclusion of the contribution to

the energy injection by galaxies active in the past, but observed to be passive at $z = 1.99$. However, there are two important assumptions behind this results: first, we suppose that the total AGN mass outflow rate is proportional to the total SFR at any time and, second, that β is constant with time.

Caveats

We justify the first assumption considering that SFR and AGN activity are correlated (Mullaney et al. 2012): statistically, on large samples the average AGN X-ray luminosity is equal to $\langle L_X \rangle = SFR \times 4.46 \times 10^{41}$ erg s^{-1}. Nevertheless, the AGN mass outflow rate might depend non-linearly on the AGN luminosity. For example, in the empirical relation by Cicone et al. (2014), $\dot{M}_{out} \propto L_{bol}^{b}$ with $b = 0.72$ (Equation 16). From Equation 17, this non-linear term becomes:

$$\dot{E}_{kin}^{AGN} = \frac{1}{2}\dot{M}_{out}^{AGN} v_{AGN}^2 = k_1 L_X^{0.72} = k_2 SFR^{0.72} \tag{21}$$

where k_1 and k_2 are constants including the bolometric correction linking L_X and L_{bol}, the velocity term $v^2/2$, and the coefficients in the Cicone et al. (2014) and Mullaney et al. (2012) relations. Simply combining Equation 19 and Equation 21, we obtain:

$$\beta = c_1 + c_2 SFR^{0.72-1} \tag{22}$$

where c_1 and c_2 are constants. Thus, the non-linear term introduced by the AGN mass outflow rate impacts our result only when the total SFR in the progenitors of CL J1449+0856 drops significantly. Equation 22 justifies also our second main assumption that β is roughly constant with time, depending only on numeric constants and the total SFR in all the cluster progenitors.

Does the total SFR in the cluster progenitors evolve with redshift? At $z > 1.99$ the SFR is spread over several subhalos that will form the observed cluster by merging. Here we trace the growth of individual dark matter halos from simulations using the Fakhouri et al. (2010) model. According to Béthermin et al. (2013), *in each subhalo* the total SFR peaks at $z \sim 2$ and then slowly decreases (black curve in Figure 36, panel b). However, to compute the total SFR contributing to the energy injection over time we have to consider *all* the subhalos. This corresponds to normalizing the individual SFR to the halo mass at each redshift (Figure 36, panel c). In this case, the function $X(z) = \langle SFR(z) \rangle / M_{halo}(z)$ mildly increases with redshift. Thus, the non-linear term in Equation 22 becomes less important at increasing redshift.

Final remarks

We attempted an alternative estimate of the total kinetic energy purely base on the tracks in Figure 36. We obtain $E_{kin} \sim 5 \times 10^{61}$ erg released by galaxies over $2 < z < 4$ computed as:

$$E_{kin} = \frac{1}{2}\dot{M}_{repl}v^2 \int_{t(z=4)}^{t(z=2)} \frac{X(t(z))}{X(t(z=2))}\, dt \tag{23}$$

where the function $X(z) = \langle SFR(z)\rangle / M_{halo}(z)$ accounts for the expected flat trend of $\langle SFR\rangle$ at $2 < z < 4$ and incorporates the integrated activity spread in halo progenitors of lower masses (Figure 36, panel c). The net effect of the integral is an increase of the time interval, from 1.7 Gyr between $2 < z < 4$ to 4.4 Gyr. This result is consistent with the one presented above, providing ~ 2 keV per particle in the hot ICM, assuming a universal baryon fraction $f_b = \Omega_b/\Omega_m = 0.15$. Here we limit the integral to $z = 4$, before which the masses of individual progenitor halos rapidly become similar to individual galaxy halos ($\approx 1 \times 10^{13}$ $M_\odot$ following Fakhouri et al. 2010). At these masses, fast winds would have easily expelled the material from the halo, that later would have been reaccreted with the halo growth. However, observed properties of local structures may disfavor this *pre-heating* scenario for energy injection (Ponman et al. 2003). We note that the tracks in Figure 36 are calibrated on the observed stellar mass function of passive and star-forming galaxies residing in halos of masses of $10^{11.5} < M_{halo} < 10^{13.5}$ $M_\odot$ at high redshift. However, the model does not assume any environmental dependence of galaxy properties, prominent at lower redshift. The transformation of *cluster* galaxies into red, passive, early-type systems at low redshift makes the predicted SFR a likely overestimation at $z \lesssim 1.5$ (Popesso et al. 2015). Below $z \sim 1.5$ the outflow energy contribution to the ICM is expected to be negligible with respect to the internal energy, as shown in Figure 36. We remark here that we do not make any prediction on the later growth of a massive central galaxy and its associated black hole, whose "radio" maintenance feedback looks necessary to avoid overcooling in the cluster core (McNamara & Nulsen 2007; Fabian 2012; Gaspari et al. 2012).

4.2.1 Comparison with cosmological simulations

We compared our observational results with the total energy injected by black holes into the ICM of systems similar to CL J1449+0856 at $z = 2$ in simulations. We used the two models from the suite of hydrodynamic cosmological simulations presented in Le Brun et al. (2014), which form an extension to the Overwhelmingly Large Simulations project (OWLS, Schaye et al. 2010). The first is a standard non-radiative model (NOCOOL), while the second further includes prescriptions for metal-dependent radiative cooling, star formation, stel-

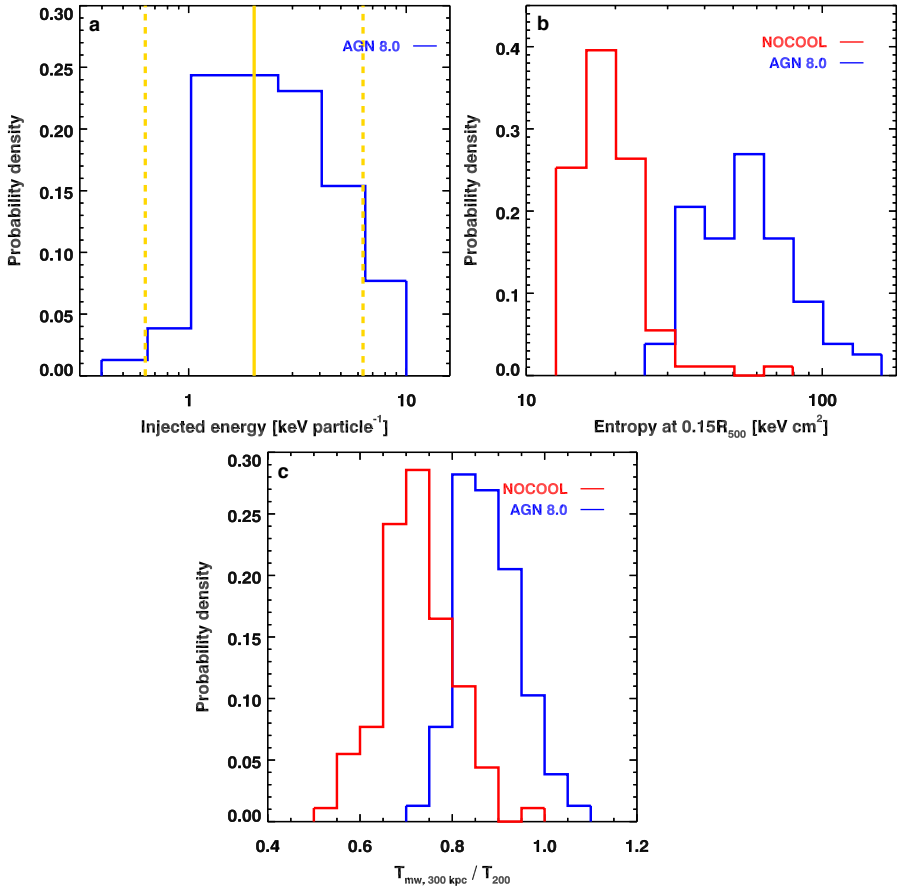

Figure 37 Temperature and entropy increase in $z = 2$ clusters when AGN feedback is active in simulations. We show the distribution of the energy per particle injected in $M_{200} = (5-7) \times 10^{13}\ M_\odot$ systems at $z = 2$ when AGN feedback is turned on in our suite of cosmo-OWLS simulations (panel a) and its effect on the mass-weighted temperature within 300 kpc in units of the virial temperature kT_{vir} (panel b) and entropy at $0.15R_{vir}$ (panel c). Blue lines indicate the reference AGN 8.0 feedback model, while red lines mark the non-radiative model (Le Brun et al. 2014). The yellow lines in panel a show our fiducial estimate of ~ 2 keV per particle from observations and a 0.5 dex uncertainty.

lar evolution, mass loss, chemical enrichment, stellar feedback, and AGN feedback. Among the models described in Le Brun et al. (2014), we selected the AGN 8.0 model as it provides the best match to the X-ray, Sunyaev-Zel'dovich, and optical observations of local groups and clusters (Le Brun et al. 2014; McCarthy et al. 2014). In these two models, we selected the halos with $M_{200} = (5-7) \times 10^{13}\ M_{\odot}$ at $z = 2$ (yielding respectively 79 and 91 such systems in the AGN 8.0 and NOCOOL physical models). For each of these structures, we computed the mass-weighted temperature within a 300 kpc aperture, the mean entropy $S = kT/n_e^{2/3}$ within $0.15\ R_{500}$, the virial temperature $k_B T_{vir}$, and the binding energy. The energy injected by all the black holes lying within R_{500} is $E_{inj} = M_{BH}(< R_{500})c^2 \epsilon_f \epsilon_r/(1-\epsilon_r)$, where $\epsilon_r = 0.1$ is the radiative efficiency of the black hole accretion disk, $\epsilon_f = 0.15$ the efficiency of the coupling of the AGN feedback to the gas, and c the speed of light. We estimate the average injected energy per particle assuming $f_b M_{500}/\mu m_p$ baryonic particles in the ICM, where $f_b = 0.15$ is the universal baryon fraction (Planck Collaboration et al. 2014), $\mu = 0.6$ is the mean molecular weight, and m_p the proton mass. We obtain that the mean injected energy is of the order of 8×10^{61} erg (≈ 2.8 keV per particle, Figure 37, panel a), which is of the same order of magnitude as the typical binding energy of the selected systems. Using M_{200} instead of M_{500} in the definition of the number of particles reduces the estimate by a factor $1.4\times$. However, we stress that this is a rough estimate of the overall effect on the whole ICM, while in the simulations the energy injection is effective mostly in a small region surrounding the AGN. All things considered, this estimate is fully consistent with our observational observational estimate of ~ 2 keV per particle. The mean temperature increases from 1.44 keV to 1.73 keV when efficient AGN feedback is included (Figure 37, panel b). Moreover, the entropy within $0.15\ R_{500}$, tracing non-gravitational heating and cooling, increases from 19.9 keV cm^2 to 58.0 keV cm^2 (Figure 37, panel c). As the mean baryonic fraction within R_{500} decreases from 14% in the non-radiative model to 10.7% in the AGN 8.0 model, some of the gas which should have been contained within R_{500} in the absence of AGN feedback has been ejected, similarly to what was previously found for progenitors of $z = 0$ groups (McCarthy et al. 2011, but see Pike et al. 2014 who find that most of the AGN feedback energy is released at $z < 1$ in their simulated clusters). Overall this set of cosmological simulations predicts an energy injection due to AGN of the same order of magnitude of our estimate based on the average properties of galaxy outflows.

4.2.2 Future Lyα surveys of high-redshift clusters

The energy injection scenario based on galaxy outflows replenishing huge gas reservoirs of cold and warm gas should apply for struc-

tures similar to CL J1449+0856 and comply with the general increase of star formation and AGN activity observed in high-redshift galaxies. Moreover, we suggest a possible connection between galaxy outflows and huge Lyα nebulae in cluster cores, so that the latter could effectively trace the energy injection at high redshift. Do we thus expect to see giant Lyα nebulae in all massive cluster progenitors? The answer could be negative. In fact, AGN activity – which illuminates the gas expelled through outflows and keeps it ionized – might be a prerequisite for the presence of Lyα systems. Absent a powerful ionizing source, dense environments hosting strong star formation activity might not show any extended Lyα blob. This might be the case for the massive halo inside the proto-cluster region at $z = 3.09$ in the SSA22 field (Steidel et al. 2000; Kubo et al. 2015). A statistical assessment of the number of active galaxies in clusters at each stage of their evolution is important to address this issue. Nevertheless, galaxy outflows remain an ubiquitous feature of high-redshift galaxies. Are the massive gas reservoirs replenished by outflows destined to collapse and form stars according to their cooling and free-fall time? The gas in outflows is not at rest by definition. Moreover both simulations (Bournaud et al. 2014) and observations (Martin & Bouché 2009) show that outflows accelerate at larger radii because of pressure gradients in steady-state flows. This results in long collapse timescales, possibly preventing the formation of stars spread over several tens of kpc. The assembly of larger samples of clusters progenitors will allow to test these predictions.

4.3 CONCLUSIONS

In this chapter we argued that the gas necessary to sustain the Lyα nebula against evaporation in the core of CL J1449+0856 at $z = 1.99$ (Chapter 3) might be provided by galaxies through massive outflows. In particular:

- From the observed total SFR and AGN bolometric luminosities, we derived mass outflow rates applying simple statistical and empirical arguments. We find that generous outflows driven by SNae ($\approx 1000\ M_\odot\ yr^{-1}$) and growing black holes ($\approx 1400\ M_\odot\ yr^{-1}$) are sufficient to replenish the nebula
- The expulsion of high velocity matter from galaxies can drive a significant injection of kinetic energy into the ICM of the order of ~ 2 keV per particle
- We obtain a reasonable agreement between our empirical estimate for the injected energy and the predictions from the state-of-the-art cosmo-OWLS simulations and with constraints set by the thermodynamic properties of local massive structures

- We find that in our baseline scenario the AGN channel provides $\sim 85\%$ of the total injected energy and $\sim 66\%$ of the mass, with the rest supplied by star formation through SNae-driven winds
- The instantaneous energy injection at $z = 1.99$ exceeds by a factor of $5\times$ the current X-ray luminosity, offsetting the global cooling from the X-ray phase. Moreover, the integrated energy injected at high redshift (prior to $z = 2$) is significant, as found in the cosmo-OWLS simulations.

However, the high star formation and black hole accretion rates deep in the potential well of this cluster support the general increase in galaxy activity observed in similar structures at comparable redshift, and challenge the current prescriptions on the fueling by cosmological cold flows penetrating in massive halos. If this structure is not just a curious anomaly, the potential presence of cold streams despite its high mass would lead to important consequences on the "halo quenching" mechanism and, thus, on galaxy formation and evolution in general. If the scenario we propose here is correct, ongoing spectroscopic follow-up of the Lyα nebula in CL J1449+0856 should reveal signatures of complex motions due to outflows and to be fairly metal-rich. Eventually, the arising coherent scenario we sketch could help to understand the global early evolution of massive structures.

5 FUTURE PERSPECTIVES

In the previous chapters, I have presented the result of the last three years of work that has already been published. This work pivoted around the study of the cluster CL J1449+0856 at $z = 1.99$ and, in particular, of the processes regulating the inflow and outflow of gas from cluster members during an epoch profoundly different from the one we witness at lower redshift. The much larger amount of cold and warm gas available inside and outside galaxies at $z = 2$ is a key to interpret the two main results of this thesis presented in Chapters 2 and 3, and it marks a major difference with respect to galaxy clusters at lower redshift. In particular, the low metal content and enhanced sSFR in massive SFGs presented in Chapter 2 would be naturally explained by copious *inflow* of gas into galaxies. In this respect, the emission of Lyα photons on large scales might just be the bright tip of the available cold gas reservoirs in the ICM. On the other hand, strong star formation and AGN activities drive *outflows* that might sustain the Lyα nebula itself (Chapter 3). This internally-driven feedback was presented as the possible source of a *positive* energy and mass injection into the ICM in Chapter 4. However, SNae and AGN *negative* feedback may well be at the origin of the simultaneous presence of passive and star-forming galaxies in the cluster core and an active quenching mechanism in the most massive members. Indeed, the quiescent galaxies in CL J1449+0856 are more massive than $M_\star = 10^{11}\ M_\odot$, the threshold above which galaxies are observed to be passive in any environment at $z = 0$ (Figure 3). Hence, environmental effects might not be the main cause of quenching in CL J1449+0856. The classical view of ram pressure and tidal stripping as mechanism depriving galaxies of the gas necessary to form stars has been briefly introduced in Section 1.2.2. However, this view is largely based on observations of rich, massive, and completely virialized clusters in the local Universe, while at progressively higher redshift both empirical evidence and theoretical modeling are currently anecdotal or totally absent, as at $z = 2$. Admittedly, the data about CL J1449+0856 do not allow us to escape this situation, nor to place any significant constraint on these mechanisms. Nonetheless, physical intuition might guide us through environmental quenching processes at high redshift. First, the universal density increase with redshift should boost the efficiency of ram pressure stripping in high-redshift structures, at fixed halo mass. On the other hand, the gas mass in galaxies dramatically increases with redshift, too, impacting the internal dynamics of galaxies and the process of full stripping of

the reservoirs through ram pressure, given the higher galaxies surface densities. However, if both galaxies' internal densities and the ICM density increase by the same factor with redshift (i.e., the overall density enhancement of the Universe), the density contrast driving the ram pressure stripping does not vary. Note also that the typical gas depletion timescales at $z \sim 2$ ($t_{dep} \sim$ few 100 Myr, Daddi et al. 2010) is shorter than the crossing time on which the ram stripping operates (for CL J1449+0856: $t_{cross} \sim 1.2$ Gyr, considering $R_{vir} = 0.5$ Mpc and a velocity dispersion of 800 km s^{-1}, Section 3.1.4). Thus, the gas is converted into stars faster than how is potentially stripped by ram pressure. Moreover, this process is very influential in the deep potential wells of massive clusters, while at group-like halo masses – as the one of high-redshift structures – it loses part of its strength. In addition, ram stripping primarily affects low-mass galaxies, which are never considered in the analysis presented in the previous chapters. In fact, the main results of these quantitative studies based on photometric, MOIRCS, and ALMA follow-ups are limited to "normal", upper main-sequence, massive galaxies ($\geqslant 10^{10}$ $M_{\odot}$ at $z = 2$). As a final remark, we note that, if significant ICM heating occurs at high-redshift, simultaneously lowering its average density as in the scenario presented in Chapter 4, the efficiency of ram pressure stripping significantly drops even in low-redshift cluster descendants (Fujita 2001), consistently with a limited impact of this process in CL J1449+0856.

Galaxy-galaxy and galaxy-cluster gravitational interactions would benefit from the lower velocity dispersion in high-redshift structures and they would be a viable way to "pre-process" galaxies and drive quenching even before the assembly of massive clusters. However, the massive SFGs presented in Chapters 2 and 4 do not show any strong signature of ongoing quenching possibly due to gravitational interactions. On the other hand, Section 2.5.2 presents an alternative positive effect of such interactions between gas-rich, high-redshift cluster members and proposes them as a possible physical explanation for the spectral properties of galaxies in CL J1449+0856.

These brief remarks are certainly not exhaustive, but they attempt to show how the evolving conditions of galaxies, clusters, and the Universe as a whole might reverse our conception of the same physical mechanisms at different redshift. Notwithstanding that, a coherent temporal evolution of clusters and galaxies *must* arise in any model aspiring to describe these objects. Focusing on the first of the main topics of this thesis, we mentioned in Chapter 2 that the metal content of local galaxies does not or mildly depends on the environment, mainly depending on the sample selection (Mouhcine et al. 2007; Cooper et al. 2008; Ellison et al. 2009; Hughes et al. 2013; Peng & Maiolino 2014), a trend observed also in some higher redshift

clusters (i.e., Sobral et al. 2016; Tran et al. 2015). This might be just in apparent contradiction with the low metal content in CL J1449+0856's members, as an enhanced SFR due to rapid gas infall is likely to enrich the ISM on short timescales. Moreover, the cluster core should be already unreachable by dense streams further reducing the metal content and postponing the re-enrichment through star formation, according to current cosmological simulations (Dekel et al. 2009a). On the other hand, if the low metal content of galaxies residing in CL J1449+0856 is due to gravitational interactions, the same effect should be visible at any redshift and, indeed, there are indications that close pairs and post-mergers are more metal poor than isolated galaxies in the SDSS (Ellison et al. 2013). However, even in this case, the same gas infall initially diluting the metal content is likely to trigger episodes of intense star-formation, which enriches the ISM and can drive these galaxies back to the mass-metallicity relation of typical field objects. In other words, both mechanisms presented in Section 2.5.2 might act on short timescales and be more likely at high redshift, while their effects can be erased by the simple growth of stellar mass and metal enrichment through star formation, leading to the situation observed – and still debated – of the local Universe.

For what concerns the second main topic of this thesis, the presence of large cold gas reservoirs, shining through the emission of Lyα photons, in the space between cluster galaxies, we spent Section 3.3.1 to show how low-redshift nebular filaments in cool-core clusters might not be easily connected to high-redshift giant Lyα nebulae, even if this suggestion remains tempting and certainly deserves further investigation. Also the energy injection scenario proposed in Chapter 4 presumably concerns structures only at high redshift. We refrained from discussing the "maintenance" mode owing to powerful radio-galaxies and AGN in the core of local clusters, which is necessary to avoid overcooling, simply because we could not place any constraints on it with the data and the analysis we carried out.

It is, thus, clear that a deeper investigation about these subjects is necessary to shed light on several aspects. Therefore, besides working at the projects presented above, I dedicated a substantial fraction of my time to thinking how to improve and build on these findings and to develop independent plans that could benefit from the expertise I have gained during my thesis. In the following, I will introduce ongoing and forthcoming projects based on successful observational proposals and collaboration with large science teams.

5.1 A COMPLETE CENSUS OF STAR-FORMATION IN CL J1449+0856

The study of star-formation occurring in CL J1449+0856's members has been central in Chapters 2 and 4. The excellent photometric and spectroscopic coverage of the field allowed for estimating accurate SFRs from SED modeling (S13), Hα fluxes (Valentino et al. 2015), and ALMA 870 μm observations (Strazzullo et al. in prep.), complementing the shallow *Spitzer* 24 μm and Herschel/PACS and SPIRE available data. However, spectroscopic incompleteness might bias the results from near-IR spectroscopy (Section 2.5.1), while confirmation of the ALMA detected sources is highly desirable to fully exploit the information from the dust continuum emission. To these aims, in collaboration with the co-authors of my articles (Valentino et al. 2015, 2016), I proposed a new spectroscopic follow-up of CL J1449+0856. In Period 95, we obtained 7.5 hours of VLT/KMOS time to target in *K* band all the confirmed star-forming members with $10^{10} \leqslant M_\star \leqslant 10^{11}$ $M_\odot$, including the two objects not followed up with Subaru/MOIRCS 2.5.1. Moreover, we targeted several other candidate members within 1 Mpc from the cluster center, in the same stellar mass range, and classified as star-forming according to their UVJ rest-frame colors (Wuyts et al. 2007; Williams et al. 2009). Finally, we dedicated part of the IFUs to the ALMA and Herschel-detected sources in the field, in order to identify possible counterparts. These *K* band KMOS observations have been carried out in April 2015 and are currently in phase of reduction. Once completed the analysis, (i) we will test the metallicity deficit in cluster individual star-forming members and its tentative correlation with an enhanced sSFR, by measuring the [N II]/Hα ratio and coupling it with [O III] and Hβ fluxes from WFC3 slitless spectroscopy, when available; (ii) we could confirm the redshift of all the remaining candidate star-forming members above 10^{10} $M_\odot$, reaching a full spectroscopic coverage of the $\sim$ 90% complete sample of cluster members in this mass regime (S13); (iii) we could estimate the total SFR with a homogeneous indicator, i.e., the Hα flux, compare the relative contribution of obscured and unobscured star-formation in a high-density environment, and investigate the possible reversal of the SFR-density relation (Elbaz et al. 2007; Tran et al. 2010; Santos et al. 2015); (iv) we will test recent suggestions from about a possible substantial contribution of $M_{halo} \sim 5 \times 10^{13}$ $M_\odot$ structures to the cosmic SFR at $z \lesssim 1.5$ (Popesso et al. 2015), but pushing the redshift limit up to $z \sim 2$, at the peak of the cosmic star formation history. (v) following up the central region of the extended Lyα nebula and the offset intracluster light in *H* band (Di Mauro et al. in prep.), we could detect possible extended optical emission lines (i.e., Hα), allowing for a physically characterization of the state of the ionized gas.

5.2 HIGH-REDSHIFT MATURE CLUSTERS

In the introduction I have mentioned different techniques to identify high-redshift structures and the unavoidable biases they introduce in the population they are sensitive to (Section 1.3). In the collaborative work presented in Strazzullo et al. (2015), we proposed to use the presence of massive, red galaxies in a forming red sequence to isolate structures similar to CL J1449+0856. Based on very accurate photometric redshifts tuned and verified on a new spectroscopic sample of 46 spectroscopic quiescent galaxies in COSMOS (Onodera et al. 2012), we selected quiescent galaxies selected from their UVJ and BzK colors and built local density maps in narrow redshift slices by means of the fifth nearest indicator Σ_5. We note that the spectroscopic sample is a crucial new element to provide accurate mapping. Strazzullo et al. (2015) isolated the three most prominent overdensities at $1.5 < z < 2.5$ and proposed them as potential mature cluster candidates, given the selection technique (Figure 38). In Period 94, we proposed and obtained 5 hours of VLT/KMOS time to follow-up the strongest overdensity of quiescent galaxies at $z > 2$ in the whole COSMOS 2 deg^2 field, with a significance of $> 8\sigma$ in the map (Figure 38, right panel). This candidate contains at least 4 massive ($> 10^{11}$ $M_\odot$, Salpeter IMF) quiescent galaxies at a concordant photometric redshift within a radius of 150 kpc, as expected for a relatively massive young cluster at this redshift similar to CL J1449+0856. Thanks to a combination of redshifts from the zCOSMOS project (Lilly et al. 2007, 2009) and of the Subaru/MOIRCS Mask 3 presented in Section 2.2 (Table 1), we have the first evidence of a redshift spike at $z \sim 2.2$ (Figure 39) from star-forming galaxies around the passive galaxy overdensity, and fully consistent with their estimated photometric redshifts. The KMOS K band observations we proposed aimed at unambiguously confirm the structure through its star-forming population. We selected a sample of 34 high-priority candidate members identified within a radius of 1 Mpc (2′ at $z = 2.2$) from the center of the overdensity of passive galaxies based on their UVJ rest-frame colors, with a photometric redshift consistent with $z = 2.2$ (Ilbert et al. 2013), and with an estimated Hα observed flux larger than 10^{-17} erg cm^{-2} s^{-1} as estimated from the SFR derived from the SED fitting we performed on UltraVISTA photometry (Muzzin et al. 2013). The Hα flux estimates were checked and calibrated against a sample of nearly 300 star-forming galaxies at $1.3 < z < 1.7$ with available spectroscopy from the FMOS-COSMOS Survey (Kashino et al. 2013; Silverman et al. 2015), and further verified on a small sample of $z \sim 2$ galaxies from our Subaru/MOIRCS program. Only half of the observations were completed before the end of Period 94 and, thus, only part of the selected sample has been effectively followed-up. The cube reduction is currently ongoing. When completed, the analysis will be an impor-

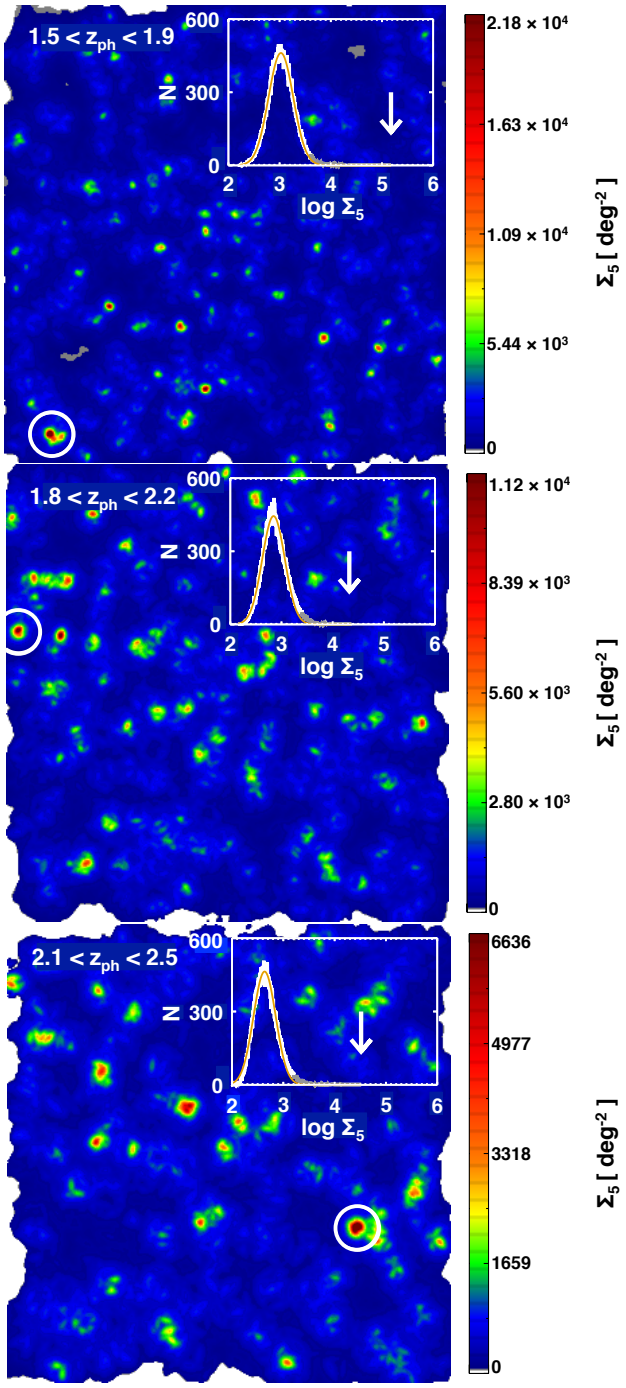

Figure 38 Examples of Σ_5 maps in redshift slices of the full passive galaxy sample in the 2 deg^2 COSMOS field (North is up, East is left). Maps are scaled so that red colors correspond to $> 5\sigma$ significance. The three cluster candidates identified as overdensities of passive galaxies are highlighted with white circles (2 proper Mpc radius). In each plot, the inset shows the distribution of $\log(\Sigma_5)$ values in the map and its Gaussian fit (white and orange lines, respectively), and the white arrow shows the peak Σ_5 value of the highlighted overdensity. The bottom panel shows the overdensity followed up with KMOS in Period 94. From Strazzullo et al. (2015).

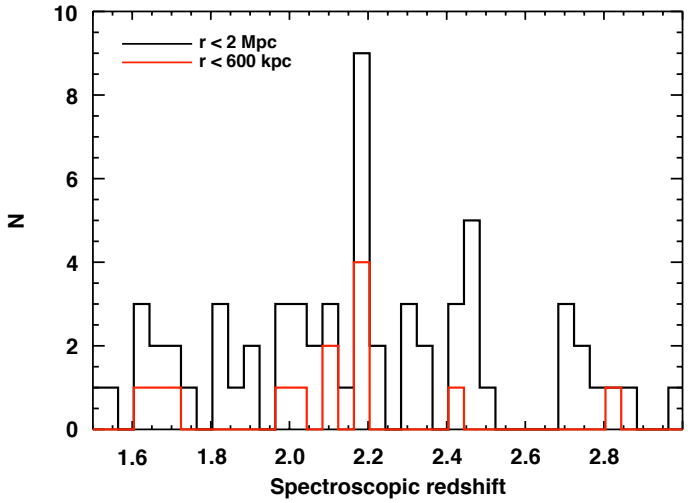

Figure 39 Spectroscopic redshift distribution around the candidate cluster at $z \sim 2.2$. Red and black lines enclose spectroscopic star-forming galaxies within 600 kpc and 2 Mpc proper radii, respectively. A clear spike is visible at $z \sim 2.18$, with a secondary prominent peak at $z \sim 2.43$ but less spatially correlated with the overdensity of passive galaxies.

tant step to evaluate the reliability of this cluster selection technique and the base for further follow-up of the quiescent population more easily accessible from space (G13, Newman et al. 2014). Moreover, it will open the possibility to directly compare CL J1449+0856 with a similar structure in terms of galaxy population, even if an X-ray detection is currently beyond the limit of the dataset available in COSMOS. The follow-up with KMOS will provide [N II] and [S II] lines in addition to Hα, allowing for investigation of the star-formation and the physical properties of the ISM as presented in Valentino et al. (2015).

5.3 SPECTROSCOPY OF THE GIANT LYα NEBULA IN CL J1449+0856

The giant Lyα nebula presented in Chapter 3 has been detected through narrow-band imaging with Keck/LRIS. This technique is extremely powerful to evaluate the total flux of the nebula, its morphology, position, and extension, but it misses important physical properties that can be assessed with a full spectrum covering the Lyα transition and the UV rest-frame wavelength. However, only very few available instruments can efficiently carry on observations at wavelengths close to 3600 Å, where Lyα emission from the nebula at $z = 1.99$ falls, due to the severe cut of transmission of the atmosphere. In Period

95, I proposed a spectroscopic follow-up with the Multi-Unit Spectroscopic Explorer (MUSE, Bacon et al. 2010) at VLT-UT4 in collaboration with other members of the extragalactic astrophysics group at CEA Saclay. The proposal had a twofold goal: on one side, we aimed at providing a rest-frame UV spectrum of an exceptionally young clump of star formation in one of the cluster members (Zanella et al. 2015), thus combing the smallest scales reachable with the instrument; on the other hand, we exploited its large field of view to detect possible extended emission arising from the giant Lyα nebula, hence exploring the large cluster scale. MUSE does not cover wavelengths below 4650 Å even in its extended mode, thus preventing us from studying the Lyα emission at $z = 1.99$. However, it does provide information about important emission lines lying in the rest-frame UV range, such as He II λ1640 Å, C II λ2326 Å, and C III] λ1909 Å. These emission lines are fundamental to assess the powering mechanism of the nebula, its kinematics, and metal-enrichment, constraining the origin of the gas. Bright high ionization lines in the observed wavelength range, i.e., He II and C III], are a clear footprint of a hard spectrum ionizing the gas, presumably an AGN or exotic extremely metal-poor Pop III stars (Prescott et al. 2009; Schaerer 2003). However, their absence might not be straightforwardly associated with alternative powering mechanisms, such as shocks (Cabot et al. 2016). In fact, the recent blind search for giant Lyα nebulae around radio-quiet, bright quasars with MUSE revealed very low He II and C IV λ1549 Å emission around (Borisova et al. 2016), despite the close vicinity of very powerful and hard-spectrum beacons. This survey also shows a separation among radio-quiet and radio-loud QSOs, the latter presumably enriching in metals and lightening giant Lyα nebulae that are kinematically hot (Borisova et al. 2016). Detection of carbon lines indicates metal enrichment, indeed, excluding flows of pristine gas as the origin for the Lyα-emitting material. Moreover, Lyα is a poor tracer for kinematics because of its resonant nature, while close emission lines would allow for detection of global movement, i.e., outflowing, inflowing, or rotating around the galaxies embedded in the nebula (Prescott et al. 2015; Martin et al. 2015).

The proposal went successfully through the selection and we were awarded 1.5 hours of Director's Discretionary Time (DDT). The first reduction of the cube did not reveal any strong signature of He II emission, while we detected C III] at a redshift consistent with $z = 1.99$. Unexpectedly, we observe C IV emission spatially overlapped with the peak of the Lyα nebula (Figure 40), despite being nominally outside the official wavelength range offered by MUSE, but still within the true blue transmission cut, as we could verify with ESO. Both lines appear narrow, but note that we cannot exclude at this stage the presence of an individual emitting galaxy contaminating

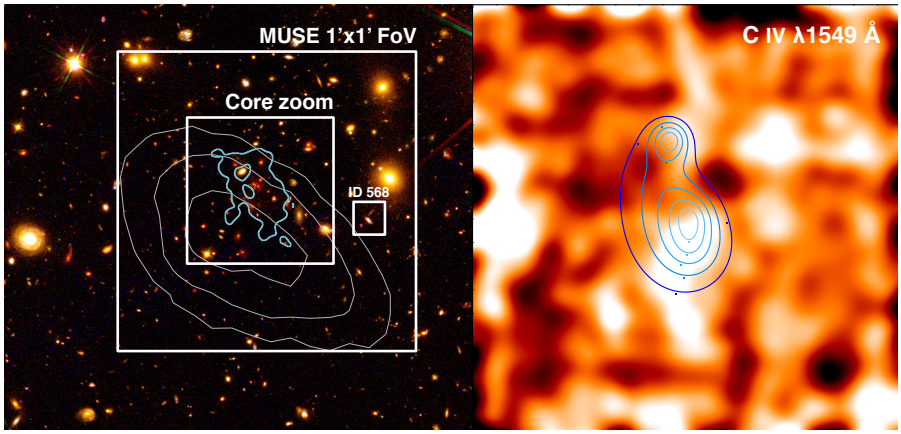

Figure 40 MUSE follow-up of the galaxy cluster CL 1449+0856 at $z = 1.99$. Left panel: three-color image showing the position of the MUSE pointing with respect to the giant Lyα nebula in the core of the cluster (Chapter 3) and the extremely young star-forming clump detected in the cluster member #568 (Zanella et al. 2015). White contours trace the X-ray extended emission detected by XMM-Newton. North is up, East is left. Right panel: cube slice corresponding to the C IV emission line at 1549 Å. The 1σ (left) and 3σ (right) contours of the extended Lyα emission are plotted as a reference.

the extended signal and that a slight redshift offset is present between the two carbon lines. Ongoing investigation of the cube will set these issues.

5.4 THE HUNT FOR LYα NEBULAE IN HIGH-REDSHIFT CLUSTERS

In parallel with the physical characterization of the giant Lyα nebula in CL J1449+0856 through spectroscopy, a second important development of the project described in Chapters 3 and 4 is the systematic follow-up of similar high-redshift structures to search for extended Lyα emission. This is required in order to generalize the findings for CL J1449+0856 or to investigate its peculiarity. Note that such a systematic search implies a reversal of the observational strategy adopted up to now: instead of blindly looking for Lyα blobs and then characterizing their environment, we should target a precise class of well-defined environment, i.e., *clusters* compatible with single halos more massive than a certain threshold, and then look for the presence of Lyα nebulae. In this way we could gain physical understanding into the Lyα nebulae-overdensity relation.

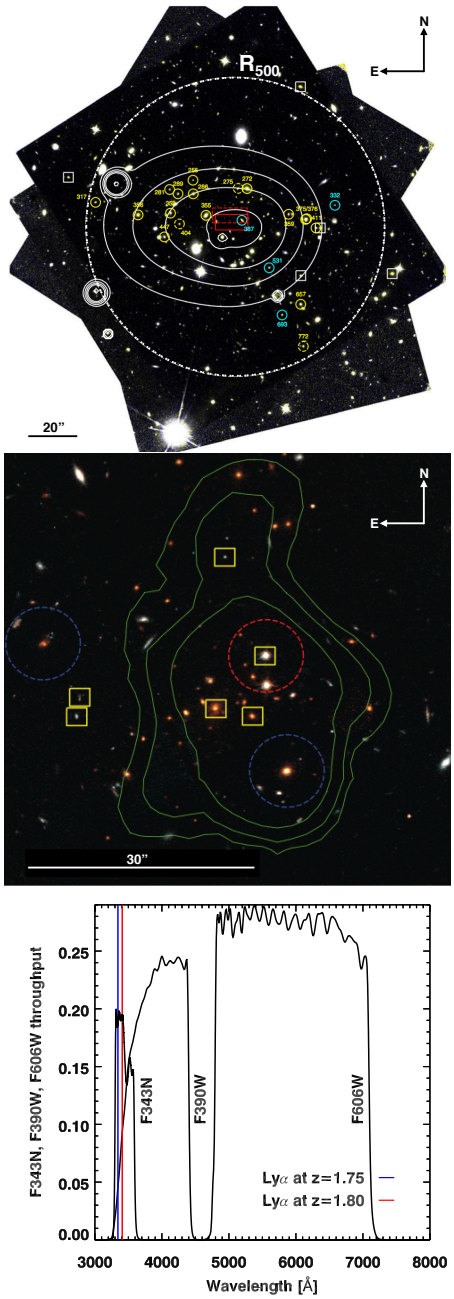

Figure 41 Top: *HST*/WFC3 F160W and F105W imaging of JKCS 041 at $z = 1.80$. White contours represent the smooth X-ray detection. Yellow and cyan circles mark confirmed passive and star-forming members, respectively. White squares mark interlopers. Red solid and dashed rectangles mark the position and 1σ uncertainty of the centroid of spectroscopic members and the mass-weighted centroid of passive members, respectively. From Newman et al. (2014). Center: Pseudo-color *HST* ACS/F814W and WFC3/F160W images of IDCS J1426+3508 at $z = 1.75$. Green contours illustrate the X-ray emission. Yellow boxes mark spectroscopically confirmed members. From Stanford et al. (2012). Bottom: WFC3/F343N, F390W, and F600LP throughput and wavelength coverage. Lyα blobs and emitters from both JKCS 041 at $z = 1.80$ (red line) and IDCS J1426+3508 at $z = 1.75$ (blue line) would be efficiently detectable using this combination of filters.

HST offers the opportunity to investigate this connection in the range of extreme conditions characterizing more massive and evolved clusters at redshift $z < 2$, when these objects start being more numerous. This is an almost prohibitive challenge for ground-based facilities due to low atmospheric transmission (Lyα is shifted to ~3400 Å at $z = 1.8$). Therefore, in Cycle 24 we asked for 15 orbits of *HST* time to look for Lyα emission with the NB filter WFC3/F343N in the two most massive, X-ray detected clusters currently known above $z > 1.7$, JKCS 041 at $z = 1.80$ (Andreon et al. 2009; Newman et al. 2014) and IDCS J1426+3508 at $z = 1.75$ (Stanford et al. 2012; Brodwin et al. 2012, 2016; Mo et al. 2016, Figure 41). Both target structures represent an additional step in the evolution of galaxy clusters with respect to CL J1449+0856. Selected as overdensities of red galaxies, they both show very prominent X-ray emission, compatible with a M_{500} mass of $\sim 3 \times 10^{14}$ $M_\odot$ (Andreon et al. 2009; Brodwin et al. 2016), and an evident red sequence of passive members, where the passive fraction is up to ~ 70% in JKCS 041 (Newman et al. 2014). Moreover, while JKCS 041 does not appear to host a cool-core (Andreon et al. 2009), IDCS J1426+3508 is the first cool-core cluster known at $z > 1.2$ (Brodwin et al. 2016): its well-characterized X-ray properties (temperature, pressure, density as a function of the cluster-centric distance) could allow for a quantitative comparison between the scenario we propose, where Lyα nebulae are photoionized and sustained by galaxy outflows, and the models reproducing cooling from the X-ray phase observed in local cool-core clusters (Sharma et al. 2012; Gaspari et al. 2012). The presence of a cool-core and possible residual cold flows increase the probability to detect extended Lyα emission derived from the extrapolation of the Lyα blob-overdensity relation to halos of $\sim 3 \times 10^{14}$ $M_\odot$. In general, the strength or lack of diffuse Lyα emission would be highly informative of its correlation with cluster properties, i.e., the temperature of the X-ray gas, the dominant galaxy population, its associated outflows, and gas reservoirs, physically characterizing the environment of Lyα nebulae. On the other hand, if our proposed scenario where Lyα blobs may trace energy injection into the ICM were correct, a non-detection in these clusters would constrain both the epoch when this injection occurs and the halo mass regimes actually affected by galaxy activity. A non-detection would also correspond to a limit on $L_{Ly\alpha}/L_X \gtrsim 10\times$ deeper than in CL J1449+0856 at $z = 1.99$, given the combination of lower surface brightness dimming, luminosity distances, and higher X-ray luminosities for the proposed targets at $z \sim 1.8$. Such a limit would allow for a first assessment of the recent suggestion that high-redshift Lyα nebulae might just reflect more extreme cooling conditions from hotter phases in the primordial Universe. The NB filter WFC3/F343N, coupled with an appropriate combination of F390W and F606W broad-bands to detect and subtract possible continuum emission (Figure 41), could potentially triple our

current sample of blobs in cluster cores. Moreover, *HST*'s exquisite 0.1" spatial resolution allows for identifying individual discrete emitters, separating their contribution to real diffuse features. *HST* is the only instrument capable of putting stringent constraints on the morphology and clumpiness of Lyα nebulae and their volume filling factor, one of the most limiting factor of present-day understanding of these objects. Modeling of the Lyα light distribution suggests that a substantial fragmentation into small clumps should be present not to overestimate the gas mass by orders of magnitude (Cantalupo et al. 2014; Arrigoni Battaia et al. 2015). However, observations from the ground do not permit to resolve any structure below 5-10 kpc, while at least a factor of 5$\times$ smaller clumps can be detected with *HST*. The morphology and exact spatial location of Lyα nebulae in clusters can be informative of their powering mechanism, as well: filamentary systems centered on the BCG would clearly recall the nebular emission powered by cooling from the X-ray phase in low-redshift cool-core clusters (McDonald et al. 2010; Gaspari et al. 2012) or cold flows, while arc-like shock fronts would suggest powering from collisional excitation rather than photoionization (Cabot et al. 2016). Moreover, the unique resolution of *HST* has some straightforward consequences on parallel science cases. In fact, in both clusters we would be able to detect Lyα emitting galaxies down to 1.2×10^{-17} erg cm^{-2} s^{-1} (5σ) out to a $\sim$ 1 Mpc scale. Excluding plausible lower redshift strong nebular emission (i.e., [O II] falls well redwards of F343N), NB imaging is a very cheap technique to detect potentially new, SF cluster members down to 2×10^9 M$_\odot$ (assuming that they are on the main sequence at this redshift), allowing for an assessment of the fraction of passive galaxies at low masses, where the role of enviromental quenching is predicted to be stronger.

At higher redshift the Lyα transition falls at more favorable wavelengths, accessible to facilities on the ground, but at the cost of the number of potential cluster targets. In a recent work (Wang et al. 2016), we reported the discovery of a compact structure at $z = 2.503$ with a 4σ X-ray detection and a population of massive galaxies in its core (Figure 42). However, a large fraction of them are strongly star-forming, compact, and dusty, a significant difference with respect to CL J1449+0856, JKCS 041, and IDCS J1426+3508. This cluster is a natural choice to extend the sample of high-redshift Lyα nebulae and, therefore, we proposed to follow it up with VLT/VIMOS 54"$\times$54" IFU. ESO accepted our request in Period 97, allocating 3 hours for the project. Moreover, in Period 98 we proposed VLT/FORS2 NB imaging of one of the most massive protoclusters known so far at $z = 2.095$ (Yuan et al. 2014; Kacprzak et al. 2015) and the structure at $z = 2.2$ from Strazzullo et al. (2015) described in Section 5.2. The former contains 57 spectroscopically confirmed members within a $\sim 10^{14}$M$_\odot$ dark matter halo split into 4 main concentrations over

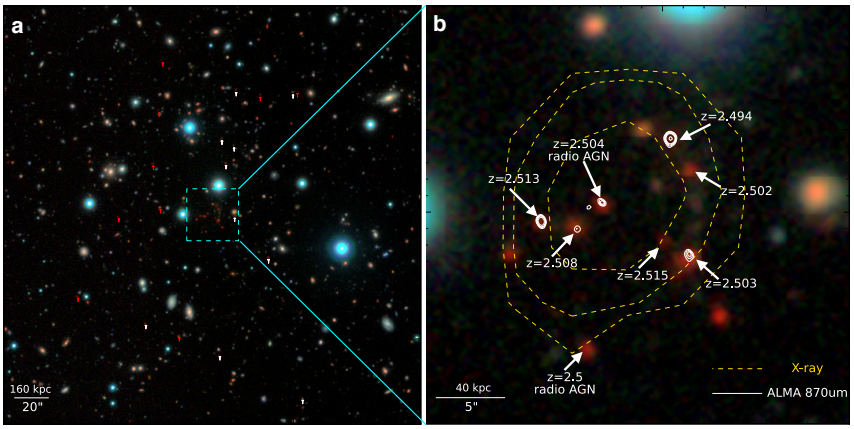

Figure 42 RGB composite color image of the region around the core of the cluster discovered by Wang et al. (2016). The R, G and B channels correspond to the *Ks*, *J* and *Y* bands from the UltraVISTA survey, respectively. Left panel: 4′×4′ region around the cluster. Red arrows indicate distant red galaxies (DRGs) outside the core with photometric redshift $2 \leqslant z \leqslant 3$, while white arrows mark spectroscopically confirmed members within 3σ of the peak of the redshift distribution ($z = 2.506 \pm 0.018$). Right panel: 30″×30″ zoom in on the cluster core. Extended X-ray emission in Chandra soft band and ALMA 870 μm continuum are overlaid respectively with yellow and white contours. From Wang et al. (2016).

5 Mpc. Being largely dominated by star-forming galaxies spread over a relatively large area, this is the less "evolved" among all the targets. The FORS2 OII/4000+45 narrow band filter perfectly covers the Lyα transition at this redshift. The observation of this kind of structures is useful to extend the range of conditions in which we can find Lyα nebulae, whose properties may be connected to the dynamical/evolutionary state of clusters. In principle, the Lyα luminosity could vary substantially within structures having comparable dark matter masses because of lacking of a powering AGN at times, fluctuations in the mass outflow rates, or statistical dispersion between dark matter mass and activity. The campaign we started is the first endeavor to observationally constrain these effects and explore the range of possibilities that the discovery of the Lyα nebula in CL J1449+0856 has opened.

BIBLIOGRAPHY

Abazajian, K. N., Adelman-McCarthy, J. K., Agüeros, M. A., et al. 2009, ApJS, 182, 543

Adelberger, K. L., Steidel, C. C., Shapley, A. E., & Pettini, M. 2003, ApJ, 584, 45

Alloin, D., Collin-Souffrin, S., Joly, M., & Vigroux, L. 1979, A&A, 78, 200

Amendola, L., Appleby, S., Bacon, D., et al. 2013, Living Reviews in Relativity, 16

Andreon, S., Maughan, B., Trinchieri, G., & Kurk, J. 2009, A&A, 507, 147

Andrews, B. H., & Martini, P. 2013, ApJ, 765, 140

Ao, Y., Matsuda, Y., Beelen, A., et al. 2015, A&A, 581, A132

Arnaud, M., Pratt, G. W., Piffaretti, R., et al. 2010, A&A, 517, A92

Arrigoni Battaia, F., Hennawi, J. F., Prochaska, J. X., & Cantalupo, S. 2015, ApJ, 809, 163

Asplund, M., Grevesse, N., Sauval, A. J., & Scott, P. 2009, ARA&A, 47, 481

Bacon, R., Accardo, M., Adjali, L., et al. 2010, in Proceedings of the SPIE, Ground-based and Airborne Instrumentation for Astronomy III, ed. I. S. McLean, S. K. Ramsey, & H. Takami, Vol. 7735 (San Francisco, CA), 773508

Baldry, I. K., Glazebrook, K., Brinkmann, J., et al. 2004, ApJ, 600, 681

Baldwin, J. A., Phillips, M. M., & Terlevich, R. 1981, PASP, 93, 5

Balogh, M. L., Schade, D., Morris, S. L., et al. 1998, ApJL, 504, L75

Bayer-Kim, C. M., Crawford, C. S., Allen, S. W., Edge, A. C., & Fabian, A. C. 2002, MNRAS, 337, 938

Beck, M., Scarlata, C., Hayes, M., Dijkstra, M., & Jones, T. J. 2016, ApJ, 818, 138

Behroozi, P. S., Conroy, C., & Wechsler, R. H. 2010, ApJ, 717, 379

Behroozi, P. S., Wechsler, R. H., & Conroy, C. 2013, ApJ, 770, 57

Bell, E. F., McIntosh, D. H., Barden, M., et al. 2004a, ApJL, 600, L11

Bell, E. F., Wolf, C., Meisenheimer, K., et al. 2004b, ApJ, 608, 752

Bertin, E., & Arnouts, S. 1996, A&AS, 117, 393

Best, P. N., Lehnert, M. D., Miley, G. K., & Röttgering, H. J. 2003, MNRAS, 343, 1

Best, P. N., Röttgering, H. J., & Longair, M. S. 2000, MNRAS, 311, 23

Béthermin, M., Wang, L., Doré, O., et al. 2013, A&A, 557, A66

Birnboim, Y., & Dekel, A. 2003a, MNRAS, 345, 349

—. 2003b, MNRAS, 345, 349

Blanton, M. R., Eisenstein, D., Hogg, D. W., Schlegel, D. J., & Brinkmann, J. 2005, ApJ, 629, 143

Blanton, M. R., & Moustakas, J. 2009, ARA&A, 47, 159
Bleem, L. E., Stalder, B., de Haan, T., et al. 2015, ApJS, 216, 27
Borisova, E., Cantalupo, S., Lilly, S. J., et al. 2016, arXiv:1605.01422, ApJ submitted
Boselli, A., & Gavazzi, G. 2006, PASP, 118, 517
Bouché, N., Cresci, G., Davies, R., et al. 2007, ApJ, 671, 303
Bouché, N., Murphy, M. T., Kacprzak, G. G., et al. 2013, Science, 341, 50
Bournaud, F., Perret, V., Renaud, F., et al. 2014, ApJ, 780, 57
Bower, R. G., Lucey, J. R., & Ellis, R. S. 1992a, MNRAS, 254, 589
—. 1992b, MNRAS, 254, 601
Bower, R. G., Morris, S. L., Bacon, R., et al. 2004, MNRAS, 351, 63
Brinchmann, J., Charlot, S., White, S. D., et al. 2004, MNRAS, 351, 1151
Brodwin, M., Gonzalez, A. H., Stanford, S. A., et al. 2012, ApJ, 753, 162
Brodwin, M., Greer, C. H., Leitch, E. M., et al. 2015, ApJ, 806, 26
Brodwin, M., McDonald, M., Gonzalez, A. H., et al. 2016, ApJ, 817, 122
Brooks, A. M., Governato, F., Quinn, T., Brook, C. B., & Wadsley, J. 2009, ApJ, 694, 396
Brusa, M., Comastri, A., Daddi, E., et al. 2005, A&A, 432, 69
Bruzual, G., & Charlot, S. 2003, MNRAS, 344, 1000
Bunker, A. J., Warren, S. J., Hewett, P. C., & Clements, D. L. 1995, MNRAS, 273, 513
Butcher, H., & Oemler Jr., A. 1978, ApJ, 219, 18
—. 1984, ApJ, 285, 426
Cabot, S. H., Cen, R., & Zheng, Z. 2016, arXiv:1603.09696, MNRAS submitted
Calzetti, D., Armus, L., Bohlin, R. C., et al. 2000, ApJ, 533, 682
Campisi, M. A., Vignali, C., Brusa, M., et al. 2009, A&A, 501, 485
Cantalupo, S., Arrigoni-Battaia, F., Prochaska, J. X., Hennawi, J. F., & Madau, P. 2014, Nature, 506, 63
Cantalupo, S., Porciani, C., Lilly, S. J., & Miniati, F. 2005, ApJ, 628, 61
Capak, P. L., Riechers, D., Scoville, N. Z., et al. 2011, Nature, 470, 233
Casey, C. M., Cooray, A., Capak, P., et al. 2015, ApJL, 808, L33
Cassata, P., Cimatti, A., Kurk, J., et al. 2008, A&A, 483, L39
Cavaliere, A. G., Gursky, H., & Tucker, W. H. 1971, Nature, 231, 437
Cen, R., & Zheng, Z. 2013, ApJ, 775, 112
Ceverino, D., Dekel, A., & Bournaud, F. 2010, MNRAS, 404, 2151
Chapman, S. C., Blain, A., Ibata, R., et al. 2009, ApJ, 691, 560
Charlot, S., & Longhetti, M. 2001, MNRAS, 323, 887
Chiang, Y.-K., Overzier, R., & Gebhardt, K. 2013, ApJ, 779, 127
—. 2014, ApJL, 782, L3
Churazov, E., Brüggen, M., Kaiser, C. R., Böhringer, H., & Forman, W. 2001, ApJ, 554, 261

Cicone, C., Maiolino, R., Sturm, E., et al. 2014, A&A, 562, A21
Cid Fernandes, R., Stasińska, G., Mateus, A., & Vale Asari, N. 2011, MNRAS, 413, 1687
Cid Fernandes, R., Stasińska, G., Schlickmann, M. S., et al. 2010, MNRAS, 403, 1036
Clements, D. L., Braglia, F. G., Hyde, A. K., et al. 2014, MNRAS, 439, 1193
Coil, A. L., Aird, J., Reddy, N., et al. 2015, ApJ, 801, 35
Conroy, C., & Wechsler, R. H. 2009, ApJ, 696, 620
Conselice, C. J., Gallagher III, J. S., & Wyse, R. F. 2001, AJ, 122, 2281
Contini, T., Garilli, B., Le Fèvre, O., et al. 2012, A&A, 539, A91
Cooper, M. C., Tremonti, C. A., Newman, J. A., & Zabludoff, A. I. 2008, MNRAS, 390, 245
Cowie, L. L., Fabian, A. C., & Nulsen, P. E. 1980, MNRAS, 191, 399
Cowie, L. L., & Songaila, A. 1977, Nature, 266, 501
Crawford, C. S., & Fabian, A. C. 1989, MNRAS, 239, 219
Cullen, F., Cirasuolo, M., Kewley, L. J., et al. 2016, arXiv:1605.04228, MNRAS submitted
Cullen, F., Cirasuolo, M., McLure, R. J., Dunlop, J. S., & Bowler, R. A. 2014, MNRAS, 440, 2300
Daddi, E., Bournaud, F., Walter, F., et al. 2010, ApJ, 713, 686
Daddi, E., Cimatti, A., Pozzetti, L., et al. 2000, A&A, 361, 535
Daddi, E., Cimatti, A., Renzini, A., et al. 2004, ApJ, 617, 746
Daddi, E., Dannerbauer, H., Elbaz, D., et al. 2008, ApJL, 673, L21
Daddi, E., Dickinson, M., Morrison, G., et al. 2007, ApJ, 670, 156
Danovich, M., Dekel, A., Hahn, O., Ceverino, D., & Primack, J. 2015, MNRAS, 449, 2087
Darvish, B., Mobasher, B., Sobral, D., et al. 2016, arXiv:1605.03182, ApJ in press
Davé, R., Finlator, K., & Oppenheimer, B. D. 2012, MNRAS, 421, 98
Davé, R., Oppenheimer, B. D., & Sivanandam, S. 2008, MNRAS, 391, 110
Dekel, A., & Birnboim, Y. 2006, MNRAS, 368, 2
Dekel, A., Birnboim, Y., Engel, G., et al. 2009a, Nature, 457, 451
Dekel, A., Sari, R., & Ceverino, D. 2009b, ApJ, 703, 785
Dekel, A., & Silk, J. 1986, ApJ, 303, 39
Dey, A., Bian, C., Soifer, B. T., et al. 2005, ApJ, 629, 654
Di Matteo, T., Springel, V., & Hernquist, L. 2005, Nature, 433, 604
Diener, C., Lilly, S. J., Knobel, C., et al. 2013, ApJ, 765, 109
Diener, C., Lilly, S. J., Ledoux, C., et al. 2015, ApJ, 802, 31
Dijkstra, M., Haiman, Z., & Spaans, M. 2006, ApJ, 649, 37
Dijkstra, M., & Loeb, A. 2008, MNRAS, 386, 492
—. 2009, MNRAS, 400, 1109
Dopita, M. A., Kewley, L. J., Sutherland, R. S., & Nicholls, D. C. 2016, Astrophysics & Space Science, 361, 61

Dopita, M. A., Sutherland, R. S., Nicholls, D. C., Kewley, L. J., & Vogt, F. P. 2013, ApJS, 208, 10
Dressler, A. 1980, ApJ, 236, 351
Eggen, O. J., Lynden-Bell, D., & Sandage, A. R. 1962, ApJ, 136, 748
Eisenhardt, P. R., Brodwin, M., Gonzalez, A. H., et al. 2008, ApJ, 684, 905
Elbaz, D., Daddi, E., Le Borgne, D., et al. 2007, A&A, 468, 33
Ellison, S. L., Mendel, J. T., Patton, D. R., & Scudder, J. M. 2013, MNRAS, 435, 3627
Ellison, S. L., Simard, L., Cowan, N. B., et al. 2009, MNRAS, 396, 1257
Elvis, M., Wilkes, B. J., McDowell, J. C., et al. 1994, ApJS, 95, 1
Erb, D. K., Shapley, A. E., Pettini, M., et al. 2006, ApJ, 644, 813
Erfanianfar, G., Popesso, P., Finoguenov, A., et al. 2016, MNRAS, 455, 2839
Fabian, A. C. 1994, ARA&A, 32, 277
—. 2012, ARA&A, 50, 455
Fabian, A. C., Crawford, C. S., Johnstone, R. M., & Thomas, P. A. 1987, MNRAS, 228, 963
Fabian, A. C., Johnstone, R. M., Sanders, J. S., et al. 2008, Nature, 454, 968
Fabian, A. C., Nulsen, P. E., & Arnaud, K. A. 1984a, MNRAS, 208, 179
Fabian, A. C., Nulsen, P. E., & Canizares, C. R. 1984b, Nature, 310, 733
Fabian, A. C., Sanders, J. S., Crawford, C. S., et al. 2003, MNRAS, 344, L48
Fakhouri, O., Ma, C.-P., & Boylan-Kolchin, M. 2010, MNRAS, 406, 2267
Fardal, M. A., Katz, N., Gardner, J. P., et al. 2001, ApJ, 562, 605
Fassbender, R., Nastasi, A., Böhringer, H., et al. 2011, A&A, 527, L10
Feruglio, C., Maiolino, R., Piconcelli, E., et al. 2010, A&A, 518, L155
Finoguenov, A., Guzzo, L., Hasinger, G., et al. 2007, ApJS, 172, 182
Fitzpatrick, E. L. 1999, PASP, 111, 63
Förster Schreiber, N. M., Genzel, R., Newman, S. F., et al. 2014, ApJ, 787, 38
Francis, P. J., Woodgate, B. E., Warren, S. J., et al. 1996, ApJ, 457, 490
Fujita, Y. 2001, ApJ, 550, 612
Gabor, J. M., & Bournaud, F. 2014, MNRAS, 437, L56
Gabor, J. M., & Davé, R. 2015, MNRAS, 447, 374
Gaspari, M., Ruszkowski, M., & Sharma, P. 2012, ApJ, 746, 94
Geach, J. E., Alexander, D. M., Lehmer, B. D., et al. 2009, ApJ, 700, 1
Genel, S. 2016, ApJ, 822, 107
Genzel, R., Förster Schreiber, N. M., Rosario, D., et al. 2014, ApJ, 796, 7
Genzel, R., Tacconi, L. J., Lutz, D., et al. 2015, ApJ, 800, 20
George, M. R., Leauthaud, A., Bundy, K., et al. 2011, ApJ, 742, 125
Gobat, R., Daddi, E., Béthermin, M., et al. 2015, A&A, 581, A56
Gobat, R., Daddi, E., Onodera, M., et al. 2011, A&A, 526, A133

Gobat, R., Strazzullo, V., Daddi, E., et al. 2013, ApJ, 776, 9
Goerdt, T., Dekel, A., Sternberg, A., et al. 2010, MNRAS, 407, 613
Gómez, P. L., Nichol, R. C., Miller, C. J., et al. 2003, ApJ, 584, 210
Gunn, J. E., & Gott III, J. R. 1972, ApJ, 176, 1
Gursky, H., Kellogg, E., Murray, S., et al. 1971, ApJL, 167, L81
Haiman, Z., Spaans, M., & Quataert, E. 2000, ApJL, 537, L5
Harrison, C. M., Alexander, D. M., Mullaney, J. R., et al. 2015, arXiv:1511.00008, MNRAS in press
Hasselfield, M., Hilton, M., Marriage, T. A., et al. 2013, Journal of Cosmology and Astroparticle Physics, 7, 008
Hatch, N. A., Crawford, C. S., & Fabian, A. C. 2007, MNRAS, 380, 33
Hatch, N. A., Crawford, C. S., Fabian, A. C., & Johnstone, R. M. 2005, MNRAS, 358, 765
Hatch, N. A., De Breuck, C., Galametz, A., et al. 2011, MNRAS, 410, 1537
Hatch, N. A., Overzier, R. A., Röttgering, H. J., Kurk, J. D., & Miley, G. K. 2008, MNRAS, 383, 931
Hayashi, M., Kodama, T., Koyama, Y., et al. 2014, MNRAS, 439, 2571
Hayes, M., Scarlata, C., & Siana, B. 2011, Nature, 476, 304
Hayward, C. C., & Hopkins, P. F. 2015, arXiv:1510.05650, MNRAS submitted
Heckman, T. M., Armus, L., & Miley, G. K. 1990, ApJS, 74, 833
Heckman, T. M., Baum, S. A., van Breugel, W. J., & McCarthy, P. 1989, ApJ, 338, 48
Heckman, T. M., Kauffmann, G., Brinchmann, J., et al. 2004, ApJ, 613, 109
Heckman, T. M., Lehnert, M. D., Strickland, D. K., & Armus, L. 2000, ApJS, 129, 493
Hennawi, J. F., & Prochaska, J. X. 2013, ApJ, 766, 58
Hill, G. J., Gebhardt, K., Komatsu, E., et al. 2008, in Astronomical Society of the Pacific Conference Series, Panoramic Views of Galaxy Formation and Evolution, ed. T. Kodama, T. Yamada, & K. Aoki, Vol. 399 (Hayama, Japan: ASP), 115
Holden, B. P., Oesch, P. A., González, V. G., et al. 2016, ApJ, 820, 73
Hopkins, P. F., Quataert, E., & Murray, N. 2012, MNRAS, 421, 3522
Hubble, E. P. 1926, ApJ, 64
Hubble, E., & Humason, M. L. 1931, ApJ, 74, 43
Hughes, T. M., Cortese, L., Boselli, A., Gavazzi, G., & Davies, J. I. 2013, A&A, 550, A115
Ichikawa, T., Suzuki, R., Tokoku, C., et al. 2006, in Proceedings of the SPIE, Ground-based and Airborne Instrumentation for Astronomy, Vol. 6269 (Orlando, FL), 38
Ilbert, O., McCracken, H. J., Le Fèvre, O., et al. 2013, A&A, 556, A55
Juneau, S., Bournaud, F., Charlot, S., et al. 2014, ApJ, 788, 88
Juneau, S., Dickinson, M., Alexander, D. M., & Salim, S. 2011, ApJ, 736, 104

Kacprzak, G. G., Yuan, T., Nanayakkara, T., et al. 2015, ApJL, 802, L26
Kaiser, N. 1986, MNRAS, 222, 323
—. 1991, ApJ, 383, 104
Kashino, D., Silverman, J. D., Rodighiero, G., et al. 2013, ApJL, 777, L8
Kashino, D., Silverman, J. D., Sanders, D., et al. 2016, arXiv:1604.06802, ApJ submitted
Kauffmann, G., White, S. D., Heckman, T. M., et al. 2004, MNRAS, 353, 713
Kennicutt Jr., R. C. 1998a, ApJ, 498, 541
—. 1998b, ARA&A, 36, 189
Kereš, D., Katz, N., Weinberg, D. H., & Davé, R. 2005, MNRAS, 363, 2
Kewley, L. J., & Dopita, M. A. 2002, ApJS, 142, 35
Kewley, L. J., Dopita, M. A., Leitherer, C., et al. 2013a, ApJ, 774, 100
Kewley, L. J., & Ellison, S. L. 2008, ApJ, 681, 1183
Kewley, L. J., Maier, C., Yabe, K., et al. 2013b, ApJL, 774, L10
Kewley, L. J., Yuan, T., Nanayakkara, T., et al. 2016, ApJ, 819, 100
Klein, R. I., McKee, C. F., & Colella, P. 1994, ApJ, 420, 213
Kobulnicky, H. A., & Kewley, L. J. 2004, ApJ, 617, 240
Kodama, T., Hayashi, M., Koyama, Y., et al. 2013, in IAU Symposium, IAU Symposium, ed. D. Thomas, A. Pasquali, & I. Ferreras, Vol. 295 (Cambridge, UK: Cambridge Univ. Press), 74
Kong, X., Daddi, E., Arimoto, N., et al. 2006, ApJ, 638, 72
Kormendy, J., & Ho, L. C. 2013, ARA&A, 51, 511
Koyama, Y., Smail, I., Kurk, J., et al. 2013, MNRAS, 434, 423
Kravtsov, A. V., & Borgani, S. 2012, ARA&A, 50, 353
Kriek, M., van Dokkum, P. G., Labbé, I., et al. 2009, ApJ, 700, 221
Kubo, M., Yamada, T., Ichikawa, T., et al. 2015, ApJ, 799, 38
Kulas, K. R., McLean, I. S., Shapley, A. E., et al. 2013, ApJ, 774, 130
Kurk, J., Cimatti, A., Zamorani, G., et al. 2009, A&A, 504, 331
Larson, R. B., Tinsley, B. M., & Caldwell, C. N. 1980, ApJ, 237, 692
Le Brun, A. M., McCarthy, I. G., & Melin, J.-B. 2015, MNRAS, 451, 3868
Le Brun, A. M., McCarthy, I. G., Schaye, J., & Ponman, T. J. 2014, MNRAS, 441, 1270
Leauthaud, A., Finoguenov, A., Kneib, J.-P., et al. 2010, ApJ, 709, 97
Ledlow, M. J., Voges, W., Owen, F. N., & Burns, J. O. 2003, AJ, 126, 2740
Lee, N., Sanders, D. B., Casey, C. M., et al. 2015, ApJ, 801, 80
Lequeux, J., Peimbert, M., Rayo, J. F., Serrano, A., & Torres-Peimbert, S. 1979, A&A, 80, 155
Lewis, I., Balogh, M., De Propris, R., et al. 2002, MNRAS, 334, 673
Lilly, S. J., Carollo, C. M., Pipino, A., Renzini, A., & Peng, Y. 2013, ApJ, 772, 119
Lilly, S. J., Le Brun, V., Maier, C., et al. 2009, ApJS, 184, 218

Lilly, S. J., Le Fevre, O., Hammer, F., & Crampton, D. 1996, ApJL, 460, L1
Lilly, S. J., Le Fèvre, O., Renzini, A., et al. 2007, ApJS, 172, 70
Lusso, E., Comastri, A., Simmons, B. D., et al. 2012, MNRAS, 425, 623
Madau, P., & Dickinson, M. 2014, ARA&A, 52, 415
Madau, P., Pozzetti, L., & Dickinson, M. 1998, ApJ, 498, 106
Magdis, G. E., Daddi, E., Béthermin, M., et al. 2012, ApJ, 760, 6
Maier, C., Lilly, S. J., Ziegler, B. L., et al. 2014, ApJ, 792, 3
Maiolino, R., Nagao, T., Grazian, A., et al. 2008, A&A, 488, 463
Mannucci, F., Cresci, G., Maiolino, R., Marconi, A., & Gnerucci, A. 2010, MNRAS, 408, 2115
Maraston, C., Pforr, J., Renzini, A., et al. 2010, MNRAS, 407, 830
Markwardt, C. B. 2009, in Astronomical Society of the Pacific Conference Series, Astronomical Data Analysis Software and Systems XVIII, ed. D. A. Bohlender, D. Durand, & P. Dowler, Vol. 411 (San Francisco, CA: ASP), 251
Martig, M., & Bournaud, F. 2007, in SF2A-2007: Proceedings of the Annual meeting of the French Society of Astronomy and Astrophysics, ed. J. Bouvier, A. Chalabaev, & C. Charbonnel (Grenoble, France), 344
Martig, M., Bournaud, F., Teyssier, R., & Dekel, A. 2009, ApJ, 707, 250
Martin, C. L., & Bouché, N. 2009, ApJ, 703, 1394
Martin, D. C., Matuszewski, M., Morrissey, P., et al. 2015, Nature, 524, 192
Masters, D., Faisst, A., & Capak, P. 2016, arXiv:1605.04314, ApJ submitted
Masters, D., McCarthy, P., Siana, B., et al. 2014, ApJ, 785, 153
Matsuda, Y., Yamada, T., Hayashino, T., et al. 2004, AJ, 128, 569
McCarthy, I. G., Le Brun, A. M., Schaye, J., & Holder, G. P. 2014, MNRAS, 440, 3645
McCarthy, I. G., Schaye, J., Bower, R. G., et al. 2011, MNRAS, 412, 1965
McCarthy, P. J., Spinrad, H., Dickinson, M., et al. 1990, ApJ, 365, 487
McDonald, M., Veilleux, S., Rupke, D. S., & Mushotzky, R. 2010, ApJ, 721, 1262
McDonald, M., Veilleux, S., Rupke, D. S., Mushotzky, R., & Reynolds, C. 2011, ApJ, 734, 95
McLean, I. S., Steidel, C. C., Epps, H., et al. 2010, in Proceedings of the SPIE, Ground-based and Airborne Instrumentation for Astronomy III, ed. I. S. McLean, S. K. Ramsey, & H. Takami, Vol. 7735 (San Francisco, CA), 77351
McNamara, B. R., & Nulsen, P. E. 2007, ARA&A, 45, 117
McNamara, B. R., Russell, H. R., Nulsen, P. E., et al. 2014, ApJ, 785, 44
Meekins, J. F., Fritz, G., Chubb, T. A., & Friedman, H. 1971, Nature, 231, 107

Mei, S., Scarlata, C., Pentericci, L., et al. 2015, ApJ, 804, 117
Merritt, D. 1983, ApJ, 264, 24
Miley, G. K., Overzier, R. A., Zirm, A. W., et al. 2006, ApJL, 650, L29
Miller, T. B., Hayward, C. C., Chapman, S. C., & Behroozi, P. S. 2015, MNRAS, 452, 878
Miyazaki, S., Komiyama, Y., Sekiguchi, M., et al. 2002, PASJ, 54, 833
Mo, W., Gonzalez, A., Jee, M. J., et al. 2016, ApJL, 818, L25
Møller, P., & Fynbo, J. U. 2001, A&A, 372, L57
Moore, B., Katz, N., Lake, G., Dressler, A., & Oemler, A. 1996, Nature, 379, 613
Moreno, J., Bluck, A. F., Ellison, S. L., et al. 2013, MNRAS, 436, 1765
Moster, B. P., Somerville, R. S., Maulbetsch, C., et al. 2010, ApJ, 710, 903
Mouhcine, M., Baldry, I. K., & Bamford, S. P. 2007, MNRAS, 382, 801
Muldrew, S. I., Hatch, N. A., & Cooke, E. A. 2015, MNRAS, 452, 2528
Mullaney, J. R., Daddi, E., Béthermin, M., et al. 2012, ApJL, 753, L30
Muzzin, A., Wilson, G., Demarco, R., et al. 2013, ApJ, 767, 39
Muzzin, A., Wilson, G., Yee, H. K., et al. 2009, ApJ, 698, 1934
Muzzin, A., Wilson, G., Yee, H. K., et al. 2012, ApJ, 746, 188
Nagao, T., Maiolino, R., & Marconi, A. 2006, A&A, 459, 85
Neistein, E., & Dekel, A. 2008, MNRAS, 388, 1792
Newman, A. B., Ellis, R. S., Andreon, S., et al. 2014, ApJ, 788, 51
Newman, S. F., Genzel, R., Förster-Schreiber, N. M., et al. 2012, ApJ, 761, 43
Nilsson, K. K., Fynbo, J. P., Møller, P., Sommer-Larsen, J., & Ledoux, C. 2006, A&A, 452, L23
Noeske, K. G., Weiner, B. J., Faber, S. M., et al. 2007, ApJL, 660, L43
Noll, S., Pierini, D., Cimatti, A., et al. 2009, A&A, 499, 69
Nulsen, P. E. 1982, MNRAS, 198, 1007
O'Dea, K. P., Quillen, A. C., O'Dea, C. P., et al. 2010, ApJ, 719, 1619
Onodera, M., Carollo, C. M., Lilly, S., et al. 2016, ApJ, 822, 42
Onodera, M., Renzini, A., Carollo, M., et al. 2012, ApJ, 755, 26
Osterbrock, D. E., & Ferland, G. J. 2006, Astrophysics of gaseous nebulae and active galactic nuclei (Sausalito, CA: Univ. Sci. Books)
Overzier, R. A., Nesvadba, N. P., Dijkstra, M., et al. 2013, ApJ, 771, 89
Pannella, M., Elbaz, D., Daddi, E., et al. 2015, ApJ, 807, 141
Papovich, C., Momcheva, I., Willmer, C. N., et al. 2010, ApJ, 716, 1503
Pasquali, A., Gallazzi, A., & van den Bosch, F. C. 2012, MNRAS, 425, 273
Peebles, P. J. 1993, Principles of Physical Cosmology (Princeton, NJ: Princeton Univ. Press)
Peng, C. Y. 2007, ApJ, 671, 1098
Peng, C. Y., Ho, L. C., Impey, C. D., & Rix, H.-W. 2002, AJ, 124, 266
—. 2010a, AJ, 139, 2097
Peng, Y.-j., Lilly, S. J., Kovač, K., et al. 2010b, ApJ, 721, 193
Peng, Y.-j., Lilly, S. J., Renzini, A., & Carollo, M. 2012, ApJ, 757, 4

Peng, Y.-j., & Maiolino, R. 2014, MNRAS, 438, 262
Pentericci, L., Kurk, J. D., Röttgering, H. J., et al. 2000, A&A, 361, L25
Pérez-Montero, E., & Contini, T. 2009, MNRAS, 398, 949
Peterson, J. R., & Fabian, A. C. 2006, Physics Reports, 427, 1
Pettini, M., & Pagel, B. E. 2004, MNRAS, 348, L59
Piconcelli, E., Jimenez-Bailón, E., Guainazzi, M., et al. 2005, A&A, 432, 15
Pike, S. R., Kay, S. T., Newton, R. D., Thomas, P. A., & Jenkins, A. 2014, MNRAS, 445, 1774
Pilyugin, L. S., Grebel, E. K., & Mattsson, L. 2012, MNRAS, 424, 2316
Planck Collaboration. 2015, A&A, 582, A30
Planck Collaboration, Ade, P. A., Aghanim, N., et al. 2014, A&A, 571, A16
Planck Collaboration, Ade, P. A., Aghanim, N., et al. 2015, A&A, 581, A14
Ponman, T. J., Cannon, D. B., & Navarro, J. F. 1999, Nature, 397, 135
Ponman, T. J., Sanderson, A. J., & Finoguenov, A. 2003, MNRAS, 343, 331
Popesso, P., Biviano, A., Finoguenov, A., et al. 2015, A&A, 579, A132
Postman, M., & Geller, M. J. 1984, ApJ, 281, 95
Pratt, G. W., Arnaud, M., Piffaretti, R., et al. 2010, A&A, 511, A85
Prescott, M. K., Dey, A., & Jannuzi, B. T. 2009, ApJ, 702, 554
—. 2012, ApJ, 748, 125
—. 2013, ApJ, 762, 38
Prescott, M. K., Momcheva, I., Brammer, G. B., Fynbo, J. P., & Møller, P. 2015, ApJ, 802, 32
Press, W. H., & Schechter, P. 1974, ApJ, 187, 425
Queyrel, J., Contini, T., Kissler-Patig, M., et al. 2012, A&A, 539, A93
Renzini, A., & Andreon, S. 2014, MNRAS, 444, 3581
Rettura, A., Martinez-Manso, J., Stern, D., et al. 2014, ApJ, 797, 109
Revaz, Y., Combes, F., & Salomé, P. 2008, A&A, 477, L33
Rodighiero, G., Brusa, M., Daddi, E., et al. 2015, ApJL, 800, L10
Rodighiero, G., Daddi, E., Baronchelli, I., et al. 2011, ApJL, 739, L40
Rodighiero, G., Renzini, A., Daddi, E., et al. 2014, MNRAS, 443, 19
Rosdahl, J., & Blaizot, J. 2012, MNRAS, 423, 344
Rousselot, P., Lidman, C., Cuby, J.-G., Moreels, G., & Monnet, G. 2000, A&A, 354, 1134
Salomé, P., Combes, F., Revaz, Y., et al. 2011, A&A, 531, A85
Salpeter, E. E. 1955, ApJ, 121, 161
Sanders, D. B., & Mirabel, I. F. 1996, ARA&A, 34, 749
Sanders, R. L., Shapley, A. E., Kriek, M., et al. 2016, ApJ, 816, 23
Santos, J. S., Altieri, B., Valtchanov, I., et al. 2015, MNRAS, 447, L65
Santos, J. S., Fassbender, R., Nastasi, A., et al. 2011, A&A, 531, L15
Sarazin, C. L. 1988, X-ray emission from clusters of galaxies (Cambridge, UK: Cambridge Univ. Press)
Sargent, M. T., Daddi, E., Béthermin, M., et al. 2014, ApJ, 793, 19

Savaglio, S., Glazebrook, K., Le Borgne, D., et al. 2005, ApJ, 635, 260
Scannapieco, E., & Brüggen, M. 2015, ApJ, 805, 158
Schaerer, D. 2003, A&A, 397, 527
Schaye, J., Dalla Vecchia, C., Booth, C. M., et al. 2010, MNRAS, 402, 1536
Schmidt, M. 1959, ApJ, 129, 243
Schreiber, C., Elbaz, D., Pannella, M., et al. 2016, A&A, 589, A35
Schreiber, C., Pannella, M., Elbaz, D., et al. 2015, A&A, 575, A74
Scoville, N., Arnouts, S., Aussel, H., et al. 2013, ApJS, 206, 3
Scoville, N., Aussel, H., Brusa, M., et al. 2007, ApJS, 172, 1
Scoville, N., Aussel, H., Sheth, K., et al. 2014, ApJ, 783, 84
Scoville, N., Sheth, K., Aussel, H., et al. 2016, ApJ, 820, 83
Shapley, A. E., Reddy, N. A., Kriek, M., et al. 2015, ApJ, 801, 88
Sharma, P., McCourt, M., Quataert, E., & Parrish, I. J. 2012, MNRAS, 420, 3174
Sharples, R., Bender, R., Agudo Berbel, A., et al. 2013, The Messenger, 151, 21
Shimakawa, R., Kodama, T., Tadaki, K.-i., et al. 2015, MNRAS, 448, 666
Silk, J., & Rees, M. J. 1998, A&A, 331, L1
Silverman, J. D., Kashino, D., Sanders, D., et al. 2015, ApJS, 220, 12
Sobral, D., Stroe, A., Koyama, Y., et al. 2016, MNRAS, 458, 3443
Speagle, J. S., Steinhardt, C. L., Capak, P. L., & Silverman, J. D. 2014, ApJS, 214, 15
Spitler, L. R., Labbé, I., Glazebrook, K., et al. 2012, ApJL, 748, L21
Spitzer, L. 1978, Physical processes in the interstellar medium (New York, NY: Wiley)
Spitzer Jr., L., & Baade, W. 1951, ApJ, 113, 413
Stanford, S. A., Brodwin, M., Gonzalez, A. H., et al. 2012, ApJ, 753, 164
Starck, J. L., Saber Naceur, M., & Murtagh, R., eds. 2010, 6th Astronomical Data Analysis Conference (Monastir, Tunisia)
Steidel, C. C., Adelberger, K. L., Shapley, A. E., et al. 2000, ApJ, 532, 170
Steidel, C. C., Adelberger, K. L., Shapley, A. E., et al. 2005, ApJ, 626, 44
Steidel, C. C., Rudie, G. C., Strom, A. L., et al. 2014, ApJ, 795, 165
Storey, P. J., & Zeippen, C. J. 2000, MNRAS, 312, 813
Strateva, I., Ivezić, Ž., Knapp, G. R., et al. 2001, AJ, 122, 1861
Strazzullo, V., Daddi, E., Gobat, R., et al. 2015, A&A, 576, L6
Strazzullo, V., Gobat, R., Daddi, E., et al. 2013, ApJ, 772, 118
Sun, M., Voit, G. M., Donahue, M., et al. 2009, ApJ, 693, 1142
Sunyaev, R. A., & Zeldovich, Y. B. 1970, Comments on Astrophysics and Space Physics, 2, 66
—. 1972, Comments on Astrophysics and Space Physics, 4, 173
Sutherland, R. S., & Dopita, M. A. 1993, ApJS, 88, 253

Tacchella, S., Dekel, A., Carollo, C. M., et al. 2016, MNRAS, 457, 2790
Tacconi, L. J., Genzel, R., Neri, R., et al. 2010, Nature, 463, 781
Tacconi, L. J., Neri, R., Genzel, R., et al. 2013, ApJ, 768, 74
Takada, M., Ellis, R. S., Chiba, M., et al. 2014, PASJ, 66, R1
Tanaka, M., Finoguenov, A., & Ueda, Y. 2010, ApJL, 716, L152
Tanaka, M., Toft, S., Marchesini, D., et al. 2013, ApJ, 772, 113
Taniguchi, Y., Shioya, Y., & Kakazu, Y. 2001, ApJL, 562, L15
Temporin, S., Duc, P.-A., Ilbert, O., & XMM-LSS/SWIRE Collaboration. 2009, Astronomische Nachrichten, 330, 915
Thomas, D., Maraston, C., Bender, R., & Mendes de Oliveira, C. 2005, ApJ, 621, 673
Thompson, T. A., Fabian, A. C., Quataert, E., & Murray, N. 2015, MNRAS, 449, 147
Toomre, A. 1977, in Evolution of Galaxies and Stellar Populations, ed. B. M. Tinsley, & R. B. Larson D. Campbell (New Haven, CT: Yale Univ. Observatory), 401
Torrey, P., Cox, T. J., Kewley, L., & Hernquist, L. 2012, ApJ, 746, 108
Tozzi, P., & Norman, C. 2001, ApJ, 546, 63
Tran, K.-V. H., Nanayakkara, T., Yuan, T., et al. 2015, ApJ, 811, 28
Tran, K.-V. H., Papovich, C., Saintonge, A., et al. 2010, ApJL, 719, L126
Tremblay, G. R., O'Dea, C. P., Baum, S. A., et al. 2015, MNRAS, 451, 3768
Tremonti, C. A., Heckman, T. M., Kauffmann, G., et al. 2004, ApJ, 613, 898
Troncoso, P., Maiolino, R., Sommariva, V., et al. 2014, A&A, 563, A58
Trump, J. R., Konidaris, N. P., Barro, G., et al. 2013, ApJL, 763, L6
Valentino, F., Daddi, E., Finoguenov, A., et al. 2016, arXiv:1605.03194, ApJ submitted
Valentino, F., Daddi, E., Strazzullo, V., et al. 2015, ApJ, 801, 132
van der Burg, R. F., Muzzin, A., Hoekstra, H., et al. 2014, A&A, 561, A79
Veilleux, S., Cecil, G., & Bland-Hawthorn, J. 2005, ARA&A, 43, 769
Venemans, B. P., Röttgering, H. J., Miley, G. K., et al. 2007, A&A, 461, 823
Vikhlinin, A., Burenin, R. A., Ebeling, H., et al. 2009, ApJ, 692, 1033
Villar-Martín, M., Sánchez, S. F., Humphrey, A., et al. 2007, MNRAS, 378, 416
Villar-Martín, M., Vernet, J., di Serego Alighieri, S., et al. 2003, MNRAS, 346, 273
Visvanathan, N., & Sandage, A. 1977, ApJ, 216, 214
Vogelsberger, M., Genel, S., Springel, V., et al. 2014, MNRAS, 444, 1518
Voit, G. M., & Bryan, G. L. 2001, Nature, 414, 425
Voit, G. M., & Donahue, M. 2015, ApJL, 799, L1
Walter, F., Decarli, R., Carilli, C., et al. 2012, Nature, 486, 233

Wang, T., Elbaz, D., Daddi, E., et al. 2016, arXiv:1604.07404, ApJ submitted
Weiner, B. J., Coil, A. L., Prochaska, J. X., et al. 2009, ApJ, 692, 187
Whitaker, K. E., Franx, M., Leja, J., et al. 2014, ApJ, 795, 104
Whitaker, K. E., van Dokkum, P. G., Brammer, G., & Franx, M. 2012, ApJL, 754, L29
White, S. D., & Rees, M. J. 1978, MNRAS, 183, 341
Whitmore, B. C., Gilmore, D. M., & Jones, C. 1993, ApJ, 407, 489
Williams, R. J., Quadri, R. F., Franx, M., van Dokkum, P., & Labbé, I. 2009, ApJ, 691, 1879
Wilman, R. J., Edge, A. C., & Swinbank, A. M. 2006, MNRAS, 371, 93
Wuyts, E., Kurk, J., Förster Schreiber, N. M., et al. 2014, ApJL, 789, L40
Wuyts, S., Labbé, I., Franx, M., et al. 2007, ApJ, 655, 51
Wylezalek, D., Galametz, A., Stern, D., et al. 2013, ApJ, 769, 79
Yabe, K., Ohta, K., Iwamuro, F., et al. 2012, PASJ, 64, 60
Yan, R., Ho, L. C., Newman, J. A., et al. 2011, ApJ, 728, 38
York, D. G., Adelman, J., Anderson Jr., J. E., et al. 2000, AJ, 120, 1579
Yoshikawa, T., Akiyama, M., Kajisawa, M., et al. 2010, ApJ, 718, 112
Yuan, T., Nanayakkara, T., Kacprzak, G. G., et al. 2014, ApJL, 795, L20
Zahid, H. J., Bresolin, F., Kewley, L. J., Coil, A. L., & Davé, R. 2012, ApJ, 750, 120
Zahid, H. J., Dima, G. I., Kudritzki, R.-P., et al. 2014a, ApJ, 791, 130
Zahid, H. J., Kashino, D., Silverman, J. D., et al. 2014b, ApJ, 792, 75
Zanella, A., Daddi, E., Le Floc'h, E., et al. 2015, Nature, 521, 54
Zibetti, S., White, S. D., Schneider, D. P., & Brinkmann, J. 2005, MNRAS, 358, 949
Ziparo, F., Popesso, P., Finoguenov, A., et al. 2014, MNRAS, 437, 458
Zwicky, F. 1933, Helvetica Physica Acta, 6, 110

A PUBLICATIONS

• **F. Valentino**, E. Daddi, A. Finoguenov, et al. 2016, *A giant Lyα nebula in the core of an X-ray cluster at $z = 1.99$: implications for early energy injection*, arXiv:1605.03194, ApJ in press.

• **F. Valentino**, E. Daddi, V. Strazzullo, et al. 2015, *Metal deficiency in cluster star-forming galaxies at $z = 2$*, ApJ, 801, 132.

• D. Kashino, J. D. Silverman, D. Sanders, J. S. Kartaltepe, E. Daddi, A. Renzini, **F. Valentino**, et al. 2016, *The FMOS-COSMOS survey of star-forming galaxies at $z \sim 1.6$. IV: Excitation state and chemical enrichment of HII regions*, arXiv:1604.06802, ApJ submitted.

• T. Wang, D. Elbaz, E. Daddi, A. Finoguenov, D. Liu, C. Schreiber, S. Martin, V. Strazzullo, **F. Valentino**, et al. 2016, *Discovery of a galaxy cluster with a violently starbursting core at $z = 2.506$*, ApJ, 828, 56.

• R. Gobat, E. Daddi, M. Béthermin, M. Pannella, A. Finoguenov, G. Gozaliasl, E. Le Floc'h, C. Schreiber, V. Strazzullo, M. Sargent, T. Wang, H. S. Hwang, **F. Valentino**, et al. 2015, *Satellite content and quenching of star formation in galaxy groups at $z \sim 1.8$*, A&A, 581, A56.

• A. Zanella, E. Daddi, E. Le Floc'h, F. Bournaud, R. Gobat, **F. Valentino**, et al. 2015, *An extremely young massive clump forming by gravitational collapse in a primordial galaxy*, Nature, 521, 54.

• V. Strazzullo, E. Daddi, R. Gobat, B. Garilli, M. Mignoli, **F. Valentino**, et al. 2015, *Passive galaxies as tracers of cluster environments at $z \sim 2$*, A&A, 576, L6.

The Astrophysical Journal, 801:132 (18pp), 2015 March 10 doi:10.1088/0004-637X/801/2/132

METAL DEFICIENCY IN CLUSTER STAR-FORMING GALAXIES AT $Z = 2$

F. Valentino[1], E. Daddi[1], V. Strazzullo[1,2], R. Gobat[1,3], M. Onodera[4], F. Bournaud[1], S. Juneau[1], A. Renzini[5], N. Arimoto[6,7], M. Carollo[4], and A. Zanella[1]
[1] Laboratoire AIM-Paris-Saclay, CEA/DSM-CNRS-Université Paris Diderot, Irfu/Service d'Astrophysique, CEA Saclay, Orme des Merisiers, F-91191 Gif sur Yvette, France; francesco.valentino@cea.fr
[2] Department of Physics, Ludwig-Maximilians-Universität, Scheinerstr. 1, D-81679 München, Germany
[3] School of Physics, Korea Institute for Advanced Study, Heogiro 85, Seoul 130-722, Korea
[4] Institute for Astronomy, ETH Zürich Wolfgang-Pauli-strasse 27, 8093 Zürich, Switzerland
[5] INAF-Osservatorio Astronomico di Padova Vicolo dell'Osservatorio 5, I-35122 Padova, Italy
[6] Subaru Telescope, National Astronomical Observatory of Japan 650 North A'ohoku Place, Hilo, HI 96720, USA
[7] Graduate University for Advanced Studies, 2-21-1 Osawa, Mitaka, Tokyo, Japan
Received 2014 October 4; accepted 2015 January 12; published 2015 March 12

ABSTRACT

We investigate the environmental effect on the metal enrichment of star-forming galaxies (SFGs) in the farthest spectroscopically confirmed and X-ray-detected cluster, CL J1449+0856 at $z = 1.99$. We combined *Hubble Space Telescope*/WFC3 G141 slitless spectroscopic data, our thirteen-band photometry, and a recent Subaru/Multi-object InfraRed Camera and Spectrograph (MOIRCS) near-infrared spectroscopic follow-up to constrain the physical properties of SFGs in CL J1449+0856 and in a mass-matched field sample. After a conservative removal of active galactic nuclei, stacking individual MOIRCS spectra of 6 (31) sources in the cluster (field) in the mass range $10 \leqslant \log(M/M_{\odot}) \leqslant 11$, we find a $\sim 4\sigma$ lower [N II]/Hα ratio in the cluster than in the field. Stacking a subsample of 16 field galaxies with Hβ and [O III] in the observed range, we measure an [O III]/Hβ ratio fully compatible with the cluster value. Converting these ratios into metallicities, we find that the cluster SFGs are up to 0.25 dex poorer in metals than their field counterparts, depending on the adopted calibration. The low metallicity in cluster sources is confirmed using alternative indicators. Furthermore, we observe a significantly higher Hα luminosity and equivalent width in the average cluster spectrum than in the field. This is likely due to the enhanced specific star formation rate; even if lower dust reddening and/or an uncertain environmental dependence on the continuum-to-nebular emission differential reddening may play a role. Our findings might be explained by the accretion of pristine gas around galaxies at $z = 2$ and from cluster-scale reservoirs, possibly connected with a phase of rapid halo mass assembly at $z > 2$ and of a high galaxy merging rate.

Key words: galaxies: clusters: individual (Cl J1449+0856) – galaxies: star formation – ISM: abundances

1. INTRODUCTION

The evolution of galaxies is regulated by the complex interplay of multiple physical mechanisms. Distinguishing the influence of external environmental effects from internal factors is crucial to reach a comprehensive understanding of these systems. From this perspective, galaxy clusters offer the perfect occasion to disentagle this situation, comparing samples of field and extreme overdensity galaxies at fixed mass. In the local universe, the influence of the strongest overdensities is manifest in well-known relations, such as the systematic variation of morphological type, luminosity, surface brightness, star formation rate (SFR), and colors with density (e.g., Dressler 1980; Gómez et al. 2003; Baldry et al. 2004; Balogh et al. 2004; Hogg et al. 2004; Blanton et al. 2005). As a result, local virialized and massive clusters are centrally dominated by massive, red, and passive early-type galaxies, while blue star-forming galaxies (SFGs) are preferentially located in the cluster outskirts and in the field. A key to deciphering the origin of the observed local environmental trends is the study of high redshift cluster galaxies as compared to the field. Unlike the extended and increasing statistics of well-studied clusters at $z < 1.5$ in the literature, only a handful of clusters above this redshift have been confirmed today (e.g., Andreon et al. 2009; Papovich et al. 2010; Fassbender et al. 2011; Gobat et al. 2011; Santos et al. 2011; Stanford et al. 2012; Zeimann et al. 2012; Muzzin et al. 2013). Studying the redshift interval above $z > 1.5$ is crucial as we approach the era when the first massive clusters begin to emerge and an epoch where galaxies were still assembling a large fraction of their stellar mass through active star formation (Daddi et al. 2007). In addition to the low statistics, the mentioned properties which designate an evolved cluster at $z = 0$ become progressively blurred at increasing redshift, making it difficult to fully characterize the evolutionary stage of overdensities and, consequently, to quantify their effect on galaxy evolution. Despite these difficulties, sustained efforts have been, and continue to be, made to detect, confirm, and characterize high-redshift clusters. In particular, the recent dramatic improvement in near-infrared (near-IR) multi-object spectrographs has opened the door to the study of the physical properties of ionized gas in SFGs through a set of emission lines that have been well studied in local objects, such as Hβ, [O III]λ5007 (hereafter [O III]), Hα, and [N II]λ6584 (hereafter [N II]). These lines also provide access to the gas-phase metallicity in SFGs, if properly calibrated. A mass–metallicity relation (MZR) has been shown to be in place from $z = 0$ (Tremonti et al. 2004) up to a redshift of $\sim$3–4 (Savaglio et al. 2005; Erb et al. 2006; Troncoso et al. 2014; Zahid et al. 2014b; Wuyts et al. 2014, and others), indicating that more massive galaxies are also more metal-rich at almost any epoch. As recent modeling suggests (e.g., Davé et al. 2012; Lilly et al. 2013), this relation may result from secular metal enrichment of the gas through stellar winds from young stars, modulated by galactic outflows and inflows and by the formation of a subsequent generation of stars. At increasing

redshift, the gas-phase metallicity in SFGs is observed to decrease, but our knowledge of possible effects of the surrounding environment on metal enrichment is still uncertain. In the local universe, the environmental effect seems to be limited, if at all present (Mouhcine et al. 2007; Cooper et al. 2008; Ellison et al. 2009; Hughes et al. 2013), and recent studies at high redshifts have focused only on few protoclusters at $z > 2$ (Kulas et al. 2013; Shimakawa et al. 2015). In this work, we present results relative to the farthest spectroscopically confirmed X-ray detected cluster discovered to date, CL J1449+0856 at $z = 1.99$ (Gobat et al. 2011, 2013, hereafter G11, G13). As indicated by the presence of a dominant population of red, massive, and passive galaxies in its core (Strazzullo et al. 2013, hereafter S13), and coupled with the X-ray detection, CL J1449+0856 is in a relatively evolved phase compared with other known structures at the same epoch, making it the potential progenitor of a massive local cluster (G11). These features physically distinguish this overdensity from lower halo mass, SFG dominated, rapidly assembling protoclusters at similar or higher redshifts (e.g., Steidel et al. 2005; Kodama et al. 2013) and potentially these intrinsically different structures may give rise to different effects on their host galaxies. We present here a recent Subaru/Multi-object InfraRed Camera and Spectrograph (MOIRCS) follow-up of the star-forming population in CL J1449+0856, for which we primarily measured Hα and [N II] emission lines. Incorporating previous information about [O III] and Hβ from *Hubble Space Telescope (HST)*/WFC3 G141 slitless spectroscopy (G13), we can estimate the metallicity through the N2 = log([N II]/Hα) and O3N2 = log[([O III]/Hβ)/([N II]/Hα)] indicators (Alloin et al. 1979), exploring different calibrations proposed in recent literature (Pettini & Pagel 2004; Steidel et al. 2014). We compare the MZR and other interstellar medium (ISM) properties of SFGs in CL J1449+0856 with a mass-matched field sample at comparable redshift, allowing for a direct probe of the environmental effects of relatively evolved overdensities on SFGs at $z = 2$.

This paper is organized as follows. In Section 2, we describe the sample selection and the near-IR spectroscopic and ancillary data used for the analysis. In Section 3, we present the full photometric and spectroscopic analysis of the data set along with the derived ISM physical condition through currently used line diagnostic diagrams. We show the results about the MZR in Section 4 and we discuss potential implications in Section 5. Section 6 summarizes the main findings of this work. Additional technical remarks are reported in the Appendix. Throughout the paper we adopt a flat ΛCDM cosmology with $\Omega_m = 0.3$, $\Omega_\Lambda = 0.7$ and $H_0 = 70\,\mathrm{km\,s^{-1}\,Mpc^{-1}}$, and a Salpeter initial mass function (IMF, Salpeter 1955). When necessary we converted results from literature obtained with other IMFs to a Salpeter IMF.

2. DATA AND SAMPLE SELECTION

Galaxy populations in CL J1449+0856 were investigated in G11, G13, and S13. The cluster is spectroscopically confirmed with currently 27 members identified with Very Large Telescope/VIMOS and FORS2, and WFC3 spectroscopy (G11, G13). Most spectroscopic redshifts in the field of CL J1449+0856 come from the WFC3 G141 spectroscopic follow-up (Figure 1), with 140 redshift determinations over a $\sim$4 arcmin^2 area, based on emission lines (typically [O II] λ3727, [Ne III], Hβ, [O III] at $z \sim 2$) or on continuum breaks in the spectral range 1.1–1.7 μm (full details can be found in G13). These include 68 [O III] emitters, 17 of which belong to the cluster. CL J1449+0856 was also imaged at wavelengths from X-ray to radio (G13). In this work, we used the same photometric catalogs as in S13, including optical/NIR photometry in 13 passbands from U to 4.5 μm. Sources were detected in the WFC3/F140W band, and photometry was measured with SExtractor (Bertin & Arnouts 1996), as well as with GALFIT (Peng et al. 2002, 2010) modeling. Based on photometric redshifts determined on such photometry, a sample of candidate cluster members was identified in the cluster's central region, virtually complete at $M \gtrsim 10^{10}\,M_\odot$, although affected by significant contamination especially below $10^{10}\,M_\odot$. Galaxies were also broadly classified as "passive" or "star-forming" based on restframe *UVJ* colors (Wuyts et al. 2007; Williams et al. 2009) and spectral energy distribution fitting (SED, S13). In this work, we focus on SFGs in the mass range of $10 \leqslant \log(M/M_\odot) \leqslant 11$. The full sample of cluster galaxies in the F140W-based catalog includes six spectroscopically confirmed and two candidate star-forming cluster members in this mass range.

For our MOIRCS near-IR follow-up, we selected a sample of 110 objects. These included 76 sources in CL 1449+0856 field, where we gave the highest priority to WFC3 spectroscopically confirmed star-forming members (10 objects: 2 with $M < 10^{10}\,M_\odot$, 6 with $10^{10}\,M_\odot \leqslant M \leqslant 10^{11}\,M_\odot$, and 2 with $M > 10^{11}\,M_\odot$) and to star-forming objects from the pool of candidate members according to their probability of belonging to the cluster (S13) and irrespectively of their mass. We note here that cluster SFGs were not specifically selected to be [O III] emitters. The two candidates in the mass range of $10 \leqslant \log(M/M_\odot) \leqslant 11$ were not observed due to geometrical constraints in slit positioning. In the area covered by WFC3, we selected 13 [O III] emitters that did not belong to the overdensity, which became part of the field control sample at $z \sim 2$. Outside the WFC3 field, where no spectroscopy was available, we selected field objects with $z_{\rm phot} \geqslant 2$ with the highest chances to detect Hα, i.e., with an estimated Hα flux $\geqslant 3 \times 10^{-17}\,\mathrm{erg\,cm^{-2}\,s^{-1}}$ from the SED-based SFR and reddening estimates (see Section 3). Finally, to further extend our field control sample, we observed 34 *BzK*-SFGs (Daddi et al. 2004) with $z_{\rm phot} \sim 2$ with an estimated Hα flux $\geqslant 3 \times 10^{-17}$ erg cm^{-2} s^{-1} in the COSMOS field (Scoville et al. 2007). A posteriori, the predicted Hα was $\sim$25% lower than the measured flux for these field Hα-selected sources, probably due to Malmquist bias. We note here that, even if the total integration time over the COSMOS field is shorter than over the cluster field, this does not substantially impact the main results of this work, based on the stacking of sources (see Section 3.2). The objects in the COSMOS field contributed to $\sim$30% of the total number of field sources in the final stacked spectrum (10/31) and reached Hα fluxes comparable to the dimmest sources in CL 1449+0856 field (3.2×10^{-17} and 3.3×10^{-17} erg cm^{-2} s^{-1} at $>5\sigma$ in the cluster and COSMOS field, respectively).

2.1. Subaru/MOIRCS Spectroscopy

We carried out near-IR spectroscopy with MOIRCS at the Subaru Telescope (Ichikawa et al. 2006). Two Hawaii-2 2048 × 2048 detectors cover the $4' \times 7'$ FoV and up to 40 slits can be placed within the inner $6'$ diameter circular region. We used the *HK*500 grism with $0''.7$ wide slits, which provides a

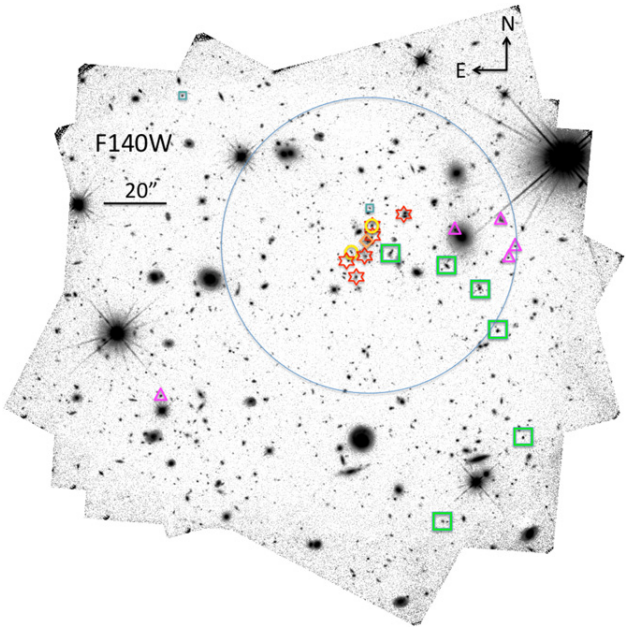

Figure 1. Deep F140W image of CL J1449+0856 and its spectroscopically confirmed members in the field observed with WFC3 (G13). Red stars mark passive galaxies. Yellow circles indicate X-ray detected AGNs. Green squares indicate SFGs in the mass range of $10 \leqslant \log(M/M_{\odot}) \leqslant 11$ and blue squares indicate SFGs in the mass range of $\log(M/M_{\odot}) < 10$, both targeted and detected with MOIRCS. Purple triangles indicate other SFGs not targeted with MOIRCS. The orange diamond shows the assembling brightest central galaxy. The blue solid circle represents the putative $R_{200} \sim 0.4$ Mpc radius (physical, G13).

resolving power of $R \simeq 500$ along the 13000–23000 spectral range. A total of three masks were designed, two for the CL J1449+0856 field and one for the COSMOS field. The observations were carried out in a single run on three consecutive nights in 2013 April. A sequence of 600s integrations was taken with a standard ABAB 1.″5 dithering pattern. Calibration frames of an A0V standard star and dome flat fields were taken at either the beginning or the end of each night. We integrated the images for a total of 7.3, 6.7, and 3.4 hr on 38, 38, and 34 galaxies for Mask 1 and 2 on CL J1449+0856 and Mask 3 in the COSMOS field, respectively, with a mean seeing of ∼0.″6 during three clear nights. The observation plan is summarized in Table 1.

We reduced the data with the MCSMDP pipeline[8](Yoshikawa et al. 2010) combined with custom IDL scripts. First, the data were flat-fielded employing dome-flat frames collected in the same configuration of science frames, and bad pixels and other detector defects were removed using masks provided in the pipeline. Then, cosmic rays were removed by combining each A frame with the corresponding dithered B image. The sky subtraction was automatically performed subtracting each B frame to the corrisponding A image. Then the distortion introduced by the detectors was corrected using the coefficients used in the MOIRCS imaging reduction package. Each 2D spectrum was then cut from every global frame and wavelength calibrated on a grid of bright OH-airglow lines (Rousselot et al. 2000), with an uncertainty of half a pixel, i.e., ∼3.5. We co-added all of the 2D spectra, down-weighting the frames taken in worse atmospheric conditions to minimize the effect of variable seeing during the observing run. We finally extracted the 1D spectra and flux-calibrated them by comparing with a standard A0V stellar spectrum. We estimated aperture corrections (∼1.3 on average) comparing the integrated flux within the *H* and *Ks* bands with the total photometric values. As a final step, we modeled the noise at each wavelength, taking into account possible slit-to-slit and wavelength-dependent sky variations.

[8] http://www.naoj.org/Observing/DataReduction/

Table 1
Observation Log

Mask ID[a]	Date[b]	Integration time[c] (hr)	Target field[d]
Mask 1	2013 Apr, 7th	4.3	CL J1449+0856
	2013 Apr, 9th	3	CL J1449+0856
Mask 2	2013 Apr, 8th	5	CL J1449+0856
	2013 Apr, 9th	1.7	CL J1449+0856
Mask 3	2013 Apr, 7th	1.7	COSMOS
	2013 Apr, 8th	1.2	COSMOS
	2013 Apr, 9th	0.5	COSMOS

Notes.
[a] ID of the three MOIRCS masks.
[b] Date of observation.
[c] Total integration time per night.
[d] Pointed target field.

We successfully detected (3σ confidence level down to an observed Hα flux of 1.4×10^{-17} erg cm^{-2} s^{-1}) at least one line in 71% of the sample (78/110 galaxies). In 71, 22, 41, and 7 galaxies we detected at 3σ Hα, [N II], [O III], and Hβ, respectively. For galaxies where we detected at least one line at 3σ, we put 2σ upper limits on the other lines, if present in the observed spectral range. When available, we averaged the line fluxes from WFC3 observations with MOIRCS-detected lines, assigning higher weights to higher signal-to-noise ratio (S/N) estimates and properly taking into account the consistency of the [O III]/Hβ ratios and the total flux scaling between the two independent measurements. A total of 49 galaxies have a detection or a 2σ upper limit on all Hβ, [O III], Hα, [N II] emission lines.

3. METHODOLOGY

3.1. SED Fitting

Stellar masses, SFRs, and dust reddening were determined using FAST (Kriek et al. 2009) on the UV to IR photometry. We used Bruzual & Charlot (2003) models with constant star formation histories (SFHs) and a Salpeter IMF (Salpeter 1955). The Calzetti et al. (2000) reddening law was used to estimate the extinction. For the COSMOS sample, for which the photometric coverage probes the rest-frame UV SED with high accuracy, we allowed for a variable UV bump in the fit (Noll et al. 2009). The slope of the attenuation law was not fitted and the derived SFR estimates are consistent with those derived with the Calzetti et al. (2000) law. We note that the choice of a different SFH, possibly rising or exponentially declining, negligibly affects our mass estimates, well within systematic uncertainties (∼0.2 dex). Indeed, for active SFGs at these redshifts, the SED fit gives in most cases very short ages and comparable *e*-folding times, such that the actual SFH is nearly constant whether or not an exponentially increasing or decreasing SFR is used (Maraston et al. 2010). On the

Table 2
Properties of the Six Confirmed Cluster Star-forming Members in the Stack

ID	R.A. (deg)	Decl. (deg)	z_{spec}	$\log(M)$ ($\log(M_\odot)$)	$E(B-V)_{neb}^{SED\,a}$	$SFR_{H\alpha}$ ($M_\odot$ yr^{-1})
ID568	222.3024796	8.9387313	1.987 ± 0.001	10.38	0.33	118 ± 9[b]
ID510	222.2997850	8.9369198	1.988 ± 0.001	10.52	0.53	158 ± 13
ID422	222.2983118	8.9335256	1.988 ± 0.001	10.53	0.43	361 ± 60
ID183	222.2961999	8.9248673	1.990 ± 0.001	10.05	0.10	24 ± 3
ID580	222.3070938	8.9397864	2.001 ± 0.001	10.54	0.43	189 ± 23
ID41	222.3029800	8.9186500	1.991 ± 0.001	10.63	0.50	125 ± 30

Notes.
[a] $E(B-V)_{neb}^{SED}$ is the nebular reddening derived from the SED modeling as $E(B-V)_{cont}/f$ (Section 3.3.3).
[b] ID568 shows peculiar WFC3 emission line maps (Zanella et al. 2015). Using the emission line maps to compute the aperture correction and the reddening prescription from Zanella et al. (2015) would lead to $SFR_{H\alpha} = 77 \pm 9\,M_\odot yr^{-1}$.

contrary, other parameters used in this work are potentially affected by the choice of the SFH, e.g., the SFR. We opted for a constant SFH as it proved to give consistent results in representing the so-called "Main Sequence" of SFGs (MS, Daddi et al. 2007; Rodighiero et al. 2014), matching the SFRs derived independently from Hα fluxes and FIR and X-ray stacking. We fitted the photometry for both the aperture-based and the GALFIT-based catalogs (see Section 2 and S13). Stellar masses and SFRs from the SExtractor catalog were corrected based on total-to-aperture flux ratios ($\lesssim$0.15 dex for the sample used here). For those galaxies for which the IRAC photometry suffers from a potentially heavy contamination from neighbors (∼10% of our sample), we excluded the 3.6–4.5 μm bands from the fitting procedure. The two photometric catalogs yield broadly consistent parameter values (e.g., a ∼0.1 dex difference in total stellar masses).

3.2. Stacking

In order to maximize the information derivable from the observed spectra and to find an average trend for the cluster and field samples, we stacked individual spectra. We blueshifted the spectra to the rest-frame and registered them on a common grid of ∼2.7 and ∼3.7 step for the cluster and field, respectively. Then for every wavelength step we averaged the flux values, weighting for the inverse variance if a sufficiently high number of spectra were co-added ($N > 10$). On the other hand, a straight mean was computed in stacking a low number of spectra ($N < 10$), not to introduce wavelength dependent biases. We note here that averaging individual spectra does not necessarily coincide with averaging spectral derived quantities. The difference between these two averaged trends depends on the relationship between line fluxes and the derived quantities. In our case, we estimated the impact of this difference on the mean metallicity calculated through the line ratio [N II]/Hα for a population of MS–SFGs. For masses of $M \geqslant 10^{10}\,M_\odot$, considering the low number statistics for the cluster sample, the two computed averages are similar (<4% difference). Therefore, we adopted the mean metallicities coming from the stacking procedure as representative of the population without applying any other correction. The details of this calculation are reported in the Appendix.

Considering the low number of sources with $\log(M/M_\odot) < 10$ and $\log(M/M_\odot) > 11$, we opted for stacking all galaxies with a spectroscopic redshift determination and Hα coverage in the mass range of $10 \leqslant \log(M/M_\odot) \leqslant 11$. To investigate possible environmental effects, we stacked the cluster and field sources separately, after a conservative active galactic nuclei (AGNs) removal (see Section 3.3.1). We stacked six sources without implementing any weighting scheme for the cluster sample at $z = 1.99$ (Table 2). In the same mass bin, we stacked 31 field sources ($\langle z \rangle = 1.92$) with Hα and [N II] in the observed range and a subsample of 16 galaxies ($\langle z \rangle = 2.14$) with Hβ and [O III] in addition. Given the number of objects, we applied the optimal weighting described above to the field sample. Unless noted otherwise, in the rest of this work, we will use the 31 sources field stack as a main term of comparison for the analysis of environmental effects to exploit at maximum the sample observed with MOIRCS and we refer to it as the "field stack." However, we made use of the 16-source stacked subsample when necessary, i.e., when [O III] or Hβ fluxes were required. The [N II]/Hα ratio in the 31-source and 16-source field stacks is consistent within the uncertainties. The stacked spectra are shown in Figures 2 and 3, and their photometric and spectroscopic properties are summarized in Tables 3 and 4. In Figure 4, we plot the continuum-subtracted stacked spectra normalized to their Hα total fluxes. Furthermore, we checked if the brightest Hα emitters biased the average spectra, stacking individual sources normalized by their observed and intrinsic Hα fluxes. In both cases, [N II]/Hα and [O III]/Hβ are fully compatible with the non- and optimally weighted measurements within 1σ error bars. We also stacked only five cluster sources at a time to check for the impact of low number statistics. In all the cases, [N II]/Hα and [O III]/Hβ ratios are consistent within 1σ with the non-weighted measurements, except for the [O III]/Hβ ratio when stacking only the upper limits on [N II] (in this case, the ratio varies within 2σ error bars, suggesting possible important physical variance within the sample). We note here that among the six cluster sources in the stack, only the brightest one in Hα is detected in [N II] at 2σ and corresponds to the lowest [N II]/Hα ratio, which is nevertheless consistent with the average value for the remaining five cluster sources. Therefore, the [N II] detection is likely the effect of the bright Hα emission. Finally, all six cluster SFGs in the $10 \leqslant \log(M/M_\odot) \leqslant 11$ mass range have a WFC3 spectrum, and for 5/6 sources the 3600–5700 rest-frame interval is covered, giving access to the [O II]λ3727 emission line ([O II] in the following). Hence, we stacked the WFC3 spectra as done for MOIRCS spectra, rescaling to match the absolute fluxes from broadband photometry. The final stacked [O III] and Hβ fluxes from the WFC3 and MOIRCS spectra result fully compatible within the uncertainties.

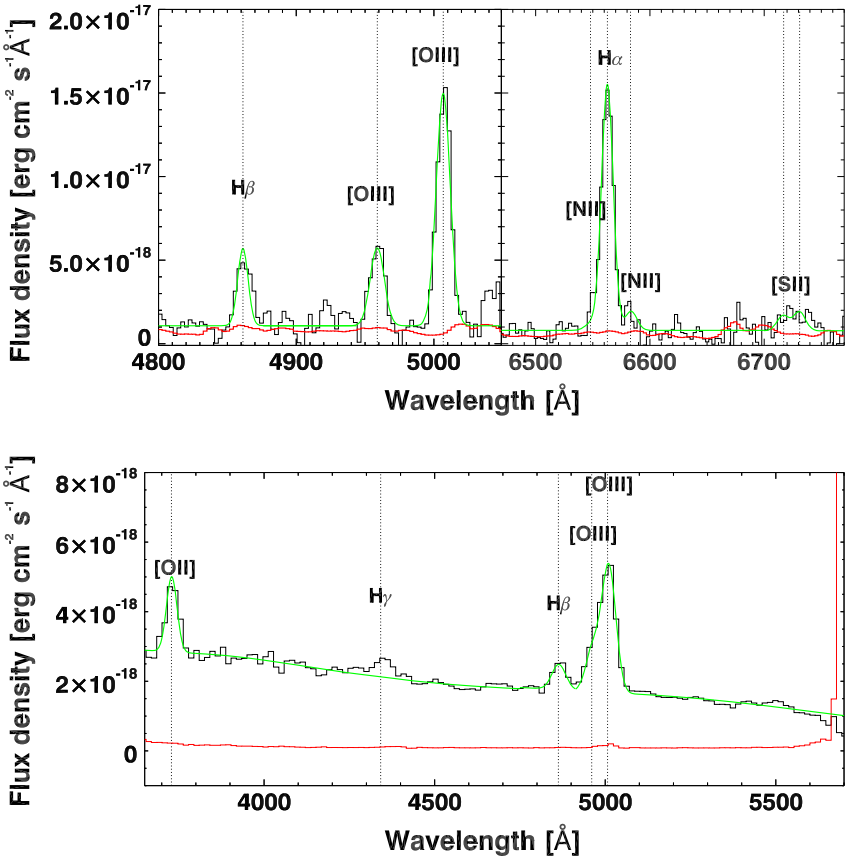

Figure 2. MOIRCS (top panel) and WFC3 (bottom panel) stacked spectra and noise of the sample of six cluster SFGs in the mass range of $10 \leqslant \log(M/M_{\odot}) \leqslant 11$. The black and red lines, respectively, represent the stacked spectra and noise. The green line shows the best fit for the emission lines. Vertical dotted lines mark the expected location of emission lines of interest, as labeled.

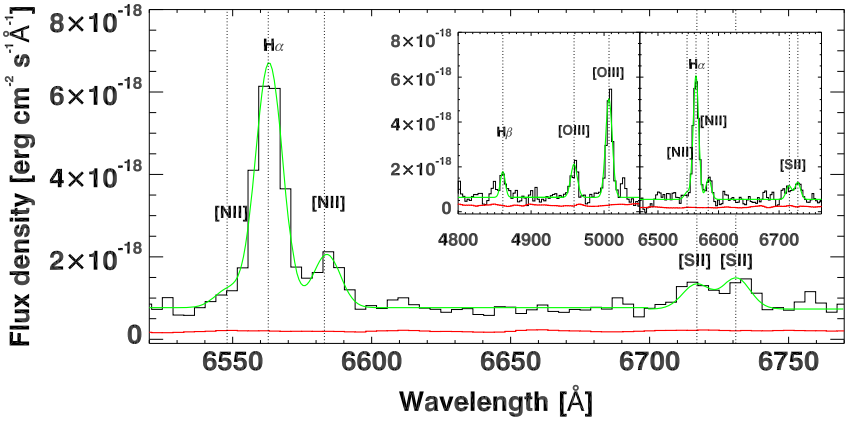

Figure 3. MOIRCS stacked spectrum and noise of the sample of 31 field SFGs in the mass range $10 \leqslant \log(M/M_{\odot}) \leqslant 11$ with Hα and [N II] in the observed wavelength range. The black and red lines, respectively, represent the stacked spectrum and noise. The green line shows the best fit for the emission lines. The onset shows the MOIRCS stacked spectrum and noise for the subsample of 16 field SFGs in the same mass range with Hβ, [O III], Hα, and [N II] in the observed wavelength range. Vertical dotted lines mark the expected location of emission lines of interest, as labeled.

3.3. Line Fluxes

We measured line fluxes fitting Gaussian profiles to the emission lines on flux calibrated and aperture corrected spectra. We used the squared inverse of the noise array to weigh the fitting and to estimate the errors on total fluxes and line positions and thus on the redshift determination. Using the IDL script MPFIT (Markwardt 2009), at the same time, we fitted three Gaussian profiles lying on a flat continuum to measure [NII]$\lambda\lambda$6548, 6583 and Hα fluxes. We modeled the local continuum around each emission line in wavelength ranges large enough to be dominated by continuum emission (∼1000). In the very few cases where a flat continuum did not provide a good model, we fitted a polynomial curve. We left the Hα central wavelength and FWHM free to vary in the fit, while we fixed the [N II] doublet lines to share a common line width value set by FWHM(Hα) (in terms of velocity), their expected positions relatively to Hα, and their flux ratio to 3.05 (Storey &

Table 3
Stacked Spectra Properties

Environment	No. sources	$\langle z \rangle$	$\log(M)$ ($\log(M_\odot)$)	SFR_{SED} ($M_\odot$ yr^{-1})	$E(B-V)_{cont}$	$SFR_{H\alpha}$ ($M_\odot$ yr)$^{-1}$	$E(B-V)_{neb}$
Cluster	6	1.99	10.47	101	0.29	112	0.32
Field	31	1.92	10.57	126	0.31	68	...
Field	16	2.14	10.52	110	0.33	75	0.48

Note. SED derived quantities are the mean values of single sources in the stacked spectra.

Table 4
Stacked Spectra Observed Fluxes

Environment	No. sources	[O II] (cgs)	Hβ (cgs)	[O III] (cgs)	Hα (cgs)	[N II] (cgs)	[S II]$_{tot}$[a] (cgs)
Cluster	6	0.800 ± 0.065[b]	0.463 ± 0.065	1.781 ± 0.043	1.915 ± 0.061	0.145 ± 0.048	0.119 ± 0.026
Field	31	...	...	...	0.754 ± 0.020	0.159 ± 0.015	0.075 ± 0.011
Field	16	...	0.128 ± 0.016	0.499 ± 0.019	0.645 ± 0.016	0.104 ± 0.012	0.070 ± 0.010

Notes. The observed line fluxes are expressed in units of 10^{-16} erg cm^{-2} s^{-1}. [O II] fluxes come from WFC3 observations (G13).
[a] Total combined flux of [S II]$\lambda\lambda$6716, 6731.
[b] Value for 5/6 cluster members with [O II] coverage.

Zeippen 2000). Similarly, we simultaneously fitted the [OIII] $\lambda\lambda$4959, 5007 lines, fixing their position and width according to Hα values and their intensity ratio to 2.98. Any other line in the observed range, both single or in multiplets, was fitted following the same procedure. We estimated flux uncertainties with MPFIT and rescaled them according to the χ^2 value when $\chi^2 > 1.5$. In addition, we ran Monte Carlo simulations, placing mock lines in empty spectral regions, recovering consistent uncertainties within ~5%, confirming the reliability of our noise estimate. We finally estimated the Hα and Hβ stellar absorption measuring the continuum at the proper wavelengths and assuming absorption equivalent widths $EW^{abs}_{H\alpha} = 3.5$ and $EW^{abs}_{H\beta} = 5$, as estimated from SED modeling. This correction is $\lesssim$15% and ~30% for Hα and Hβ, respectively.

3.3.1. Line Diagnostics Diagrams

Following the pioneering work by Baldwin et al. (1981), many studies have shown that the proper combination of ratios of collisionally excited and recombination lines can provide useful information not only about the element abundances in the gas in galaxies, but also about its ionization state and the primary ionizing source (e.g., Kewley & Dopita 2002; Kewley et al. 2013a). In this work, we investigate the gas state using the [N II]/Hα–[O III]/Hβ diagram, commonly referred to as the BPT diagram. This can be used to distinguish line-emitting galaxies mainly powered by an AGN from those dominated by star formation: the radiation field emitted by the disk accreting around an AGN is harder, increasing the oxygen and nitrogen ionization and producing larger [O III] and [N II] fluxes with respect to the values reached by SF-powered ionization. However, the situation may be considerably different at higher redshifts: an evolution of the electron density, the ionization parameter, or the hardness of the radiation field can shift the locus of the SF sequence. Recent developments in multi-object near-IR spectroscopy have allowed for the observation of an increasing number of samples of line emitters, extending the study of the potential evolution of line ratios with cosmic time (e.g., Kewley et al. 2013a; Holden et al. 2014) and the role of selection effects (Juneau et al. 2014) to earlier epochs, up to $z \geqslant 1.5$. Recent results by Steidel et al. (2014, S14 in the following) for a sample of $z \sim 2.3$ SFGs point toward a substantial vertical shift in the BPT diagram due to a harder field ionizing the ISM, qualitatively in agreement with some theoretical expectations (Kewley et al. 2013a, 2013b; but see, e.g., Coil et al. 2014; Shapley et al. 2014 for alternative results). Interestingly, S14 interpret the locus of SFGs mainly as an "ionization parameter" sequence, in contrast to the usual interpretation of a "gas-phase metallicity" sequence given in the local universe (Kewley & Ellison 2008). Figure 5 shows our sample in the BPT diagram and a reference sample at $z \sim 1.55$ from the Subaru/FMOS survey (Zahid et al. 2014b). A low-redshift ($0.04 < z < 0.2$) sample of 299,098 galaxies selected from SDSS DR7 (Abazajian et al. 2009) is shown for comparison. Following Juneau et al. (2014), galaxies were selected to have well-constrained [O III]/Hβ and [N II]/Hα line ratios ($S/N > 3/\sqrt{2}$, corresponding to each line with $S/N > 3$ or to combinations of a weaker and a stronger line, provided that the overall line ratio is constrained to this minimum significance). Line flux measurements and uncertainties were taken from the MPA/JHU catalogs, and adjusted as detailed by Juneau et al. (2014). A systematic shift with respect to the locus of SFGs in the local universe is present, qualitatively in agreement with a possible increase of the hardness of the radiation field, even if the data at our disposal do not allow us to recognize a specific direction of the shift. To exclude AGNs from our sample, we used the conservative line of exclusion as a function of redshift provided by Equation (5) in Kewley et al. (2013a). Alternative emission line diagnostics relying on [O III]/Hβ and either host color or stellar mass have been developed (e.g., Juneau et al. 2011; Yan et al. 2011). However, ~50% of the field stacked sample (15/31 sources) does not have Hβ in the observed range. To obviate this issue, we coupled the BPT diagnostics with the [N II]/Hα–observed Hα equivalent width (EW(Hα)) diagram (Figure 6). The local SDSS sample is shown again for comparison (here we considered only galaxies with $S/N(EW(H\alpha)) > 3$, cutting the BPT local sample to 272,562 objects). In this diagram, [N II]/Hα traces the ionized

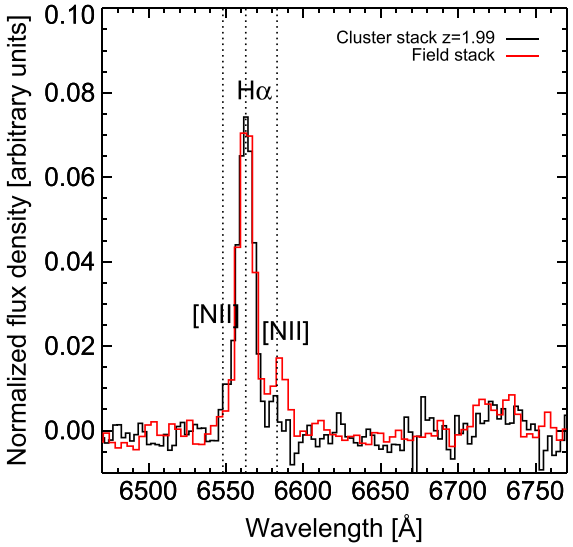

Figure 4. Black and red lines, respectively, represent the continuum-subtracted MOIRCS stacked spectra of the sample of 6 cluster SFGs and 31 field SFGs in the mass range of $10 \leqslant \log(M/M_{\odot}) \leqslant 11$ with Hα and [N II] in the observed wavelength range, normalized to Hα fluxes. Vertical dotted lines mark the expected location of emission lines of interest, as labeled.

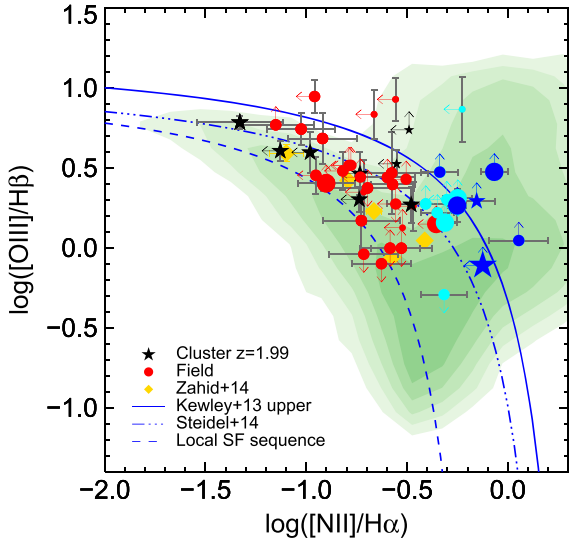

Figure 5. BPT diagram for the MOIRCS spectroscopic sample. Red circles and black stars represent the field and cluster samples, respectively. Cyan and blue symbols mark the objects excluded from the SF sample as AGNs from X-ray, radio, [N II]/Hα–EW(Hα), or the solid curve shown (see the text and Figure 6 for details). Symbol sizes scale as the stellar mass. Golden diamonds represent the stacked points from the FMOS survey at $z \sim 1.55$ (Zahid et al. 2014b). Arrows indicate 2σ upper and lower limits both for the x and y axes. The blue dashed line shows the local SF sequence (Equation (3), Kewley et al. 2013a), the blue dash–dotted line indicates the empirical SF sequence at $z \sim 2.3$ from Steidel et al. (2014), and the blue solid line is the AGN-SFG dividing line at $z = 2$ (Equation (5), Kewley et al. 2013a). Green shaded contours show the SDSS $z \sim 0.1$ sample.

gas conditions, as higher [N II]/Hα values are connected to harder powering sources, while EW(Hα) measures the power of the ionizing source in relation with the continuum emission of the underlying stellar populations (Cid Fernandes et al. 2010, 2011). In this diagram, all of the potential AGNs that we selected on the BPT basis occupy the same region at high [N II]/Hα ratios. In total, we conservatively excluded 22 objects as AGN-powered sources and none of these sources were included in the stacked spectra. Four points above the nominal line of exclusion in the BPT were not discarded as their upper limits on [N II]/Hα are still compatible with the star-forming region in the [N II]/Hα–observed EW(Hα) diagram. We note that 3/4 objects have $\log(M/M_{\odot}) < 10$ and thus are not part of the stacked spectra. Excluding the fourth BPT potential outlier from the field stacked spectrum would slightly strengthen the significance (well within the uncertainties) of the main results of this work, increasing the [N II]/Hα field average value (see below). Even if we cannot exclude potential AGN contamination for these sources, we lack definitive evidence that they are mainly AGN-dominated and, keeping the most conservative approach in terms of significance of the final results, we retained these four objects in the final samples. Among these 22 sources, 2 are known to be a soft and a hard X-ray AGN in CL J1449+0856, both with $\log(M/M_{\odot}) > 11$ (G13), while 2 other field objects are massive radiogalaxies in the COSMOS field. All of these independently known AGNs lie either above the line of exclusion in the BPT diagram or above $\log([\text{N II}]/\text{H}\alpha) = -0.4$ in the [N II]/Hα–observed EW (Hα) plane, as expected. We note here that the choice of the AGNs to remove does not change if we consider a dereddened EW(Hα). In Figure 6, we show in addition the position of the cluster and field stacked values. Comparing these two, we note that the cluster and field samples show a $>4\sigma$ significant difference in [N II]/Hα. Considering the subsample of 16 field galaxies with all the BPT lines, the difference is still tentatively present ($\sim 2.7\sigma$), even if the significance is reduced due to lower number statistics and S/N. Moreover, in this case the cluster and field [O III]/Hβ ratios are fully compatible within the error bars (0.585 ± 0.062 and 0.591 ± 0.058 dex, respectively). As a consequence, the ([O III]/Hβ)/([N II]/Hα) ratio is compatible between the two samples, given the increased uncertainties. Figure 6 shows also a 0.37 dex difference ($\sim 4.7\sigma$ significant) in the observed EW(Hα) between the cluster and the field, which reflects the 2.5 times higher observed Hα luminosity in the cluster stack (see Section 3.3.4 for further discussion). Finally, we observe a significant [S II] $\lambda\lambda$6716, 6731 emission in the stacked spectra, but the S/N is not high enough to accurately measure the ratio of the two lines and hence directly estimate the electron density n_e (Osterbrock & Ferland 2006). Therefore, we fixed this ratio compatibly with typical n_e values in [H II] regions (n_e = 100–1000 cm^{-3}, Osterbrock & Ferland 2006) and measured the total combined flux $[\text{SII}]_{\text{tot}} = [\text{S II}]\lambda6716{+}\lambda6731$ reported in Table 4.

3.3.2. Gas-phase Metallicities

Different methods have been proposed through the years to estimate the gas-phase metallicity in galaxies. The safest method involves the ratio of the [O III]λ4363 auroral line and lower excitation lines as [O III]$\lambda\lambda$4959, 5007, which allows us to directly evaluate the oxygen abundance through the gas electron temperature (T_e). However, [O III]λ4363 is weak even in low-metallicity regions and generally difficult to measure in high-redshift galaxies. Other empirical methods have been proposed to circumvent this problem, calibrating the ratios of stronger lines against T_e in H II regions. Alternatively, theoretical photoionization models may be employed to predict the line fluxes and derive the gas-phase abundances (see Kewley & Ellison 2008 for a census of gas-phase metallicity

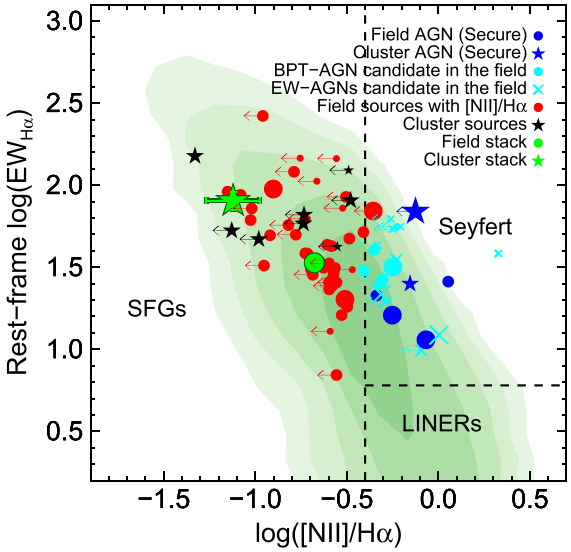

Figure 6. [N II]/Hα–rest-frame reddening uncorrected EW(Hα) diagram for the MOIRCS spectroscopic sample. Red circles and black stars represent the field and cluster samples, respectively. Blue circles and stars, respectively, represent field and cluster AGNs known from X-ray, radio, and BPT diagram. Cyan symbols represent AGN candidates in the present diagram and in the BPT. Symbol sizes scale as the stellar mass. Arrows indicate 2σ upper limits. The green circle and star represent the field and cluster stack, respectively. Green shaded contours show the SDSS $z \sim 0.1$ sample.

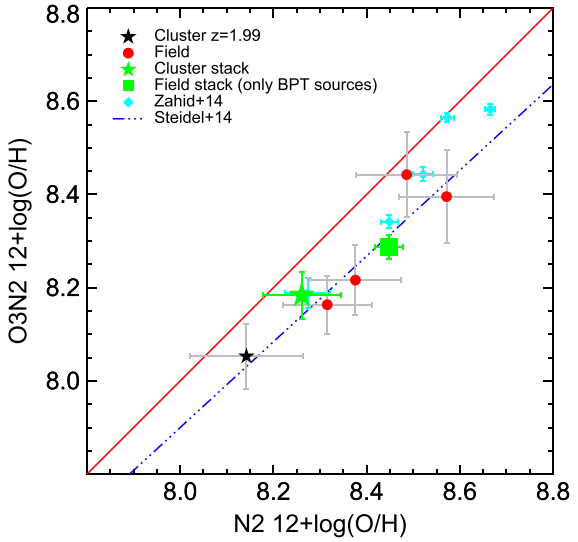

Figure 7. Gas-phase metallicities derived using the N2 and O3N2 indicators calibrated by Pettini & Pagel (2004). Red circles and black stars, respectively, mark individual field and cluster 3σ detections of each line in the O3N2 indicator. The green filled square and star, respectively, represent the measurement for the subsample of 16 field SFGs and cluster stacked sample in the $10 \leqslant \log(M/M_{\odot}) \leqslant 11$ range. Cyan circles mark the stacked values at $z \sim 1.55$ from (Zahid et al. 2014b). The blue dashed–dotted line is the linear relation between N2 and O3N2 for the $z \sim 2.3$ from Steidel et al. (2014). A one-to-one red line is shown as a comparison.

calibrations). In general, the use of different methods leads to a systematic difference in absolute metallicity values of up to ~0.3 dex (Kewley & Ellison 2008). Relative comparisons among different samples from different studies are still meaningful if all the measurements are reported to the same calibration system. For this work, we decided to use the N2 = log([N II]/Hα) metallicity indicator, given the presence of both [N II] and Hα in a relatively clear window of the K_s band at $z = 2$. Pettini & Pagel (2004, PP04 in the following) calibrated N2 against the T_e method in a local sample of H II regions, expressing the gas-phase metallicity as

$$12 + \log(\mathrm{O/H})_{\mathrm{N2,PP04}} = 0.57 \times \mathrm{N2} + 8.90 \quad (1)$$

with a quoted uncertainty of ~0.18 dex. Partial drawbacks of using N2 are its sensitivity to the ionization parameter $\mathcal{U}$ and the saturation of the index at solar metallicities and above, as [N II] becomes the dominant coolant (Baldwin et al. 1981; Kewley & Dopita 2002). The impact of this saturation does not seem to dramatically affect the final metallicity estimate, resulting in a ~0.03 dex underestimate of the final abundance (Zahid et al. 2014a). Other indicators do not suffer from this saturation issue and could potentially be used to confirm the metallicity estimate. When all lines were available, we used the O3N2 = log[([O III]/Hβ)/([N II]/Hα)] as an alternative metallicity indicator. In this case, the PP04 calibration gives

$$12 + \log(\mathrm{O/H})_{\mathrm{O3N2,PP04}} = -0.32 \times \mathrm{O3N2} + 8.73 \quad (2)$$

with a quoted uncertainty of ~0.14 dex. The inclusion of [O III] in the ratio should guarantee sensitivity to increasing metallicity even above solar, as [O III] continues to decrease while [N II] saturates. In practice, we could estimate this index at 3σ confidence only for very few individual sources and for the stacked spectra (Figure 7). In the local universe, these two indicators provide consistent metallicity estimates (Kewley & Ellison 2008). On the contrary, for our samples of high-z galaxies the N2 indicator returns systematically higher gas-phase metallicities compared to the O3N2 indicator (Figure 7), in agreement with other recent findings (Erb et al. 2006; Yabe et al. 2012; Zahid et al. 2014b; S14). Different interpretations and prescriptions to avoid systematic errors have been proposed in several studies (i.e., S14), even if all of them remain quite speculative in the absence of a direct 12 + log(O/H) measurement, i.e., by means of the T_e method. However, all of the studies agree on a probable overall change of the ISM conditions in high-z galaxies with respect to the local universe, as indicated by independent observations (Magdis et al. 2012; Kashino et al. 2013). In principle, an evolution in the hardness of the radiation field, electron density, ionization parameter, or nitrogen-to-oxygen ratio can make the calibration intrinsically wrong for high-redshift galaxies. In their recent work, S14 recalibrated the N2 indicator on a sample of local H II regions matching the physical conditions of their $z \sim 2.3$ galaxies, obtaining

$$12 + \log(\mathrm{O/H})_{\mathrm{N2,S14}} = 0.36 \times \mathrm{N2} + 8.62 \quad (3)$$

with a quoted total scatter of ~0.13 dex. S14 found that N2 is less sensitive to metallicity variations than implied by the PP04 calibration, which substantially overpredicts the metallicities at high redshifts. On the contrary, after S14 recalibration, the O3N2 indicator predicts metallicities similar to those given by the PP04 calibration, especially with the inclusion of a term depending on N/O (Pérez-Montero & Contini 2009):

$$12 + \log(\mathrm{O/H})_{\mathrm{O3N2,S14}} = -0.28 \times \mathrm{O3N2} + 8.66 \quad (4)$$

with a total uncertainty of ~0.12 dex. Reducing the sensitivity of the N2 calibrator to the gas-phase metallicity and leaving intact the one of O3N2, the two ratios predict consistent abundances at $z \sim 2$.

Table 5
Gas-phase Metallicity Estimates for the Stacked Spectra

Environment	$\log(M)$	$12 + \log(O/H)$[a]			
		N2		O3N2	
	$\log(M_\odot)$	PP04[b]	S14[c]	PP04[b]	S14[c]
Cluster	10.47	8.261 ± 0.083	8.216 ± 0.053	8.184 ± 0.051	8.182 ± 0.044
Field	10.57	8.514 ± 0.025	8.376 ± 0.016	8.287 ± 0.025[d]	8.273 ± 0.022[d]

[a] For comparison, the solar value is $12 + \log(O/H) = 8.69$ (Asplund et al. 2009).
[b] Pettini & Pagel (2004) calibration.
[c] Steidel et al. (2014) calibration.
[d] Values for the subsample of 16 field SFGs with Hβ and [O III] in the observed wavelength range.

As mentioned, a cause of concern when estimating gas-phase oxygen abundance through indirect indicators involving other species as N2 and O3N2 is the abundance of these elements relative to oxygen. In the case of N2 and O3N2 indicators, an assumption on the N/O ratio is implied in every calibration, explicitly or implicitly, and ignoring the N/O ratio could result in a systematic effect in the O/H estimation (Pérez-Montero & Contini 2009). An estimation of N/O can be derived from the $N2O2 = \log([N\,II]/[O\,II])$ ratio, as calibrated in the local universe by Pérez-Montero & Contini (2009):

$$\log(N/O) = 0.93 \times N2O2 - 0.20 \quad (5)$$

with a standard deviation of the residuals of 0.24 dex. We could estimate N/O for the cluster stacked sample thanks to the WFC3 [O II] determination after proper dust reddening correction (see next section). This was not possible for the field sample, preventing a fully consistent environmental comparison of N/O. In our case, the inclusion of a N/O correction term in the PP04 N2 calibration (Equation (13) from Pérez-Montero & Contini 2009) leaves virtually unchanged the metallicity estimate for the cluster ($a \sim 0.05$ dex difference, well within the calibration errors). The observed cluster N/O ratio ($\log(N/O) = -1.18 \pm 0.15$) is lower than the solar value ($\log(N/O) \simeq -0.86$, Pilyugin et al. 2012), and close to the "primary" nitrogen abundance predicted by current models ($\log(N/O) \simeq -1.5$, Charlot & Longhetti 2001; Pilyugin et al. 2012; Pérez-Montero & Contini 2009; Andrews & Martini 2013; Dopita et al. 2013) in agreement with the estimated low gas-phase metallicity value. Interestingly, recent works on samples at redshift $z \sim 2$ found a N/O ratio consistent with the solar value and only slowly or not varying with the O/H ratio, and hence with the gas-phase metallicity, at least for highly star-forming systems typical at these redshifts ($SFR \geqslant 10\,M_\odot yr^{-1}$, Andrews & Martini 2013, S14). An alternative explanation is that $z \sim 2$ SFGs show higher N/O ratios at fixed metallicities than local counterparts at low masses ($M \lesssim 10^{10.11}\,M_\odot$ in Shapley et al. 2014, and $M \sim 10^9\,M_\odot$ Masters et al. 2014). If we consider N/O ratios from literature as representative of a general field sample (but check Kulas et al. 2013 for the study of protocluster members in S14 sample) in a mass range and excitation conditions similar to those of our cluster sample, they result to be ~0.2 dex higher than the value measured on the cluster stacked spectrum.

Further indications of the lower metal content in cluster sources are the lower $[N\,II]/[S\,II]_{tot}$ and higher $(H\alpha+[N\,II])/[S\,II]_{tot}$ ratios than the field counterparts (Nagao et al. 2006), even if affected by substantial uncertainties. Moreover, for the cluster stacked sample we estimated the ionization parameter and the gas-phase metallicity using the iterative method of Kobulnicky & Kewley (2004), which involves the $R_{23} = ([O\,II]\lambda3727+[O\,III]\lambda\lambda4959,5007)/H\beta$ and $O_{32} = [O\,III]\lambda\lambda4959,5007/[O\,II]\lambda3727$ indicators. Hβ, and [O III] fluxes. After applying the Kewley & Ellison (2008) conversion to PP04 N2 metallicities, we obtain $12 + \log(O/H) = 8.217$ with ~0.15 dex accuracy, thus compatible with our estimate based on $[N\,II]/H\alpha$ (Table 5). We also obtained a ionization parameter $\mathcal{U} \simeq -2.61$, which is comparable to values measured in high-redshift galaxies ($-2.9 < \mathcal{U} < -2.0$, Kewley et al. 2013a, and references therein). Hence a high-ionization parameter may not be the main driver of the $[N\,II]/H\alpha$ difference that we observed between cluster and field, even if we cannot completely exclude possible effects connected to $\mathcal{U}$ in our analysis.

Overall, while various metallicity estimators may differ on an absolute scale, the systematic difference found between the cluster and the field is robust. Given the lower number of sources with safe O3N2 measurements, we privileged N2 as the primary metallicity indicator. All the gas-phase metallicity estimates are reported in Table 5: in the same mass range, the cluster sample results 0.09–0.25 dex (using $O3N2_{S14}$ and $N2_{PP04}$, respectively) more metal-poor than the field sample, depending on the calibration used.

3.3.3. Nebular $E(B-V)$ Estimate

The dust reddening on stellar light ($E(B-V)_{cont}$) was estimated through SED fitting. However, the amount of dust attenuation toward the emission lines ($E(B-V)_{neb}$) is typically larger than $E(B-V)_{cont}$. Calzetti et al. (2000) find a factor $f = E(B-V)_{cont}/E(B-V)_{neb} = 0.44$ between the two color excesses in the local universe, adopting the Fitzpatrick (1999) law for the nebular reddening and their own law for the continuum reddening ($f = 0.52$ using the Calzetti et al. 2000 reddening law for both the nebular emissions and the continuum). Recent works suggest that this continuum-to-nebular emission differential reddening factor is generally higher for high-redshift galaxies, reducing the difference between stellar and nebular continuum (Kashino et al. 2013; Pannella et al. 2014). Here we attempt to estimate this factor using the Balmer decrement Hα/Hβ and assuming a Case B recombination with a gas temperature of $T = 10^4$ K and an electron density $n_e = 100\,cm^{-3}$, according to which the intrinsic ratio Hα/Hβ is equal to 2.86 (Osterbrock & Ferland 2006). From the observed Hα and Hβ values it is

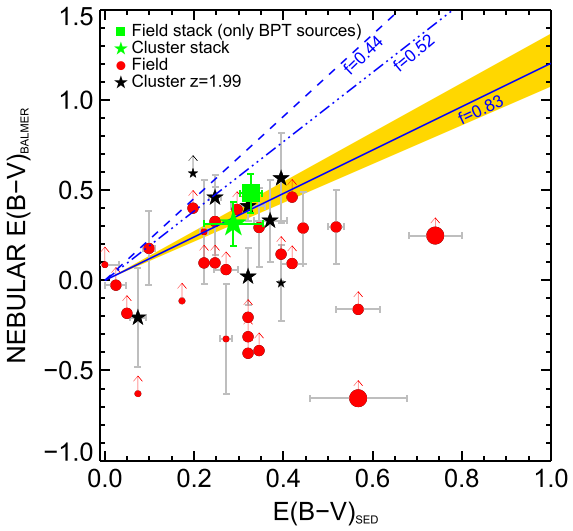

Figure 8. Reddening estimates based on SED fitting and Balmer decrement. Red circles and black stars, respectively, mark field and cluster SFGs with 3σ Hα and Hβ detections. Symbol sizes scale as stellar mass. Arrows mark 3σ lower limits. The green square and star indicate the subsample of 16 field sources with measured [O III] and Hβ and the cluster stacked values, respectively. The blue dashed and dotted–dashed lines represent the $f = 0.44$ ($f = 0.52$) ratio $E(B-V)_{\rm cont}/E(B-V)_{\rm neb}$ obtained in the local universe applying Fitzpatrick–Calzetti (Calzetti–Calzetti) laws for the nebular and continuum reddening, respectively. The blue solid line and the shaded area represent the same ratio using a Calzetti law for both the nebular and continuum reddening and the relative uncertainties quoted in Kashino et al. (2013) for the sample of $z \sim 1.55$ galaxies from the FMOS survey, where $f = 0.83$.

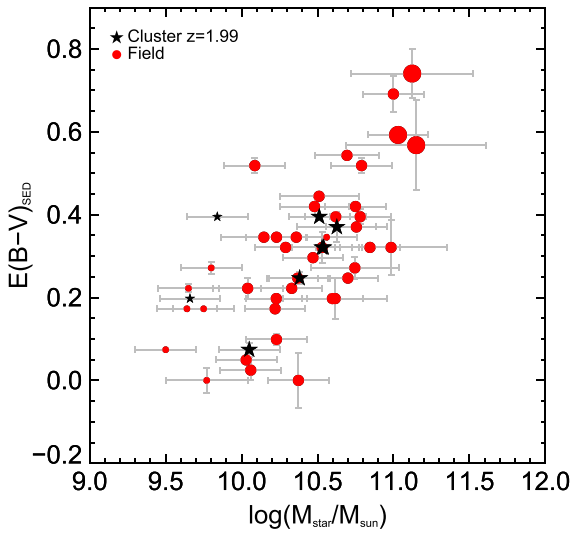

Figure 9. Mass-reddening relation for the MOIRCS spectroscopic sample of SFGs. Red circles and black stars mark the field and cluster samples, respectively. Symbol sizes scale as the stellar mass.

possible to compute

$$E(B-V)_{\rm neb} = \frac{2.5}{k_{\rm H\beta} - k_{\rm H\alpha}} \log\left[\frac{\rm H\alpha/H\beta}{2.86}\right] \quad (6)$$

assuming a proper extiction law. In this work, we assumed the Calzetti et al. (2000) law for both the nebular and continuum reddening, for which $k_{\rm H\beta} = 4.598$ and $k_{\rm H\alpha} = 3.325$.

A limited sample of galaxies with a safe 3σ Hβ detection is available to measure the Balmer decrement on an object-by-object basis. However, we used the values from the stacked spectra to assess this issue for the mean population of SFGs in our sample. In Figure 8, we show the relation between SED based $E(B-V)_{\rm cont}$ and $E(B-V)_{\rm neb}$ derived from the Balmer decrement. The best fitting slope for the 3σ detected stacked values is 0.74 ± 0.22, consistent within the uncertainties with the results from the FMOS survey at $z \sim 1.55$ (Kashino et al. 2013), but still formally in agreement with the local value obtained using the same reddening law. Our best-fit value is in agreement with the alternative estimate that we derived from the fitting of the $E(B-V)_{\rm cont}$-$\rm SFR^{uncorr}_{H\alpha}/SFR^{uncorr}_{UV}$ relation as in Figure 3 of Kashino et al. (2013), namely $f = 0.74 \pm 0.05$.

We checked for possible environmental signatures in the stellar mass-reddening relation (MRR), comparing the cluster and field samples. Figure 9 shows the MRR for our sample of cluster and field SFGs. Both the stellar mass and the reddening estimates come from the SED fitting procedure. In Figure 9, both the cluster and field samples follow the same trend, not revealing any environmental signature in the MRR. Applying a simple linear regression separately for the two samples, we obtain compatible slopes: 0.78 ± 0.42 and 0.59 ± 0.07 for the cluster and field sample, respectively.

3.3.4. A Significant Difference in the Observed EW(Hα)

As shown in Figure 6, there is a 0.37 dex difference ($\sim 4.7\sigma$ significant) in the observed EW(Hα) between the cluster and the field. Such a difference may arise from an enhanced specific star formation rate (sSFR), a variation in the dust reddening correction $E(B-V)$, or in the continuum-to-nebular emission differential reddening factor f between cluster and field, as $\rm EW(H\alpha) \propto sSFR \times 10^{0.4E(B-V)_{cont} k_{H\alpha}(1/f-1)}$. Assuming a common f value in cluster and field SFGs and the average $E(B-V)_{\rm cont}$ values in Table 3, the difference in the observed EW(Hα) is translated into a significant difference in intrinsic EW(Hα) and ascribable to enhanced sSFR in cluster sources. As f is physically linked to the average geometric dust distribution in galaxies star-forming regions (Kashino et al. 2013), there are no immediately evident reasons why the environment should play a role in setting this factor. Hence, considering f constant within different environments would not be a strong assumption. However, we could let this parameter free as well, resulting in a more conservative approach: in this case, the f factor for the field stack is tentatively lower than for the cluster sample, reducing the difference in intrinsic EW (Hα). Moreover, individual estimates of f are hampered by large error bars on the Balmer decrement measurements (Figure 8), not allowing to fully decouple sSFR and reddening effects. Since the two stacked samples have similar stellar masses, an enhancement in sSFR would reflect the 2.5 times higher Hα observed luminosity in the cluster stack (Tables 3–4). However, when converting Hα fluxes to SFR applying the Kennicutt (1998) conversion and the reddening correction, the values for cluster and field are formally compatible. In Figure 10, we show the field and cluster sources in the final stacked samples in the stellar mass–$\rm SFR_{H\alpha}$, $\rm SFR_{SED}$ plane. All the SFRs have been rescaled by a factor of $[(1+z)/(1+1.99)]^{2.8}$ to match the cluster redshift. We adopted the MS parametrization given in Sargent et al. (2014) as a reference. In the right panel, individual cluster sources seem tentatively more star-forming than the field counterparts, populating the upper envelope of the MS, and the lowest [N II]/Hα ratio corresponds to the highest $\rm SFR_{H\alpha}$. However, the average properties of the

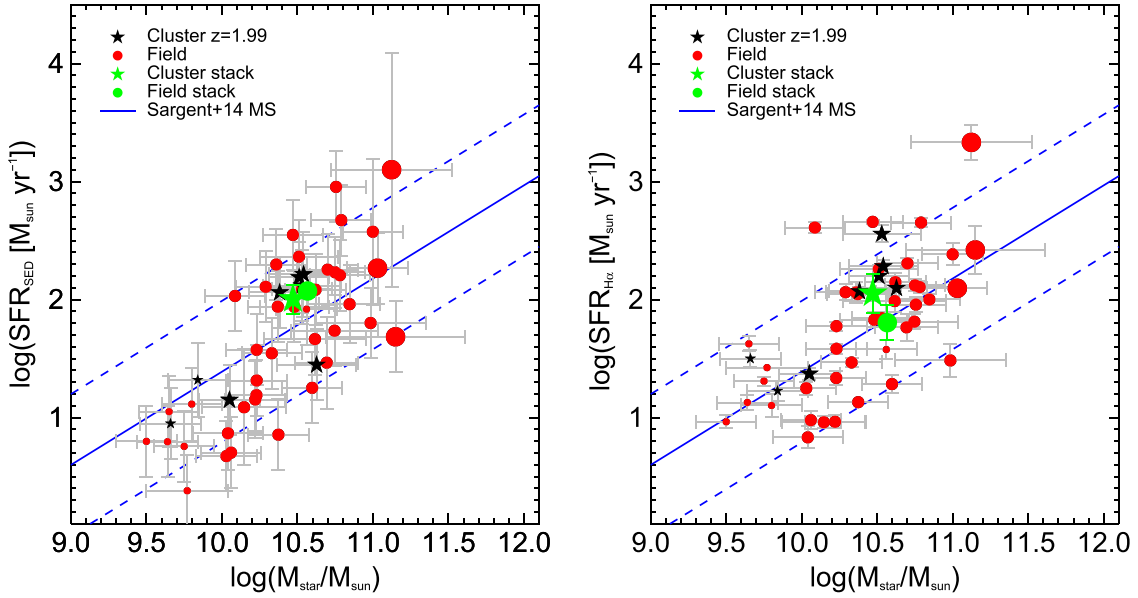

Figure 10. Stellar mass vs. SFR. Red circles and black stars mark the field and cluster SFGs, respectively. Symbol sizes scale as the stellar mass. The green circle and star indicate the field and cluster stacked values, respectively. The blue solid line indicates the MS at $z = 2$ as parametrized in Sargent et al. (2014). The blue dashed lines mark the ± 0.6 dex scatter. Left panel: Hα derived SFR. Right panel: SED derived SFR.

cluster and field populations in the same mass regime are formally compatible, as shown by the stacked values, and this is likely due to the uncertainties on individual f factor estimates. The stacked values are also compatible when considering SFR_{SED}, as shown in left panel of Figure 10, but this may be partly due to the longer timescales probed by the UV stellar emission as a SFR indicator with respect to Hα ($t_{UV} \sim 100$ Myr, $t_{H\alpha} \sim 10$ Myr), which makes SFR_{SED} insensitive to potentially recent episodes of star formation in cluster sources with respect to the field. For reference, we show the comparison between SED- and Hα-based SFRs in Figure 11, where SFR_{SED} for the stacked samples is the mean of the single sources values.

In the most conservative approach, considering the uncertainties on the f factor, we cannot fully disentangle the reddening and sSFR (or SFR) effects in producing the observed EW(Hα) difference. However, reasonably assuming the f factor as independent of the environment and the average $E(B-V)_{cont}$ values from SED modeling, we can decouple the two effects, ascribing the enhanced observed EW(Hα) in cluster sources to an enhancement in sSFR. In any case, we emphasize how Figure 6 shows another significant difference between cluster and field SFGs resulting from this work, in addition to the lower gas-phase metallicity.

4. THE MASS–METALLICITY RELATION

The presence of a correlation between stellar mass and metallicity in SFGs has been known for a long time (Lequeux et al. 1979), both locally (Tremonti et al. 2004) and at increasing redshift (Erb et al. 2006; Kewley & Ellison 2008; Zahid et al. 2012, 2014a; Cullen et al. 2014; Steidel et al. 2014; Wuyts et al. 2014, and many others). This relation can be interpreted as the result of the interplay among the accretion of metal-poor pristine gas, star formation episodes, and enriched gas expulsion through stellar winds (Davé et al. 2012; Lilly et al. 2013; Zahid et al. 2014a). At higher redshifts the overall observed metallicity is lower than in local galaxies, virtually shifting the observed MZR vertically with redshift. In Figure 12, we show the observed [N II]/Hα ratio, a proxy for gas-phase metallicity, as a function of stellar mass. A $>4\sigma$ significant lower ratio is observed in the cluster stack with respect to the field mass-matched sample. This result is unchanged if we consider as a field [N II]/Hα representative value the linear interpolation at $z = 1.99$ of the $z \sim 1.55$ and $z \sim 2.3$ values from Zahid et al. (2014b) and S14, at fixed mass. Quantitatively, the metallicity difference between the cluster and field samples depends on the adopted calibration for [N II]/Hα as shown in the left panels of Figure 13. In the same figure, we show the metallicity derived from the O3N2 indicator (right panels) for the subsample of 16 intermediate mass field SFGs with Hβ and [O III] measurements. Also in this case, given the comparable [O III]/Hβ values of the cluster and the field samples, the difference in the final metallicity values reflects the different [N II]/Hα ratio through the slope of the adopted linear O3N2 calibration—i.e., through the sensitivity to metallicity variations assigned to [N II]/Hα. Metallicity differences vary between 0.09 and 0.25 dex from $O3N2_{S14}$ and $N2_{PP04}$ calibrations, respectively. Given the low number statistics, we do not attempt any fit to the observed points in Figure 12, neither stacked nor single.

Recently, the possible introduction of a third term in the MZR has been advocated to reduce the intrinsic scatter of the relation. Mannucci et al. (2010) proposed to add the SFR to build the so-called "Fundamental Mass-Metallicity Relation" (FMR) and provided a suitable description of it through the $\mu_\alpha = \log(M/M_\odot) - \alpha \log(SFR/M_\odot\ yr^{-1})$ parameter. They found that the minimum scatter for their local sample from the SDSS is reached for $\alpha = 0.32$, and that this value does not evolve at least up to $z \sim 2.5$. This latter finding is somewhat in contrast with recent works at $z \gtrsim 1.5$ (Wuyts et al. 2014; Zahid et al. 2014a, 2014b; S14) and, partially, with the results of the present study (but see Maier et al. 2014 for the impact of the choice of the FMR extrapolation on the evolution with z). Figure 14 shows the FMR projection on the $\mu_{0.32}$-12 + log(O/H)

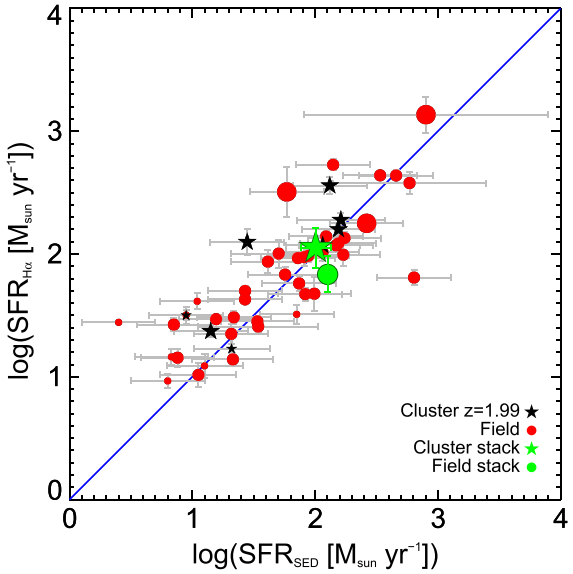

Figure 11. SFR estimates from SED fitting and intrinsic Hα luminosities for the MOIRCS spectroscopic sample of SFGs. Red circles and black stars, respectively, mark the field and cluster samples with 2σ detected Hα line. Symbol sizes scale as the stellar mass. The green circle indicates the field stacked value. The green star indicates the cluster stacked value. A one-to-one blue line is shown as a comparison.

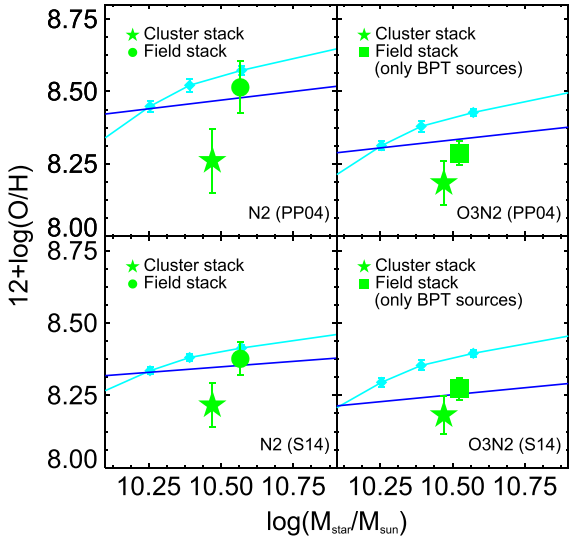

Figure 13. MZR for the MOIRCS spectroscopic stacked samples in the mass range $10 \leqslant \log(M/M_{\odot}) \leqslant 11$. The green circle and square indicate the 31-source and 16-source field stacked values, respectively. The green star indicates the cluster stacked value. Cyan diamonds represent the stacked points from the FMOS survey at $z \sim 1.55$ (Zahid et al. 2014b) and the blue solid line is the relation for the $z \sim 2.3$ sample from Steidel et al. (2014, Equation (17)), both rescaled to match the metallicity calibration in each panel (see the legend).

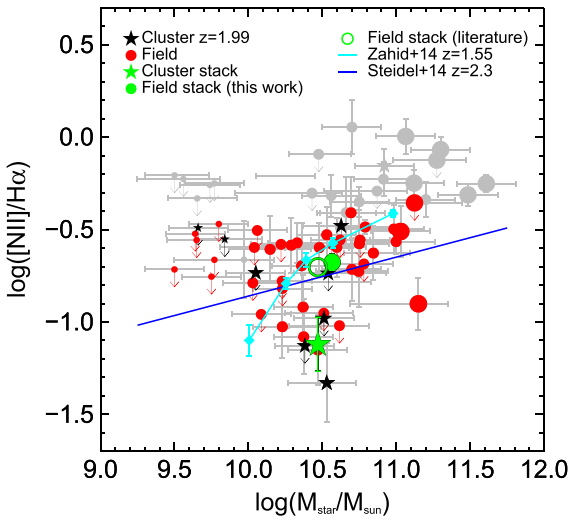

Figure 12. Mass–[N II]/Hα relation for the MOIRCS spectroscopic sample. Red circles and black stars represent the field and cluster samples, respectively. Gray symbols mark the objects excluded from the SF sample as AGNs (see Section 3.3.1). Arrows indicate 2σ upper limits. Symbol sizes scale as the stellar mass. The green solid circle and star represent the field and cluster stacked samples, respectively. The green empty circle marks the expected field position at $z = 2$ from the interpolation of literature data (see the text for details). Cyan diamonds represent the stacked points from the FMOS survey at $z \sim 1.55$ (Zahid et al. 2014b). The blue solid line is the relation for the $z \sim 2.3$ sample from Steidel et al. (2014, Equation (20)).

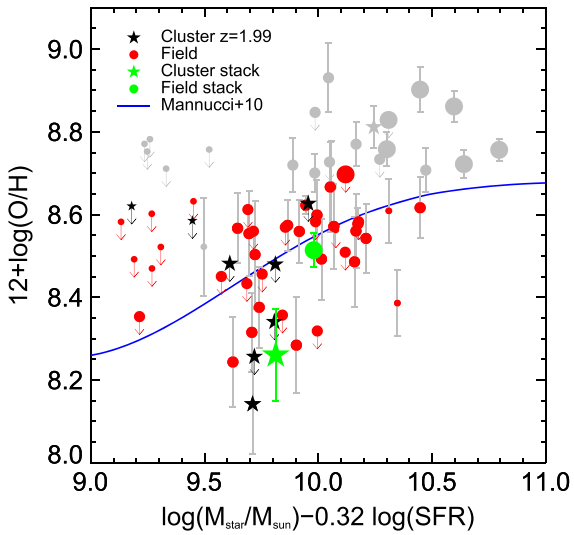

Figure 14. FMR for the MOIRCS spectroscopic sample. Red circles and black stars represent the field and cluster samples, respectively. Gray symbols mark the objects excluded from the SF sample as AGNs (see Section 3.3.1). Arrows indicate 2σ upper limits. Symbol sizes scale as the stellar mass. The green solid circle and star represent the field and cluster stacked samples, respectively. SFRs are estimated from Hα fluxes (see Section 3.3.4 for details). The gas-phase metallicity is estimated from the N2 indicator as calibrated by Pettini & Pagel (2004). The blue solid line represents the polynomial parametrization of the FMR by (Mannucci et al. 2010, Equation (4)).

plane as parametrized in Equation (4) of Mannucci et al. (2010), where we used SFR$_{H\alpha}$. Again, the choice of the indicator (and especially of its calibration) is decisive for the absolute value of the metallicity, which enters the FMR. In Figure 14, we show the PP04 N2 calibration, which, in the case of the field sample, is consistent with the FMR trend, after a proper conversion from the Maiolino et al. (2008) calibration system to PP04. In the same figure, the cluster value is tentatively inconsistent ($\sim 2.7\sigma$) with an unevolving FMR up to $z \sim 2.5$. After proper metallicity rescaling, we observe a similar inconsistency with the prediction of the analytically derived Z (M, SFR) by Lilly et al. (2013; left panel of their Figure 7).

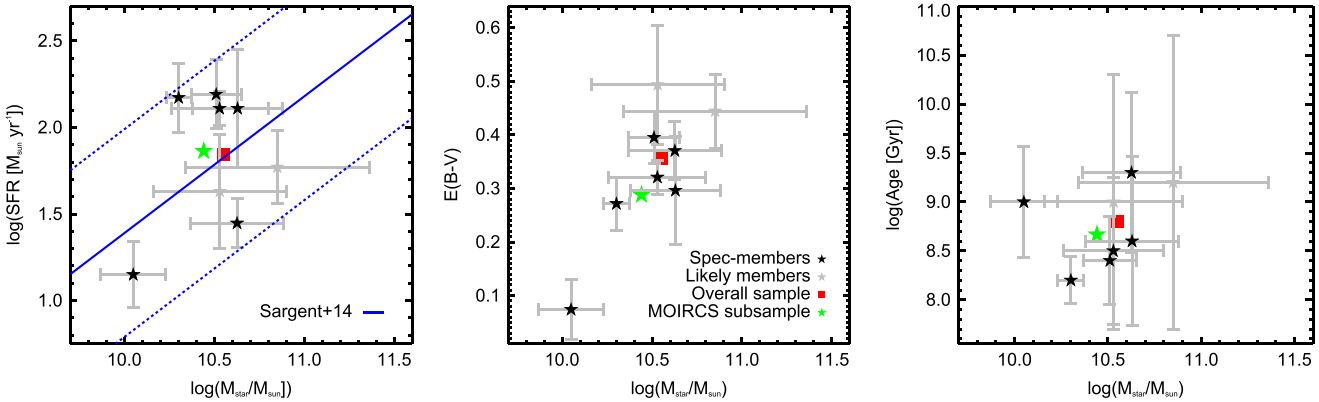

Figure 15. Photometric properties of the cluster "parent" sample from which the high priority sample for MOIRCS follow-up has been extracted. In each panel, black stars mark the six WFC3 spectroscopically confirmed SF cluster members in the $10 \leqslant \log(M/M_{\odot}) \leqslant 11$ mass range, which have been followed-up with MOIRCS and stacked. Gray stars mark the candidate members in the same mass range not observed with MOIRCS. The green star and red square indicate the mean value for the sample of followed-up sources and for the overall population, respectively. Left panel: stellar mass vs. SED-based SFR. The MS at $z = 2$ is represented with a ± 0.6 dex scatter as parametrized by Sargent et al. (2014). Central panel: mass–reddening relation. Right panel: mass–luminosity-weighted age relation for constant SFH.

5. DISCUSSION

5.1. Potential Selection Effects

We checked for possible biases in our field sample comparing it to trends from other surveys at similar redshifts and extrapolating them to $z = 1.99$ (Section 4). As shown in Figure 12, our selection of field sources gives results that are consistent with much broader samples in the literature (Zahid et al. 2014b, S14). This shows that our selection is not biased toward specific high-redshift galaxy populations, but extracts a representative sample of MS-SFGs at $z \sim 2$. This result is confirmed stacking only *sBZK*-, Hα-selected galaxies from the COSMOS mask and comparing them to the general field sample, as we recover fully consistent line ratios (within 1σ uncertainties).

Moreover, for the higher priority assigned to the WFC3-confirmed cluster members over candidates, another possible selection bias could have occurred in the cluster sample. In particular, even if not specifically [O III]-selected, 5/6 SF cluster members in the final stack have an [O III] detection from WFC3, which could have introduced a bias toward the metal poorer cluster members. To check this possibility we investigated the properties of the whole "parent" pool of spectroscopically confirmed and candidate star-forming members in the mass range $10 \leqslant \log(M/M_{\odot}) \leqslant 11$ from which we chose the high priority sample to observe. The mass cut, the constraints on the quality of photometric data, and the SF classification reduced the original pool to eight members in the investigated mass bin. 6/8 are the WFC3 spectroscopically confirmed members that we observed with MOIRCS and which were stacked. The other two sources are candidate members that were not inserted in the final MOIRCS mask because of geometrical constraints in slit positioning. The photometric properties of these eight galaxies are shown in Figure 15. Furthermore, we investigated the reasons for the WFC3 non-detection of the two candidate members, checking whether or not the absence of [O III] detection could have been due to high metallicities, which could have potentially influenced our subsequent analysis of the cluster metal content. From the SED-based SFR and $E(B-V)$ estimates and assuming an intrinsic Hα/Hβ ratio equal to 2.86, we derived the expected Hβ observed flux. In both cases, it fell well below the WFC3 3σ detection threshold (2×10^{-17} erg cm^{-2} s^{-1}, G13), showing that these two sources are intrinsically faint rather than metal-rich (if the latter was the case, we should have detected them in Hβ but not in [O III]). Moreover, assuming the WFC3 detection threshold, the predicted Hβ flux, and an empirical track describing the observed population at $z = 2$ in the BPT diagram, we estimated the [N II]/Hα ratio for these two sources and the metallicity with N2, confirming their homogeneity with the sample of the six galaxies that we stacked. This result does not change using tracks describing only cluster sources, the whole sample of $z \sim 2$ galaxies, or a trend from the literature. We thus conclude that the intrinsic faintness combined with potentially high orders of contamination in the slitless spectroscopy did not allow a detection and a redshift estimate with WFC3. In the Appendix, we show the WFC3 G141 spectra for these two sources. In addition, we could exclude significant biases introduced by low number statistics for the cluster sample (Section 3.2). Therefore, we can be reasonably confident that evident selection effects are not invalidating the analysis presented in this work.

5.2. The Environmental Effect

5.2.1. Comparison with Other Works

The debate about the environmental signatures in the chemical enrichment of cluster galaxies is still ongoing, even in the local universe. The situation for high-redshift clusters is almost unexplored up to date. Kulas et al. (2013) studied the MZR for a sample of 23 SFGs belonging to a $z = 2.3$ protocluster (Steidel et al. 2005). They find a 0.15 dex metallicity enhancement for galaxies inside the overdensity with respect to field counterparts at low masses ($\log(M/M_{\odot}) \lesssim 10.1$, Chabrier IMF), but no difference at higher masses. Similarly, Shimakawa et al. (2015) find higher gas-phase metallicities in protocluster members than in the field at $z = 2.1$–2.5 below $10^{11}\,M_{\odot}$. These results are in contrast with the main finding of this work. Unfortunately, we cannot study possible mass trends, given the low number of SFGs in CL J1449+0856 and the high-mass limit for completeness. Moreover the mass range that we explored is somewhere in between the mass bins defined in Kulas et al. (2013), increasing the difficulty of a

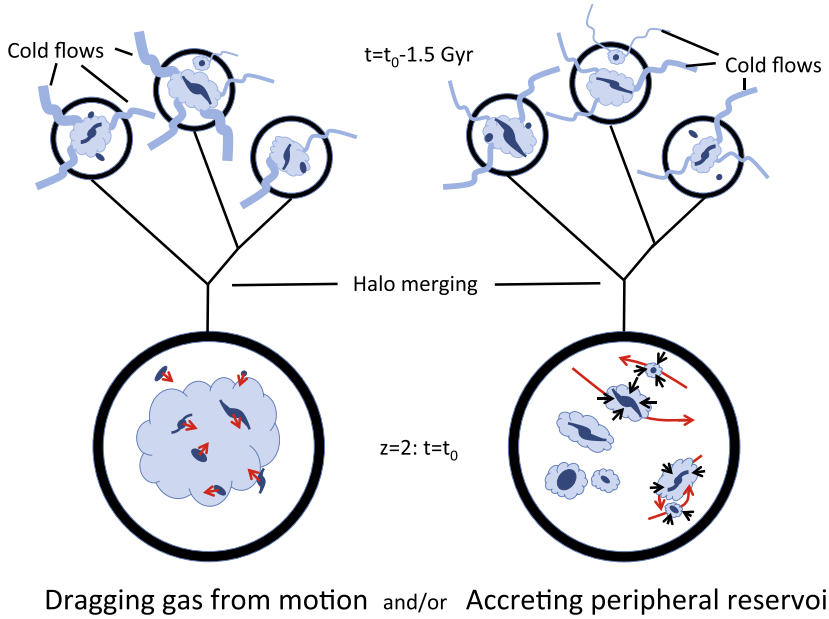

Figure 16. Sketch of the speculative model of gas accretion for SFGs residing in CL J1449+0856. The left branch refers to the possible creation of a gas rich environment in clusters close to a phase of major assembly. The right branch shows the impact of galaxy encounters on the gas halos around each galaxy. The vertical direction marks the time: at the top a phase of gas enrichment occurs ∼1.5 Gyr before a major phase of assembly of CL J1449+0856 at $z \geqslant 2$.

direct comparison. Furthermore, we note that contamination from AGNs is a potential issue in selecting SFGs at high redshift: the inclusion of type-2 AGNs, which could be hosted in a non-negligible fraction of high-mass galaxies at $z > 1$ (e.g., Trump et al. 2013), can bias the [N II]/Hα ratio toward higher values and hence their gas-phase metallicities derived from $N2$. Kulas et al. (2013) selected sources according to UV emission, which should prevent strong AGN contamination (see Steidel et al. 2014). Shimakawa et al. (2015) rejected AGNs using a slight modification of the BPT diagram relying on Hα fluxes and reddening correction to estimate Hβ fluxes. In this work, we coupled the BPT and [N II]/Hα–EW(Hα) diagrams, including X-ray and radio criterion and these different AGN exclusion criteria could have impacted the final results. Furthermore, despite being at comparable redshifts, these overdensities and CL J1449+0856 are structurally different. A pondered definition of *protoclusters* and *clusters* is beyond the scope of this work, but we remark that these different structures may potentially give rise to different effects on their host galaxies, and thus straight comparisons should be made with caution.

5.2.2. The Past History of CL J1449+0856: a Recent Transitional Phase of Stellar Mass Assembly?

The observations presented in this paper have highlighted the presence of a $> 4\sigma$ significant difference in [N II]/Hα ratio between a sample of SFGs belonging to CL J1449+0856 and a mass-matched sample in the field. This difference is directly translated in a metallicity difference with all the indicators employed in the analysis, so that cluster sources are a factor of 0.09–0.25 dex (using $O3N2_{S14}$ and $N2_{PP04}$, respectively) more metal-poor than the field counterparts. What follows is a speculation about the origin of this effect. As discussed above, CL J1449+0856 is partially virialized, but a relatively recent phase of assembly must have occurred. According to the model of halo mass growth by Fakhouri et al. (2010), a halo of $5 \times 10^{13}\,M_{\odot}$, such as the one hosting CL J1449+0856 (from X-ray emission, G13), should have increased its mass of a factor of times two (times five) in the previous ∼1 Gyr (∼1.5 Gyr) of its lifetime. The recent coalescence of multiple less-massive halos could have impacted the hosted galaxies in a twofold way, which is graphically sketched in Figure 16. First, the single bricks forming the final halo could have been gas enriched through cold streams and subsequently merged, thus creating an environment rich in pristine gas. The accretion of cold gas, even in quite massive halos at redshifts close to the formation epoch of CL J1449+0856 progenitors, is consistent with model predictions, if high density, steady, cold streams penetrating the shock heated medium are considered (Birnboim & Dekel 2003; Kereš et al. 2005; Brooks et al. 2009; Dekel et al. 2009a, 2009b). In Figure 17, the mass growth track for CL J1449+0856 halo (Fakhouri et al. 2010) crosses the line separating the hot ISM and cold streams in hot ISM regimes ∼1 Gyr before $z = 2$ and thus the progenitors of the cluster halo could have been recently enriched with cold gas, before merging. If this gas is not prevented from cooling (Fabian 1994; Revaz et al. 2008; Salomé et al. 2011), given the high dark matter density in $z \gtrsim 2$ halos, it might be dragged and accreted on the galaxies simply moving across it, diluting the metal content. This first effect might not be effective at lower redshifts, where the gas reservoirs in halos are at lower densities, prevented from cooling after the cluster full virialization, chemically enriched by gigayears of stellar formation, and not replenished by cosmological inflows. This latter aspect is illustrated in Figure 17, where the mass growth tracks for a halo of $5 \times 10^{13}\,M_{\odot}$ at $z = 0$, 1 do not enter the region of cold streams in hot media on timescales of the order of ∼1 Gyr. Moreover, in a ΛCDM universe, the baryon growth rate scales as $(1+z)^{2.25}$ at fixed mass (Neistein & Dekel 2008). Thus, at low redshifts the progenitors of a halo of such mass cannot be easily refurnished with cold gas.

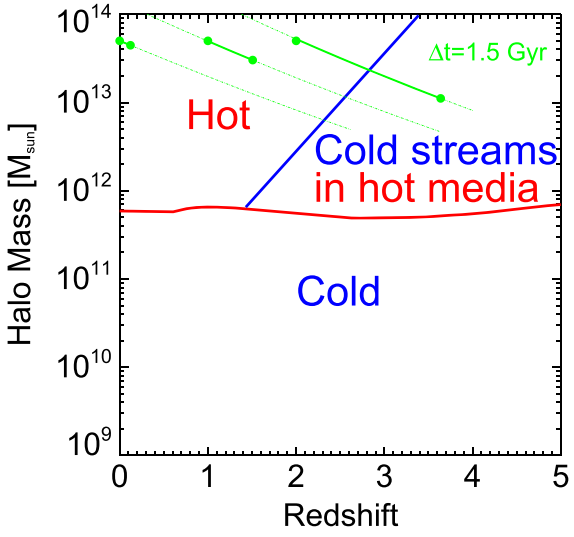

Figure 17. Analytic prediction of the "hot," "cold," and "cold streams in hot media" regimes in the mass-redshift space from Dekel et al. (2009b). The green tracks show the mass growth for halos of $5 \times 10^{13}\,M_{\odot}$ at $z = 0$, 1, 2 (Fakhouri et al. 2010). The solid segments represent a lookback time interval of 1.5 Gyr starting from the redshift of reference.

Second, a recent epoch of the high merging rate of dark matter halos could have favored encounters, fly-bys, and mergers among the galaxies hosted in the merging halos, given the low (but increasing) cluster velocity dispersion. An encounter can trigger the accretion of the reservoirs of cold, rich, and pristine gas located in the halos of single galaxies at $z \gtrsim 2$, continuously replenished by cosmological inflows (Ceverino et al. 2010; Gabor & Bournaud 2014). The accretion of such gas would lower the metallicity, as observed in our sample, and subsequently enhance the SF. In addition, galaxy minor and major mergers could lower the metal abundance themselves (Contini et al. 2012; Queyrel et al. 2012). Moreover, the final cluster potential well in which the galaxies reside and interact can facilitate the merging events through the so-called "gravitational focusing" effect (Martig & Bournaud 2007; Moreno et al. 2013), accelerating the gas accretion from the galaxy outskirts. Recent observational studies have shown an SFR increase and metallicity decrease (up to ~0.07–0.09 dex) in close pairs and post-mergers in the local universe (Ellison et al. 2013). This result is supported by simulations suggesting that mergers induce the funneling of gas reservoirs from the peripheric regions of galaxies toward the center, diluting the metallicity and triggering new SF (Torrey et al. 2012). This second effect could be effective in terms of gas accretion on galaxies entering the halo of low-redshift clusters, generating an SFR enhancement in the cluster outskirts, as observed for example in Virgo (Temporin et al. 2009). However, given the chemical enrichment due to stellar formation in the last 10 Gyr, the gas accretion might not be effective in reducing the metallicity at low redshift. Deep F140W images of our sample of cluster SFGs in the final stack are shown in Figure 18. Every object shows a disturbed morphology and/or a close companion, which might be a hint of high gas fractions or a close encounter, even if the lack of a redshift determination for the companions does not allow us to draw a robust conclusion (see, e.g., Zanella et al. 2015 for the specific case of ID568, Figure 18, fifth panel). We defer to a future work the detailed study of galaxy morphologies in CL J1449+0856 and a proper comparison with a morphologically characterized field sample.

The transitional epoch that we have just described could be a key phase for galaxy clusters with the assembly of a substantial fraction of stellar mass in SFGs. In a time interval of 500 Myr, the typical doubling time at $z = 2$ (Daddi et al. 2007) and the typical scale of gas consumption in SFGs (Daddi et al. 2010), each galaxy in our cluster sample would form stars for a total of ~ 3–$6 \times 10^{10}\,M_{\odot}$, given the average SFR we measure ($\mathrm{SFR_{H\alpha}} = 112\ M_{\odot}\mathrm{yr}^{-1}$, $\mathrm{SFR_{SED}} = 73\,M_{\odot}\,\mathrm{yr}^{-1}$). This would double the stellar mass already present in cluster SFGs and increase the overall cluster stellar mass in spectroscopically confirmed members by ~15–35% in this time interval or, if we extend this reasoning to the past history of the cluster, SFGs could have assembled an important part of the total stellar mass in a relatively short period of time during this phase.

We can gain physical insight about the metal deficiency for cluster SFGs with a simple computation. To explain a 0.15 dex metallicity difference (a factor of ~40%), given that $M_{\star} \simeq M_{\mathrm{gas}}$ in MS-SFGs at $z \sim 2$ (Bouché et al. 2007; Daddi et al. 2008), we would need a mass of accreted pristine gas of $2 \times 10^{10}\,M_{\odot}$ to dilute the metal content of each galaxy. If we assume the presence in the cluster halo of a gas mass–free to cool down and to be dragged and accreted by SFGs in their motion equal to ~15% of the total halo mass ($M_{\mathrm{halo}} = 5 \times 10^{13}\,M_{\odot}$), the mass accretion rate would be $35\,M_{\odot}\ \mathrm{yr}^{-1}$, assuming a gravitational focusing term $\simeq 5$, a velocity dispersion of $500\,\mathrm{km\,s}^{-1}$, $R_{200} = 0.4$ Mpc, and $R_{\mathrm{gal}} \sim 4$ kpc as a typical SFG radius ($\dot{M}_{\mathrm{acc}} = \rho_{\mathrm{gas,halo}} \cdot \pi \mathrm{R}_{\mathrm{gal}}^{2} \cdot v_{\mathrm{disp}} \cdot f_{\mathrm{grav}}\ [M_{\odot}\,\mathrm{yr}^{-1}]$). However, if we consider only the highest density regions at the core of the cluster ($R_{\mathrm{clu}} \sim 200$ kpc), where the gas is likely to collect, the accreted gas mass could rapidly increase by a factor of ~8, enough to halve the metal content of the galaxy. The complementary mechanism linked to galaxy encounters could provide an extra gas accretion rate of $\geqslant 45\,M_{\odot}\ \mathrm{yr}^{-1}$, considering the galaxy density within the cluster ($\sim 75\ \mathrm{Mpc}^{-3}$ within R_{200}) and a typical distance for a fly-by of 50 kpc ($\dot{M}_{\mathrm{acc}} = M_{\mathrm{res}} \cdot n_{\mathrm{coll}} \cdot f_{\mathrm{grav}}\ [M_{\odot}\,\mathrm{yr}^{-1}]$, where $\mathrm{n_{coll}}$ is the collision rate and M_{res} the galaxy halo gas reservoir). The reservoirs available in the galaxy outskirts are expected from simulations to be a few $10^{9}\,M_{\odot}$ within a 15 kpc radius around the galaxy (Ceverino et al. 2010; Gabor & Bournaud 2014) and they can be replenished only as long as cold inflows can reach the galaxy, which may not be true once the galaxy enters deeply in the cluster halo. Moreover, we cannot rule out the possibility that the local density may be a more important driver than cluster membership (i.e., large scale environment). Unfortunately, the very low number statistics of cluster SFGs does not allow for a proper comparison among objects within and outside the virial radius to check for the effective influence of the underlying overdensity on the metallicity, neither considering stacked spectra. Future spectroscopic follow-up of the remaining population of spectroscopically confirmed and candidate SF members will be decisive to clarify this complex picture.

6. SUMMARY AND CONCLUSIONS

We have presented the results of the MOIRCS near-IR spectroscopic follow-up of the SF population residing in CL J1449+0856 at $z = 2$. Adding the pre-existing thirteen-band photometry of the field and the deep grism G141 slitless

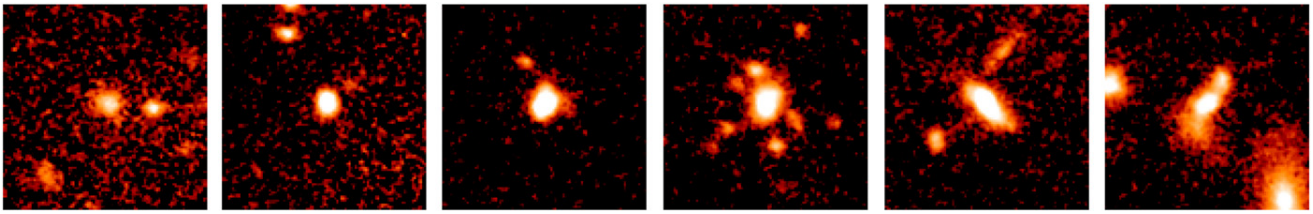

Figure 18. F140W 3″ × 3″ (∼ 25 × 25 kpc) cutouts of our sample of cluster SFGs in the mass range $10 \leqslant \log(M/M_{\odot}) \leqslant 11$ (north is up, east is left).

spectroscopy of WFC3, we studied the properties of our sample of cluster SFGs in the mass range of $10 \leqslant \log(M/M_{\odot}) \leqslant 11$ with respect to a mass-matched field sample at comparable redshifts through stacking. In our analysis, we showed the following.

1. The field and cluster samples of SFGs in the studied mass range show comparable [O III]/Hβ ratios, but a $\sim 4\sigma$ significant difference in [N II]/Hα ratios. Using different calibrations of the N2 and O3N2 metallicity indicators, the lower [N II]/Hα ratio measured in cluster SFGs is translated in a ∼0.09–0.25 dex (using $O3N2_{S14}$ and $N2_{PP04}$, respectively) metal deficiency for the objects belonging to the overdensity. The low metallicity value in cluster sources is confirmed using R_{23} and O_{32} indicators. Furthermore, it is supported by the low N/O ratio that we measured ($\log(N/O) = -1.18 \pm 0.15$). The ionization parameter in the cluster stacked sample from R_{23}, O_{32} ($\mathcal{U} \simeq -2.61$) is higher than typical values for local galaxies, but consistent with other determinations at high redshift.
2. We observe $\sim 4.7\sigma$ significant 2.5 times higher Hα luminosity and EW(Hα) in the cluster stack, likely due to enhanced sSFR, even if lower dust reddening and/or an uncertain environmental dependence of the continuum-to-nebular emission differential reddening f may play a role. Thus the metal deficiency observed in the cluster sources appears to be correlated with an increase in the SFR with respect to the field; however, we report a $\sim 2.7\sigma$ inconsistency with the prediction of a FMR not evolving up to $z = 2.5$.
3. The nebular lines reddening at $z \sim 2$ is ∼ 1.4 times higher than that of stellar continuum estimated through SED fitting, lower than the previous estimates from local measurements and in agreement with recent studies at $z \geqslant 1.5$ (Kashino et al. 2013; Pannella et al. 2014).
4. Our sample of high redshift galaxies are offset from the local SF sequence on the BPT emission-line diagnostic diagram. This result is in agreement with previous studies at similar redshifts (Erb et al. 2006; Yabe et al. 2012; Steidel et al. 2014; Zahid et al. 2014b, and others), pointing toward a possible evolution with redshift of the physical conditions of the line emitting regions.
5. The metal deficiency in this $z = 1.99$ cluster could be due to the accretion of pristine gas, which might have diluted the metal content. We speculate that the accretion of large galactic scale gas reservoirs facilitated by the gravitational focusing effect may be responsible for the observed low metal abundance in star-forming cluster members.

We acknowledge the constructive comments from the anonymous referee, which significantly improved the content and presentation of the results. F.V., E.D., and A.Z. were supported by grants ERC-StG UPGAL 240039 and ANR-08-JCJC-0008. F.B. and S.J. acknowledge support from the European Research Council through grant ERC-StG-257720. N.A. has been supported by the Grant-in-Aid for the Scientific Research Fund under grant No. 23224005. This work is based on data collected at Subaru Telescope, which is operated by the National Astronomical Observatory of Japan.

APPENDIX A

As noted in Section 3.2, averaging single spectra does not necessarily coincide with averaging spectral derived quantities. The difference between these two averaged trends depends on the relationship between the the fluxes of single lines and the derived quantities. In our case, we have evaluated the impact of this difference on the mean metallicity calculated through the strong line ratio [N II]/Hα for a population of MS SFGs. Assuming a functional form for the $M_{\star}$–SFR relation and the Hα–SFR conversion, one can easily convert the stellar mass of a galaxy into its intrinsic Hα luminosity and, given an MRR, into the observable Hα flux at a fixed redshift. For this exercise, we have used Sargent et al. (2014) MS parametrization as a function of redshift and the standard Kennicutt (1998) relation to pass from Hα intrisic luminosities to SFRs. As an MRR, we have used the observed trend of our overall sample of SFGs given by the SED fitting described in Section 3.1 and shown in Figure 9. Then, we can convert the stellar mass into the gas-phase metallicity using a parametrization of the MZR (or of the FMR if we want to include the effect of the SFR). Here we have used the Zahid et al. (2014a) parametrization, given its simple form. Finally, we need a conversion from gas-phase metallicities to observed line fluxes. We adopt here the Pettini & Pagel (2004) calibration of the [N II]/Hα ratio, but in principle we could test any other strong-line ratio. All of these relations are somehow scattered and we have adopted the quoted scatters to introduce a Gaussian random noise to make our simple simulation more realistic. Given all of these relations, we simply generate a random sample of masses in an interesting mass range and derive two estimates of the average metallicity. First, we simply compute the average of the single metallicities in mass bins as obtained from the MZR (Z_{av}); then, we compute the mean metallicity in the same mass bins as derivable from an hypothethic stacking of the spectra of single galaxies, namely from the average of single line fluxes (Z_{stack}). Analytically, it can be shown that Z_{av} and Z_{stack} depend on [N II] and Hα fluxes in different ways, so that a priori they

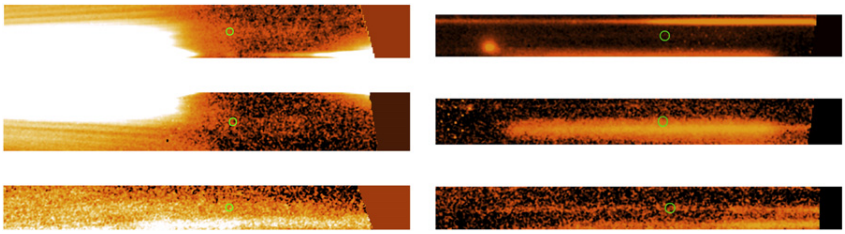

Figure 19. WFC3 G141 slitless spectra of the two cluster candidate members with masses $10 \leqslant \log(M/M_{\odot}) \leqslant 11$ that were not observed with MOIRCS. Left column: ID 424. Right column: ID 660. The three spectra correspond to separate *HST* visits (G13). Green circles mark the expected position of [O III] if the sources were at $z = 1.99$.

can be different:

$$\log\left[\frac{Z_{\rm av}}{Z_{\rm stack}}\right] = \log\left(\frac{1}{N}\right) + \log\left[\sum_{i=1}^{N}\left(\frac{[\rm N\,II]}{\rm H\alpha}\right)_i^{0.57}\right] - \log\left[\left(\frac{\sum_{i=1}^{N}[\rm N\,II]_i}{\sum_{i=1}^{N}\rm H\alpha_i}\right)^{0.57}\right] \quad \text{(A.1)}$$

where N is the total amount of observed galaxies and 0.57 is the slope of PP04 calibration. Given the parametrizations we adopted, the difference between the two mean estimates decreases with increasing stellar mass. Moreover, averaging the metallicity in smaller mass bins gives rise to smaller differences between $Z_{\rm av}$ and $Z_{\rm stack}$. Finally, a high number of observed points is more robust against the scatter of the relations we used, reducing the possibility to find huge log $(Z_{\rm av}/Z_{\rm stack})$ ratios in a mass bin. We have stacked sources in a limited high-mass regime $(10 \leqslant \log(M/M_{\odot}) \leqslant 11)$ where we have a relatively low number statistics for the cluster sample $(N \sim 10)$ and a fairly more robust sample of field galaxies $(N \sim 30)$. For a simulated sample of 10 galaxies at $z = 2$ in the mass bin $10 \leqslant \log(M/M_{\odot}) \leqslant 11$, the median difference is log $(Z_{\rm av}/Z_{\rm stack}) = 0.018$ $(\sim 4\%)$ with a semi-interquartile range of 0.022 dex over 1000 runs of the simulation. At the same redshift and mass bin but for $N = 30$ observed points, the median difference is reduced to log $(Z_{\rm av}/Z_{\rm stack}) = 0.008$ $(\sim 1\%)$ with a semi-interquartile range of 0.005 dex. At these masses the impact of adopting one approach or the other is restrained, but it could be more important at lower masses—due to the steeper MZR—at which the stacking technique is usually widely used.

APPENDIX B

In Figure 19, we show the WFC3 G141 slitless spectra for two candidate members with masses of $10 \leqslant \log(M/M_{\odot}) \leqslant 11$ that were not inserted in MOIRCS masks because of geometrical constraints in slit positioning. Contamination from high orders severily affected these spectra in two of the three *HST* visits, limiting the usable integration time to 4/18 orbits and leading to a higher detection threshold. This did not allow us to detect these intrinsically faint objects (see Section 5.1).

REFERENCES

Abazajian, K. N., Adelman-McCarthy, J. K., Agüeros, M. A., et al. 2009, ApJS, 182, 543
Alloin, D., Collin-Souffrin, S., Joly, M., & Vigroux, L. 1979, A&A, 78, 200
Andreon, S., Maughan, B., Trinchieri, G., & Kurk, J. 2009, A&A, 507, 147
Andrews, B. H., & Martini, P. 2013, ApJ, 765, 140
Asplund, M., Grevesse, N., Sauval, A. J., & Scott, P. 2009, ARA&A, 47, 481
Baldry, I. K., Glazebrook, K., Brinkmann, J., et al. 2004, ApJ, 600, 681
Baldwin, J. A., Phillips, M. M., & Terlevich, R. 1981, PASP, 93, 5
Balogh, M. L., Baldry, I. K., Nichol, R., et al. 2004, ApJL, 615, L101
Bertin, E., & Arnouts, S. 1996, A&AS, 117, 393
Birnboim, Y., & Dekel, A. 2003, MNRAS, 345, 349
Blanton, M. R., Eisenstein, D., Hogg, D. W., Schlegel, D. J., & Brinkmann, J. 2005, ApJ, 629, 143
Bouché, N., Cresci, G., Davies, R., et al. 2007, ApJ, 671, 303
Brooks, A. M., Governato, F., Quinn, T., Brook, C. B., & Wadsley, J. 2009, ApJ, 694, 396
Bruzual, G., & Charlot, S. 2003, MNRAS, 344, 1000
Calzetti, D., Armus, L., Bohlin, R. C., et al. 2000, ApJ, 533, 682
Ceverino, D., Dekel, A., & Bournaud, F. 2010, MNRAS, 404, 2151
Charlot, S., & Longhetti, M. 2001, MNRAS, 323, 887
Cid Fernandes, R., Stasińska, G., Mateus, A., & Vale Asari, N. 2011, MNRAS, 413, 1687
Cid Fernandes, R., Stasińska, G., Schlickmann, M. S., et al. 2010, MNRAS, 403, 1036
Coil, A. L., Aird, J., Reddy, N., et al. 2014, arXiv:1409.6522
Contini, T., Garilli, B., Le Fèvre, O., et al. 2012, A&A, 539, A91
Cooper, M. C., Tremonti, C. A., Newman, J. A., & Zabludoff, A. I. 2008, MNRAS, 390, 245
Cullen, F., Cirasuolo, M., McLure, R. J., Dunlop, J. S., & Bowler, R. A. A. 2014, MNRAS, 440, 2300
Daddi, E., Bournaud, F., Walter, F., et al. 2010, ApJ, 713, 686
Daddi, E., Cimatti, A., Renzini, A., et al. 2004, ApJ, 617, 746
Daddi, E., Dannerbauer, H., Elbaz, D., et al. 2008, ApJL, 673, L21
Daddi, E., Dickinson, M., Morrison, G., et al. 2007, ApJ, 670, 156
Davé, R., Finlator, K., & Oppenheimer, B. D. 2012, MNRAS, 421, 98
Dekel, A., Sari, R., & Ceverino, D. 2009a, ApJ, 703, 785
Dekel, A., Birnboim, Y., Engel, G., et al. 2009b, Natur, 457, 451
Dopita, M. A., Sutherland, R. S., Nicholls, D. C., Kewley, L. J., & Vogt, F. P. A. 2013, ApJS, 208, 10
Dressler, A. 1980, ApJ, 236, 351
Ellison, S. L., Mendel, J. T., Patton, D. R., & Scudder, J. M. 2013, MNRAS, 435, 3627
Ellison, S. L., Simard, L., Cowan, N. B., et al. 2009, MNRAS, 396, 1257
Erb, D. K., Shapley, A. E., Pettini, M., et al. 2006, ApJ, 644, 813
Fabian, A. C. 1994, ARA&A, 32, 277
Fakhouri, O., Ma, C.-P., & Boylan-Kolchin, M. 2010, MNRAS, 406, 2267
Fassbender, R., Nastasi, A., Böhringer, H., et al. 2011, A&A, 527, L10
Fitzpatrick, E. L. 1999, PASP, 111, 63
Gabor, J. M., & Bournaud, F. 2014, MNRAS, 437, L56
Gobat, R., Daddi, E., Onodera, M., et al. 2011, A&A, 526, A133
Gobat, R., Strazzullo, V., Daddi, E., et al. 2013, ApJ, 776, 9
Gómez, P. L., Nichol, R. C., Miller, C. J., et al. 2003, ApJ, 584, 210
Hogg, D. W., Blanton, M. R., Brinchmann, J., et al. 2004, ApJL, 601, L29
Holden, B. P., Oesch, P. A., Gonzalez, V. G., et al. 2014, arXiv:1401.5490
Hughes, T. M., Cortese, L., Boselli, A., Gavazzi, G., & Davies, J. I. 2013, A&A, 550, A115
Ichikawa, T., Suzuki, R., Tokoku, C., et al. 2006, in Proc. SPIE, 6269, 38
Juneau, S., Dickinson, M., Alexander, D. M., & Salim, S. 2011, ApJ, 736, 104
Juneau, S., Bournaud, F., Charlot, S., et al. 2014, ApJ, 788, 88
Kashino, D., Silverman, J. D., Rodighiero, G., et al. 2013, ApJL, 777, L8
Kennicutt, R. C., Jr. 1998, ARA&A, 36, 189
Kereš, D., Katz, N., Weinberg, D. H., & Davé, R. 2005, MNRAS, 363, 2
Kewley, L. J., & Dopita, M. A. 2002, ApJS, 142, 35
Kewley, L. J., Dopita, M. A., Leitherer, C., et al. 2013a, ApJ, 774, 100
Kewley, L. J., & Ellison, S. L. 2008, ApJ, 681, 1183
Kewley, L. J., Maier, C., Yabe, K., et al. 2013b, ApJL, 774, L10

Kobulnicky, H. A., & Kewley, L. J. 2004, ApJ, 617, 240
Kodama, T., Tadaka, K.-i., Hayashi, M., et al. 2013, in IAU Symp. 295, The Intriguing Life of Massive Galaxies, ed. D. Thomas, A. Pasquali, & I. Ferreras (Cambridge: Cambridge Univ. Press), 74
Kriek, M., van Dokkum, P. G., Labbé, I., et al. 2009, ApJ, 700, 221
Kulas, K. R., McLean, I. S., Shapley, A. E., et al. 2013, ApJ, 774, 130
Lequeux, J., Peimbert, M., Rayo, J. F., Serrano, A., & Torres-Peimbert, S. 1979, A&A, 80, 155
Lilly, S. J., Carollo, C. M., Pipino, A., Renzini, A., & Peng, Y. 2013, ApJ, 772, 119
Magdis, G. E., Daddi, E., Béthermin, M., et al. 2012, ApJ, 760, 6
Maier, C., Lilly, S. J., Ziegler, B. L., et al. 2014, ApJ, 792, 3
Maiolino, R., Nagao, T., Grazian, A., et al. 2008, A&A, 488, 463
Mannucci, F., Cresci, G., Maiolino, R., Marconi, A., & Gnerucci, A. 2010, MNRAS, 408, 2115
Maraston, C., Pforr, J., Renzini, A., et al. 2010, MNRAS, 407, 830
Markwardt, C. B. 2009, in ASP Conf. Ser. 411, Astronomical Data Analysis Software and Systems XVIII, ed. D. A. Bohlender, D. Durand, & P. Dowler (San Francisco, CA: ASP), 257
Martig, M., & Bournaud, F. 2007, SF2A-2007: Proceedings of the Annual Meeting of the French Society of Astronomy and Astrophysics 344, ed. J. Bouvier, A. Chalabaev, & C. Charbonnel
Masters, D., McCarthy, P., Siana, B., et al. 2014, ApJ, 785, 153
Moreno, J., Bluck, A. F. L., Ellison, S. L., et al. 2013, MNRAS, 436, 1765
Mouhcine, M., Baldry, I. K., & Bamford, S. P. 2007, MNRAS, 382, 801
Muzzin, A., Wilson, G., Demarco, R., et al. 2013, ApJ, 767, 39
Nagao, T., Maiolino, R., & Marconi, A. 2006, A&A, 459, 85
Neistein, E., & Dekel, A. 2008, MNRAS, 388, 1792
Noll, S., Pierini, D., Cimatti, A., et al. 2009, A&A, 499, 69
Osterbrock, D. E., & Ferland, G. J. (ed.) 2006, Astrophysics of Gaseous Nebulae and Active Galactic Nuclei (Sausalito, CA: Univ. Sci. Books)
Pannella, M., Elbaz, D., Daddi, E., et al. 2014, arXiv:1407.5072
Papovich, C., Momcheva, I., Willmer, C. N. A., et al. 2010, ApJ, 716, 1503
Peng, C. Y., Ho, L. C., Impey, C. D., & Rix, H.-W. 2002, AJ, 124, 266
Peng, C. Y., Ho, L. C., Impey, C. D., & Rix, H.-W. 2010, AJ, 139, 2097
Pérez-Montero, E., & Contini, T. 2009, MNRAS, 398, 949
Pettini, M., & Pagel, B. E. J. 2004, MNRAS, 348, L59
Pilyugin, L. S., Grebel, E. K., & Mattsson, L. 2012, MNRAS, 424, 2316
Queyrel, J., Contini, T., Kissler-Patig, M., et al. 2012, A&A, 539, A93
Revaz, Y., Combes, F., & Salomé, P. 2008, A&A, 477, L33
Rodighiero, G., Renzini, A., Daddi, E., et al. 2014, MNRAS, 443, 19
Rousselot, P., Lidman, C., Cuby, J.-G., Moreels, G., & Monnet, G. 2000, A&A, 354, 1134
Salomé, P., Combes, F., Revaz, Y., et al. 2011, A&A, 531, A85
Salpeter, E. E. 1955, ApJ, 121, 161
Santos, J. S., Fassbender, R., Nastasi, A., et al. 2011, A&A, 531, L15
Sargent, M. T., Daddi, E., Béthermin, M., et al. 2014, ApJ, 793, 19
Savaglio, S., Glazebrook, K., le Borgne, D., et al. 2005, ApJ, 635, 260
Scoville, N., Aussel, H., Brusa, M., et al. 2007, ApJS, 172, 1
Shapley, A. E., Reddy, N. A., Kriek, M., et al. 2014, arXiv:1409.7071
Shimakawa, R., Kodama, T., Tadaki, K.-i., et al. 2015, MNRAS, 448, 666
Stanford, S. A., Brodwin, M., Gonzalez, A. H., et al. 2012, ApJ, 753, 164
Steidel, C. C., Adelberger, K. L., Shapley, A. E., et al. 2005, ApJ, 626, 44
Steidel, C. C., Rudie, G. C., Strom, A. L., et al. 2014, ApJ, 795, 165
Storey, P. J., & Zeippen, C. J. 2000, MNRAS, 312, 813
Strazzullo, V., Gobat, R., Daddi, E., et al. 2013, ApJ, 772, 118
Temporin, S., Duc, P.-A., & Ilbert, O. (XMM-LSS/SWIRE Collaboration) 2009, AN, 330, 915
Torrey, P., Cox, T. J., Kewley, L., & Hernquist, L. 2012, ApJ, 746, 108
Tremonti, C. A., Heckman, T. M., Kauffmann, G., et al. 2004, ApJ, 613, 898
Troncoso, P., Maiolino, R., Sommariva, V., et al. 2014, A&A, 563, A58
Trump, J. R., Konidaris, N. P., Barro, G., et al. 2013, ApJL, 763, L6
Williams, R. J., Quadri, R. F., Franx, M., van Dokkum, P., & Labbé, I. 2009, ApJ, 691, 1879
Wuyts, E., Kurk, J., Förster Schreiber, N. M., et al. 2014, ApJL, 789, L40
Wuyts, S., Labbé, I., Franx, M., et al. 2007, ApJ, 655, 51
Yabe, K., Ohta, K., Iwamuro, F., et al. 2012, PASJ, 64, 60
Yan, R., Ho, L. C., Newman, J. A., et al. 2011, ApJ, 728, 38
Yoshikawa, T., Akiyama, M., Kajisawa, M., et al. 2010, ApJ, 718, 112
Zahid, H. J., Bresolin, F., Kewley, L. J., Coil, A. L., & Davé, R. 2012, ApJ, 750, 120
Zahid, H. J., Dima, G. I., Kudritzki, R.-P., et al. 2014a, ApJ, 791, 130
Zahid, H. J., Kashino, D., Silverman, J. D., et al. 2014b, ApJ, 792, 75
Zanella, A., Daddi, E., Le Ploc'h, E., et al. 2015, Natur, in press
Zeimann, G. R., Stanford, S. A., Brodwin, M., et al. 2012, ApJ, 756, 115

Draft version August 10, 2016
Preprint typeset using LaTeX style emulateapj v. 05/12/14

A GIANT Lyα NEBULA IN THE CORE OF AN X-RAY CLUSTER AT $z = 1.99$: IMPLICATIONS FOR EARLY ENERGY INJECTION

Francesco Valentino [1,2], Emanuele Daddi[1], Alexis Finoguenov[3,4], Veronica Strazzullo[1,5], Amandine Le Brun[1], Cristian Vignali[6,7], Frédéric Bournaud[1], Mark Dickinson[8], Alvio Renzini[9], Matthieu Béthermin[10], Anita Zanella[1], Raphaël Gobat[1,11], Andrea Cimatti[6,7], David Elbaz[1], Masato Onodera[12,13], Maurilio Pannella[1,5], Mark Sargent[14], Nobuo Arimoto[13,15], Marcella Carollo[12], and Jean-Luc Starck[1]

Draft version August 10, 2016

Abstract

We present the discovery of a giant $\gtrsim$100 kpc Lyα nebula detected in the core of the X-ray emitting cluster CL J1449+0856 at $z = 1.99$ through Keck/LRIS narrow-band imaging. This detection extends the known relation between Lyα nebulae and overdense regions of the Universe to the dense core of a $5-7\times10^{13}$ M$_\odot$ cluster. The most plausible candidates to power the nebula are two Chandra-detected AGN host cluster members, while cooling from the X-ray phase and cosmological cold flows are disfavored primarily because of the high Lyα to X-ray luminosity ratio ($L_{\rm Ly\alpha}/L_{\rm X} \approx 0.3$, $\gtrsim 10-1000\times$ higher than in local cool-core clusters) and by current modeling. Given the physical conditions of the Lyα-emitting gas and the possible interplay with the X-ray phase, we argue that the Lyα nebula would be short-lived ($\lesssim$ 10 Myr) if not continuously replenished with cold gas at a rate of $\gtrsim$ 1000 M$_\odot$ yr^{-1}. We investigate the possibility that cluster galaxies supply the required gas through outflows and we show that their total mass outflow rate matches the replenishment necessary to sustain the nebula. This scenario directly implies the extraction of energy from galaxies and its deposition in the surrounding intracluster medium, as required to explain the thermodynamic properties of local clusters. We estimate an energy injection of the order of $\approx$ 2 keV per particle in the intracluster medium over a 2 Gyr interval. In our baseline calculation AGN provide up to 85% of the injected energy and 2/3 of the mass, while the rest is supplied by supernovae-driven winds.

Keywords: Keywords: Galaxies: clusters: individual (CL J1449+0856), intracluster medium - galaxies: star formation, active, high-redshift

1. INTRODUCTION

Since their first discovery in the late 1990s (Francis et al. 1996; Steidel et al. 2000), high-redshift, extended ($\gtrsim$ 100 kpc), and luminous (few $10^{43}-10^{44}$ erg s^{-1}) gas reservoirs shining by the emission of Lyα photons have progressively become a matter of debate. Despite two decades of investigation, several aspects of these "Lyα nebulae" remain puzzling, including the origin of the Lyα-emitting gas, its powering mechanism, the possible effects on the evolution of the embedded galaxies, and, ultimately, its fate (i.e., Matsuda et al. 2004; Dey et al. 2005; Geach et al. 2009; Prescott et al. 2009; Cantalupo et al. 2014). Understanding where Lyα nebulae fit in the current theoretical framework of structure formation has sparked particular interest, since they call into question a cornerstone of modern astrophysics: the complex interplay of supply, consumption, and expulsion of gas that shapes high-redshift systems. In this work we focus on a specific feature of Lyα nebulae: the connection with their surrounding environment. This perspective complements the approaches already presented in the literature and allows us to shed light on several of the problematics listed above. First, there are observational hints that Lyα nebulae preferentially reside in overdense regions of the Universe or sparse protoclusters (Steidel et al. 2000; Matsuda et al. 2004; Venemans et al. 2007). This suggests a possible connection with the formation of massive structures, even if it is not clear in which density regimes this correlation holds. Interestingly, in the local Universe the presence of kpc-size, filamentary reservoirs of ionized gas in the center of "cool-core" X-ray emitting clusters (CCs) has been known for decades (Fabian et al. 1984b; Heckman et al. 1989; Hatch et al. 2007; McDonald et al. 2010; Tremblay et al. 2015). From this angle, it is tempting to view the high-redshift Lyα

[1] Laboratoire AIM-Paris-Saclay, CEA/DSM-CNRS-Université Paris Diderot, Irfu/Service d'Astrophysique, CEA Saclay, Orme des Merisiers, F-91191 Gif sur Yvette, France
[2] francesco.valentino@cea.fr
[3] Department of Physics, University of Helsinki, Gustaf Haällströmin katu 2a, 00014 Helsinki, Finland
[4] Center for Space Sciences and Technology, University of Maryland, Baltimore County, 1000 Hilltop cir., Baltimore, MD 21250, USA
[5] Department of Physics, Ludwig-Maximilians-Universität, Scheinerstr. 1, 81679 München, Germany
[6] Dipartimento di Fisica e Astronomia, Università degli Studi di Bologna, Viale Berti Pichat 6/2, 40127 Bologna, Italy
[7] INAF Osservatorio Astronomico di Bologna, Via Ranzani 1, 40127 Bologna, Italy
[8] National Optical Astronomy Observatories, 950 N Cherry Avenue, Tucson, AZ 85719, USA
[9] INAF-Osservatorio Astronomico di Padova Vicolo dell'Osservatorio 5, I-35122 Padova, Italy
[10] European Southern Observatory, Karl-Schwarzschild-Str. 2, 85748 Garching, Germany
[11] School of Physics, Korea Institute for Advanced Study, Hoegiro 85, Dongdaemun-gu, Seoul 02455, Republic of Korea
[12] Institute for Astronomy, ETH Zürich Wolfgang-Pauli-strasse 27, 8093 Zürich, Switzerland
[13] Subaru Telescope, National Astronomical Observatory of Japan 650 North A'ohoku Place, Hilo, HI 96720, USA
[14] Astronomy Centre, Department of Physics and Astronomy, University of Sussex, Brighton, BN1 9QH, UK
[15] Graduate University for Advanced Studies, 2-21-1 Osawa, Mitaka, Tokyo, Japan

nebulae as the counterparts of local filaments, with sizes and luminosities reflecting the extreme conditions of the primordial Universe (McDonald et al. 2010; Arrigoni-Battaia et al. 2015). However, the detailed physics of the nebular emission is still debated even for local clusters, despite the quality of the available data. A mix of different heating mechanisms is probably at the origin of the emission by the ionized filaments, with a possible important role played by young stars formed *in-situ* (Tremblay et al. 2015 and references therein). The origin of the cold gas has not been fully clarified either: even if modern models of auto-regulated cooling from the X-ray emitting intracluster medium (ICM) successfully reproduce several properties of the nebulae in CCs (i.e., Gaspari et al. 2012; Voit & Donahue 2015; Tremblay et al. 2015), the cold gas might also originate from a starburst event or the active galactic nuclei (AGN) in the central brightest cluster galaxy (BCG, Hatch et al. 2007), or be uplifted by propagating radio-jets and buoyant X-ray bubbles (Churazov et al. 2001; Fabian et al. 2003), or stripped in a recent merger (Bayer-Kim et al. 2002; Wilman et al. 2006). Therefore physical insights might not be straightforwardly gained from the simple observation of local filaments.

An attempt at assessing the validity of this suggestion can be done through the observation of giant Lyα nebulae in the core of high-redshift galaxy clusters. To date, we have lacked strong observational evidence primarily because of the scarcity of *bona fide* X-ray emitting structures discovered at $z \geq 1.5$ (i.e., Andreon et al. 2009; Papovich et al. 2010; Santos et al. 2011; Stanford et al. 2012; Gobat et al. 2011, 2013; Brodwin et al. 2015). Here we study in detail the case of the most distant among these X-ray detected structures, CL J1449+0856 at $z = 1.99$ (Gobat et al. 2011, 2013; Strazzullo et al. 2013, G11, G13 and S13 hereafter). Its extended emission from hot plasma and the dominant population of red, massive, and passive galaxies in the compact core (G11, G13, S13) place it in a more advanced evolutionary stage than protoclusters at similar redshift and make it a suitable candidate to start the search for nebulae in far away clusters. In this work we present the results of a recent narrow-band imaging campaign we conducted with Keck/LRIS, with which we identified a ~ 100 kpc Lyα-emitting nebula in the cluster core. However, the detailed analysis of the conditions of the nebula and its environment shows some tensions with the current picture of filaments in local clusters. Even if cooling from the X-ray emitting plasma may partially contribute to the Lyα luminosity, the nebula is plausibly powered by AGN in the cluster core.

Motivated by this discovery, we further investigate the relationship between the Lyα nebula, galaxy activity in the form of star formation and black hole growth, and the total energy content of the ICM at this early stage of the cluster evolution. The latter is a controversial issue in modern astrophysics. In fact, it has been known for more than two decades that the observed X-ray properties of the ICM in nearby clusters are inconsistent with the predictions from pure gravitational settling and an extra energy contribution is missing (Kaiser 1991; Ponman et al. 1999; Tozzi & Norman 2001). In cosmological simulations this energy is provided by star-forming galaxies (SFGs) and AGN through outflows, and their efficiencies can be calibrated to reproduce the properties of the local Universe (e.g., Le Brun et al. 2014; Pike et al. 2014). Although the most successful models are those in which heating of the ICM happens early, such as (cosmo-)OWLS (Schaye et al. 2010; McCarthy et al. 2011), this process is still poorly constrained observationally: the timing and duration of this phenomenon, its main energy source (galactic winds from either supernovae or AGN), and the energy transfer mechanism are subject to debate (i.e., McCarthy et al. 2011; Davé et al. 2008; McNamara & Nulsen 2007; Fabian 2012). Here we argue that the presence of the Lyα nebula is interlaced with the observed vigorous activity of galaxies in the cluster core and that it may signpost a significant energy injection into the ICM. Eventually, we estimate the amount of this injection due to strong galaxy feedback during a phase that, if prevalent in high-redshift structures, would be crucial to set the final energy budget and metal content of present-day clusters.

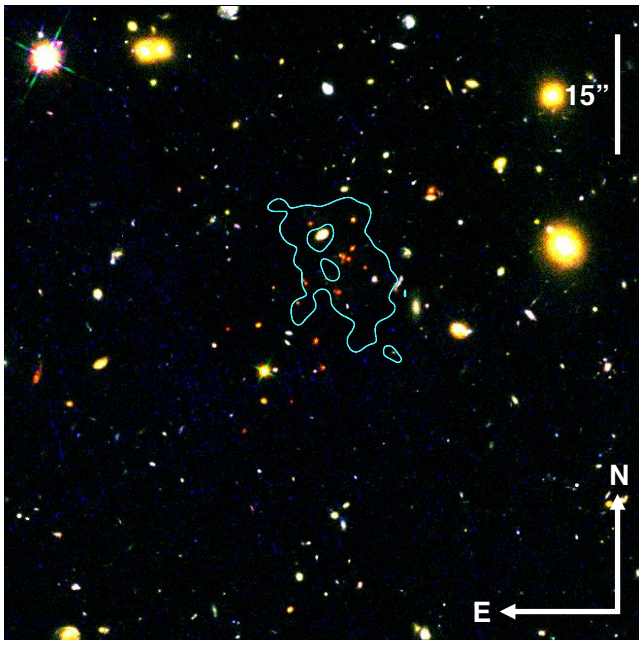

Figure 1. Cluster of galaxies CL J1449+0856 at $z = 1.99$. HST/F140W (red), F105W (green), and F606W (blue) RGB-composite image of CL J1449+0856. The central concentration of red galaxies represents the core of the cluster. The cyan line marks the 1σ contour of the Lyα nebula from the wavelet reconstruction.

This paper is organized as follows: in Section 2 we present the narrow- and broad-band imaging observations that led to the discovery of the Lyα nebula, along with the results of a recent Chandra follow-up of CL J1449+0856; in Section 3 we discuss the physical properties of the Lyα nebula, the possible powering mechanisms, and the timescales regulating its evolution, concluding that a substantial gas replenishment is necessary to feed the system. In Section 4 we focus on galaxy outflows as a plausible source of gas replenishment and we study the corresponding injection of energy into the ICM. Concluding remarks are presented in Section 5. Unless stated otherwise, we assume a ΛCDM cosmology with $\Omega_{\rm m} = 0.3$, $\Omega_\Lambda = 0.7$, and $H_0 = 70$ km s^{-1} Mpc^{-1} and a Salpeter initial mass function (Salpeter 1955). All magnitudes are expressed in the AB system.

2. OBSERVATIONS AND DATA ANALYSIS

In this section we present the Keck/LRIS narrow-band imaging of CL 1449+0856. We also describe recent Chandra observations which we use to update the cluster X-ray properties previously constrained by XMM-Newton follow-up only. Specifically, we revise the total extended X-ray luminosity, gas temperature, and halo mass, presenting a new estimate from the velocity dispersion.

2.1. *The Lyα nebula detection: narrow-band imaging*

We observed CL J1449+0856 (Figure 1) for 3.5 h with the narrow-band filter NB3640 installed in the blue arm of the Keck/LRIS camera on March 27, 2014, reaching a magnitude limit of 27.1 (5σ) in a $r = 0.6$" circular aperture. The average seeing during the observation was 0.79" (full width half maximum). We processed the images in a standard way with the publicly available LRIS pipeline[16]. In particular, we modeled and subtracted a super-sky image obtained as the clipped median of all the widely dithered, processed frames. We co-added individual frames weighting them by measured seeing and transparency variations during the observing night. We then combined the final narrow-band image with an aligned U-band frame from VLT/FORS2 (5σ limiting magnitude of 27.4, S13) using the formalism presented in Bunker et al. (1995) to obtain a Lyα emission map (Figure 2 and 11 in Appendix). Color corrections are negligible, given the optimal overlap of the central effective wavelengths of the narrow- and broad-band filters (3640, 3607 Å respectively). We checked the absolute flux calibration against Sloan Digital Sky Survey data, finding an agreement within 0.01 magnitude. We selected individual Lyα absorbers and emitters by running SExtractor in dual image mode on a χ^2 detection image and on narrow- and broad-band images. We built the χ^2 detection image averaging the U and NB3640 frames weighting by their signal-to-noise ratio squared. Besides an obscured AGN (#661 in G13, see 3.3.1 below for further details), we detected only two individual bright peaks in the Lyα emission map of the cluster core ($\sim 5\sigma$) both through a classical aperture photometry approach and a wavelet analysis (Figure 3). However, they are not associated with known cluster members within a 1" radius in the adjacent U and B bands, nor in the deeper, but redder HST/F140W band or in the X-ray bands, suggesting that these peaks are not associated with SFGs in the cluster core. The uncertainty on the position of 5σ peaks of Lyα emission is 0.07". The bright knots may just be the densest regions of the extended Lyα nebula and the granularity (Figure 2, panel c) could suggest the presence of gas substructures (Cantalupo et al. 2014) or shock fronts currently beyond our detection threshold. To further confirm the detection of Lyα photons on large scales, we performed a wavelet analysis with an iterative multi-resolution thresholding and a Gaussian noise model[17] (Starck et al. 2010). The basic concept underlying wavelet decomposition is to split an image into a set of spatial frequencies, each one including the signal from sources with power on that scale. The original image is exactly recovered by adding all the "slices". The advantage of this technique is to reduce (or remove) the impact of small–scale objects when looking for large–scale structures and its efficacy for detecting Lyα nebulae has already been shown (Prescott et al. 2012, 2013). We used this technique for the purpose of visualization (Figure 1, 2, and 11 in Appendix) and to cross-check the results from a classical aperture photometry approach. After subtraction of the contribution from the point-like, obscured AGN (< 8% of the total emission), we measure a total flux of $(8.1 \pm 1.0) \times 10^{-16}$ erg cm^{-2} s^{-1} in a ~ 140 arcsec^2 polygonal aperture enclosing the whole nebula, fully consistent with the results provided by the wavelet analysis. The residual Lyα flux surrounding the AGN in the wavelet image is extended on scales larger than the point spread function (PSF, with a full width half maximum of 0.79") and contributes to the luminosity of the nebula. We also retained the flux from the other individual bright peaks since no counterparts are detected in any other band. We estimated the 1σ uncertainty as the rms of the distribution of fluxes inside circular apertures of area equal to the one in which we measured the flux of the nebula. The total flux corresponds to an observed luminosity of $L_{\mathrm{Ly}\alpha} = (2.3 \pm 0.3) \times 10^{43}$ erg s^{-1}.
The morphology of the Lyα nebula is elongated from AGN #661 towards the center of the cluster, suggesting a physical connection (Section 3.3.1). The asymmetric shape and the mis-centered location of the AGN is observed in several other nebulae at high redshift (i.e., Borisova et al. 2016) and it might simply reflect the AGN illumination cone and the gas distribution in the cluster, which naturally concentrates towards the bottom of the potential well. In fact, the peaks of the Lyα luminosity and the extended X-ray emission traced by XMM-Newton and Chandra (Section 2.3) are spatially coincident in projection, and so is the peak of the stellar mass density distribution (Figure 4), implying that the nebula effectively sits in the cluster core. Note that the peaks mapped by XMM-Newton and Chandra are consistent within the positional uncertainties (16" and 4" respectively). In Figure 5 we show the radial profile of the Lyα surface brightness and the projected stellar mass density. For both profiles we fixed the same center at the peak of the projected stellar mass density distribution. Moreover, we merged the measurements at the two farthest positions from the cluster center to increase the signal, and we subtracted the contribution of AGN #661. As opposed to the stellar component that traces the cluster potential well, the Lyα surface brightness profile appears flat over the whole extension of the nebula. A drop is expected to occur at some radius, but Figure 5 suggests that this happens at larger scales than for the stellar component.

2.2. *Extended continuum emission*

We measured the continuum emission associated with the Lyα nebula from a pure "continuum emission map" (Bunker et al. 1995) and both Subaru/Suprime-Cam B (G11) and Keck/LRIS V band imaging. We do not expect strong emission lines from sources at $z = 2$ to fall in the observed B and V bands. These frames are respectively 2.5× and 3.3× deeper than the continuum image and provide a better constraint on the Lyα equivalent width of the nebula (EW(Lyα)). In unobscured

[16] `http://www.astro.caltech.edu/~dperley/programs/lpipe.html`
[17] `http://www.cosmostat.org/software/isap/`

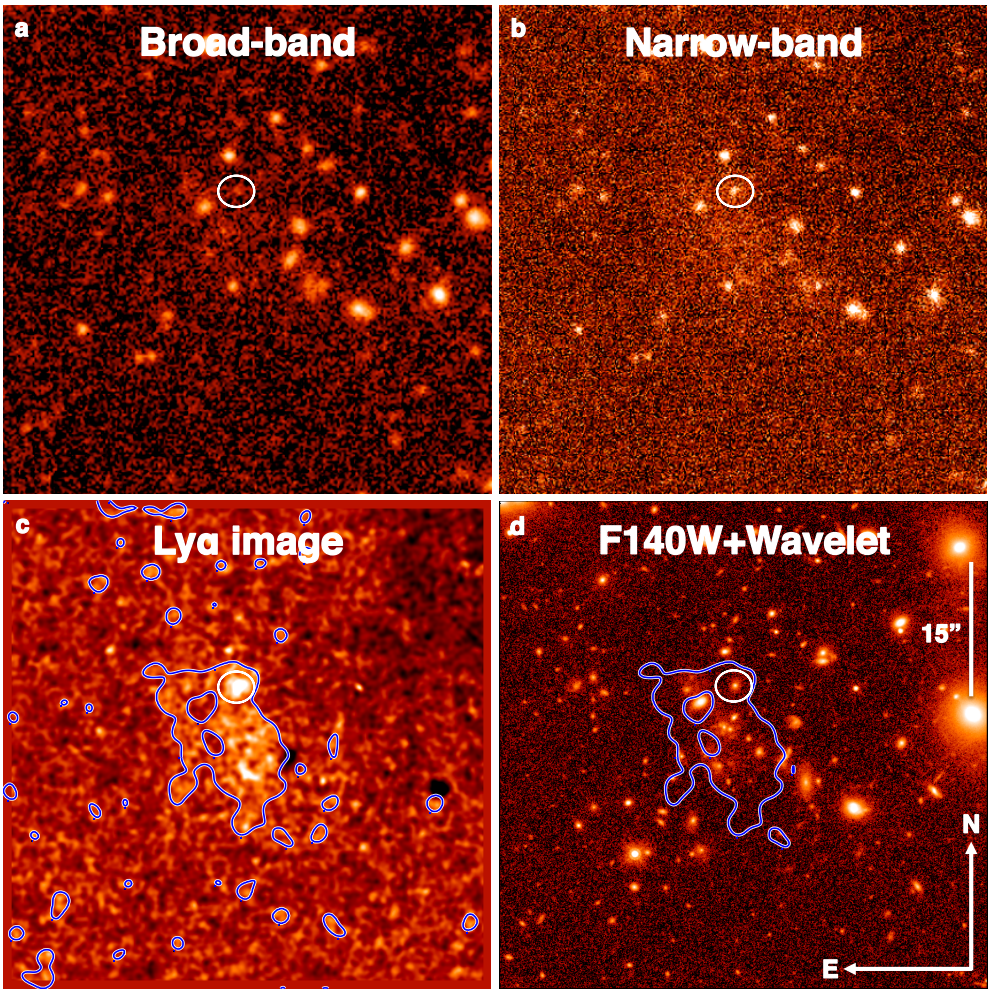

Figure 2. 100-kpc extended Lyα nebula at $z = 1.99$. Images of CL J1449+0856 in the broad U band (panel **a**) and NB3640 narrow-band (panel **b**), and a continuum-subtracted Lyα emission line map smoothed on scales of 1” (panel **c**). The white circle indicates the heavily obscured AGN #661 (G13). The extended emission southward is the Lyα nebula. Panel **d** shows the HST/WFC3 F140W image. In panels **c** and **d** the blue line marks the 1σ contour of the large scale Lyα emission from the wavelet reconstruction after the subtraction of point-like sources. For reference, 15” correspond to ~ 125 kpc at $z = 1.99$.

SFGs, the flux density F_ν is roughly constant at wavelengths bluer than 2000 Å, and thus possible color biases in the evaluation of the EW(Lyα) using B and V bands continuum are limited. We measured the continuum emission only where we detected the extended Lyα emission at more than 5σ significance (Figure 11 in Appendix, panel d). Evident B and V band sources were masked so as not to contaminate the diffuse emission. In none of the frames we individually detected a significant integrated continuum emission. Assuming a constant F_ν and combining the three bands, we estimated an average continuum emission of $(3.38 \pm 0.95) \times 10^{-19}$ erg cm^{-2} s^{-1} Å^{-1} and a corresponding Lyα equivalent width of EW(Lyα) $= 271^{+107}_{-60}$ Å, compatible with the 2σ lower limit we derived from the sole continuum image (EW(Lyα) > 192 Å). We note here that the 3σ detection is formally reached only by including the V-band, which could contain residual contaminating emission from red passive galaxies. Thus, it would be appropriate to regard the quoted EW measurement as a lower limit.

2.3. *Chandra X-ray observations*

CL J1449+0856 has been imaged both with XMM-Newton (80 ks, G11, Brusa et al. 2005) and Chandra (94 ks, Campisi et al. 2009). Details of the XMM-Newton detection have already been reported in G11. However, that analysis suffered from a large uncertainty on the localization of the cluster center. Based on the statistical analysis of galaxy groups in COSMOS (George et al. 2011), the difference between the most massive members and the X-ray peak positions is typically 15″ (Figure 4, panel b). The measured distance between the core of the cluster and the XMM position is 9″.

Archival ACIS-I Chandra observations of the field consist of a mosaic of three partially overlapping pointings of ≈30 ks each, covering a total area of ≈500 arcmin^2 at different depths. These three observations (5032, 5033, and 5034) were performed in June 2004 by the Advanced CCD Imaging Spectrometer (ACIS) with the I0 CCD at the aimpoint and all ACIS-I CCDs in use. Faint mode was used for the event telemetry, and ASCA grade 0, 2, 3, 4, and 6 events were used in the analysis (full details are reported in Campisi et al. 2009). In Cycle 16 we followed-up the field with the ACIS-S camera (aim-

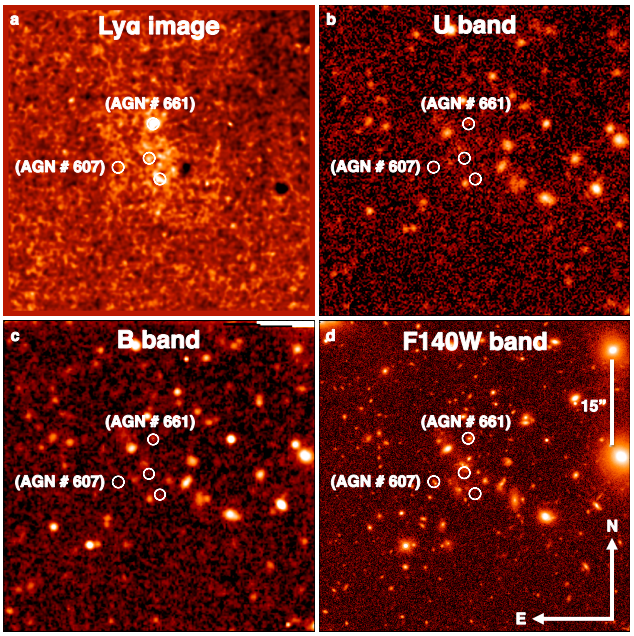

Figure 3. Bright knots in the Lyα nebula. Lyα emission line map smoothed over a 1" area (panel **a**) and U-band (panel **b**), B-band (panel **c**), and F140W band (panel **d**) images of CL J1449+0856. Individual Lyα emitters detected at $\sim 5\sigma$ are marked (white circles). The position of the AGN # 607 is reported for clarity, but this source is not identified as a Lyα emitter. For reference, 15" correspond to $\sim$ 125 kpc at $z = 1.99$.

point at CCD=7) for a nominal exposure of 94.81 ks in very faint mode. This new Chandra observation has a higher spatial resolution because pointed at the location of the diffuse emission and, thus, improves the localization of the cluster core and the association between the extended X-ray source and the optical/near-IR counterpart. For both ACIS-I and ACIS-S data, reprocessing was carried out using CIAO version 4.6 and adopting the latest relevant calibration products. From a wavelet reconstruction of the ACIS-S image, we detected a $> 4\sigma$ extended feature co-aligned with the core (Figure 4, panel a). The X-ray source is centered on coordinates 14:49:13.670, +8:56:28.25 with a 1σ uncertainty on the position of $4''$ (Figure 4, panel b) and a distance to the cluster core of $5''$. We measured the extended source flux in the area where the significance of the wavelet map was higher than 2σ. We derived ACIS-S and ACIS-I counts independently, using the same extraction region. Within a $10''$ aperture, the net (i.e., background-subtracted) number of counts from the extended source in ACIS-S is 11.0 ± 5.3 (94 ks exposure) in the $0.5 - 2$ keV band, corresponding to an aperture flux of $(8.5 \pm 3.0) \times 10^{-16}$ erg cm^{-2} s^{-1}. The ACIS-I counts and aperture flux are 5.2 ± 2.5 and 1.2×10^{-15} erg cm^{-2} s^{-1} respectively (49 ks exposure). The average flux of the source is therefore $(1.0 \pm 0.4) \times 10^{-15}$ erg cm^{-2} s^{-1}. This corresponds to an observed total X-ray luminosity of $L_{\rm X} = (9 \pm 3) \times 10^{43}$ erg s^{-1} in the $0.1 - 2.4$ keV rest-frame band within R_{500}, defined as the radius enclosing a mean overdensity 500$\times$ larger than the critical density of the Universe. We do not detect bright radio sources close to the cluster core in deep Jansky Very Large Array observations at 3 GHz down to 2.7 μJy (rms), except for two galaxies with a $\sim$ 30 μJy continuum emission, fully consistent with pure star formation activity seen at ultra-violet and infra-red wavelengths. Thus, inverse Compton scattering off extended radio-galaxy jets is not likely to be the origin of the extended X-ray emission as in potentially similar cases (i.e., Miley et al. 2006).

2.4. *Halo mass and gas temperature*

Scaling the observed total X-ray luminosity within R_{500} (Leauthaud et al. 2010), we estimated a halo virial mass of $M_{\rm halo} = (5-7) \times 10^{13}$ M$_\odot$ and a virial radius of $R_{\rm vir} = 0.5 \pm 0.1$ Mpc, in agreement with previous determinations (G11, G13). This estimate is consistent with that expected from a total stellar mass enclosed in cluster members of 2×10^{12} M$_\odot$, in particular in six massive and passive galaxies in the core (S13, $M_{\rm halo} = 4-7 \times 10^{13}$ M$_\odot$, including the latest calibration by van der Burg et al. 2014). We independently evaluated $M_{\rm halo}$ from the velocity dispersion derived from *HST*/WFC3 and Subaru/MOIRCS spectroscopy (G13, Valentino et al. 2015). After excluding obvious interlopers at redshift $z < 1.95$ and $z > 2.05$, we estimated the systemic redshift and the velocity dispersion fixing the reduced $\chi^2_{\rm red} = (\sum_{i=1}^{N} (z_{\rm i} - z_{\rm sys})^2 / (\sigma^2_{z_{\rm i}} + \sigma^2_{\rm disp}))/{\rm dof} = 1$, applying a clipping at 3σ, and iterating until convergence. This procedure allows us to fully take into account the uncertainties on spectroscopic redshifts. We then estimated the uncertainties as the 15.87 - 84.13 percentile ranges of the distribution of 15,000 bootstrap simulations. We obtain $z_{\rm sys} = 1.995^{+0.003}_{-0.004}$ and $\sigma_{\rm vel} = (830 \pm 230)$ km s^{-1}. We find consistent results modeling a Gaussian curve on the galaxy redshift distribution (Figure 6). Assuming virialization, we find a 1σ lower limit on the virial mass of $M_{\rm halo} \gtrsim 4 \times 10^{13}$ M$_\odot$ obtained adopting the 1σ lower limit on $\sigma_{\rm vel}$. Then, we calculated a total intracluster mass in the hot phase of $M_{\rm ICM} \approx 0.08 \times M_{\rm halo} \approx 5 \times 10^{12}$ M$_\odot$ (Renzini & Andreon 2014). The gas fraction may vary with redshift, but even considering a value close to the universal baryon fraction, the main result of this work would not change. Assuming spherical geometry for the halo and a mean molecular weight of $\mu = 0.6$, the average particle density is $(8 \pm 2) \times 10^{-4}$ cm^{-3} within the virial radius. Finally, we estimated a temperature of 2.1 keV from the $L_{\rm X} - T$ relation (Finoguenov et al. 2007) and an absorbing column density of $N_{\rm H}$=2×10^{20} cm^{-2}. We stress here that the current X-ray dataset allows only for an estimate of the integrated X-ray luminosity $L_{\rm X}$. We do not have in-hand the spatial profiles of X-ray derived quantities such as the temperature, entropy, density, or the metallicity of the hot ICM. In order to estimate these physical quantities, we rely on the extrapolation of well established relations at low and moderate redshift ($z < 1$).

3. PHYSICS OF THE Lyα NEBULA

In this section we study the physics of the Lyα nebula. First, we estimate the mass and electron density from its luminosity and size. We then explore the possible powering mechanisms and conclude that the most plausible source of ionizing photons are AGN embedded in the nebula, with a possible contribution from dissipation of the mechanical energy due to galaxy outflows. Finally, we discuss the typical timescales regulating the evolution of the nebula. We find that, barring an observational coin-

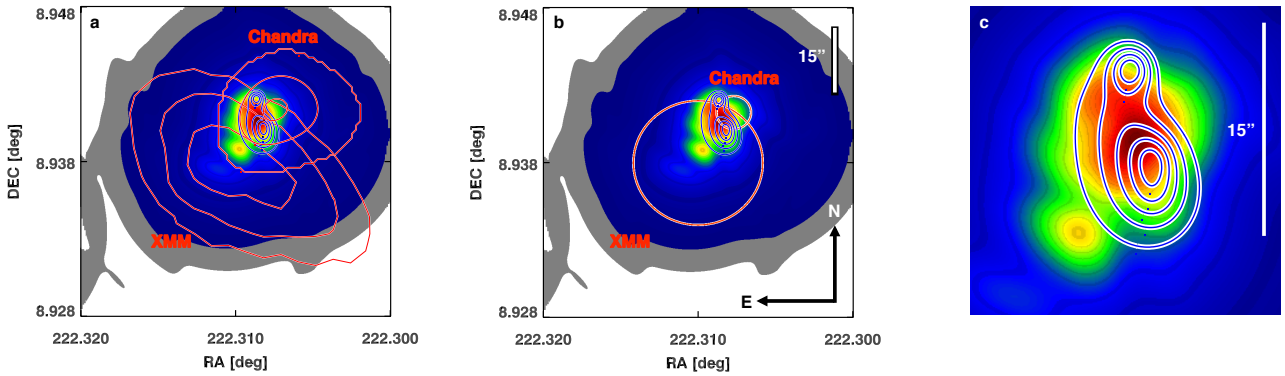

Figure 4. Spatial distributions of stellar mass density, Lyα surface brightness, and X-ray extended emission. Stellar density maps are derived from a mass complete sample of cluster members and candidates with $M_\star \geq 10^{10.4}$ M$_\odot$ (S13, background colored image in panels **a**, **b**, and **c**). The prominent stellar mass density peak represents the cluster core region (red area). Lyα nebula $\geq 3\sigma$ contours from wavelet reconstruction are superimposed (blue lines). Note that point-like sources have been subtracted before tracing the contours. Extended X-ray contours from XMM-Newton and Chandra observations (red lines) are displayed in panel **a**. The positional uncertainties of the peak of the X-ray extended emission from both sets of observations are shown in panel **b** (red circles). A zoom on the central region is shown in panel **c**. For reference, 15" correspond to ~ 125 kpc at $z = 1.99$.

cidence, in our favored scenario the nebula is constantly replenished with cold gas to survive evaporation due to the surrounding hot X-ray plasma.

3.1. *Mass and density*

Assuming photoionization, we can estimate the mass $M_{\mathrm{Ly}\alpha}$ and the electron density n_e of the ionized gas from the Lyα luminosity (McCarthy et al. 1990; Dey et al. 2005):

$$M_{\mathrm{Ly}\alpha} = 1.25\, m_\mathrm{p}\, n_\mathrm{e}\, f\, V = (1-10)\times 10^9\,\mathrm{M}_\odot \quad (1)$$

where m_p is the proton mass, f the volume filling factor, and V the volume of the nebula. For the sake of simplicity, we assumed a spherical geometry for the nebula with a radius $R_\mathrm{neb} = 46$ kpc, the average value of the long and short axes measured in the wavelet reconstructed image. The choice of the shape does not affect the final result of this work, i.e., adopting a cylindrical symmetry the volume changes by $\approx 10\%$. We assumed $f = 10^{-3} - 10^{-5}$ as detailed in next section. The electron density is derived from the Lyα luminosity estimate through:

$$L_{\mathrm{Ly}\alpha} = \frac{j_{\mathrm{Ly}\alpha}}{j_{\mathrm{H}\beta}}\,\alpha^{\mathrm{eff}}_{\mathrm{H}\beta}\, h\nu_{\mathrm{H}\beta}\, n_\mathrm{e}\, n_\mathrm{p}\, f\, V \rightarrow n_\mathrm{e} = 0.9 - 9\,\mathrm{cm}^{-3} \quad (2)$$

where $j_{\mathrm{Ly}\alpha}$ and $j_{\mathrm{H}\beta}$ are the emission coefficients for Lyα and Hβ, $\alpha^{\mathrm{eff}}_{\mathrm{H}\beta}$ is the effective recombination coefficient for Hβ, $h\nu_{\mathrm{H}\beta}$ is the energy of an Hβ photon, and n_p the proton number density ($n_\mathrm{e} \approx 1.2\, n_\mathrm{p}$ accounting for doubly ionized helium). The range of n_e values corresponds to $f = 10^{-3} - 10^{-5}$, assuming case B recombination (Osterbrock & Ferland 2006) and $T = 10^4$ K. We notice that the gas appears marginally optically thick to ionizing radiation, given the column density of neutral hydrogen averaged over the projected area of the nebula of $\langle N_\mathrm{HI}\rangle \approx 10^{17.2}$ cm^{-2} (Hennawi & Prochaska 2013, Eq. 11). Moreover, $n_\mathrm{e} \propto \left(\sqrt{f}\right)^{-1}$ and $M_{\mathrm{Ly}\alpha} \propto \sqrt{f}$, reducing the 2 orders of magnitude range of uncertainty that we allowed for f. Finally, $M_{\mathrm{Ly}\alpha}$ might be a lower limit for the total mass of cold gas reservoirs in the cluster if AGN are the powering sources (see Section 3.3), as beamed emission may illuminate only a portion of the gas. In addition, the true Lyα luminosity may be higher than reported due to dust and neutral hydrogen absorption.

3.2. *Volume filling factor*

The mass and density of the nebula depend on the volume filling factor f, which is not directly constrained by our observations. However, it is reasonable to assume pressure equilibrium between the ionized gas and the hot X-ray ICM, allowing us to put an upper limit on the possible values of f. To estimate the pressure exerted by the hot ICM, we assumed the universal pressure profile of galaxy clusters (Arnaud et al. 2010), properly rescaled in mass and redshift, as representative for CL J1449+0856. Then, dividing the pressure by $\sim 10^4$ K, the typical temperature of the Lyα gas, we obtained the radial density profile of a medium in pressure equilibrium with the X-ray emitting plasma. The range of possible values of n_e over the radial extension of the nebula is $n_\mathrm{e} \sim 1 - 10$ cm^{-3}, corresponding to $f \sim 10^{-3} - 10^{-5}$, a pressure of $p \sim 10^4 - 10^5$ K cm^{-3}, and masses of ionized gas of $M_{\mathrm{Ly}\alpha} \sim (1-10)\times 10^9$ M$_\odot$. Absent an observed X-ray profile, this is an order of magnitude calculation, given that the pressure profile in low mass systems might be different and, notably, flatter than in clusters (Le Brun, McCarthy & Melin 2015), leaving the door open for larger values of f and lower densities. However, in addition to pressure equilibrium, higher values of f ($\sim 0.01 - 1$) are disfavored by a simple argument based on gravitational stability: if larger and more massive clouds were in place, they would be Jeans-unstable and form new stars, a scenario disfavored by the observed high value of EW(Lyα) (Section 3.3.2). On the contrary, solutions with $f \lesssim 10^{-3}$ are gravitationally stable, considering the simplified case of auto-gravitating spheres of gas at 10^4 K stably ionized.

On the other hand, much smaller values of f are not easily maintained for long timescales. As recognized in classical works (Fabian et al. 1987; Crawford & Fabian 1989), lower volume filling factors and higher densities

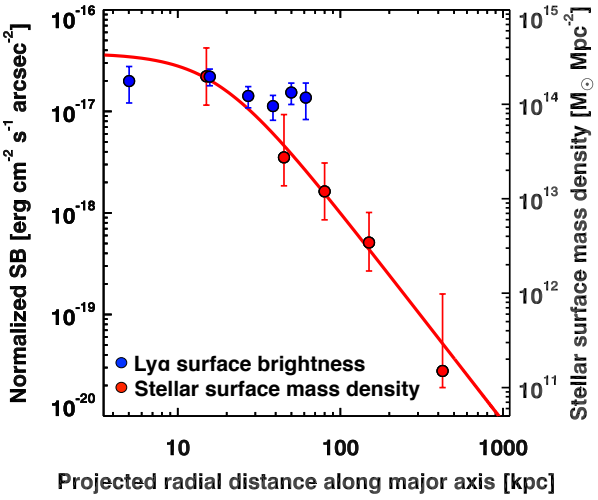

Figure 5. Lyα nebula and projected stellar mass density profiles. We show the stellar mass density (red circles) and normalized Lyα surface brightness (blue circles) radial profiles. The center of the profiles are spatially coincident and fixed at the position of the barycenter of stellar mass (S13). For the Lyα surface brightness profile we merged the measurements at the two farthest positions from the cluster center to reach the formal detection threshold. Moreover, the Lyα flux of AGN #661 has been subtracted in the corresponding bin. For the stellar mass density profile, error bars include both the Poisson error and the uncertainties in membership determination (S13). For the surface brightness profile, error bars represent the 1σ uncertainties on flux measurements. The best fit of the stellar mass profile is a classical beta-model (S13).

would imply clouds dissipating by thermal expansion on short timescales (10^5 yr), with consequent difficulties to explain the size of the nebula and its lifetime.

3.3. *Powering mechanism and origin of the gas*

We consider five different physical scenarios to explain the extended Lyα emission: hard ionizing spectra of AGN impacting gas reservoirs in the cluster core, the continuous formation of young massive stars, cooling of dense cosmological cold flows penetrating into the dark matter halo, cooling of plasma from the X-ray phase, and dissipation of the mechanical energy from galaxy outflows in the core. Eventually, we point the AGN radiation field as the most plausible powering source of the Lyα nebula, with a potential contribution from shocks induced by galaxy outflows.

3.3.1. *AGN in the cluster core*

Two spectroscopically confirmed X-ray AGN in the cluster core (#607, 661 in G13) are suitable candidates for ionizing the nebula. The depth of the new Chandra observation, coupled with an optimal on-axis alignment, allowed us to perform a basic X-ray spectral analysis despite the limited photon statistics (34 and 20 net counts in the observed $0.5-7$ keV band for sources #607 and 661, respectively). Source #607 is characterized by a power-law spectrum with photon index $\Gamma = 2.0 \pm 0.6$; the observed $2-10$ keV flux is $1.7^{+1.1}_{-0.6} \times 10^{-15}$ erg cm^{-2} s^{-1}, corresponding to a rest-frame $2-10$ keV luminosity of $5.2^{+3.4}_{-1.8} \times 10^{43}$ erg s^{-1}, typical of a luminous Seyfert galaxy. The X-ray spectrum of source #661, the point-like Lyα emitter (Figure 2), is flat: fitting the data with a power-law model provides $\Gamma = -0.7^{+0.8}_{-0.9}$, highly indicative of strong obscuration. We then included an absorption component and fixed the photon index to 1.8, as expected for the intrinsic AGN emission (e.g., Piconcelli et al. 2005). This model results in a column density of $N_{\rm H} = 9.3^{+5.6}_{-4.0} \times 10^{23}$ cm^{-2}, i.e., consistent with marginal Compton-thick absorption (1.5×10^{24} cm^{-2}). The tentative detection of an iron Kα emission line at 6.4 keV (with equivalent width of ≈ 2.4 keV rest frame), if confirmed, would further support the heavily obscured nature of source #661. The derived $2-10$ keV flux is $(7.4 \pm 2.2) \times 10^{-15}$ erg cm^{-2} s^{-1}, corresponding to a rest-frame luminosity of $L_{2-10\,\rm keV} = 2.9^{+0.6}_{-0.5} \times 10^{44}$ erg s^{-1}, placing source #661 in the quasar regime. We do not detect any bright counterpart in deep Jansky Very Large Array observations at 3 GHz down to 2.7 μJy (rms), and we thus classify source #661 as radio-quiet. From aperture photometry, we estimated a Lyα flux of $(6.7 \pm 0.7) \times 10^{-17}$ erg cm^{-2} s^{-1}, corresponding to a luminosity of $(1.9 \pm 0.2) \times 10^{42}$ erg s^{-1}. The spectral energy distribution (SED) of #661 is shown in Figure 7. From SED modeling, which benefits from near-, mid- and far-IR observations from Spitzer and Herschel, we estimated a bolometric luminosity for the AGN of $(2.7 \pm 1.5) \times 10^{45}$ erg s^{-1}. A similar value ($3.2 \pm 0.6 \times 10^{45}$ erg s^{-1}) is derived using the observed [O III]λ5007 Å luminosity obtained from recent Subaru/MOIRCS spectroscopy of the galaxy (Valentino et al. 2015), converted into a bolometric luminosity as $L_{\rm bol}/L_{\rm [OIII]} = 3500$ (Heckman et al. 2004). Assuming the luminosity-dependent bolometric correction as in Lusso et al. (2012), we predict an intrinsic $2-10$ keV luminosity for source #661 of $1.6^{+1.6}_{-0.5} \times 10^{44}$ erg s^{-1}. This value is consistent, within the uncertainties due to the adopted relations and measurements, with that derived from the X-ray spectral analysis reported above.

Furthermore, we normalized the "radio-quiet AGN" template by Elvis et al. (1994) to match the estimated $L_{\rm bol}$. We then integrated over wavelengths bluer than the Lyman continuum limit to obtain the ionizing photon flux ϕ from both sources. We obtained $\phi \sim 1.3 \times 10^{55}$ and $\phi \sim 7.3 \times 10^{54}$ photons s^{-1} for source #661 and #607, respectively. Taking into account the distance between the AGN and the peak of diffuse Lyα emission, a conical illumination pattern of the neutral gas, and a covering factor of the ionized gas $f_{\rm C} \sim 1$ consistent with the observations (Section 3.5), we estimate that $(6.5-15.3)\%$ and $(14.5-49.2)\%$ of ionizing photons from #661 and #607 reach and ionize the gas. The number of ionizing photons necessary to explain the observed Lyα luminosity is:

$$\phi = \frac{L_{Ly\alpha}}{h\,\nu_{\rm Ly\alpha}} \frac{1}{\xi_{Ly\alpha}} \approx 1.8 \times 10^{54}\,{\rm photons\,s^{-1}} \qquad (3)$$

where $\xi_{\rm Ly\alpha} = 0.68$ is the fraction of ionizing photons converted in Lyα (Spitzer 1978). Thus, the AGN are likely capable of producing a sufficient amount of ionizing radiation to power the gas emission, even if $f_{\rm C}$ were a factor of several times smaller. We note that the flat Lyα surface brightness distribution in Figure 5 is not *a priori* in contradiction with powering from the AGN.

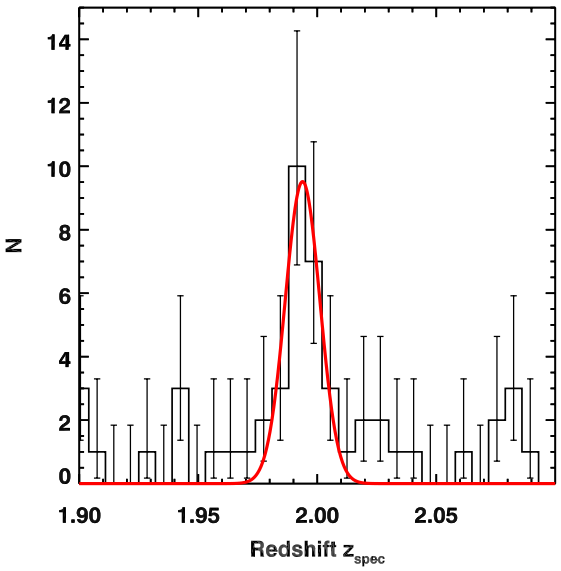

Figure 6. Cluster redshift distribution. The black histogram shows the redshift distribution of galaxies in CL J1449+0856. The red curve is the best Gaussian model fitting the curve. The uncertainties represent the formal 68.3% Poisson confidence interval.

The geometry of the system, the absorbing torus around the AGN, and the distribution of the cold clouds impact the observed profile: the flatness might just reflect covering factors close to unity. In fact, for volume filling factors $f = 10^{-3} - 10^{-5}$ and a covering factor $f_C \sim 1$, energetic photons from the AGN may ionize gas at large distances. Finally, we note that resonant pure scattering of Lyα photons from #661 can hardly contribute to the diffuse luminosity farther than ~ 10 kpc - less than 10% of the whole extension of the nebula -, as detailed radiative transfer modeling shows (Cantalupo et al. 2005; Dijkstra et al. 2006).

3.3.2. *Young massive stars*

Ongoing and continuous formation of young stars spread over the nebula might be a possible alternative ionizing source (Miley et al. 2006). The total star formation rate (SFR) inferred from the Lyα luminosity is (21 ± 3) M$_\odot$ yr^{-1} (Kennicutt 1998), assuming an intrinsic ratio of $L_{\rm Ly\alpha}/L_{\rm H\alpha} = 8.7$ (Case B recombination, Osterbrock & Ferland 2006). This estimate should be regarded as a strong lower limit on the total SFR since we do not correct $L_{\rm Ly\alpha}$ for dust obscuration and scattering from neutral hydrogen. However, both truly diffuse star formation and the emergence of undetected galaxies populating the low-mass end of the mass function and contributing to the diffuse emission (Zibetti et al. 2005) are disfavored: the high value of EW(Lyα)$= 271^{+107}_{-60}$ Å implies ages too young to be reasonably observable (Section 2.2 and Figure 7 in Schaerer 2003). Assuming a continuous star formation history, we should observe stars younger than $\lesssim 3$ Myr distributed over a 100-kpc scale, much larger than the typical super-star cluster size. For comparison, EW(Lyα) is ~ 100 Å for the continuous star formation regime. A single, simultaneous star-burst event on the same scale seems even less likely. Small effects due to the choice of the initial mass function or metallicity do not change these results, unless considering extreme Population III stars (Schaerer 2003). We stress here that the weak continuum detection is formally reached only by averaging the U frame with redder bands, which could contain residual contaminating emission from red passive galaxies. In addition, the Lyα flux is not corrected for dust absorption and scattering from neutral hydrogen. Hence, the quoted EW measurement is reasonably a lower limit of the true value.

3.3.3. *Cosmological cold flows*

Another viable origin for the Lyα photons is the cooling of the dense streams penetrating into dark matter halos currently predicted by hydrodynamical cosmological simulations (Dekel et al. 2009; Goerdt et al. 2010). The current status of these models disfavors this scenario showing that, given the halo mass of CL J1449+0856, these cold flows should have stopped reaching the cluster core ~ 1 Gyr prior to observation, being shock-heated to the virial temperature (Valentino et al. 2015). Nevertheless, in the cluster core we estimate a total SFR of ≈ 1000 M$_\odot$ yr^{-1} (Section 4.1) that must be constantly fueled by fresh cold gas given the 0.5 Gyr gas depletion timescale typical at $z = 2$ (Daddi et al. 2010; Tacconi et al. 2013). This points to an inconsistency with the prescriptions of present day models. Note, however, that the mass and redshift regimes at which cold flows should not penetrate into the hot ICM have not been observationally confirmed yet, and suffer from substantial scatter in simulations (Dekel et al. 2009). In addition, there are hints that within this scatter a cluster progenitor at $z = 2$ may be crossed by dense gas streams supporting high SFRs and powering extended Lyα nebulae (Danovich et al. 2015). For the rest of the paper, we will adopt the predictions of current cosmological simulations, excluding a substantial contribution to the Lyα luminosity from cold flows. We defer a more detailed discussion to future work.

3.3.4. *Classical cooling flows and cool-cores*

Cooling from the X-ray emitting phase to a cold $\sim 10^4$ K temperature is known to occur at low redshift and is generally considered the origin of the nebular filaments observed in cool-core clusters (CCs, Fabian et al. 1984b; Heckman et al. 1989; Hatch et al. 2007; McDonald et al. 2010; Tremblay et al. 2015). More extreme manifestations of the same mechanism are the classical cooling flows, though obvious cases are not currently known in the local Universe (Peterson & Fabian 2006). Even though we cannot properly classify CL J1449+0856 as CC or non-CC according to the standard X-ray based definition owing to poor X-ray sensitivity at $z = 2$, we find several inconsistencies between this cluster and the typical local CCs or classical cooling flows. First, *the ratio between the Lyα luminosity of the nebula and the total X-ray luminosity of the ICM is orders of magnitude larger in CL J1449+0856 than predicted for classical cooling flows or observed in local CCs.* In CL J1449+0856 we find $L_{\rm Ly\alpha}/L_{\rm X} \sim 0.3$, while $L_{\rm Ly\alpha}/L_{\rm X} \sim 10^{-3}$ and $\sim 0.5 \times 10^{-3}$ for classical stationary cooling flows (Cowie et al. 1980; Bower et al. 2004; Geach et al. 2009) and CCs, respectively. To compute

the ratio for local CCs, we collected measurements of extended Hα luminosities from the survey by McDonald et al. (2010) and the X-ray flux observed with ROSAT (Ledlow et al. 2003). Assuming $L_{\rm Ly\alpha}/L_{\rm H\alpha} = 8.7$ (Case B recombination, Osterbrock & Ferland 2006), we derived an average $L_{\rm Ly\alpha}/L_{\rm X}$ ratio of 5×10^{-4} (40% less when including only the extended filaments and not the flux from the BCG) for 13 structures in the Abell catalog. This is a conservative upper limit, since our Lyα measurement for CL J1449+0856 is not corrected for reddening nor scattering. The only cases when $L_{\rm Ly\alpha}/L_{\rm X} \sim 0.01$ happen in presence of strong radio-galaxies (i.e., Hydra A), while we exclude emission from such sources in CL J1449+0856 thanks to our deep JVLA 3 GHz maps down to 2.7 μJy (rms). This was already recognized in the seminal paper by Heckman et al. (1989) where the highest $L_{\rm Ly\alpha}/L_{\rm X}$ ratios strongly correlate with the presence of a bright radio-galaxy in the core (Cygnus A, 3C 295, Perseus) and consequently show high excitation lines in the spectra of the nebulae. For reference, the widely studied case of the Perseus cluster (i.e., Fabian et al. 1984a; Conselice et al. 2001; Hatch et al. 2005, 2007) shows $L_{\rm Ly\alpha}/L_{\rm X} \lesssim 5{\times}10^{-3}$. We stress once more that we do not measure a proper observed X-ray profile for the cluster. Thus we cannot isolate the core luminosity (better correlated with the nebular luminosities, Figure 9 and 11 in Heckman et al. 1989), but we can only compare global properties (their Figure 10). Overall, the Lyα nebula we discovered is hugely overluminous with respect to local analogs: only $\ll 1\%$ of its luminosity could be explained if CL J1449+0856 were the high-redshift version of a typical low-redshift CC.

Moreover, local nebular filaments are frequently connected with episodes of star formation. If not in the filaments themselves - observationally there is not clear evidence disproving this possibility (McDonald et al. 2010; O'Dea et al. 2010; Tremblay et al. 2015) - star formation should occur at least in the central galaxies, fueled by the gas cooled from the X-ray phase. The presence of large molecular gas reservoirs associated with the filaments (Salomé et al. 2011; McNamara et al. 2014) further supports this argument. In CL J1449+0856 this is not observed: the peak of the extended Lyα emission (once removed the contribution of the offset point-like AGN) does not overlap with any cluster member, nor to any evident source in all bands from U to near-infrared *HST*/F140W. In this sense, if cooled gas is flowing towards the bottom of the potential well where the peak of the Lyα emission lies (Figure 4), it is not triggering star formation nor AGN feedback in any object.

Finally, as we will show later in Section 4.2, SFGs and AGN in the cluster core can inject a huge amount of energy into the surrounding medium. Considering only mechanical energy, this quantity is 5$\times$ higher than the observed X-ray luminosity at $z = 1.99$, largely enough to offset *global* catastrophic cooling from the ICM and to strongly disfavor the hypothesis of a classical cooling flow. However, *local* rapid cooling may arise at the peak of the density distributions in the ICM, caused by onset of thermal instabilities. This argument is at the base of modern feedback regulated models of ICM cooling, which have proved to successfully reproduce several properties of the local nebular filaments (Gaspari et al. 2012; Sharma et al. 2012). Here we cannot directly test the simple prescription proposed in these models based on the ratio between the free-fall time and the timescale necessary to start the thermal instabilities. Nevertheless, we note that feedback is likely to play a role (Section 4.2), even if a circular 'on-off' auto-regulated regime might not be easily established at high redshift, given the long gas depletion timescales in galaxies ($0.5-1$ Gyr, Daddi et al. 2010; Tacconi et al. 2013) compared with the age of the Universe.

We conclude that the observed Lyα emission is not due to cooling from the X-ray phase in the form of a classical stationary flow. On the other hand, if moderate cooling partially contributes to the total Lyα luminosity regulated by feedback, it generates very peculiar features not observed in local CCs.

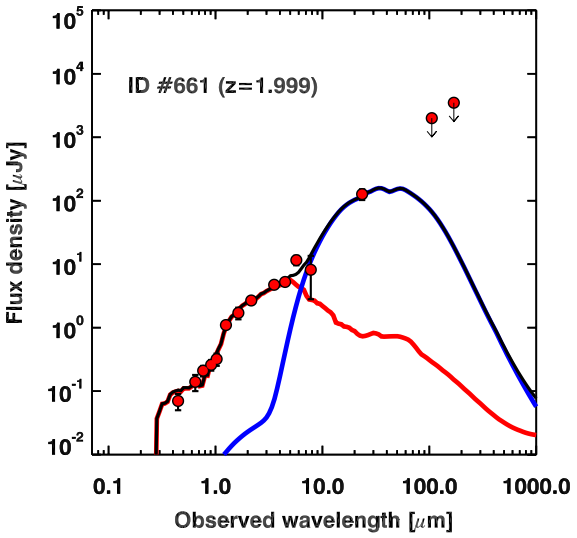

Figure 7. SED modeling of the marginally Compton-thick AGN #661. *U*-band to Herschel/SPIRE 250 μm observations are shown (red circles). The contributions of stars (red line) and the AGN (blue line) are shown independently. The full model is the sum of the two components (black line). The spectroscopic redshift is from Subaru/MOIRCS (Valentino et al. 2015).

3.4. *Shocks*

Lyα emission could be powered by shocks induced by galaxy outflows on the surrounding pressurized ICM. We constrain the maximum fraction of total kinetic energy injected by winds that is lost by radiative losses simply dividing the total power radiated through emission lines ($\approx 2\times$ the observed total Lyα luminosity $L_{\rm Ly\alpha}$) by the instantaneous energy injection ensuing galaxy outflows $\dot{E}_{\rm kin}$ (Section 4.2). This fraction ($\sim 10\%$) is presumably a strong upper limit, considering the large number of ionizing photons emitted by AGN and star-forming galaxies in the core, and the low density of the ICM. If shocks were dominating the Lyα emission, we could not estimate the mass from Eq. 1, but rely on alternative working hypotheses, i.e., pressure equilibrium and geometrical assumptions. Future spectroscopic follow-up will help to quantify the contribution of shocks to the nebular emission, i.e., from UV lines ratios (Dey et al.

2005; Prescott et al. 2009).

3.5. *Time evolution of the Lyα nebula*

The evolution and the lifetime of the Lyα nebula are globally driven by cooling and heating processes, the dynamics of the gas, and their typical associated timescales. In the following, we envisage the time evolution of the system assuming that it is stable and exploring different physical scenarios.

3.5.1. *Dynamics*

As mentioned in Section 3.2, a single massive nebula at rest at the bottom of the potential well would rapidly collapse and form stars, since the pressure exerted by the particles of a 10^4 K, Lyα-emitting gas would be insufficient to balance the effect of gravity. This scenario is not consistent with our observations (Section 3.3). On the other hand, the Lyα nebula may be globally at rest at the bottom of the potential well if structured in smaller and denser clouds moving with a typical velocity comparable with the velocity dispersion of the cluster. However, the Lyα clouds would dissipate energy through turbulence. If not energized by external factors, they would inevitably start cooling and collapsing. All things considered, if the Lyα nebula were globally at rest in the dark matter halo, it would quickly disappear on a cooling timescale, making our discovery an unconvincingly lucky coincidence. Planned spectroscopic follow-ups will directly probe the dynamical state of the nebula and test our predictions.

3.5.2. *Cooling and heating*

Absent a strong powering mechanism, the continuous irradiation of Lyα photons would lead to the quick collapse and disappearance of the clouds. This would happen on timescales of $t_{\rm cool} \approx 2.07 \times 10^{11}\,{\rm s}\,(T/10^4\,{\rm K})(n_{\rm e}/1\,{\rm cm}^{-3})^{-1} \times (\Lambda(T)/10^{-23}\,{\rm erg\,cm^3\,s^{-1}})^{-1} \sim 0.1$ Myr, where $T = 10^4$ K is the gas temperature, $n_{\rm e} \sim 1 - 10$ cm^{-3} the electron density corresponding to plausible values of the volume filling factor ($f = 10^{-3} - 10^{-5}$), and $\Lambda(T)$ the cooling function (Dey et al. 2005; Sutherland & Dopita 1993). Strong cooling of the Lyα clouds is disfavored by the large extension of the nebula and the absence of features of recent star-formation occurring in the ICM (Section 3.3). Moreover, the cold gas is immersed in a bath of energetic photons produced by the AGN that can keep a large fraction of it ionized. This would be compatible with the geometry of the system and dust absorption (Section 3.3.1). In addition, magnetic fields in the ICM can insulate and stabilize the ionized clouds, further preventing cooling and prolonging their lifetime up to ∼ 10 Myr, as proposed for nebular filaments in local CCs (Conselice et al. 2001; Fabian et al. 2003, 2008).

Conversely, Lyα-emitting gas clouds in macroscopic motion with respect to the hot medium, can be thermalized through hydrodynamical instabilities and shocks. We estimate the timescale for the interaction between the cold and hot ICM phases following Klein et al. (1994):

$$t_{\rm therm} = \left(\frac{n_{\rm e}^{\rm Ly\alpha}}{n_{\rm e}^{\rm hot}}\right)^{1/2} \frac{R_{\rm cloud}}{c_{\rm s}^{\rm hot}} \qquad (4)$$

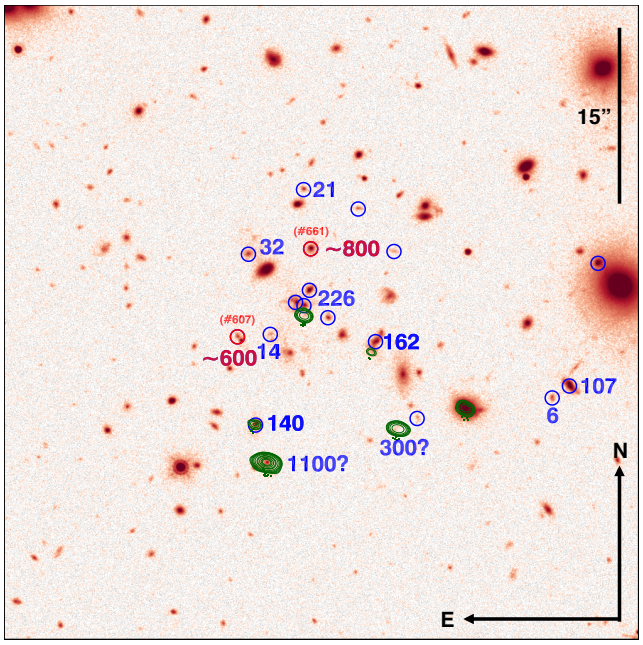

Figure 8. Map of the activity in the central cluster region. For each cluster star-forming (blue circles) or AGN (red circles) member in the *HST*/WFC3 F140W image, we indicate the indirect estimates of the outflow rate in $M_\odot$ yr^{-1} as derived in Section 4.1. When available, we provide the SFR estimated from the continuum at 870 μm from ALMA observations (green contours). Question marks denote outflow rates associated to ALMA sources without redshift confirmation and hence not included in our most conservative approach.

where $R_{\rm cloud}$ is the radius of individual Lyα-emitting clouds, and $c_{\rm s}^{\rm hot} \approx 500$ km s^{-1} the sound speed in the hot medium. This speed is also comparable with the velocity dispersion in the cluster (Section 2.4). For simplicity, we adopted the classical hydrodynamical, non-radiative case where we considered the effects of hot winds moving at a typical speed of the order of $c_{\rm s}^{\rm hot}$, much greater than the sound speed in the cold gas. However, a fully numerical treatment including radiative losses gives similar results (Scannapieco & Brüggen 2015). We allowed for possible clumpiness in the nebula assuming $R_{\rm cloud} < R_{\rm neb}$ when the volume filling factor is $f < 1$, where $R_{\rm neb} = 46$ kpc is the radius of the whole nebula (Section 3.1). To constrain $R_{\rm cloud}$, we adopted a pure geometrical approach (Hennawi & Prochaska 2013). Assuming spherical clumps spatially uniformly distributed in the spherical nebula of radius $R_{\rm neb}$ and with a single uniform clumps' gas density, we can link f to $R_{\rm cloud}$ through the covering factor $f_{\rm C}$:

$$f = f_{\rm C}\frac{R_{\rm cloud}}{R_{\rm neb}} \qquad (5)$$

The relative smooth morphology of the nebula and the flat surface brightness profile are consistent with $f_{\rm C}$ of the order of unity, although we cannot determine its accurate value. Assuming $f = 10^{-3} - 10^{-5}$, we obtain a typical timescale for thermalization of $t_{\rm therm} \sim 0.1 - 3$ Myr. Relaxing the constraint on the covering factor up to a factor of 5, we find $t_{\rm therm} \sim 0.5 - 10$ Myr, consistent with the lower limit on the lifetime of filaments in local CCs.

As a direct consequence, barring an improbable observational coincidence, maintaining the nebula stable

against evaporation requires a replenishment of cold gas at a rate of $\dot{M}_{\rm repl} = M_{\rm Ly\alpha}/t_{\rm therm} \gtrsim 1000$ M$_\odot$ yr^{-1}. Note that this estimate is sensitive to the presence of colder gas reservoirs not shining in Lyα and possible localized cooling partially compensating the heating, which could lower the final value. On the other hand, the quoted number could be regarded as a lower limit, since the parameters in the equations could substantially increase the replenishment rate in the plausible ranges we considered. The replenishment rate is directly proportional to $f_{\rm C}$, but mildly depends on f through both terms of the fraction ($\dot{M}_{\rm repl} \propto f^{-0.25}$), making the minimum replenishment stable against the range of values we allowed for the filling factor. Physically, the smaller the volume filling factor, the smaller the total mass of the nebula, but the shorter the evaporation time of the denser and clumpier gas. The density contrast term and the size of the clumps act in opposite way on $t_{\rm therm}$, with $R_{\rm cloud}$ dominating the final value: smaller clumps are crossed by shocks or hydrodynamical perturbations more rapidly than larger clouds and, consequently, they are disrupted faster.

If not continuously sustained against evaporation, the nebula would disappear on timescales of $t_{\rm therm}$ or, analogously, very short timescales imply unphysical replenishment rates $\dot{M}_{\rm repl}$ to explain the presence of the nebula. We note that the evaporation timescale is shorter than the nebula crossing time ($\sim$ 90 Myr), given a radius of $R = 46$ kpc and a typical wind speed of 500 km s^{-1} (i.e., Förster-Schreiber et al. 2014). This raises the problem of explaining the extension of the nebula, since the Lyα-emitting clouds should evaporate well before filling the observed volume. The issue would be naturally fixed if the clouds primarily form *in situ* by cooling from the X-ray emitting ICM. Globally, this is unlikely to be the case especially far away from the cluster center, where cooling times from bremsstrahlung are long. However, *local* thermal instabilities might be established in the densest portions of the ICM, providing part of the cold gas needed. On the other hand, if the gas replenishment is due to galaxies (as we envisage in the next section), the size of the nebula is explained both by the distribution of cluster members over a large area, since in this case clouds being injected at different positions would not need to cross the whole nebula, and by recent models of radiatively cooling winds (Thompson et al. 2015). Moreover, galaxies are rapidly moving in the cluster core and, consequently, winds are naturally spread over large portions of the nebula.

4. DISCUSSION

In the previous section we have shown that the nebula must be constantly replenished of cold gas at a rate of $\gtrsim 1000$ M$_\odot$ yr^{-1} in order to shine for timescales longer than $\approx$ 10 Myr. Here we focus on galaxy outflows as a plausible mechanism to supply this gas. We introduce independent constraints on the amount of gas released by galaxies based on the observed star formation and AGN activities and we show that outflows are sufficient to explain the presence of the nebula. We further discuss the implications of mass and energy extraction from galaxies and the ensuing injection into the ICM, a process necessary to explain the thermodynamics of local clusters. We also draw a comparison with state-of-the-art cosmological simulations to test the consistency of our estimate.

4.1. *Gas replenishment through galaxy outflows*

The gas necessary to sustain the Lyα nebula can be supplied by galaxy members through supernovae- (SNe) and AGN-driven outflows, a feature ubiquitously observed in high-redshift galaxies (i.e., Newman et al. 2012; Förster-Schreiber et al. 2014; Genzel et al. 2014; Harrison et al. 2015) and strongly supported by theoretical models and cosmological and zoom-in simulations (i.e., Davé et al. 2008; Hopkins et al. 2012; Lilly et al. 2013; Gabor & Bournaud 2014). Is the galaxy activity in CL J1449+0856's core sufficient to provide a minimal mass rate of $\gtrsim 1000$ M$_\odot$ yr^{-1} as required by the Lyα nebula? To answer this question, we computed the total mass outflow rate considering both contributions from the observed SFR and AGN activity (Figure 8). We converted members' SFRs into mass outflow rates $\dot{M}_{\rm out}$ by multiplying by a conservative mass loading factor $\eta = \dot{M}_{\rm out}/{\rm SFR} = 1$. This is likely to be a lower limit for the ionized and molecular gas expelled by galaxies, both observationally and theoretically (i.e., Newman et al. 2012; Hopkins et al. 2012; Gabor & Bournaud 2014, Hayword et al. 2015). This order of magnitude is also necessary to explain the metal enrichment of the ICM. Indeed, the same amount of metals is locked into stars and distributed in the ICM, favoring the equality $\dot{M}_{\rm out} \approx$ SFR (i.e., Renzini & Andreon 2014). The SFRs were derived either from SED modeling from our 13-band photometry (S13), Hα from our recent Subaru/MOIRCS follow-up (Valentino et al. 2015), or 870 μm continuum detection in ALMA maps applying a Main-Sequence galaxy template (Magdis et al. 2012). ALMA observations, reduction and analysis will be presented in a forthcoming paper (Strazzullo et al in prep.). The total SFR in the central region is SFR ≈ 1000 M$_\odot$ yr^{-1}. An individual bright ALMA source stands out in the cluster field. Its 870 μm flux is $F_{870\mu{\rm m}} = 5.5$ mJy, corresponding to a total infra-red luminosity between $8-1000$ μm of $L_{\rm IR} = 6.6\times10^{12}$ L$_\odot$ and SFR $= 1100$ M$_\odot$ yr^{-1} at $z = 1.99$ (Figure 8). The measurement errors are negligible with respect to the 0.15 dex uncertainty due to modeling (Strazzullo et al. in prep.). As there is no spectroscopic confirmation that the ALMA source is a member of the cluster, we have conservatively excluded it from the SFR accounting. We note that, if confirmed to be part of the cluster, this source would increase by a factor of 2$\times$ the total SFR in the core.

The growth of black holes further contributes to the mass outflow rates. We estimated its order of magnitude by directly converting $L_{\rm bol}$ into mass outflow rates using the empirical calibration by Cicone et al. (2014). In this case, we obtain $\approx$ 600 and 800 M$_\odot$ yr^{-1} for #607 and #661, respectively. Moreover, it appears that we have not captured the system during a phase of exceptional AGN activity. In fact, the integrated SFR/$L_{\rm X}$ ratio observed in the cluster core is close to the cosmic average value (Mullaney et al. 2012). The predicted X-ray luminosity is $\langle L_{\rm X}\rangle = {\rm SFR}\times4.46\times10^{41}$ erg s^{-1} $\approx 4.5\times10^{44}$ erg s^{-1}, while the observed value from the two AGN is 3.4×10^{44} erg s^{-1}. We remark that the calibration by Cicone et al.

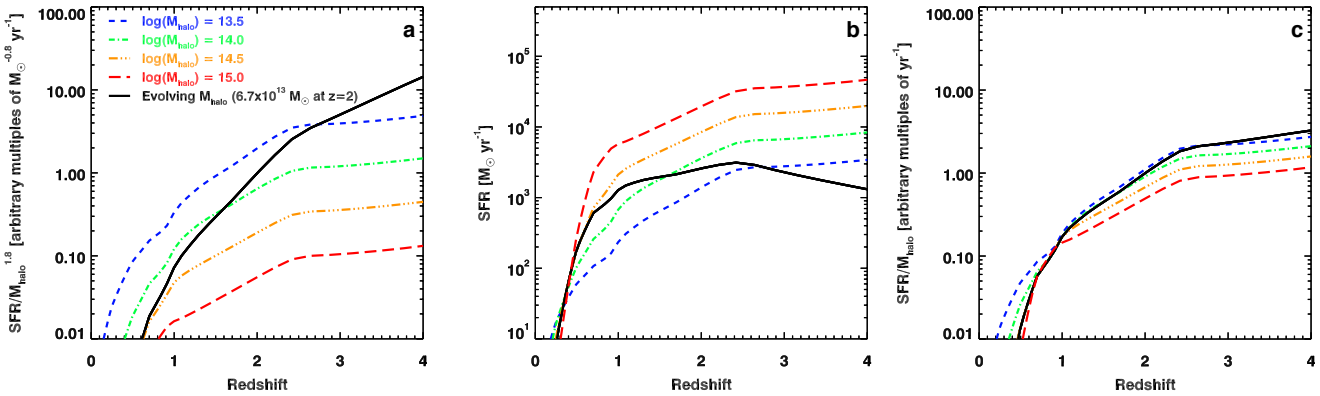

Figure 9. Expected efficacy of outflow energy injection as a function of halo mass and redshift. Based on the empirical mapping of the star formation and galaxy clustering evolution through cosmic time (Béthermin et al. 2013), we model the redshift evolution of the outflow energy injection over the thermal energy of the ICM (panel **a**). The mechanical energy injection scales as the integrated SFR in the halo, while the total thermal energy of the hot ICM increases as $E_{\rm therm} \propto T_{\rm vir}\, M_{\rm gas} \propto M_{\rm halo}^{1.8}$, assuming a gas fraction varying with the halo mass (Renzini & Andreon 2014). Hence, the y axis in panel **a** represents the 'efficacy' of the energy injection. In panel **b** we show the evolution of the SFR as a function of redshift and halo mass in Béthermin et al. (2013). The ratio SFR/$M_{\rm halo}$ changes slowly between $2 < z < 4$ (panel **c**).

(2014) is based on a sample of local bright IR galaxies with previously known outflows, which, in principle, may overestimate the outflow rates if the relation captures a phase shorter than the AGN duty cycle. On the other side, contribution from phases other than molecular and the uncertain CO luminosity-to-gas mass conversion can increase the outflow rates derived with this calibration. Indeed, strong nuclear ionized winds are now observed in fractions up to 50-70% of high-redshift AGN (Harrison et al. 2015), showing how common these features are. Moreover, the calibration by Cicone et al. (2014) is in line with the expectations from simulations reproducing the relations among black hole and galaxy bulge masses or velocity dispersions. In terms of the ratio between the kinematic energy released by AGN per unit time and their bolometric luminosity, simulations usually assume a coupling efficiency $\epsilon_{\rm f} \sim 0.05-0.15$ (i.e., Di Matteo et al. 2005; Le Brun et al. 2014, and Section 4.3 below). As we show in Section 4.2.1, the instantaneous kinetic energy associated with AGN and mass outflow rates estimated from the Cicone et al. (2014) relation is indeed $\sim$ 5% of the observed bolometric luminosities. Therefore, all things considered, we do include an AGN contribution following Cicone et al. (2014) in our fiducial estimate of the total mass outflow rate.

Finally, we note that the reasonable agreement between the replenishment rate estimates from the galaxy activity in the core and from the Lyα nebula would be just incidental if the Lyα emission were predominantly powered by shocks induced by galaxy outflows on the surrounding pressurized ICM (see Section 3.4), suggesting a lesser contribution from this mechanism. In this case, the estimate of the replenishment rate reported in Section 3.5 would not be valid. However, the independent constraint on the energy injection by galactic winds presented in the following section would be unaffected.

4.2. *Energy injection into the ICM*

Together with mass, outflows extract energy from galaxies and then deposit it into the surrounding ICM through dissipation, shocks or turbulence. In the following sections we estimate the *kinetic* energy injection, neglecting alternative contributions, i.e. from radiation.

4.2.1. *Instantaneous injection*

First, we can estimate the *instantaneous* injection of energy at the time of observation:

$$\dot{E}_{\rm kin} = \frac{1}{2}\dot{M}_{\rm out} v^2 \qquad (6)$$

where $\dot{M}_{\rm out}$ is the total amount of gas ejected per unit time at $z = 1.99$ by galaxies and v is the outflow velocity. We do not measure v in individual members in our sample, but its statistical average is quite well constrained by increasing samples of high-redshift observations. Therefore, our estimate of $\dot{E}_{\rm kin}$ should be taken in a statistical sense. We assign a wind speed of 500 km s^{-1} to SN-driven outflows for each star-forming galaxy, while for AGN-driven outflows we assume a typical speed of 1000 km s^{-1} (Genzel et al. 2014; Förster-Schreiber et al. 2014; Cicone et al. 2014). Given the baseline mass outflow rate in Section 4.1, we obtain $\dot{E}_{\rm kin}(z = 1.99) \sim 5 \times 10^{44}$ erg s^{-1}. This energy is a factor of 20 $\times$ (5$\times$) larger than the observed Lyα (X-ray) extended luminosity. The 5$\times$ factor with respect to the X-ray luminosity is sufficient to offset the global radiative cooling of the hot plasma. Assuming the balance between heating and the observed cooling rate as in local clusters would thus imply an energy injection 5$\times$ lower than estimated above. However, net heating is necessary to justify the presence of the Lyα nebula, since the cooling from the X-ray globally occurs on long timescales and is not sufficient to explain the Lyα emission (Section 3.3.4). The injected energy is coming predominantly from AGN activity ($\sim$ 85%) with a non-negligible contribution from star formation ($\sim$ 15%), while, in terms of mass, AGN are responsible for up to 2/3 of the total gas released into the ICM. SFGs would dominate the mass and energy injection only if we largely overestimated the contribution from AGN. We note that CL J1449+0856 is not anomalous in terms of star formation activity with respect to potentially similar

structures at comparable redshift (i.e., Tran et al. 2010; Yuan et al. 2014; Santos et al. 2015; Gobat et al. 2015) and it is globally consistent with the tracks reported in Figure 9 based on the model by Béthermin et al. (2013). The instantaneous energy input from AGN corresponds only to $0.05\,L_{\rm bol}^{\rm AGN}$, a factor of 3× lower than typically assumed in simulations (Section 4.3), supporting the estimate of the mass outflow rates reported in Section 4.1, while from star formation it is just $0.003\,L_{\rm bol}^{\rm SFGs}$. In general, given the SFR/$L_{\rm X}$ cosmic average (Mullaney et al. 2012) and the adopted calibrations, we expect AGN outflows to provide $5-10\times$ more energy than winds induced by star formation.

4.2.2. *Integrated energy injection*

We can now estimate the *total* energy injection up to $z = 1.99$, integrating $\dot{E}_{\rm kin}$ over time prior to observation:

$$E_{\rm kin} = \int_{t(z\geq1.99)} \dot{E}_{\rm kin}\,dt \tag{7}$$

For simplicity, we assume that the *instantaneous* energy injection is proportional to the SFR:

$$\dot{E}_{\rm kin} = \beta\,{\rm SFR} \tag{8}$$

where $\beta(z = 1.99) \sim 1.6 \times 10^{49}$ erg ${\rm M}_\odot{}^{-1}$. Then from Eq. 7:

$$\begin{aligned} E_{\rm kin} =& \int_{t(z\geq1.99)} \beta\,{\rm SFR}(t)\,dt \\ =& \frac{\beta}{1-R}\int_{t(z\geq1.99)} {\rm SFR}(t)(1-R)\,dt \\ =& \frac{\beta}{1-R}\,M_\star \end{aligned} \tag{9}$$

where $M_\star$ is the total stellar mass of 2×10^{12} ${\rm M}_\odot$ observed at $z = 1.99$ (Section 2.4 and S13) and $R = 0.4$ is the mass return into the interstellar medium (Bruzual & Charlot 2003). Eventually, we obtain $E_{\rm kin} = 5 \times 10^{61}$ erg. Considering a universal baryon fraction of $f_{\rm b} = 0.15$ in the ICM (Planck Collaboration XVI 2014), the total energy per particle in the hot ICM then is ~ 2 keV. This value is $\sim 10\%$ of the binding energy of the halo at $z = 1.99$ and of the same order of magnitude in cluster progenitors. Hence, part of the ICM particles might have been expelled by the structure at some early stage. The integrated energy is also comparable with the thermal energy per particle $E_{\rm therm} = 3/2\,k\,T$. Indeed, assuming virialization, $kT = kT_{\rm vir} = GM_{\rm halo}\mu m_{\rm H}/2R_{\rm vir} \sim 1.9$ keV and, thus, $E_{\rm therm} \sim 2.8$ keV. This is an order of magnitude estimate, as the structure is unlikely to be fully virialized at this stage – simulations suggest a thermodynamic temperature $15-20\%$ smaller than $T_{\rm vir}$ (Section 4.3). We stress here that our estimate of the integrated energy injection is affected by uncertainties on the total mass outflow rate, outflow velocities, the halo mass, and its baryon content and it depends on the assumptions we described. All things considered, the estimate may well increase or decrease by a factor of ~ 0.5 dex.

This approach relies on the use of $M_\star$ in CL J1449+0856 as a proxy for the total mass ejected through outflows in the past. This presumes the adoption of a mass loading factor of $\eta = 1$ and that v depends on local galaxy properties not evolving with time. The advantage of using $M_\star$ is the straightforward inclusion of the contribution to the energy injection by galaxies active in the past, but observed to be passive at $z = 1.99$. However, there are two important assumptions behind this results: first, we suppose that the total AGN mass outflow rate is proportional to the total SFR at any time and second, that β is constant with time.

4.2.3. *Caveats*

We justify the first assumption considering that SFR and AGN activity are correlated (Mullaney et al. 2012): statistically, on large samples the average AGN X-ray luminosity is equal to $\langle L_{\rm X}\rangle = {\rm SFR} \times 4.46 \times 10^{41}$ erg s^{-1}. Nevertheless, the AGN mass outflow rate might depend non-linearly on the AGN luminosity. For example, in the empirical relation by Cicone et al. (2014), $\dot{M}_{\rm out} \propto L_{\rm bol}^{\rm b}$ with b = 0.72. From Eq. 6, this non-linear term becomes:

$$\dot{E}_{\rm kin}^{\rm AGN} = \frac{1}{2}\dot{M}_{\rm out}^{\rm AGN} v_{\rm AGN}^2 = k_1\,L_{\rm X}^{0.72} = k_2\,{\rm SFR}^{0.72} \tag{10}$$

where k_1 and k_2 are constants including the bolometric correction linking $L_{\rm X}$ and $L_{\rm bol}$, the velocity term $v^2/2$, and the coefficients in the Cicone et al. (2014) and Mullaney et al. (2012) relations. Simply combining Eq. 8 and Eq. 10, we obtain:

$$\beta = c_1 + c_2\,{\rm SFR}^{0.72-1} \tag{11}$$

where c_1 and c_2 are constants. Thus, the non-linear term introduced by the AGN mass outflow rate impacts our result only when the total SFR in the progenitors of CL J1449+0856 drops significantly. Eq. 11 justifies also our second main assumption that β is roughly constant with time, depending only on numeric constants and the total SFR in all the cluster progenitors.

Does the total SFR in the cluster progenitors evolve with redshift? At $z > 1.99$ the SFR is spread over several subhalos that will form the observed cluster by merging. Here we trace the growth of individual dark matter halos from simulations using the Fakhouri et al. (2010) model. According to Béthermin et al. (2013), in each subhalo the total SFR peaks at $z \sim 2$ and then slowly decreases (black curve in Figure 9, panel b). However, to compute the total SFR contributing to the energy injection over time we have to consider *all* the subhalos. This corresponds to normalizing the individual SFR to the halo mass at each redshift (Figure 9, panel c). In this case, the function $X(z) = \langle{\rm SFR}(z)\rangle/M_{\rm halo}(z)$ mildly increases with redshift. Thus, the non-linear term in Eq. 11 becomes less important with redshift.

4.2.4. *Final remarks*

We attempted an alternative estimate of the total kinetic energy purely base on the tracks in Figure 9. We obtain $E_{\rm kin} \sim 5 \times 10^{61}$ erg released by galaxies over $2 < z < 4$ computed as:

$$E_{\rm kin} = \frac{1}{2}\dot{M}_{\rm repl}v^2 \int_{t(z=4)}^{t(z=2)} \frac{X(t(z))}{X(t(z=2))}\,{\rm d}t \tag{12}$$

where the function $X(z) = \langle{\rm SFR}(z)\rangle/M_{\rm halo}(z)$ accounts for the expected flat trend of $\langle{\rm SFR}\rangle$ at $2 < z < 4$ and

incorporates the integrated activity spread in halo progenitors of lower masses (Figure 9, panel c). The net effect of the integral is an increase of the time interval, from 1.7 Gyr between $2 < z < 4$ to 4.4 Gyr. This result is consistent with the one presented above, providing ~ 2 keV per particle in the hot ICM, assuming a universal baryon fraction $f_{\rm b} = \Omega_{\rm b}/\Omega_{\rm m} = 0.15$.
Here we limit the integral to $z = 4$, before which the masses of individual progenitor halos rapidly become similar to individual galaxy halos ($\approx 1 \times 10^{13}$ M$_\odot$ following Fakhouri et al. (2010)). At these masses, fast winds would have easily expelled the material from the halo, that later would have been reaccreted with the halo growth. However, observed properties of local structures may disfavor this scenario for energy injection (Ponman et al. 2003).
We note that the tracks in Figure 9 are calibrated on the observed stellar mass function of passive and star-forming galaxies residing in halos of masses of $10^{11.5} < M_{\rm halo} < 10^{13.5}$ M$_\odot$ at high redshift. However, the model does not assume any environmental dependence of galaxy properties, prominent at lower redshift. The transformation of *cluster* galaxies into red, passive, early-type systems at low redshift makes the predicted SFR a likely overestimation at $z \lesssim 1.5$ (Popesso et al. 2015). Below $z \sim 1.5$ the outflow energy contribution to the ICM is expected to be negligible with respect to the internal energy, as shown in Figure 9. We remark here that we do not make any prediction on the later growth of a massive central galaxy and its associated black hole, whose "radio" maintenance feedback looks necessary to avoid overcooling in the cluster core (McNamara & Nulsen 2007; Fabian 2012; Gaspari et al. 2012).

4.3. *Comparison with cosmological simulations*

We compared our observational results with the total energy injected by black holes into the ICM of systems similar to CL J1449+0856 at $z = 2$ in simulations. We used the two models from the suite of hydrodynamical cosmological simulations presented in Le Brun et al. (2014), which form an extension to the Overwhelmingly Large Simulations project (OWLS, Schaye et al. 2010). The first is a standard non-radiative model (NOCOOL), while the second further includes prescriptions for metal-dependent radiative cooling, star formation, stellar evolution, mass loss, chemical enrichment, stellar feedback, and AGN feedback. Among the models described in Le Brun et al. (2014), we selected the AGN 8.0 model as it provides the best match to the X-ray, Sunyaev-Zel'dovich, and optical observations of local groups and clusters (Le Brun et al. 2014; McCarthy et al. 2014). In these two models, we selected the halos with $M_{200} = (5-7) \times 10^{13}$ M$_\odot$ at $z = 2$ (yielding respectively 79 and 91 such systems in the AGN 8.0 and NOCOOL physical models). For each of these structures, we computed the mass-weighted temperature within a 300 kpc aperture, the mean entropy $S = kT/n_{\rm e}^{2/3}$ within $0.15\,R_{500}$, the virial temperature $kT_{\rm vir}$, and the binding energy. The energy injected by all the black holes lying within R_{500} is $E_{\rm inj} = M_{\rm BH}(< R_{500})c^2\epsilon_{\rm f}\epsilon_{\rm r}/(1-\epsilon_{\rm r})$, where $\epsilon_{\rm r} = 0.1$ is the radiative efficiency of the black hole accretion disk, $\epsilon_{\rm f} = 0.15$ the efficiency of the coupling of the AGN feedback to the gas, and c the speed of light. We estimate the average injected energy per particle assuming $f_{\rm b}M_{500}/\mu m_{\rm p}$ baryonic particles in the ICM, where $f_{\rm b} = 0.15$ is the universal baryon fraction (Planck Collaboration XVI 2014), $\mu = 0.6$ is the mean molecular weight, and $m_{\rm p}$ the proton mass. We obtain that the mean injected energy is of the order of 8×10^{61} erg (≈ 2.8 keV per particle, Figure 10, panel a), which is of the same order of magnitude as the typical binding energy of the selected systems. Using M_{200} instead of M_{500} in the definition of the number of particles reduces the estimate by a factor 1.4×. However, we stress that this is a rough estimate of the overall effect on the whole ICM, while in the simulations the energy injection is effective mostly in a small region surrounding the AGN. All things considered, this estimate is fully consistent with our observational estimate of ~ 2 keV per particle. The mean temperature increases from 1.44 keV to 1.73 keV when efficient AGN feedback is included (Figure 10, panel b). Moreover, the entropy within $0.15\,R_{500}$, tracing non-gravitational heating and cooling, increases from 19.9 keV cm^2 to 58.0 keV cm^2 (Figure 10, panel c). As the mean baryonic fraction within R_{500} decreases from 14% in the non-radiative model to 10.7% in the AGN 8.0 model, some of the gas which should have been contained within R_{500} in the absence of AGN feedback has been ejected, similarly to what was previously found for progenitors of $z = 0$ groups (McCarthy et al. 2011, but see Pike et al. 2014 who find that most of the AGN feedback energy is released at $z < 1$ in their simulated clusters). Overall this set of cosmological simulations predicts an energy injection due to AGN of the same order of magnitude of our estimate based on the average properties of galaxy outflows.

4.4. *Future Lyα surveys of high-redshift clusters*

The energy injection scenario based on galaxy outflows replenishing huge gas reservoirs of cold and warm gas should apply for structures similar to CL J1449+0856 and comply with the general increase of star formation and AGN activity observed in high-redshift galaxies. Do we thus expect to see giant Lyα nebulae in all massive cluster progenitors? The answer could be negative. In fact, AGN activity – which illuminates the gas expelled through outflows and keeps it ionized – might be a prerequisite for the presence of Lyα systems. Absent a powerful ionizing source, dense environments hosting strong star formation activity might not show any extended Lyα blob. This might be the case for the massive halo inside the proto-cluster region at $z = 3.09$ in the SSA22 field (Steidel et al. 2000; Kubo et al. 2015). A statistical assessment of the number of active galaxies in clusters at each stage of their evolution is important to address this issue. Nevertheless, galaxy outflows remain an ubiquitous feature of high-redshift galaxies. Are the massive gas reservoirs replenished by outflows destined to collapse and form stars according to their cooling and free-fall time? The gas in outflows is not at rest by definition. Moreover both simulations (Bournaud et al. 2014) and observations (Martin & Bouché 2009) show that outflows accelerate at larger radii because of pressure gradients in steady-state flows. This results in long collapse timescales, possibly preventing the formation of stars spread over several tens of kpc. The assembly of larger samples of clusters progenitors will allow to test

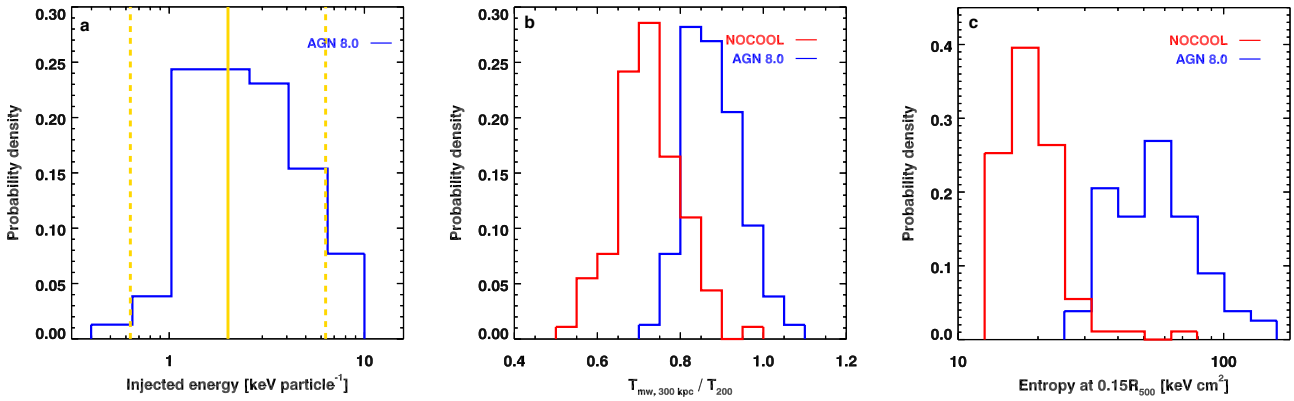

Figure 10. Temperature and entropy increase in $z = 2$ clusters when AGN feedback is active in simulations. We show the distribution of the energy per particle injected in $M_{200} = (5-7) \times 10^{13}$ M$_\odot$ systems at $z = 2$ when AGN feedback is turned on in our suite of cosmo-OWLS simulations (panel **a**) and its effect on the mass-weighted temperature within 300 kpc in units of the virial temperature $kT_{\rm vir}$ (panel **b**) and entropy at $0.15R_{\rm vir}$ (panel **c**). Blue lines indicate the reference AGN 8.0 feedback model, while red lines mark the non-radiative model (Le Brun et al. 2014). The yellow lines in panel **a** show our fiducial estimate of ~ 2 keV per particle from observations and a 0.5 dex uncertainty.

these predictions.

5. CONCLUSIONS

In this work we presented the discovery of a giant 100-kpc extended Lyα nebula in the core of a $5-7\times10^{13}$ M$_\odot$, X-ray detected cluster at $z = 1.99$. This discovery reveals the coexistence of warm ionized blobs and the hot intergalactic medium and extends the known relation between Lyα nebulae and overdense regions of the Universe to the dense core of a relatively mature cluster. We pinpointed two X-ray AGN as the most likely candidates to power the nebula, disfavoring ionization from very young stars and cooling from the X-ray phase in the form of a stationary classical cooling flow. In principle, regulated cooling as in local cool-core clusters could partially contribute to the Lyα luminosity, but several inconsistencies between CL J1449+0856 and local systems are evident. Above all, the ratio between the Lyα luminosity and the total X-ray luminosity is a factor $10 - 1000\times$ higher in CL J1449+0856 than in local CCs even in those cases where strong radio-sources are present (i.e., Perseus). Dissipation of mechanical energy injected by galaxy outflows may also contribute to the total Lyα luminosity. The interaction between the Lyα nebula and the surrounding hot ICM requires a $\gtrsim$ 1000 M$_\odot$ yr^{-1} gas replenishment rate to sustain the nebula against evaporation. We explore galaxy outflows in the cluster core as a possible source of gas supply and find that the generous total SFR ($\approx$ 1000 M$_\odot$ yr^{-1}) and the outflow rate owing to the growth of supermassive black holes ($\approx$ 1400 M$_\odot$ yr^{-1}) are sufficient to replenish the nebula. This directly implies a significant injection of kinetic energy into the ICM up to ≈ 2 keV per particle, in agreement with the predictions from the cosmo-OWLS simulations and with constraints set by the thermodynamic properties of local massive structures. In our baseline scenario the AGN channel provides up to 85% of the total injected energy, with the rest supplied by star formation through SNe-driven winds. The instantaneous energy injection exceeds by a factor of 5 the current X-ray luminosity, offsetting the global cooling from the X-ray phase. Nevertheless, the high star formation and black hole accretion rates deep in the potential well of this cluster support the general increase in galaxy activity observed in similar structures at comparable redshift and challenge the current prescriptions on the fueling by cosmological cold flows penetrating in massive halos. If this structure is not just a curious anomaly, the potential presence of cold streams despite its high mass would lead to important consequences on the "halo quenching" mechanism and, thus, on galaxy formation and evolution in general.

The advent of forthcoming facilities will allow us to drastically reduce observational uncertainties and avoid a heavy resort to assumptions. Measurements of temperature, pressure, and entropy profiles of the hot ICM in young clusters will be possible with the foreseen Athena X-ray satellite, while the systematic follow-up of Lyα emission in clusters at $z > 2-3$ could start soon with new wide field integral field spectrographs on large telescopes, like MUSE and KCWI. Spectroscopy in the ultra-violet range provides crucial information on the kinematics of the nebula, the metal enrichment, and its main powering mechanism. If the scenario we propose here is correct, we expect the Lyα nebula to show signatures of complex motion due to outflows and to be fairly metal-rich. Eventually, the arising coherent scenario we sketch could help to understand the global early evolution of massive structures.

We acknowledge the constructive comments of the referee and we thank Daniel Perley for the support during the reduction of Keck/LRIS data with his pipeline. Some of the data presented therein were obtained at the W.M. Keck Observatory, which is operated as a scientific partnership among the California Institute of Technology, the University of California and the National Aeronautics and Space Administration. Keck telescope time was granted by NOAO (Prop. ID: 2014A-0131), through the Telescope System Instrumentation Program (TSIP). TSIP is funded by NSF. The Observatory was made possible by the generous financial sup-

port of the W.M. Keck Foundation. The authors wish to recognize and acknowledge the very significant cultural role and reverence that the summit of Mauna Kea has always had within the indigenous Hawaiian community. We are most fortunate to have the opportunity to conduct observations from this mountain. The scientific results reported in this article also are based in part on observations made by the Chandra X-ray Observatory. AF acknowledges the Chandra grant GO4-15133A to UMBC. This paper also makes use of the following ALMA data: ADS/JAO.ALMA#2012.1.00885.S. ALMA is a partnership of ESO (representing its member states), NSF (USA) and NINS (Japan), together with NRC (Canada), NSC and ASIAA (Taiwan), and KASI (Republic of Korea), in cooperation with the Republic of Chile. The Joint ALMA Observatory is operated by ESO, AUI/NRAO and NAOJ. We acknowledge financial support from the Agence Nationale de la Recherche (contracts #ANR-12-JS05-0008-01) and the EC through the European Research Council Starting grants StG-257720 and StG-240039, and the Advanced grant FP7-340519.

REFERENCES

Andreon, S., Maughan, B., Trinchieri, G., & Kurk, J. 2009, A&A, 507, 147
Arnaud, M., Pratt, G. W., Piffaretti, R., et al. 2010, A&A, 517, A92
Arrigoni-Battaia, F., Hennawi, J. F., Prochaska, J. X. & Cantalupo, S. 2015, ApJ, 809, 163
Bayer-Kim, C. M., Crawford, C. S., Allen, S. W., Edge, A. C., & Fabian, A. C. 2002, MNRAS, 337, 938
Béthermin, M., Wang, L., Doré, O., et al. 2013, A&A, 557, A66
Borisova, E., Cantalupo, S., Lilly, S. J., et al. 2016, ArXiv e-prints, arxiv:1605.01422
Bournaud, F., Perret, V., Renaud, F., et al. 2014, ApJ, 780, 57
Bower, R. G., Morris, S. L., Bacon, R., et al. 2004, MNRAS, 351, 63
Brodwin, M. and McDonald, M. and Gonzalez, A. H., et al. 2015, ArXiv e-prints, arxiv:1504.01397
Brusa, M., Comastri, A., Daddi, E., et al. 2005, A&A, 432, 69
Bruzual, G. & Charlot, S. 2006, MNRAS, 344, 1000
Bunker, A. J., Warren, S. J., Hewett, P. C., & Clements, D. L. 1995, MNRAS, 273, 513
Campisi, M. A., Vignali, C., Brusa, M., et al. 2009, A&A, 501, 485
Cantalupo, S., Porciani, C., Lilly, S. J. & Miniati, F. 2005, ApJ, 628, 61
Cantalupo, S., Arrigoni-Battaia, F., Prochaska, J. X., Hennawi, J. F., & Madau, P. 2014, Nature, 506, 63
Churazov, E., Brüggen, M., Kaiser, C. R., Böhringer, H., & Forman, W. 2001, ApJ, 554, 261
Cicone, C., Maiolino, R., Sturm, E., et al. 2014, A&A, 562, A21
Conselice, C. J., Gallagher, III, J. S., & Wyse, R. F. G. 2001, AJ, 122, 2281
Cowie, L. L., Fabian, A. C., & Nulsen, P. E. J. 1980, MNRAS, 191, 399
Crawford, C. S., & Fabian, A. C. 1989, MNRAS, 239, 219
Daddi, E., Bournaud, F., Walter, F., et al. 2010, ApJ, 713, 686
Danovich, M., Dekel, A., Hahn, O., Ceverino, D., & Primack, J. 2015, MNRAS, 449, 2087
Davé, R., Oppenheimer, B. D., & Sivanandam, S. 2008, MNRAS, 391, 110
Dekel, A., Birnboim, Y., Engel, G., et al. 2009, Nature, 457, 451
Dey, A., Bian, C., Soifer, B. T., et al. 2005, ApJ, 629, 654
Dijkstra, M., Haiman, Z., & Spaans, M. 2006, ApJ, 649, 37
Di Matteo, T., Springel, V., & Hernquist, L. 2005, Nature, 433, 604
Elvis, M., Wilkes, B. J., McDowell, J. C., et al. 1994, ApJS, 95, 1
Fabian, A. C. 2012, ARA&A, 50, 455
Fabian, A. C., Johnstone, R. M., Sanders, J. S., et al. 2008, Nature, 454, 968
Fabian, A. C., Nulsen, P. E. J., & Arnaud, K. A. 1984a, MNRAS, 208, 179
Fabian, A. C., Nulsen, P. E. J., & Canizares, C. R. 1984b, Nature, 310, 733
Fabian, A. C., Crawford, C. S., Johnstone, R. M., & Thomas, P. A. 1987, MNRAS, 228, 963
Fabian, A. C., Sanders, J. S., Crawford, C. S., et al. 2003, MNRAS, 344, L48
Fakhouri, O., Ma, C.-P., & Boylan-Kolchin, M. 2010, MNRAS, 406, 2267
Finoguenov, A., Guzzo, L., Hasinger, G., et al. 2007, ApJS, 172, 182
Förster Schreiber, N. M., Genzel, R., Newman, S. F., et al. 2014, ApJ, 787, 38
Francis, P. J., Woodgate, B. E., Warren, S. J., et al. 1996, ApJ, 457, 490
Gabor, J. M., & Bournaud, F. 2014, MNRAS, 441, 1615
Gaspari, M., Ruszkowski, M., & Sharma, P. 2012, ApJ, 746, 94
Geach, J. E., Alexander, D. M., Lehmer, B. D., et al. 2009, ApJ, 700, 1
Genzel, R., Förster Schreiber, N. M., Rosario, D., et al. 2014, ApJ, 796, 7
George, M. R., Leauthaud, A., Bundy, K., et al. 2011, ApJ, 742, 125
Gobat, R., Daddi, E., Onodera, M., et al. 2011, A&A, 526, A133
Gobat, R., Strazzullo, V., Daddi, E., et al. 2013, ApJ, 776, 9
Gobat, R., Daddi, E., Béthermin, M., et al. 2015, A&A, 581, A56
Goerdt, T., Dekel, A., Sternberg, A., et al. 2010, MNRAS, 407, 613
Harrison, C. M., Alexander, D. M., Mullaney, J. R., et al. 2015, ArXiv e-prints, arxiv:1511.00008
Hatch, N. A., Crawford, C. S., & Fabian, A. C. 2007, MNRAS, 380, 33
Hatch, N. A., Crawford, C. S., Fabian, A. C., & Johnstone, R. M. 2005, MNRAS, 358, 765
Hatch, N. A., Overzier, R. A., Röttgering, H. J. A., Kurk, J. D., & Miley, G. K. 2008, MNRAS, 383, 931
Heckman, T. M., Baum, S. A., van Breugel, W. J. M., & McCarthy, P. 1989, ApJ, 338, 48
Heckman, T. M., Kauffmann, G., Brinchmann, J., et al. 2004, ApJ, 613, 109
Hennawi, J. F., & Prochaska, J. X. 2013, ApJ, 766, 58
Hopkins, P. F., Quataert, E., & Murray, N. 2012, MNRAS, 421, 3522
Kaiser, N. 1991, ApJ, 383, 104
Kennicutt, Jr., R. C. 1998, ARA&A, 36, 189
Klein, R. I., McKee, C. F., & Colella, P. 1994, ApJ, 420, 213
Kubo, M., Yamada, T., Ichikawa, T., et al. 2015, A&A, in press
Le Brun, A. M. C., McCarthy, I. G., Schaye, J., & Ponman, T. J. 2014, MNRAS, 441, 1270
Le Brun, A. M. C., McCarthy, I. G., & Melin, J.-B. 2015, MNRAS, 451, 3868
Leauthaud, A., Finoguenov, A., Kneib, J.-P., et al. 2010, ApJ, 709, 97
Ledlow, M. J., Voges, W., Owen, F. N. & Burns, J. O. 2003, AJ, 126, 2740
Lilly, S. J., Carollo, C. M., Pipino, A., Renzini, A., & Peng, Y. 2013, ApJ, 772, 119
Lusso, E., Comastri, A., Simmons, B. D., et al. 2012, MNRAS, 425, 623
Magdis, G. E., Daddi, E., Béthermin, M., et al. 2012, ApJ, 760, 6
Martin, C. L. and Bouché, N. 2009, ApJ, 703, 1394
Matsuda, Y., Yamada, T., Hayashino, T., et al. 2004, AJ, 128, 569
McCarthy, I. G., Le Brun, A. M. C., Schaye, J., & Holder, G. P. 2014, MNRAS, 440, 3645
McCarthy, I. G., Schaye, J., Bower, R. G., et al. 2011, MNRAS, 412, 1965
McCarthy, P. J., Spinrad, H., Dickinson, M., et al. 1990, ApJ, 365, 487
McDonald, M., Veilleux, S., Rupke, D. S. N., & Mushotzky, R. 2010, ApJ, 721, 1262
McNamara, B. R., & Nulsen, P. E. J. 2007, ARA&A, 45, 117
McNamara, B. R., Russell, H. R., Nulsen, P. E. J. et al. 2014, ApJ, 785, 44
Miley, G. K., Overzier, R. A., Zirm, A. W., et al. 2006, ApJ, 650, L29

Mullaney, J. R., Daddi, E., Béthermin, M., et al. 2012, ApJ, 753, L30
Navarro, J. F., Frenk, C. S., & White, S. D. M.. 1997, ApJ, 490, 493
Newman, S. F., Genzel, R., Förster-Schreiber, N. M., et al. 2012, ApJ, 761, 43
O'Dea, K. P., Quillen, A. C., O'Dea, C. P., et al. 2010, ApJ, 719, 1619
Osterbrock, D. E., & Ferland, G. J. 2006, Astrophysics of gaseous nebulae and active galactic nuclei
Papovich, C., Momcheva, I., Willmer, C. N. A., et al. 2010, ApJ, 716, 1503
Peterson, J. R., & Fabian, A. C. 2006, Phys. Rep., 427, 1
Piconcelli, E., Jimenez-Bailón, E., Guainazzi, M., et al. 2005, A&A, 432, 15
Pike, S. R., Kay, S. T., Newton, R. D. A., Thomas, P. A., & Jenkins, A. 2014, MNRAS, 445, 1774
Planck Collaboration XVI, Ade, P. A. R., Aghanim, N., Armitage-Caplan, C., et al. 2014, A&A, 571, A16
Ponman, T. J., Cannon, D. B., & Navarro, J. F. 1999, Nature, 397, 135
Ponman, T. J., Sanderson, A. J. R., & Finoguenov, A. 2003, MNRAS, 343, 331
Popesso, P., Biviano, A., Finoguenov, A., et al. 2015, A&A, 579, A132
Prescott, M. K. M., Dey, A., & Jannuzi, B. T. 2009, ApJ, 702, 554
—. 2012, ApJ, 748, 125
—. 2013, ApJ, 762, 38
Renzini, A., & Andreon, S. 2014, MNRAS, 444, 3581
Salomé, P., Combes, F., Revaz, Y. et al. 2011, A&A, 531, A85
Santos, J. S., Fassbender, R., Nastasi, A., et al. 2015, A&A, 531, L15
Santos, J. S., Altieri, B., Valtchanov, I., et al. 2015, MNRAS, 447, L65
Scannapieco, E., & Brüggen, M. 2015, ApJ, 805, 158
Schaerer, D. 2003, A&A, 397, 527
Schaye, J., Dalla Vecchia, C., Booth, C. M., et al. 2010, MNRAS, 402, 1536
Sharma, P., McCourt, M., Quataert, E. & Parrish, I. J. 2012, MNRAS, 420, 3174
Spitzer, L. 1978, Physical processes in the interstellar medium
Stanford, S. A., Brodwin, M., Gonzalez, A. H., et al. 2012, ApJ, 753, 164
Starck, J. L., Saber Naceur, M., & Murtagh, R., eds. 2010, 6th Astronomical Data Analysis Conference
Steidel, C. C., Adelberger, K. L., Shapley, A. E., et al. 2000, ApJ, 532, 170
Strazzullo, V., Gobat, R., Daddi, E., et al. 2013, ApJ, 772, 118
Sutherland, R. S., & Dopita, M. A. 1993, ApJS, 88, 253
Tacconi, L. J., Neri, R., Genzel, R., et al. 2013, ApJ, 768, 74
Thompson, T. A., Fabian, A. C., Quataert, E. & Murray, N. 2015, MNRAS, 449, 147
Tozzi, P., & Norman, C. 2001, ApJ, 546, 63
Tran, K.-V. H., Papovich, C., Saintonge, A., et al. 2010, ApJ, 719, L126
Tremblay, G. R., O'Dea, C. P., Baum, S. A., et al. 2015, MNRAS, 451, 3768
Valentino, F., Daddi, E., Strazzullo, V., et al. 2015, ApJ, 801, 132
van der Burg, R. F. J., Muzzin, A., Hoekstra, H., et al. 2014, A&A, 561, A79
Venemans, B. P., Röttgering, H. J. A., Miley, G. K., et al. 2007, A&A, 461, 823
Voit, G. M., & Donahue, M. 2015, ApJ, 799, L1
Wilman, R. J., Edge, A. C., & Swinbank, A. M. 2006, MNRAS, 371, 93
Yuan, T., Nanayakkara, T., Kacprzak, G. G., et al. 2014, ApJ, 795, L20
Zibetti, S., White, S. D. M., Schneider, D. P., & Brinkmann, J. 2005, MNRAS, 358, 949

APPENDIX

We show the unsmoothed Lyα image from the Keck/LRIS narrow-band follow-up of CL J1449+0856 in panel (a) of Figure 11. The only purpose is to demonstrate that the Lyα emission is not dominated by individual galaxies, but it is distributed fairly homogeneously over several square arcsec. The very low surface brightness regimes probed in this image make the identification of the nebula difficult by eye. It is easier to recognize it by comparing the original narrow- and broad-band images shown in Figure 2 or, alternatively, with a moderate smoothing (1", Figure 2 and 11 panels b-d). To guide the eye and pinpoint the peak of the extended emission, in panels (b-d) of Figure 11 we show the contours of the wavelet reconstructed Lyα image. In each panel we show the contours after the subtraction of point-like sources, retaining only the signal on larger scales, namely the Lyα nebula. Panel (b) shows the maximum extension of the Lyα nebula, while the smoother denoised contours in panels (c) and (d) allow for identifying the peak of the extended emission. The appearance of two peaks in panel (c) depends on the number of scales adopted to slice the image with the wavelet technique and does not affect the main findings of this work. The region spanned by the $\geq 5\sigma$ detection in panel (d) is the same used to measure the extended continuum emission (Section 2.2). In every panel the number of contours is chosen arbitrarily to highlight the peak of the emission and does not correspond to a fixed step in surface brightness.

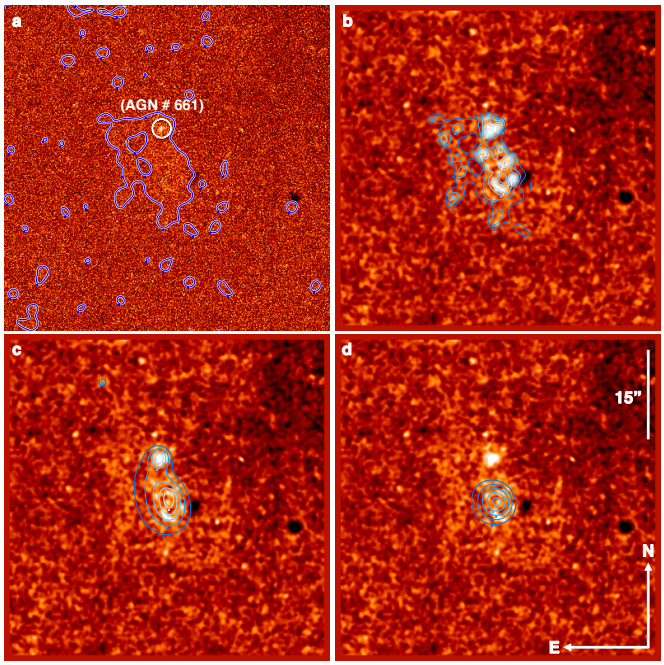

Figure 11. Wavelet reconstruction of the Lyα image. We show the original unsmoothed Lyα emission line map of the central region of CL J1449+0856 in panel **a**. The 1σ contour of the large scale Lyα emission from the wavelet reconstruction (blue line) and the X-ray obscured AGN (white circle) are marked for reference. Panels **b, c**, and **d** show the reconstructed wavelet contours at $\geq 1\sigma$, $\geq 3\sigma$, and $\geq 5\sigma$ respectively (blue lines) of the Lyα emission line map. Point-like sources have been subtracted before computing the surface brightness contours. The number of contours is arbitrary and chosen to pinpoint the peak of the extended emission. For reference, 15” correspond to ~ 125 kpc at $z = 1.99$.

B | PROPOSALS

B.1 APPROVED PROPOSALS

• **F. Valentino**, E. Daddi, V. Strazzullo, et al. 2014, *A $z \sim 2.2$ galaxy cluster confirmation and its metallicity content*, VLT/KMOS 2.5/5 hours observed (ongoing reduction).

• **F. Valentino**, E. Daddi, R. Gobat, et al. 2015, *The demographics of the star-forming population in an X-ray detected cluster at $z = 1.99$: low metallicities and enhanced star formation rates*, VLT/KMOS 7.5/7.5 hours observed (ongoing reduction).

• **F. Valentino**, A. Zanella, E. Daddi, et al. 2015, *Investigating galaxy evolution on large and small scales: two compelling puzzles to be solved by a MUSE*, VLT/MUSE 1.5/1.5 hours observed (DDT, fully reduced, analysis ongoing).

• **F. Valentino**, E. Daddi, V. Strazzullo, et al. 2015-2016, *CO investigation of an extreme $10\times$ sky overdensity of ALMA-850 μm sources around a cluster at $z = 2$*, IRAM – Plateau de Bure Interferometer/NOEMA $0/50 + 5$ hours observed.

• E. Daddi, **F. Valentino**, V. Strazzullo, et al. 2016, *Lyα nebulae and the pre-heating of cluster progenitor atmospheres*, VLT/VIMOS 0/3 hours observed.

• Several proposals ($\sim$ 15) accepted at VLT/KMOS, VLT/SINFONI, ALMA, Gemini/GMOS, Gemini/FLAMINGOS-2, IRAM – Plateau de Bure Interferometer/NOEMA as co-I.

B.2 PENDING PROPOSALS

• **F. Valentino**, E. Daddi, V. Strazzullo, et al. 2016, *Can we use giant Lyα nebulae to trace the early heating of intracluster plasma in cluster progenitors?*, VLT/FORS2 1 night. [Update: Approved]

• **F. Valentino**, E. Daddi, M. Giavalisco, et al. 2016, *Can giant Lyα nebulae trace energy injection into intracluster media? A spatial exploration of their connection with evolved clusters at $z > 1.7$*, *HST*/WFC3 15 orbits.

[Update: Rejected]

• **F. Valentino**, E. Daddi, G. Magdis, et al. 2016, *A [CI] survey of high-redshift main sequence galaxies*, ALMA 8 hours. [Update: Approved]